A measurement of the differential cross-section for inclusive $\tau\tau$ production at high-mass in proton-proton collisions at the ATLAS detector

LUZHAN YUE

UNIVERSITY COLLEGE LONDON
DEPARTMENT OF PHYSICS & ASTRONOMY

SUBMITTED TO UNIVERSITY COLLEGE LONDON (UCL) IN PARTIAL FULFILMENT OF THE REQUIREMENTS FOR THE AWARD OF THE DEGREE OF DOCTOR OF PHILOSOPHY.

PRIMARY SUPERVISOR: **PROF. JONATHAN BUTTERWORTH**
SECONDARY SUPERVISOR: **PROF. CHAMKAUR GHAG**
EXAMINING COMMITTEE: **PROF. ERAM RIZVI**
PROF. GAVIN HESKETH

THESIS SUBMISSION DATE: **19TH MARCH 2025**

Declaration

I, **Luzhan Yue**, confirm that the work presented in this thesis is my own. Where information has been derived from other sources, I confirm that this has been indicated in the thesis.

Luzhan Yue
London, United Kingdom
19th March 2025

Abstract

This thesis primarily focuses on describing the design and results of the high mass $\tau\tau$ measurement using the 139 fb^{-1} Run 2 data collected at 13 TeV during proton-proton collisions at the Large Hadron Collider (LHC) with the ATLAS detector. This analysis explores a kinematic region that was not previously probed for the τ lepton, with an emphasis on flexibility and reuseability through a model-independent approach. By utilising the visible final states with $m_{\ell\ell} > 100$ GeV, the study aims to explore the high mass regions that closely aligned with the detector's acceptance, known as the fiducial region. The motivation for this high-mass $\tau\tau$ measurement stems from the anomalies observed in the rare decays of b mesons at the LHCb [1], which suggest deviations that could be more pronounced in third-generation leptons [2]. These anomalies could potentially be explained by the leptoquark model [3] and vector-like-leptons (VLL) model [4]. As an example of using such measurement to set limits and enhance re-interpretation power in searches for new physics, a `CONTUR` [5]-driven reinterpretation study is preformed using existing measurements to set constraints on the simplest VLL doublet model [4]. The result suggests an improvement from around 280 GeV to around 410 GeV on the third-generation doublet VLL mass `CONTUR`-limit by adding this new $\tau\tau$ measurement.

Impact Statement

Understanding the fundamental nature of the universe is one of humanity's most profound scientific pursuits. The Large Hadron Collider (LHC) at CERN provides an exciting opportunity for people to explore the fundamental interactions at the highest possible energies, enabling us to rigorously test the Standard Model (SM) and search for new physics beyond it. Using data collected by the ATLAS detector, one of the key avenues for probing new physics is the study of high-mass $\tau\tau$ final states, which serves as a sensitive probe for potential new physics signals.

This thesis contributes to these efforts within the ATLAS experiment, focusing on the measurement of the $\tau\tau$ mass distribution and enhancing the sensitivity of measured data for reinterpretation studies. By using a model-independent measurement approach, which maximises the impact of the measured data, this work strengthens constraints on potential Beyond Standard Model (BSM) physics and provides valuable tools for future LHC analyses.

Beyond its immediate contributions to LHC physics, the analytical frameworks and statistical approaches presented in this thesis such as the Bayesian statistics, large data analytics, offer broader applications in interdisciplinary fields of the data science regime and other real-world applications.

Acknowledgements

I would like to express my deepest gratitude to my supervisor, Prof. Jonathan Butterworth, for first and foremost accepting me as his student five years ago. This journey would not have been possible without that very first step. I feel incredibly fortunate to have had the opportunity to work with him throughout both my Master's and PhD. His encouragement, patience, and insightful advice have profoundly shaped my growth as a researcher, and I could not have asked for a kinder, smarter, and more supportive mentor.

I am also immensely thankful to Dr. Christian Gütschow, who generously shared his technical expertise, deep understanding of physics, and valuable experiences with me, which is something I consider truly invaluable. He was always willing to lend his time to me whenever I asked for his guidance and has supported at every stage of my PhD journey since the start of the analysis, for which I am deeply grateful. I owe him a great debt of gratitude for his generosity, patience, and mentorship.

I would also like to extend my heartfelt thanks to my fellow disciple and friend, Peng Wang, who has not only been a collaborator but also a constant source of encouragement and camaraderie throughout the analysis journey. I am extremely greatful to have had her joined the analysis, sharing the highs and lows of our work in the measurement together has made the experience all the more rewarding and fun. I would also like to acknowledge my friend, Yuanda Zhu, who contributed during the early stages of the measurement and engaged in meaningful discussions that helped shape my understanding of the measurement. Similarly, a heartfelt thank you to my friend Yoran Yeh, who, despite working on a different analysis, was always willing to share insights and offer valuable advice that greatly assisted me in navigating my own research.

To the wider analysis team—Dr. Chris Pollard, Prof. Chris Hays, Simon Koch, Giovanni Padovano, Federico Morodei, Tomoya Lizawa, and Caio Daumann, thank you for

your insightful discussions, constructive feedback, and collaborative spirit that made this process so much more engaging, fulfilling and enjoyable.

Beyond academia, I am deeply grateful to my family and my girlfriend, Sherry, whose unwavering support and encouragement have carried me through the most challenging moments. Their belief in me has always been a source of strength and motivation.

Finally, I want to express my appreciation to everyone who has been part of this journey, whether through their direct contributions, thoughtful discussions, or simply offering words of encouragement along the way. This thesis is not just my work but a reflection of the collective kindness, generosity, and brilliance of all the incredible people I have had the privilege to work with. I am truly grateful to have been surrounded by such an inspiring and supportive group.

Contents

List of Figures

List of Tables

Chapter 1

Introduction

The study of particle (High-energy) physics stands as one of the most captivating and fundamental pursuits in our quest to explain the universe. At its core, particle physics aims to unravel the smallest constituents of matter and the fundamental forces governing their interactions, seeking answers to age-old questions: What is universe made of? Can we predict everything with a single theory? How will the universe end? These inquiries have long inspired brilliant minds, driving physicist and philosophers to monumental discoveries and theoretical breakthroughs that have reshaped our understanding of the world we thought we knew and paved the way for revolutionary technological innovations. Yet, as we move further into the mysteries of the universe, we realise how much remains to be understood, which is a realisation that fuels our enthusiasms and determination to uncover the ultimate truths. For this PhD thesis, I will be presenting the works that I have performed as one of the member of a particle physics research group that was the first to perform an analysis on the high-mass $\tau\tau$ data from the ATLAS experiment. The thesis will discuss the design, operation and results from the analysis, along with detailed experimental and theoretical backgrounds.

The most successful theory to date in addressing our present world is the Standard Model (SM), recognised as a significant milestone in our comprehension of the fundamental structure of the universe. To advance our understanding and answer the questions, there are still two broad objectives ahead. Firstly, we need to validate the current SM by examining its validity across different domains and the extent to which the current theory and the observed data can constrain new models. Secondly, despite its successes on establishing a theoretical framework for interactions, the fact that the SM remains incomplete necessitates the search for physics beyond the SM (BSM), such as dark matter, a complete theory of neutrinos, quantum gravity, and meanwhile integrating these concepts into the existing theoretical framework by looking for observational support for validations and corrections. Hence, these pursuits motivated the construction of dedicated experiments like the Large Hadron Collider (LHC), representing one of the most advanced projects in experimental particle physics. The LHC operates on the energy-frontier, facilitating the exploration of particle physics at the high-energy regimes and is capable of generating particle signals that are not observable in everyday life through proton collisions, which enables various searches and measurements. Proton collisions occur at the focal points of four main experiments around the LHC ring: ATLAS, CMS, LHCb, and ALICE. Notably, the ATLAS and CMS experiments have announced the discovery of the Higgs Boson, marking the most significant breakthroughs in 21st-century particle physics.

The measurement outlined in this thesis diverges from the conventional methodology employed in BSM searches, which typically involves dedicated direct searches at the detector level. Instead, the measurement is tailored to facilitate complementary theory comparisons and recyclability. In this thesis, the focus will be to introduce the design and outcomes of such a measurement performed on the high-mass regime of a fundamental lepton particle τ that decays into various hadronic signals. Subsequently, the discussion will extend to the implications of such a measurement and its role in establishing constraints on diverse BSM models on corresponding phase spaces.

The measurement, which differs from the traditional way for BSM hunting using dedicated direct searches at the detector-level aims to offer a broader perspective by incorporating model-independence, thereby enriching our understanding of the SM and the BSM physics while maximising the utility of experimental data. The thesis begins with introductions to the theoretical and experimental premise for performing the measurement, followed by presenting the design and result of such a measurement on the high-mass τ signals. The results are then compared with state-of-the-art SM predictions, and then eventually discuss how such a measurement will help setting constraints on various BSM models' regions.

The thesis structure is summarised and outlined as follows:

- Chapter 2 offers a brief overview of the SM, and the BSM model on Vector-like-Leptons, setting the foundation for the subsequent discussions.
- Chapter 3 provides an detailed description of the experimental setups of the ATLAS experiment, along with an introduction to the corresponding simulations employed in the analysis.
- Chapter 4 is the centerpiece of the thesis, focusing on the measurement details and highlighting the unfolding methodology employed to obtain the results from using the LHC Run-II data and simulations.
- Chapter 5 discuss the concept of setting constraints and describe how the di-τ measurement is applied within this context using the `CONTUR` [6] toolkit to set constraints for the Vector-like-Leptons model discussed in chapter 2, and compare the result to the most-recent ATLAS dedicated search on the same model.
- Chapter 6 concludes the thesis by giving a summary of the main results.

1.1 Declaration of contributions

The measurement is part of the ATLAS collaboration involving contributions from many people. The Monte Carlo simulations and data collection relied on a diverse team including engineers, technicians, experimentalists, theorists, and computer engineers, totalling around 5000 members. The measurement, serving as a data analysis project is a group effort monitored by the ATLAS collaboration. The analysis team members that have conducted the analysis are primarily from academic institutes and the existence of the analysis-related content presented within this thesis would not have been possible without their efforts. The author were responsible for the unfolding measurement related studies that are discussed in section 4. The areas of analysis that contributed by the author are outlined below:

- Monte Carlo sample validation and cross-checks, all subsections in section 4.6.
- Binning optimisation for observable, section 4.6.2.
- Development of a unfolding pipeline incorporated all functions needed to produce the result, all subsections in section 4.6.
- Unfolding closure tests using Monte Carlo samples, section 4.6.
- Monte Carlo re-weighting tests, section 4.6.5.
- Unfolding hyperparameter optmisation, section 4.6.8.
- Signal injection tests, section 4.6.6.
- Unfolding uncertainties propagation, sections 4.7.
- Particle-level result recycling and validation (`RIVET` routine), section 4.6.7.
- Experimental uncertainties pruning, section 4.7.
- Unfolding the data to produce the final measured results, section 4.9.
- Data preparation onto Hepdata [7] and re-interpretation on the third-generation VLL model using `CONTUR`, section 5.

Collaborative efforts from the UCL analysis team members, Professor Jonathan Butterworth, Dr. Christian Gütschow and Peng Wang were used for these outlined sections. For other sections of the analysis that were mentioned in this thesis including detector-level fitting, background (fakes) estimations, theoretical BSM interpretations, the author have not directly worked on these areas.

Chapter 2

The best particle physics theory so far: The Standard Model

The SM, developed throughout the latter half of the 20th century, provides a comprehensive framework that describes the behavior of elementary particles and their interactions through fundamental forces including the electromagnetic force, the weak force and the strong force, but excludes the gravity. The SM has been grouped into various subgroups with overlaps based on the properties of the particles. The introduction to the SM will start from this group-wise perspective.

In the SM, elementary particles are categorised into two main classes: fermions and bosons, figure 2.1 shows an illustration of the summary table. The fermions consists of quarks and leptons which are sub-classified groups. They are the building blocks of matter and antimatter (using their corresponding antiparticles which have identical mass but opposite charge) and possess half-integer values of intrinsic spin. The quarks are located at the top right section of figure 2.1 and are having a total of six flavours: up (u), down (d), charm(c), strange(s), top(t), bottom(b). These names were chosen somewhat whimsically, but they do carry some meaning related to their properties and behaviours.

- **Up and down quarks**: These were named by Murray Gell-Mann, who proposed the quark model where the names describe the fractional electric charge of these particles [8]. The up quark has a charge of $\frac{2}{3}$ and the down quark has a charge of -$\frac{1}{3}$.
- **Strange and charm quarks**: The name *strange* quark was proposed by Gell-Mann

and George Zweig to describe a new type of particle that was observed in cosmic ray experiments in 1950s. The term *strangeness* was introduced to account for the unusually long lifetime of these particles, which appeared anomalous compared to other particles discovered at the time [8]. The charm quark was later discovered in 1974 in experiments at the Stanford Linear Accelerator Center (SLAC) and Brookhaven National Laboratory. The name *charm* was selected to highlight its charming properties, including its relatively heavy mass and the role it played in the at-the-time newly emerging theory of quantum chromodynamics (QCD). The strange and charm quarks are exhibiting a charge of $\frac{2}{3}$ and -$\frac{1}{3}$ respectively [8].

- **Top and bottom quarks**: These names were chosen to complement the up and down quarks. The top quark, discovered in 1995 at Fermilab is the most massive of all known quarks, while the bottom quark (also known as the beauty quark) is relatively heavy as well. The name *top* reflects the hierarchy of masses among the quarks and the name *bottom* was chosen to create a semantic symmetry in the naming scheme. The top and bottom quarks carry electric charges of $\frac{2}{3}$ and -$\frac{1}{3}$ respectively [8].

Quarks also carry an additional property called colour charge (red, green, blue), which is analogous to the electric charge to represent their participation in the strong interaction governed by Quantum Chromodynamics (QCD). The asymptotic freedom property make the strength of the strong interaction decreases as the quarks comes closer together at close distance and the infrared slavery property make the strength of the strong force increase as the distance increases. This property leads to quark confinement, meaning quarks are always found within composite particles called hadrons.

Leptons make up the other half of the fermion class. Unlike quarks, which are confined within composite particles by the strong force, leptons remain elementary and do not participate in the strong force. Instead, they interact through the electromagnetic force and the weak force, which are collectively described by the electroweak theory.

The term *lepton* derived from the Greek word *lepto* meaning light or small to reflect the lighter nature and elementary status of these particles compared to their quark counterparts. The lepton family includes three charged particles: the electron (e), the muon (μ) and the tau (τ). The lepton number conservation law in particle physics dictate that lepton numbers must be conserved in interactions. Each type of charged leptons has an associated lepton number and can only be conserved in many interactions when including another type of chargeless particle named *neutrinos*. Each charged lepton is associated with a corresponding type of neutrino sharing the same lepton number. These three neutrinos: ν_e, ν_μ, ν_τ are also classified as leptons. The charged leptons exhibit a clear mass hierarchy: the electron is the lightest and most stable, followed by the heavier muon and tau. This generational structure mirrors that of the quarks and forms the basis for classifying fermions into three generations, with each generation corresponding to a column in the fermion sector of the Standard Model table, as illustrated in Figure 2.1. The electrically neutral neutrinos are grouped with their corresponding charged leptons within each generation. While the Standard Model originally assumed neutrinos to be massless, experimental evidence from dedicated neutrino oscillation studies has confirmed that neutrinos do, in fact, possess non-zero mass. The precise nature and origin of these masses remain open questions, making neutrino physics an ongoing active area of research.

In addition to fermions, the other major class of particles is bosons. Unlike fermions, which obey the Pauli exclusion principle and serve as the matter particles, bosons have integer spin and do not follow the exclusion principle. Bosons arise naturally in the mathematical framework of quantum field theory, in which particles are interpreted as excitations of fundamental fields that permeate all of space and time. Each type of particle corresponds to a distinct field, and interactions between these fields are mediated by the exchange of virtual bosons. Each fundamental force is associated with its own set of mediating bosons.

The existence of bosons is a direct consequence of gauge symmetry, which is a foundational principle in quantum field theory that requires the laws of physics to remain invariant under specific local transformations. Gauge theories such as quantum electrodynamics (QED), the electroweak theory, and quantum chromodynamics (QCD), which forms the basis of the Standard Model, are built upon this principle. The requirement of gauge invariance in these theories naturally gives rise to the gauge bosons that mediate the electromagnetic, weak, and strong interactions.

- **Photon (γ)**: The photon is associated with the electromagnetic force, which is described by QED. QED is based on the principle of U(1) gauge symmetry, where U(1) represents the unitary group of complex numbers with unit modulus. The gauge symmetry characteristic of QED suggests gauge invariance under local phase transformations of the charged particles and photon fields.

The gauge symmetry leads to the existence of a mass-less, spin-1 boson which known as the photon. The photon mediates the electromagnetic interactions between charged particles such as electrons and muons through the exchange of virtual photons.

- ***W* and *Z* Bosons**: The W and Z bosons mediate the weak force, which is unified with electromagnetism in the electroweak theory. This theory is based on the gauge symmetry group SU(2) $\otimes$ U(1), where SU(2) represents the special unitary group of 2×2 matrices. The gauge symmetry gives rise to three spin-1 gauge bosons from SU(2) and one from U(1), which mix after spontaneous symmetry breaking to form the physical W and Z bosons, as well as the massless photon. The W bosons are electrically charged, while the Z boson is neutral. These bosons mediate weak interactions such as beta decay and neutrino scattering.

- **Gluon (g)**: Gluons are the mediators of the strong force, which is described by Quantum Chromodynamics (QCD). QCD is a non-Abelian gauge theory based on the SU(3) gauge symmetry, where SU(3) denotes the special unitary group of 3×3 matrices with unit determinant. This symmetry gives rise to eight massless spin-1 gauge bosons, known as gluons, which carry colour charge and couple to both quarks and other gluons. Gluons mediate the strong interaction, binding quarks together within hadrons such as protons and neutrons.

- **Higgs boson**: The Higgs boson is associated with the mechanism of electroweak symmetry breaking, which gives mass to the W and Z bosons through the spontaneous breaking of the SU(2) $\otimes$ U(1) gauge symmetry.

- **Graviton**: A theoretical force carrier particle for gravity which have not yet been discovered and not part of the current SM.

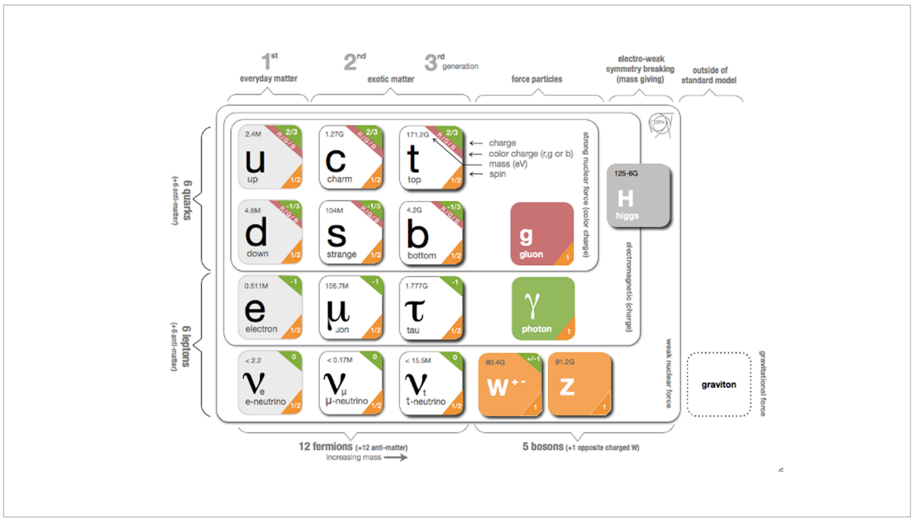

(a)

Figure 2.1: illustration of the standard model. Figure from ref[9]

2.1 Quantum electrodynamics (QED)

As previously discussed, the SM is a quantum field theory composed of multiple gauge theories, each associated with a fundamental interaction. The full gauge symmetry group of the SM is $SU(3)_C \otimes SU(2)_L \otimes U(1)_Y$, where the subscripts refer to colour charge C, left-handed isospin L, and hypercharge Y respectively. According to Noether's theorem [10], each continuous symmetry corresponds to a conserved quantity. The SM interactions are derived by demanding the Lagrangian be invariant under local gauge transformations associated with these symmetries.

To illustrate this idea, consider the electromagnetic interaction described by quantum electrodynamics (QED). In the classical limit, the dynamics of the electromagnetic field are encoded in Maxwell's Lagrangian:

$$\mathcal{L}_{\text{EM}} = -\frac{1}{4} F_{\mu\nu} F^{\mu\nu} \tag{2.1.1}$$

where $F_{\mu\nu} = \partial_\mu A_\nu - \partial_\nu A_\mu$ is the electromagnetic field strength tensor, and A_μ is the four-potential. This Lagrangian is invariant under the local $U(1)$ gauge transformation:

$$A_\mu \longrightarrow A_\mu + \partial_\mu \alpha(x) \tag{2.1.2}$$

This gauge symmetry leads directly to the conservation of electric current $j^\mu = \bar{\psi}\gamma^\mu\psi$, and consequently, implies conservation of electric charge (i.e. $\partial_\mu j^\mu = 0$). To move towards the QED, the spinor field Dirac Lagrangian is used to yield the quantised Dirac field to describe the behaviours of fermions, the Dirac Lagrangian is as followed:

$$\mathcal{L}_{\text{Dirac}} = \bar{\psi}(i\gamma^{\mu}\partial_{\mu} - m)\psi \tag{2.1.3}$$

Here, ψ is the Dirac spinor, $\bar{\psi} = \psi^{\dagger}\gamma^{0}$ is the adjoint spinor, γ^{μ} are the gamma matrices and m is the fermion mass. This Lagrangian is invariant under global but not local U(1) phase transformations:

$$\psi(x) \longrightarrow e^{i\alpha(x)}\psi(x) \tag{2.1.4}$$

Therefore, to restore local gauge invariance, the partial derivative is replaced with a covariant derivative that introduces a new gauge field A_{μ}:

$$\partial_{\mu} \longrightarrow D_{\mu} = \partial_{\mu} + iqA_{\mu} \tag{2.1.5}$$

This replacement introduces a coupling between the fermion field and the gauge field, where q is the coupling constant between the field and the electromagnetic field, which is the particle's electric charge. Then, the gauge-invariant Lagrangian, combining the Dirac and electromagnetic field becomes:

$$\mathcal{L}_{\text{Dirac}} = \bar{\psi}(i\gamma^{\mu}D_{\mu} - m)\psi - \frac{1}{4}F_{\mu\nu}F^{\mu\nu} \tag{2.1.6}$$

Expanding the covariant derivative leads to the QED Lagrangian for a specific fermion with charge q:

$$\mathcal{L}_{\text{QED}} = \bar{\psi}(i\gamma^{\mu}\partial_{\mu} - m)\psi - q\bar{\psi}\gamma^{\mu}A_{\mu}\psi - \frac{1}{4}F_{\mu\nu}F^{\mu\nu} \tag{2.1.7}$$

This expression consists of three terms: the free Dirac fermion field, the gauge field kinetic term describing photon propagation, and the interaction term between the fermion and the gauge field (i.e. electromagnetic coupling). This Lagrangian is fully invariant under local U(1) transformations and forms the basis of QED.

The middle term, $-q\bar{\psi}\gamma^{\mu}A_{\mu}\psi$, is particularly important, as it represents the interaction between the charged fermion and the electromagnetic field. This term arises directly from the requirement of local U(1) gauge invariance and reflects the coupling of the photon (the quantum of the field A_μ) to the fermionic current $\bar{\psi}\gamma^\mu\psi$. Without this term, the theory would describe only free particles. Its presence is what makes QED an interacting theory, and the coupling constant q quantifies the strength of the electromagnetic interaction.

2.2 Quantum chromodynamics (QCD)

Quantum chromodynamics (QCD) is the quantum field theory that describes the strong interaction in the SM. Unlike QED, which is based on the Abelian U(1) gauge group, QCD is based on the non-Abelian gauge group $\mathrm{SU(3)_c}$, where the subscript c denotes the colour charge carried by quarks and gluons. An Abelian gauge group, like U(1), has commuting generators and leads to non-interacting gauge bosons such as photons. In contrast, a non-Abelian gauge group, like SU(3) has non-commuting generators, resulting in gauge bosons (gluons) that can self-interact. This self-interaction is a key feature that distinguishes QCD from QED.

The QCD group (SU(3)) has eight generators, corresponding to the eight gluon fields that mediate the strong force. Each quark flavour (six in total) comes in three colour charges: red, green and blue. These colours are purely analogical and do not refer to visible colour; they reflect a mathematical property required to describe the strong interaction consistently. For a single quark flavour, the Lagrangian has the form of the Dirac Lagrangian:

$$\mathcal{L}_{\text{quark}} = \bar{\psi}(i\gamma^\mu\partial_\mu - m)\psi \tag{2.2.1}$$

To maintain local $\mathrm{SU}(3)_c$ gauge invariance, a covariant derivative is introduced:

$$D_\mu = \partial_\mu + ig_s G^a_\mu T^a \tag{2.2.2}$$

Here, G^a_μ are the eight gluon fields, g_s is the QCD coupling constant, and T^a are the 3×3 Gell-Mann matrices corresponds to the generators of the SU(3) gauge group (labelled by index $a = 1, \ldots, 8$).

The covariant derivative acting on a quark field becomes:

$$D_\mu \psi = (\partial_\mu + i g_s G^a_\mu T^a)\psi \tag{2.2.3}$$

Substituting this into the Lagrangian, we obtain the gauge-invariant quark term:

$$\mathcal{L}_{\text{quark}} = \bar{\psi}(i\gamma^\mu D_\mu - m)\psi = \bar{\psi}(i\gamma^\mu(\partial_\mu + i g_s G^a_\mu T^a) - m)\psi \tag{2.2.4}$$

The introduction of the covariant derivative leads to the appearance of the gluon interaction term. An SU(3) has eight linearly independent traceless Hermitian matrices, this results in eight gluon fields mentioned above, G^a_μ, one for each generator T^a.

The gluon field strength tensor is defined as:

$$G^a_{\mu\nu} = \partial_\mu G^a_\nu - \partial_\nu G^a_\mu + g_s f^{abc} G^b_\mu G^c_\nu \tag{2.2.5}$$

Here, f^{abc} are the structure constants of SU(3). This expression resembles the electromagnetic field strength tensor but includes the non-linear term $g_s f^{abc} G^b_\mu G^c_\nu$, which arises due to the non-Abelian nature of SU(3). This is the term that allowed gluons carry colour charge and can interact with each other.

Combining the quark and gluon terms, the full QCD Lagrangian is:

$$\mathcal{L}_{\text{QCD}} = \sum_f \bar{\psi}_f(i\gamma^\mu D_\mu - m_f)\psi_f - \frac{1}{4} G^a_{\mu\nu} G^{a\mu\nu} \tag{2.2.6}$$

where the sum is over all quark flavours f. This is written explicitly because all quark flavours carry colour charge and couple universally to gluons through the QCD coupling g_s, regardless of their electric charge or mass. In contrast, although the QED Lagrangian can, in principle, be expressed as a summation over all charged particle species, the form shown in equation 2.1.7 is typically written per particle species instead of a sum, as the QED interaction strength depends on electric charge, which varies among different particles. Additionally, since leptons do not carry colour charge, there is no analogous summation over colour states in QED.

The second term describes the kinetic term for the gluon fields, including their self-interactions. Expanding this leads to terms involving three and four gluon fields:

$$\mathcal{L}_{\text{gluon}} \supset g_s f^{abc}(\partial_\mu G^a_\nu) G^{\mu b} G^{\nu c} + \frac{g_s^2}{4} f^{abe} f^{cde} G^a_\mu G^b_\nu G^{\mu c} G^{\nu d} \tag{2.2.7}$$

These terms give rise to the three-gluon and four-gluon vertices that appear in Feynman diagrams of QCD processes. QCD also exhibits two essential features: **asymptotic freedom** and **confinement**. Asymptotic freedom means that at high energies (short distances), the QCD coupling becomes small, and quarks behave almost as free particles. This contrasts with QED, where the interaction becomes stronger at shorter distances. The strength of the QCD interaction is characterised by the running coupling constant:

$$\alpha_s = g_s^2/4\pi \tag{2.2.8}$$

Results from deep inelastic scattering experiments confirmed that α_s decreases as energy increases. Conversely, at low energies (large distances), α_s grows and quarks become confined within colour-neutral bound states (hadrons). This confinement means that quarks are never observed in isolation; when attempting to separate quarks, the energy input eventually leads to quark-antiquark pair production as it is energetically preferred to create new quarks before the original quarks are separated, forming new hadron bound states. This process is known as hadronisation and is a central feature in the analysis of collider data.

2.3 Electroweak unification

The electroweak theory unifies the electromagnetic and weak interactions into a single theoretical framework. This unification is based on the gauge group $\mathrm{SU}(2)_L \times \mathrm{U}(1)_Y$, where $\mathrm{SU}(2)_L$ corresponds to weak isospin and $\mathrm{U}(1)_Y$ corresponds to weak hypercharge. The weak hypercharge Y is related to the electric charge Q by the Gell-Mann–Nishijima formula:

$$Q = T_3 + \frac{Y}{2} \tag{2.3.1}$$

where T_3 is the third component of the weak isospin.

The weak interaction distinguishes between left-handed and right-handed components of fermion fields; it only couples to left-handed fermions and right-handed anti-fermions. Fermions are described by Dirac spinor fields, which can be decomposed using the projection operators:

$$\psi_L = \frac{1-\gamma^5}{2}\psi, \quad \psi_R = \frac{1+\gamma^5}{2}\psi \tag{2.3.2}$$

Left- and right-handed fermions transform differently under the gauge group. In particular, left-handed fermions form $\mathrm{SU}(2)_L$ doublets with isospin $I = \frac{1}{2}$, while right-handed fermions are $\mathrm{SU}(2)_L$ singlets with $I = 0$.

Left-handed lepton and quark doublets:

$$L_e = \begin{pmatrix} \nu_e \\ e \end{pmatrix}_L, \quad L_\mu = \begin{pmatrix} \nu_\mu \\ \mu \end{pmatrix}_L, \quad L_\tau = \begin{pmatrix} \nu_\tau \\ \tau \end{pmatrix}_L, q_u = \begin{pmatrix} u \\ d' \end{pmatrix}_L, \quad q_c = \begin{pmatrix} c \\ s' \end{pmatrix}_L, \quad q_t = \begin{pmatrix} t \\ b' \end{pmatrix}_L, \tag{2.3.3}$$

Right-handed singlets:

$$e_R, \quad \mu_R, \quad \tau_R, \quad u_R, \quad d_R, \quad c_R, \quad s_R, \quad t_R, \quad b_R \tag{2.3.4}$$

Here, the down-type quark states d', s', b' are flavour eigenstates and related to the mass eigenstates via the Cabbibo-Kobayashi-Maskawa (CKM) matrix.

$$\begin{pmatrix} d' \\ s' \\ b' \end{pmatrix} = \begin{pmatrix} V_{ud} & V_{us} & V_{ub} \\ V_{cd} & V_{cs} & V_{cb} \\ V_{td} & V_{ts} & V_{tb} \end{pmatrix} \begin{pmatrix} d \\ s \\ b \end{pmatrix} \tag{2.3.5}$$

As in QED and QCD, gauge invariance is achieved by introducing a covariant derivative:

$$D_\mu\psi = \left(\partial_\mu - ig\frac{\tau^i}{2}W_\mu^i - ig'\frac{Y}{2}B_\mu\right)\psi \tag{2.3.6}$$

where g and g' are the $\mathrm{SU}(2)_L$ and $\mathrm{U}(1)_Y$ coupling constants, τ^i are the Pauli matrices (i.e. Generators of $\mathrm{SU}(2)_L$), and Y is the hypercharge. This introduces four gauge fields:

three W^i_μ for $\mathrm{SU}(2)_L$ and one B_μ for $\mathrm{U}(1)_Y$. The electroweak bosons $W^\pm$, Z, and γ are arise from linear combinations of these fields. The charged weak bosons are defined by:

$$W^+_\mu = \frac{1}{\sqrt{2}}(W^1_\mu - iW^2_\mu) \tag{2.3.7}$$

$$W^-_\mu = \frac{1}{\sqrt{2}}(W^1_\mu + iW^2_\mu) \tag{2.3.8}$$

The mixing of the W^3_μ and B_μ fields forms the neutral bosons Z and γ, defined by the Weinberg rotation:

$$A_\mu = B_\mu \cos\theta_W + W^3_\mu \sin\theta_W \tag{2.3.9}$$

$$Z_\mu = -B_\mu \sin\theta_W + W^3_\mu \cos\theta_W \tag{2.3.10}$$

where θ_W is the Weinberg angle.

The full electroweak Lagrangian can be written as:

$$\mathcal{L}_{\mathrm{EW}} = \mathcal{L}_{\mathrm{gauge}} + \mathcal{L}_{\mathrm{fermion}} \tag{2.3.11}$$

The field strength tensor of $\mathrm{SU}(2)_L$ and $\mathrm{U}(1)_Y$ are:

$$W^i_{\mu\nu} = \partial_\mu W^i_\nu - \partial_\nu W^i_\mu + g\epsilon^{ijk}W^j_\mu W^k_\nu \tag{2.3.12}$$

$$B_{\mu\nu} = \partial_\mu B_\nu - \partial_\nu B_\mu \tag{2.3.13}$$

Equation 2.3.12 resembles the QCD field strength tensor, with the final term indicating self-interaction of the non-Abelian gauge fields (bosons). Equation 2.3.13 is structurally identical to the QED field strength tensor.

The gauge sector Lagrangian is:

$$\mathcal{L}_{\mathrm{gauge}} = -\frac{1}{4}W^i_{\mu\nu}W^{\mu\nu i} - \frac{1}{4}B_{\mu\nu}B^{\mu\nu} \tag{2.3.14}$$

For the fermion sector, the total Lagrangian includes both the kinetic terms and the interactions with the gauge fields is:

$$\mathcal{L}_{\text{fermion}} = \sum_{\psi} \bar{\psi} i \gamma^{\mu} D_{\mu} \psi \tag{2.3.15}$$

Thus, the generalised form of electroweak Lagrangian becomes:

$$\mathcal{L} = \sum_{\psi} \bar{\psi} i \gamma^{\mu} D_{\mu} \psi - \frac{1}{4} W^{i}_{\mu\nu} W^{\mu\nu i} - \frac{1}{4} B_{\mu\nu} B^{\mu\nu} \tag{2.3.16}$$

where the sum runs over all fermion fields. While this expression is written in a compact form, the covariant derivative D_{μ} depends on the specific weak isospin and hypercharge quantum numbers of each fermion field. These quantum numbers determine how each field couples to the $\mathrm{SU}(2)_L$ and $\mathrm{U}(1)_Y$ gauge fields. Therefore, in practice, the gauge interactions differ across fermions, and this dependence must be taken into account when expanding the Lagrangian for specific particle species.

This formulation successfully unifies the electromagnetic and weak interactions. However, it does not yet account for the observed masses of the W and Z bosons. Gauge invariance forbids the introduction of explicit mass terms for gauge bosons. This is not a problem for QED and QCD as photon and gluons are indeed massless. In contrast, the weak bosons are massive, and a mechanism is required to generate their masses while preserving gauge symmetry. This problem is resolved through spontaneous symmetry breaking via the Higgs mechanism, as discussed in sections 2.4.

2.4 Spontaneous symmetry breaking

Spontaneous symmetry breaking is a phenomenon in which the ground state (vacuum state) of a system does not exhibit the symmetry of the underlying Lagrangian or Hamiltonian. In classical field theory, the Lagrangian can be written as:

$$\mathcal{L} = T - V \tag{2.4.1}$$

Where T is the kinetic term and V is the potential. For a scalar field ϕ, the Lagrangian takes the form:

$$\mathcal{L} = \frac{1}{2}\partial_\mu\phi\partial^\mu\phi - V(\phi) \tag{2.4.2}$$

Consider a potential of the form:

$$V(\phi) = \frac{\lambda}{4}(\phi^2 - v^2)^2 \tag{2.4.3}$$

Substituting this potential, the Lagrangian becomes:

$$\mathcal{L} = \frac{1}{2}\partial_\mu\phi\partial^\mu\phi - \frac{\lambda}{4}(\phi^2 - v^2)^2 \tag{2.4.4}$$

This potential is symmetric under the transformation $\phi \longrightarrow -\phi$ and has two degenerate minima at $\phi = \pm v$. If the field settles in one of these minima (e.g., $\phi = v$), the symmetry is spontaneously broken, i.e. the vacuum no longer respects the symmetry of the Lagrangian.

We can examine small fluctuations η around the vacuum by shifting the field:

$$\phi = \phi_0 + \eta \tag{2.4.5}$$

Substituting this into the potential:

$$\begin{aligned} V(\phi) &= \frac{\lambda}{4}((v+\eta)^2 - v^2)^2 \\ &= \frac{\lambda}{4}(2v\eta + \eta^2)^2 \\ &= \frac{\lambda}{4}(4v^2\eta^2 + 4v\eta^3 + \eta^4) \end{aligned} \tag{2.4.6}$$

Then, if neglecting higher-order terms in η, we approximate:

$$V(\eta) \approx \lambda v^2\eta^2 \tag{2.4.7}$$

The corresponding Lagrangian becomes:

$$\mathcal{L} \approx \frac{1}{2}\partial_\mu\eta\partial^\mu\eta - \lambda v^2\eta^2 \tag{2.4.8}$$

This resembles a free scalar field with mass, if compare to the standard expression of scalar field with mass m:

$$-\frac{1}{2}m^2\eta^2 = -\lambda v^2\eta^2 \tag{2.4.9}$$

The mass is given by:

$$m^2 = 2\lambda v^2 \tag{2.4.10}$$

Thus, spontaneous symmetry breaking generates a mass term for the scalar fluctuation η.

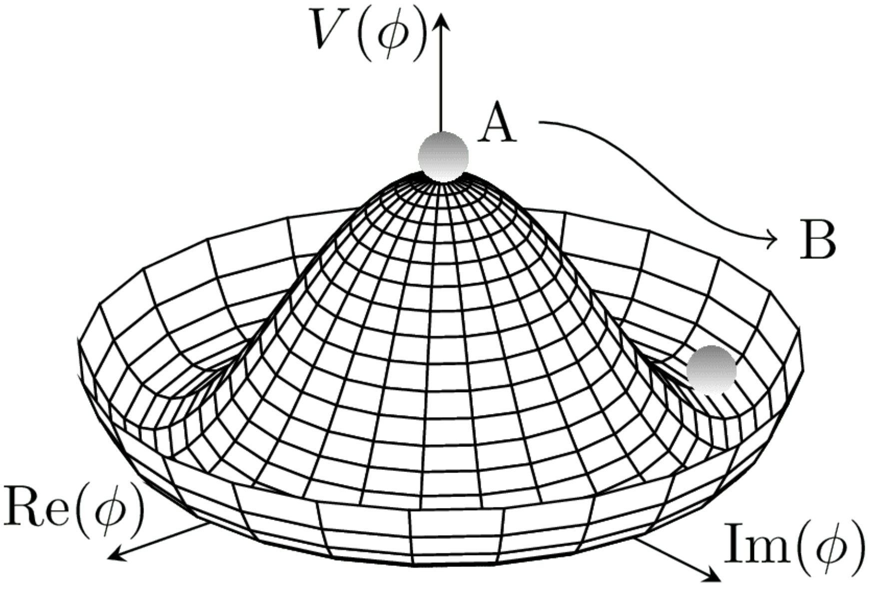

(a)

Figure 2.2: illustration of the spontaneous symmetry breaking of the higgs potential, image from ref [11].

2.4.1 Higgs mechanism

The previous section illustrated how a scalar field can acquire mass via spontaneous symmetry breaking under a discrete transformation $\phi \to -\phi$. The Higgs mechanism generalises this idea to a complex scalar field that transforms under a local U(1) gauge symmetry.

Consider a complex scalar field ϕ coupled to a gauge field A_μ with the Lagrangian:

$$\mathcal{L} = (D_\mu\phi)^\dagger(D_\mu\phi) - V(\phi) \tag{2.4.11}$$

Here, the covariant derivative is introduced:

$$D_\mu = \partial_\mu - igA_\mu \tag{2.4.12}$$

and the potential is:

$$V(\phi) = -\mu^2\phi^\dagger\phi + \lambda(\phi^\dagger\phi)^2 \tag{2.4.13}$$

This potential is symmetric under the phase transformation $\phi \longrightarrow e^{i\alpha}\phi$. It is minimised when:

$$\phi^\dagger\phi = \frac{\mu^2}{2\lambda} \equiv \frac{v^2}{2}$$

This leads to a degenerate set of vacuum states. Choosing a vacuum expectation value (VEV) such that $\langle\phi\rangle = \frac{v}{\sqrt{2}}$, we expand ϕ around this vacuum as:

$$\phi = \frac{1}{\sqrt{2}}(v + \eta + i\xi) \tag{2.4.14}$$

where η and ξ are real fields representing fluctuations. Substituting into the Lagrangian (neglecting ξ for now):

$$\mathcal{L} = \left(\partial_\mu - igA_\mu\right)\frac{1}{\sqrt{2}}(v+\eta)\left(\partial^\mu + igA^\mu\right)\frac{1}{\sqrt{2}}(v+\eta) - V\left(\frac{1}{\sqrt{2}}(v+\eta)\right) \tag{2.4.15}$$

This expands to:

$$\mathcal{L} = \frac{1}{2}(\partial_\mu\eta)(\partial^\mu\eta) + \frac{1}{2}g^2v^2A_\mu A^\mu - \frac{\mu^2}{2}(v+\eta)^2 - \frac{\lambda}{4}(v+\eta)^4 \tag{2.4.16}$$

Further simplification gives:

$$\begin{aligned}\mathcal{L} =& \frac{1}{2}(\partial_\mu\eta)(\partial^\mu\eta) + \frac{1}{2}g^2v^2A_\mu A^\mu - \frac{\mu^2v^2}{2} - \mu^2v\eta - \frac{\mu^2}{2}\eta^2 \\ &- \frac{\lambda v^4}{4} - \lambda v^3\eta - \lambda v^2\eta^2 - \frac{\lambda v}{2}\eta^3 - \frac{\lambda}{4}\eta^4\end{aligned} \tag{2.4.17}$$

From Eq. 2.4.17, we identify the mass terms:

- The term $\frac{1}{2}g^2v^2A_\mu A^\mu$ implies the gauge boson mass $m_A = gv$.
- The term $\frac{1}{2}(2\lambda v^2)\eta^2$ gives the Higgs mass $m_\eta = \sqrt{2\lambda}v$.

The ξ field that was previously ignored corresponds to the massless Goldstone boson. In the context of the U(1) gauge symmetry, gauge transformation can be performed under the freedom of choosing the unitary gauge to simplify the equations as this gauge removes the Goldstone boson from the spectrum. In this unitary gauge, the ξ field is set to zero to field η. To physically interpret this choice, after the spontaneous symmetry breaking, the ξ field gets "eaten" by the gauge boson, providing it with a longitudinal degree of freedom and giving it mass. Mathematically, this choice of gauge is motivated by the term $gvA_\mu(\partial^\mu\xi)$ that presented in the Lagrangian shown in eq. 2.4.17. Had ξ not been removed, the Lagrangian would contain this mixing term $gvA_\mu\partial^\mu\xi$, indicating a non-diagonal bilinear term mixing A_μ and ξ. This demonstrates that the fields are not independent degrees of freedom and interactions between them can lead to a transformation of one field to another, which motivates removing ξ via gauge fixing as it indicates that the fields are misidentified into non-independent degree of freedom.

Finally, Eq. 2.4.17 includes cubic and quartic η terms (η^3 and η^4), indicating the existance of Higgs self-interactions with 3-point and 4-point vertices.

2.4.2 Massive bosons through Higgs mechanism

The gauge bosons acquire mass through their interaction with the Higgs field via the Higgs mechanism. The Higgs potential is given by:

$$V(\Phi) = -\mu^2\Phi^\dagger\Phi + \lambda(\Phi^\dagger\Phi)^2 \tag{2.4.18}$$

with Φ being the Higgs field scalar doublet:

$$\Phi = \begin{pmatrix} \phi^+ \\ \phi^0 \end{pmatrix}$$

Choosing the vacuum expectation value (VEV) as:

$$\langle\Phi\rangle = \frac{1}{\sqrt{2}}\begin{pmatrix}0\\v\end{pmatrix}, \quad v = \sqrt{\frac{\mu^2}{\lambda}}$$

We may now derive the value of the potential at the minimum (the vacuum energy). Substitute the VEV into the potential:

$$V_0 = V(\langle\Phi\rangle) = -\mu^2\left(\frac{v^2}{2}\right) + \lambda\left(\frac{v^2}{2}\right)^2$$

This simplifies to:

$$V_0 = -\frac{\mu^2 v^2}{2} + \frac{\lambda v^4}{4}$$

Using $v^2 = \mu^2/\lambda$, we substitute back to get:

$$V_0 = -\frac{\mu^4}{4\lambda}$$

This V_0 represents the vacuum energy associated with the Higgs field after symmetry breaking.

To understand how the Higgs field gives mass to the electroweak gauge bosons, we substitute the Higgs VEV into the covariant derivative defined in Eq. 2.3.6. This helps identify the terms responsible for the mass generation and are used in the next subsections. Substituting v into the electroweak covariant derivative (Eq. 2.3.6):

$$(D_\mu\langle\Phi\rangle) = \left(\partial_\mu - i\frac{g}{2}\tau^i W^i_\mu - i\frac{g'}{2}B_\mu\right)\frac{1}{\sqrt{2}}\begin{pmatrix}0\\v\end{pmatrix}$$

This simplifies to:

$$(D_\mu\langle\Phi\rangle) = \frac{v}{\sqrt{2}}\left(-i\frac{g}{2}\tau^i W^i_\mu\begin{pmatrix}0\\1\end{pmatrix} - i\frac{g'}{2}B_\mu\begin{pmatrix}0\\1\end{pmatrix}\right) \tag{2.4.19}$$

2.4.3 *W* boson mass

From Eq. 2.4.19, the terms involving W^1_μ and W^2_μ are:

$$D_\mu \langle \Phi \rangle = \frac{v}{\sqrt{2}} \left(-i\frac{g}{2} W_\mu^1 \tau^1 - i\frac{g}{2} W_\mu^2 \tau^2 \right) \begin{pmatrix} 0 \\ 1 \end{pmatrix}$$

which simplifying gives:

$$D_\mu \langle \Phi \rangle = \frac{v}{\sqrt{2}} \left(-i\frac{g}{2} (W_\mu^1 - W_\mu^2) \right) \begin{pmatrix} 0 \\ 1 \end{pmatrix} \tag{2.4.20}$$

Thus, Define:

$$W_\mu^1 - W_\mu^2 = \sqrt{2} W_\mu^+ \tag{2.4.21}$$

The W boson mass arises from the kinetic term:

$$\mathcal{L}_{\text{kin}} = |D_\mu \langle \Phi \rangle|^2 = \frac{v^2}{2} \left(\frac{g}{2} \right)^2 (W_\mu^1 W^{\mu 1} + W_\mu^2 W^{\mu 2}) \tag{2.4.22}$$

With W_μ^1 and W_μ^2 in terms of $W^\pm$:

$$W_\mu^1 = \frac{1}{\sqrt{2}} (W_\mu^+ + W_\mu^-), \quad W_\mu^2 = \frac{i}{\sqrt{2}} (W_\mu^- - W_\mu^+)$$

Then:

$$W_\mu^1 W^{\mu 1} + W_\mu^2 W^{\mu 2} = 2 W_\mu^+ W^{\mu -}$$

So:

$$\mathcal{L}_{\text{kin}} = \frac{v^2 g^2}{8} \cdot 2 W_\mu^+ W^{\mu -} = \frac{v^2 g^2}{4} W_\mu^+ W^{\mu -}$$

The quadratic term gives the W boson mass:

$$M_W = \frac{gv}{2} \tag{2.4.23}$$

2.4.4 *Z* boson and photon mass

Again, from Eq. 2.4.19, the terms involving W_μ^3 and B_μ are:

$$\frac{v}{\sqrt{2}}\left(-i\frac{g}{2}W_\mu^3 - i\frac{g'}{2}B_\mu\right)\begin{pmatrix}0\\1\end{pmatrix} \tag{2.4.24}$$

The kinetic term with the VEV substitution becomes:

$$\mathcal{L}_{\text{kin}} = \frac{v^2}{2}\left(\frac{g^2}{4}(W_\mu^3)^2 + \frac{g'^2}{4}(B_\mu)^2 + \frac{gg'}{4}W_\mu^3 B_\mu\right) \tag{2.4.25}$$

Using the definitions:

$$W_\mu^3 = Z_\mu \cos\theta_W + A_\mu \sin\theta_W, \quad B_\mu = A_\mu \cos\theta_W - Z_\mu \sin\theta_W$$

Substitute into Eq. 2.4.25, and collect $Z_\mu Z^\mu$ terms:

$$\mathcal{L}_{\text{mass}} = \frac{v^2}{2}\left(\frac{g^2 + g'^2}{4}\right)Z_\mu Z^\mu \tag{2.4.26}$$

The photon mass term vanishes:

$$\mathcal{L}_{\text{mass}} = 0 \cdot A_\mu A^\mu \tag{2.4.27}$$

So:

$$M_Z = \frac{v}{2}\sqrt{g^2 + g'^2}, \quad M_A = 0 \tag{2.4.28}$$

Thus, spontaneous symmetry breaking of the $\mathrm{SU}(2)_L \times \mathrm{U}(1)_Y$ gauge symmetry generates masses for W and Z bosons while leaving the photon massless. This is due to the fact that a residual unbroken symmetry remains, corresponding to the electromagnetic U(1) gauge group. This residual symmetry ensures the conservation of electric charge and the masslessness of the photon.

2.4.5 Yukawa coupling: fermion masses

In the Standard Model, fermions acquire mass as a consequence of spontaneous symmetry breaking, through their interactions with the Higgs field via Yukawa couplings. When the Higgs field develops a vacuum expectation value (VEV), these interactions generate effective mass terms for the fermion fields. The Yukawa Lagrangian for a fermion ψ interacting with the Higgs field Φ is given by:

$$\mathcal{L}_{\text{Yukawa}} = -y_\psi(\bar{\psi}_L \Phi \psi_R + \psi_L \Phi^\dagger \bar{\psi}_R) \tag{2.4.29}$$

where:

- y_ψ is the Yukawa coupling constant.
- $\bar{\psi}_L$ is the left-handed component of the fermion field.
- ψ_R is the right-handed component of the fermion field.
- Φ is the Higgs field.
- The second term is the Hermitian conjugate of the first term

Using the spontaneous symmetry breaking VEV of the Higgs field:

$$\langle \Phi \rangle = \frac{1}{\sqrt{2}} \begin{pmatrix} 0 \\ v \end{pmatrix}$$

the Yukawa Lagrangian becomes:

$$\mathcal{L}_{\text{Yukawa}} = -y_\psi \bar{\psi}_L \frac{1}{\sqrt{2}} \begin{pmatrix} 0 \\ v \end{pmatrix} \psi_R + \text{Hermitian conjugate}$$

Including the Hermitian conjugate explicitly:

$$\mathcal{L}_{\text{Yukawa}} = -\frac{y_\psi v}{\sqrt{2}} \bar{\psi}_L \psi_R - \frac{y_\psi v}{\sqrt{2}} \bar{\psi}_R \psi_L \tag{2.4.30}$$

Combining the terms into a Dirac mass term:

$$\mathcal{L}_{\text{Yukawa}} = -\frac{y_\psi v}{\sqrt{2}} (\bar{\psi}_L \psi_R + \bar{\psi}_R \psi_L) = -\frac{y_\psi v}{\sqrt{2}} \bar{\psi} \psi \tag{2.4.31}$$

Thus, the mass of the fermion ψ is given by:

$$m_\psi = \frac{y_\psi v}{\sqrt{2}} \tag{2.4.32}$$

Therefore, fermion masses arise from the Yukawa interaction once the Higgs field acquires a non-zero VEV, with the magnitude of each fermion's mass determined by its corresponding Yukawa coupling. These coupling constants are fixed phenomenologically to match the observed fermion masses.

2.5 Vector-like leptons model

The Standard Model has been remarkably successful, but several open questions remain unanswered, motivating the search for Beyond the Standard Model (BSM) physics. Some of these open issues include the origin of neutrino masses, the hierarchy problem, the nature of dark matter, and the observed matter-antimatter asymmetry in the universe. These theoretical limitations, combined with precision measurements from experiments, provide strong motivation for the development of BSM models.

Vector-like leptons (VLLs) offer a well-motivated and minimal extension to the SM. They appear in many BSM theories, including models of compositeness, extra dimensions, and certain realisations of grand unification. Unlike SM fermions, both the left- and right-handed components of VLLs transform identically under the electroweak gauge group, allowing mass terms without relying on Higgs Yukawa interactions. This property enables the introduction of new leptonic states while preserving gauge invariance.

Because VLLs can mix with SM leptons, they may lead to distinctive signatures at colliders, particularly in final states involving charged leptons. Among the various decay channels, the $\tau\tau$ final state is especially sensitive to VLL-induced effects:

- Third-generation couplings are favoured in several BSM scenarios, enhancing sensitivity to VLLs decaying into τ leptons.

- The high mass of the τ lepton makes it a natural probe of new physics that couples more strongly to heavy fermions.

- Although τ reconstruction is more challenging than for e or μ, dedicated algorithms and calibration strategies at the LHC enable high-mass $\tau\tau$ searches to probe unique BSM parameter space.

This section introduces the simplified doublet VLL model studied in this thesis. While the analysis and interpretation are presented in Section 5, the theoretical structure is detailed here to maintain continuity with the SM formalism.

A generalised VLL model, which couples to SM leptons and can be adapted to any generation is presented in Reference [12]. Although not directly employed in this analysis, it provides a helpful foundation for explaining the simplified VLL model used here. Charged VLLs (τ') and neutral VLLs (ν') can appear as singlets or doublets under the SM electroweak symmetry group $SU(2)_L \times U(1)_Y$. Their interactions with gauge bosons are summarised in the following Lagrangians:

Singlet Case:

$$L_{\text{singlet}} = eA^\mu \bar{\tau}'_0 \gamma_\mu \tau'_0 - \frac{2c_W^2}{2g_W s_W^2} Z^\mu \bar{\tau}'_0 \gamma_\mu \tau'_0 \tag{2.5.1}$$

Doublet Case:

$$\begin{aligned} L_{\text{doublet}} = {} & eA^\mu \bar{\tau}' \gamma_\mu \tau' - 2g_W \left[W^{\mu +} \bar{\tau}' \gamma_\mu \nu' + W^{\mu -} \bar{\nu}' \gamma_\mu \tau' \right] \\ & - \frac{2c_W}{g_W} Z^\mu \left[\bar{\nu}' \gamma_\mu \nu' + \bar{\tau}' \gamma_\mu (-1 + 2s_W^2) \tau' \right] \end{aligned} \tag{2.5.2}$$

In the singlet case, only the charged VLLs couple to the photon and Z boson. In the doublet scenario, both charged and neutral VLLs couple to the Z boson and interact via W-mediated charged currents. Additionally, in the doublet representation, the charged and neutral VLLs mix via weak charged-current interactions. The mixing angles s_W and c_W (representing the sine and cosine of the electroweak mixing angle θ_W) relate the fields of the electroweak gauge group $SU(2)_L \times U(1)_Y$ to the Z boson.

In this model, the transition from weak eigenstates (τ'_0, ν'_0) to mass eigenstates (τ', ν') involves mixing:

$$\begin{aligned} l_0^{L/R} &= (c_{\tau'} l)^{L/R} - (s_{\tau'} \tau')^{L/R}, \\ \tau_0'^{L/R} &= (c_{\tau'} \tau')^{L/R} + (s_{\tau'} l)^{L/R}, \\ \nu_0^{L/R} &= (c_{\nu'} \nu)^{L/R} - (s_{\nu'} \nu')^{L/R}, \\ \nu_0'^{L/R} &= (c_{\nu'} \nu')^{L/R} + (s_{\nu'} \nu)^{L/R}. \end{aligned} \tag{2.5.3}$$

Here, c and s denote the cosine and sine of the respective mixing angles. The presence of non-zero mixing enables VLL decays into SM leptons, giving rise to observable signatures at the LHC.

where c and s represent the cosine and sine of the respective mixing angles for each case. The presence of non-zero mixing allows VLLs to decay into SM leptons, making them contributing to the detectable final states at the LHC. As a summary, the general fermion mass acquiring matrix for the singlet case takes the form:

$$M = \begin{pmatrix} y_L v_0 & \epsilon v \\ 0 & M_{\tau'} \end{pmatrix} \tag{2.5.4}$$

For the doublet case, the mass matrix takes the transposed form compared to the singlet scenario. The diagonal elements correspond to the masses of the weak eigenstates: the SM lepton and the VLL. y_L is the SM Yukawa coupling for the SM lepton and v_0 here is the VEV. The off-diagonal elements represent the mixing between them. The lower-left zero reflects the absence of a direct Yukawa coupling between the VLL and the Higgs field. However, after electroweak symmetry breaking and mixing with the SM leptons, the VLLs acquire effective couplings to the Higgs boson. The upper-right term, ϵv, encodes Higgs-induced mixing between the SM lepton and VLL.

To preserve consistency with SM Higgs measurements, the mixing parameter ϵ must be small so that it does not significantly alter the Higgs couplings to the SM leptons, which would lead to detectable deviations in lepton decay branching ratios. In this limit, the mass eigenvalues of the VLL and SM leptons are approximately:

$$M_{\mathrm{VLL}} \approx M_{\tau'}, \quad M_{\ell} \approx y_L v_0 \tag{2.5.5}$$

Now that the general VLL model has been introduced, we turn to a simplified benchmark scenario of the model that serves as the focus of this study. The simplified singlet/-doublet VLL model used in this study was proposed by Kumar and Martin [4] that reduces the number of free parameters while maintaining the key features of VLL interactions. The model carries the following assumptions:

- Mixing occurs only with the τ lepton.
- Charged and neutral VLLs have degenerate mixing angles: $s_L^{\tau'} = s_L^{\nu'}$, $s_R^{\tau'} = s_R^{\nu'}$.

- No mixing with right-handed neutrinos: $s_R^{\nu'} = 0$.

As shown in Ref. [13], the minimal singlet VLL model is difficult to probe at proton–proton colliders. Therefore, this study focuses on the minimal doublet VLL model, which offers better discovery prospects. The model is implemented in Universal FeynRules Object [14] (UFO) format and interfaced with `CONTUR`, exploring the parameter space spanned by $M_{\tau'}$ and the mixing strength ϵ, each with predefined ranges.

2.5.1 Production channels and decay modes

Since the VLLs interact through the electroweak force, vector-like leptons are produced at the LHC predominantly through electroweak processes, particularly Drell–Yan pair production and W/Z boson exchange. The production cross-sections in the doublet VLL model are much larger than the singlet VLL model [4]. The production cross-section depends strongly on the electroweak quantum numbers of the VLLs. In the doublet model, the presence of both charged and neutral VLLs enhances production rates compared to the singlet case, due to their additional couplings to W bosons and accompanied by an additional ν' production. This enhancement leads to significantly larger cross-sections and improved sensitivity in doublet scenarios [4]. Consequently, the LHC prospects for excluding or discovering VLLs are much stronger in the doublet model. For this reason, the analysis in this thesis adopts the doublet VLL framework as its baseline.

The following subsections describe the production mechanisms and decay modes of VLLs in more detail.

Pair production via Drell-Yan Processes

The dominant production mechanism for VLLs is electroweak pair production via the s-channel exchange of neutral gauge bosons (Z/γ^*) [12]:

$$pp \to Z/\gamma^* \to \tau'^+\tau'^- \tag{2.5.6}$$

$$pp \to Z/\gamma^* \to \nu'\bar{\nu}' \tag{2.5.7}$$

These processes are mediated by the Drell-Yan mechanism, where a quark-antiquark pair from the proton collisions annihilate into a virtual Z/γ^* boson, which then decays into a pair of charged (τ') or neutral (ν') VLLs.

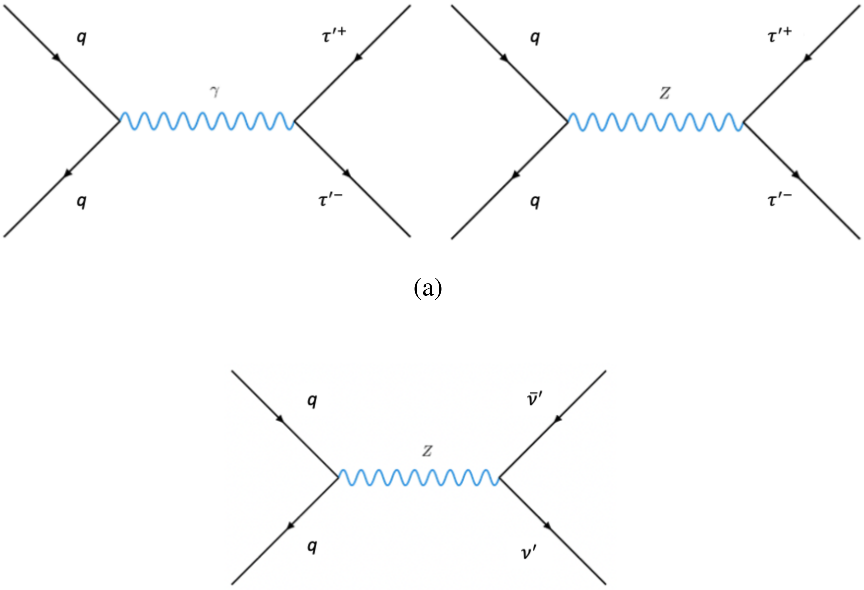

(a)

(b)

Figure 2.3: (a) Charged VLL pair production via neutral bosons through proton-proton collision. (b) Neutral VLL production via the same mechanism. Figures taken from Ref. [12].

Single production via W-boson Exchange

In addition to pair production, VLLs can also be produced singly in association with a SM lepton via W boson exchange [12]:

$$pp \to W^{\pm} \to \tau'^{+}(\tau'^{-})\nu'(\bar{\nu}') \tag{2.5.8}$$

This process occurs when a quark-antiquark pair annihilates into a virtual W boson, which then decays into a charged VLL and a neutral VLL. The correspond Feynman diagram is shown in Figure 2.4.

Vector-like Leptons Decay Modes

As a consequence of their mixing with SM leptons via the small parameter ϵ, vector-like leptons decay into SM bosons: W, Z, and the Higgs boson h. The interaction Lagrangian describing τ' and ν' decays in the doublet model is [4]:

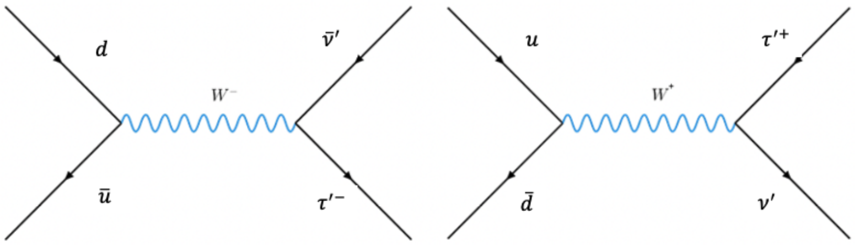

(a)

Figure 2.4: Feynman diagram for associate VLL production through proton-proton collision. Figures taken from Ref. [12].

$$
\begin{aligned}
L_{\text{int}} = g^{W^+}_{\bar{\tau}^\dagger \bar{\nu}'} &\left[W^+_\mu(\tau^\dagger \bar{\sigma}^\mu \nu') + W^-_\mu(\bar{\nu}'^\dagger \bar{\sigma}^\mu \bar{\tau})\right] \\
&+ g^Z_{\bar{\tau}^\dagger \bar{\tau}'} Z^\mu(\bar{\tau}^\dagger \bar{\sigma}^\mu \bar{\tau}' + \bar{\tau}'^\dagger \bar{\sigma}^\mu \bar{\tau}) + \left(y^h_{\tau' \bar{\tau}} h \tau' \bar{\tau} + \text{c.c.}\right)
\end{aligned}
\tag{2.5.9}
$$

The coupling strengths can be derived from the mass matrix in Eq. 2.5.4. The mixing between interaction and mass eigenstates is:

$$
\begin{pmatrix} \tau \\ \tau' \end{pmatrix} = \begin{pmatrix} 1 & \epsilon \\ -\epsilon & 1 \end{pmatrix} \begin{pmatrix} \tau_{\text{SM}} \\ \tau'_{\text{heavy}} \end{pmatrix}
\tag{2.5.10}
$$

To leading order in ϵ, this leads to the mass expressions:

$$
\tau = \tau_{SM} - \epsilon \tau'
\tag{2.5.11}
$$

$$
\tau' = \tau'_{heavy} + \epsilon \tau_{SM}
\tag{2.5.12}
$$

If start from the original SM electroweak interaction of the τ lepton couples to the W-boson:

$$
L_{\text{int}} = g_W W^{+\mu} \bar{\tau} \gamma^\mu \nu + g_W W^{-\mu} \bar{\nu} \gamma^\mu \tau
\tag{2.5.13}
$$

By substituting the τ mass eigenstate into the SM weak interaction introducing mixing to the Lagrangian terms gives:

$$
L_{\text{int}} = g_W W^{+\mu} (\bar{\tau}_{\text{SM}} - \epsilon \bar{\tau}') \gamma^\mu \nu + g_W W^{-\mu} \bar{\nu} \gamma^\mu (\tau_{\text{SM}} - \epsilon \tau')
\tag{2.5.14}
$$

Then expanding and rearrange gives new terms::

$$L_{\text{int}} = g_W W^{+\mu} \bar{\tau}_{\text{SM}} \gamma^{\mu} \nu + g_W W^{-\mu} \bar{\nu} \gamma^{\mu} \tau_{\text{SM}} - \epsilon g_W W^{+\mu} \bar{\tau}' \gamma^{\mu} \nu - \epsilon g_W W^{-\mu} \bar{\nu} \gamma^{\mu} \tau' \tag{2.5.15}$$

The first two terms are original SM interactions, and the final two terms introduce new interactions between the τ' and the SM neutrinos, proportional to the small mixing parameter ϵ. From the (almost) diagonalisation of the mass matrix, and with $\epsilon v \ll M_{\tau'}$, Using the small-ϵ approximation:

$$\epsilon = \frac{\epsilon v}{M_{\tau'}} \tag{2.5.16}$$

The electroweak vacuum expectation value is related to the W-boson mass by:

$$M_W = \frac{g_w v}{2} \tag{2.5.17}$$

Then, using the expression for ϵ and substituting the arranged expression $v = \frac{2M_W}{g_W}$, the expression of ϵ becomes:

$$\epsilon = \frac{2\epsilon M_W}{g_W M_{\tau'}} \tag{2.5.18}$$

Then, by inserting this expression for ϵ to the last two terms of Eq. 2.5.15, the new ϵ scaled coupling $-\epsilon g_W$, where now being written as $g_{W^+}^{\bar{\tau}^{\dagger}\bar{\nu}'}$ becomes:

$$g_{W^+}^{\bar{\tau}^{\dagger}\bar{\nu}'} = -\frac{\epsilon M_W}{M_{\tau'}} \tag{2.5.19}$$

This is coupling expression for the charged current part of the Lagrangian shown in Eq. 2.5.9. The other two coupling expressions can also be derived in a similar manner by substituting the mass eigenstate into the SM interaction Lagrangian and using known SM relationships between the boson masses and couplings. The resulted expressions are listed here for information:

$$g_Z^{\bar{\tau}^{\dagger}\bar{\tau}'} = -\frac{\epsilon M_Z}{\sqrt{2} M_{\tau'}} \tag{2.5.20}$$

$$y_h^{\tau'\tau} = -\frac{\epsilon}{\sqrt{2}} \tag{2.5.21}$$

The mixing between SM leptons and VLLs modifies the gauge and Higgs interactions, introducing new interaction terms proportional to the mixing parameter ϵ. This implies that for small ϵ, the new interactions remain suppressed.

Using the previously derived interaction strengths between VLLs and SM bosons, we now compute the decay widths for various VLL decay modes. The general two-body decay width formula is given by:

$$\Gamma(X \to AB) = \frac{1}{32\pi}\frac{1}{M_X}\lambda^{1/2}(1, r_A, r_B)|M|^2 \tag{2.5.22}$$

Here, M_X is the mass of the decaying particle, M_A, M_B are the mass of the final state particles, r_A, r_B are the squared mass ratios $\frac{M_A^2}{M_X^2}$ and $\frac{M_B^2}{M_X^2}$ and $\lambda(1, r_B, r_A) = 1 + r_A^2 + r_B^2 - 2r_A - 2r_B - 2r_A r_B$ is the Källén function [15]:

$$\lambda(1, r_A, r_B) = 1 + r_A^2 + r_B^2 - 2r_A - 2r_B - 2r_A r_B \tag{2.5.23}$$

Branching ratio of $\tau' \to Z\tau$

To illustrate the decay mechanism of vector-like leptons, we derive the partial width for $\tau' \to Z\tau$ as an example. Starting from the relevant interaction Lagrangian term with coupling $g_Z^{\bar{\tau}^\dagger \bar{\tau}'}$:

$$M = g_Z^{\bar{\tau}^\dagger \bar{\tau}'} \bar{u}(p_\tau)\gamma^\mu u(p_{\tau'})\epsilon_\mu^*(p_Z) \tag{2.5.24}$$

Where $\bar{u}(p_\tau)$ and $\bar{u}(p_{\tau'})$ are the Dirac spinors for τ and τ', $\epsilon_\mu^*(p_Z)$ is the polarisation vector of the Z boson and $p_{\tau'}$, p_τ are the respective momenta. By computing the squared matrix element and summing over spins and polarizations, we obtain:

$$|M|^2 = |g_Z^{\bar{\tau}^\dagger \bar{\tau}'}|^2 \sum_{\text{spins, pol.}} \bar{u}(p_\tau)\gamma^\mu u(p_{\tau'})\epsilon_\mu^*(p_Z) \times (\text{conjugate term}) \tag{2.5.25}$$

Using standard trace identities and applying the polarization sum for the Z boson,

$$\sum_{\lambda} \epsilon^{*}\mu(p_Z)\epsilon\nu(p_Z) = -g_{\mu\nu} + \frac{p_{Z\mu}p_{Z\nu}}{M_Z^2} \tag{2.5.26}$$

we obtain:

$$\begin{aligned} &\sum_{\text{spins}} \bar{u}(p_\tau)\gamma^\mu u(p_{\tau'})\bar{u}(p_\tau)\gamma^\nu u(p_{\tau'}) = \\ &\qquad 4\left[p_\tau^\mu p_{\tau'}^\nu + p_\tau^\nu p_{\tau'}^\mu - g^{\mu\nu}(p_\tau \cdot p_{\tau'})\right] \end{aligned} \tag{2.5.27}$$

The resulted spin-summed squared amplitude from Eq. 2.5.25 by inserting the above ingredients becomes:

$$\sum_{\text{spins},\lambda} |M|^2 = |g_Z^{\bar{\tau}^\dagger\tau'}|^2 4\left[p_\tau^\mu p_{\tau'}^\nu + p_\tau^\nu p_{\tau'}^\mu - g^{\mu\nu}(p_\tau \cdot p_{\tau'})\right]\left[-g_{\mu\nu} + \frac{q_\mu q_\nu}{M_Z^2}\right] \tag{2.5.28}$$

Now by separately taking the trace of the transverse piece ($-g_{\mu\nu}$) and the longitudinal piece ($\frac{q_\mu q_\nu}{M_Z^2}$) along with some index contractions, the traces are:

$$T_{\text{trans}} = -8(p_\tau \cdot p_{\tau'}) \tag{2.5.29}$$

$$T_{\text{long}} = \frac{4}{M_Z^2}\left[2(p_\tau \cdot p_Z)(p_{\tau'} \cdot p_Z) - (p_\tau \cdot p_{\tau'})M_Z^2\right] \tag{2.5.30}$$

Then these expression can be simplified using the rest frame of τ', and considering the regime with $M_{\tau'} \gg M_\tau$ (i.e. $p_\tau = 0$). The sum of the traces becomes:

$$T_{\text{trans}} + T_{\text{long}} = 4(\frac{M_{\tau'}^2 - M_Z^2}{2})(-2 + \frac{1}{r_Z}) \tag{2.5.31}$$

where $r_Z \equiv \frac{M_Z^2}{M_{\tau'}^2}$. By using this r_Z expression, the trace sum can be simplified to:

$$T_{trans} + T_{long} = 2M_{\tau'}^2(1 - r_Z)(\frac{1}{r_Z} - 2) \tag{2.5.32}$$

Now, by inserting the sum of traces into equation 2.5.28, the squared matrix becomes:

$$|M|^2 = |g_Z^{\bar{\tau}^\dagger\tau'}|^2 M_{\tau'}^2(1 - r_Z)(\frac{1}{r_Z} - 2) \tag{2.5.33}$$

Lastly, by substituting this derived expression back to equation 2.5.22, the final decay width for the $\tau' \rightarrow Z\tau$, with the assumption of having $r_\tau \equiv \frac{M_\tau^2}{M_{\tau'}^2}$ being very small, can be found as:

$$\Gamma(\tau' \rightarrow Z\tau) = \frac{M_{\tau'}}{32\pi}(1 - r_Z)^2(-2 + 1/r_Z)|g_Z^{\bar{\tau}^\dagger \bar{\tau}'}|^2 \tag{2.5.34}$$

Where $\lambda(1, r_z, r_\tau)$ is approximated to $(1 - r_Z)^2$ given that r_τ is very small.

The resulted branching ratio matches the expression provided in reference paper [4]. Again, by following similar derivations for other decay channels, the full picture of decay width are [4]:

$$\Gamma(\tau' \rightarrow W\nu) = 0 \tag{2.5.35}$$

$$\Gamma(\tau' \rightarrow Z\tau) = \frac{M_{\tau'}}{32\pi}(1 - r_Z)^2(2 + 1/r_Z)|g_Z^{\bar{\tau}^\dagger \bar{\tau}'}|^2 \tag{2.5.36}$$

$$\Gamma(\tau' \rightarrow h\tau) = \frac{M_{\tau'}}{32\pi}(1 - r_h)^2|y_h^{\tau'\tau}|^2 \tag{2.5.37}$$

$$\Gamma(\nu' \rightarrow W\tau) = \frac{M_{\nu'}}{32\pi}(1 - r_W)^2(2 + 1/r_W)|g_W^{+\bar{\tau}^\dagger \bar{\nu}'}|^2 \tag{2.5.38}$$

$$\Gamma(\nu' \rightarrow Z\nu) = \Gamma(\nu' \rightarrow h\nu) = 0 \tag{2.5.39}$$

These branching ratios only depends on the single free parameter $M_{\tau'}$ as all widths are proportional to ϵ^2. For parameter space with $M_{\tau'} \gg M_h, M_Z, M_W$, the resulted doublet model branching ratio for τ' asymptotically approach [4]:

$$BR(\tau' \rightarrow W\nu) : BR(\tau' \rightarrow Z\tau) : BR(\tau' \rightarrow h\tau) = 0 : 1 : 1 \tag{2.5.40}$$

For ν', the model assumes no mass mixing between ν' and the SM neutrinos [4], therefore, its dominantly decays to a W-boson and a SM τ lepton with,

$$BR(\nu' \to W^+\tau^-) : BR(\nu' \to W^-\tau^+) = 1 \tag{2.5.41}$$

The large decay ratio of the VLLs into the states with τ leptons helps the discovery prospect of the doublet model, and the $\tau\tau$ cross-sections measured during the High-mass $\tau\tau$ measurement is expected to contribute towards setting exclusions for this VLL model.

2.6 Summary

This chapter has outlined the theoretical foundation of the SM and the VLL model, which also settles the theoretical aspects of the di-τ measurement presented later in this thesis. While the SM has been remarkably successful, it is widely regarded as incomplete. For example, it does not incorporate gravity, nor does it explain phenomena such as dark matter, the structure of the Higgs potential, or the origin of the electroweak scale. These open questions have motivated the development of BSM theories and extensive experimental searches for new physics.

Measurements at high energies offer a powerful probe of BSM effects, even when new particles lie beyond the direct reach of current colliders. In this context, the di-τ final state is of particular interest. As the heaviest of the charged leptons, the τ lepton couples more strongly to the Higgs field and to hypothetical new scalar or pseudoscalar resonances. Many BSM models therefore predict enhanced couplings to third-generation leptons, making high-mass di-τ production a sensitive channel for testing the SM and exploring BSM scenarios, including those involving leptoquarks and VLLs. The analysis strategy and interpretation are described in detail in Sections 4 and 5.

Chapter 3

The Large Hadron Collider and the ATLAS Experiment

The Large Hadron Collider (LHC), operated by the European Organization for Nuclear Research (CERN) near Geneva in Switzerland represents a remarkable achievement in experimental physics and engineering, alongside other large particle physics experiments. Decades have been spent by people from hundreds of institutes around the world to build this world's largest and most powerful particle accelerator. The LHC is housed in a 27-kilometer circular tunnel buried approximately 100 meters underground across the border between Switzerland and France. The history of using particle accelerators for particle physics researches is long and the LHC was conceived in the 1980s as a successor to CERN's previous accelerator: the Large Electron-Positron (LEP) collider, with the ambitious goal of exploring the deepest mysteries of the universe by probing the fundamental particles and forces, where the colliding particles are changed from electrons to protons and heavy ions (primarily lead nuclei) to explore the energy-frontier.

The primary objective of the LHC was to create the extreme conditions that exists only at very high energy (almost immediately after the big bang) to enable the study of the unresolved mysteries such as the origin of mass, the potential existence of new particles predicted by the SM and other BSM models. The environment was created by accelerating the protons to nearly the speed of light and colliding then at extreme energy (13.6 TeV for the current Run-3).

The construction of the LHC began in 1998 and involves overcoming significant technical and engineering challenges. The 27 km ring tunnel holds a ring of over 1,200 superconducting dipole magnets along with an advanced cryogenic system to cool these magnets to 1.9 Kelvin along with radio-frequency (RF) cavities which bend and accelerate the particles. The collider's sophisticated design allowed it to handle the forces generated by the acceleration and collision processes. Precise alignments are required for the proton beams to interact (hit each other) at the designated points, where these points are surrounded by the particle detector experiments. There are four main experiments around the LHC ring: ATLAS, CMS, LHCb and ALICE. They work independently under different groups but with frequent cross-experiment communications to share ideas and results. The ATLAS and CMS are general purpose detectors that were independently designed to achieve the same goal. LHCb is dedicated to probing physics involving the b-hadrons in the proton-proton (pp) collision and is also the experiment that have produced the anomaly that became one of the motivation for the di-τ measurement that is discussed in section 4. Lastly, the ALICE experiment is specialised to understand physics for the quark-gluon plasma through heavy-ion collisions.

The protons in the LHC are sourced from hydrogen, where the hydrogen gas is ionised by stripping away the electrons, leaving only the proton. The extracted protons are then fed into several machines to boost them into higher and higher energy. The first step is a linear accelerator named **LINAC2** (**LINAC4** for the upgraded system) [16] in which the proton beams are formed and accelerated to an energy of 50 MeV (**LINAC2**) or 160 MeV (**LINAC4**) using radio-frequency electric fields. The protons from the **LINAC** are then injected into the Proton Synchrotron Booster (PSB) which further accelerate then to 1.4 GeV. The next step in chain is the Proton Synchrotron (PS) where the energy of the proton are further increased to 25 GeV. Then, the protons are piped into the Super Proton Synchrotron (SPS) with a circumference of 6.9 km, which would boosts their energy to 450 GeV before injected into the LHC. The LHC has two beam pipes in which the protons travelling in opposite directions. The protons in the beam pipes are then finally accelerated to their final energy in around 20 minutes using the radio-frequency (RF) cavity and superconducting magnets cooled to 1.9 Kelvin. The RF cavities are hollow metallic chambers coated with superconducting material along the beam that are filled with a time-varying electric field, where electric field is generated from the voltage generator using a voltage oscillating at 400 MHz. When the protons passed through the cavity, energy is gained from the force of the electric field and accelerated. In total, the LHC uses 16 RFs (8 per beam) and is capable of increasing the proton energy to 14 times of the energy initially from the SPS. The total centre of mass energy in Run-2 reach 13 TeV (6.5 TeV per beam) and the current Run-3 have further increased the energy to 13.6 TeV.

3.1 LHC beams and physics concepts

To properly introduce the experiment, some key concepts and terminology related to beam dynamics and performance must first be explained. Since the LHC beams consist of many protons, they exhibit a spatial and momentum spread. Two important quantities used to describe and quantify beam quality are the emittance (ϵ) and the β function. The emittance measures the spread in position and angle (or momentum) of the particles in a beam and defines the area occupied in transverse phase space:

$$\epsilon = \sqrt{\langle x^2 \rangle \langle x'^2 \rangle - \langle x x' \rangle^2} \tag{3.1.1}$$

This expression quantifies the RMS spread in transverse position x and angle x'. A low emittance implies that particles are closely packed in phase space, indicating a high-quality beam with particles more tightly bunched in phase space.

The β function describes how the beam size evolves along the accelerator and is related to the emittance by:

$$\sigma_x(s) = \sqrt{\epsilon \beta(s)} \tag{3.1.2}$$

where $\sigma_x(s)$ is the transverse beam size at position s. A smaller β value implies tighter focusing.

Alongside the centre-of-mass energy, a key performance indicator for the LHC is the instantaneous luminosity. The definition of luminosity in particle physics is the number of particles passing through a unit area per unit time. It connects to beam quality parameters (ϵ and β) and cross-section σ via:

$$\mathcal{L} = \frac{1}{\sigma} \cdot \frac{dN}{dt} \tag{3.1.3}$$

While the luminosity is defined via σ, in practice, we cannot use the total proton-proton cross-section σ_{tot} because it include many processes that are not detected in the experiment. Since $\frac{dN}{dt}$ only reflects events that pass detector and trigger thresholds, using σ_{tot} would lead to a significant mismatch. Instead, luminosity is measured using well-understood processes with precisely known cross sections and clean signatures, such as the $Z \to ll$. Assuming Gaussian beam profiles, the LHC luminosity becomes:

$$\mathcal{L} = \frac{N_b^2 \cdot f \cdot n}{4\pi\sigma_x\sigma_y} \tag{3.1.4}$$

where N_b is the number of protons per bunch, f is the revolution frequency, n is the number of bunches, and $\sigma_{x,y}$ is the transverse beam sizes in the horizontal and vertical directions. The equation assumed both beams are identical with the same shape and the general form is:

$$\mathcal{L} = \frac{N_b^2 \cdot f \cdot n}{2\pi \sum_x \sum_y} \tag{3.1.5}$$

where the denominator components are expressed as:

$$\sum_x = \sqrt{\sigma_{x1}^2 + \sigma_{x2}^2}, \quad \sum_y = \sqrt{\sigma_{y1}^2 + \sigma_{y2}^2} \tag{3.1.6}$$

and are equal to the convolution of the beam sizes. Eq. 3.1.4 assumed $\sigma_{x1} = \sigma_{x2} = \sigma_{y1} = \sigma_{y2}$.

The LHC beams are composed of multiple tightly grouped protons in bunches to maximise the chances of interesting collisions between the protons. These bunches are timed to collide at designated points with high luminosity. Due to the high density of protons in each bunch, multiple collisions can occur at each crossing, resulting in *pile-up*. Pile-up events complicate reconstruction, as additional tracks and energy deposits can obscure the primary hard-scattering process and needed to be distinguished. Pile-up is a critical challenge for precision measurements and searches for rare processes. Accurately identifying and subtracting pile-up contributions is essential to improve the signal-to-noise ratio and

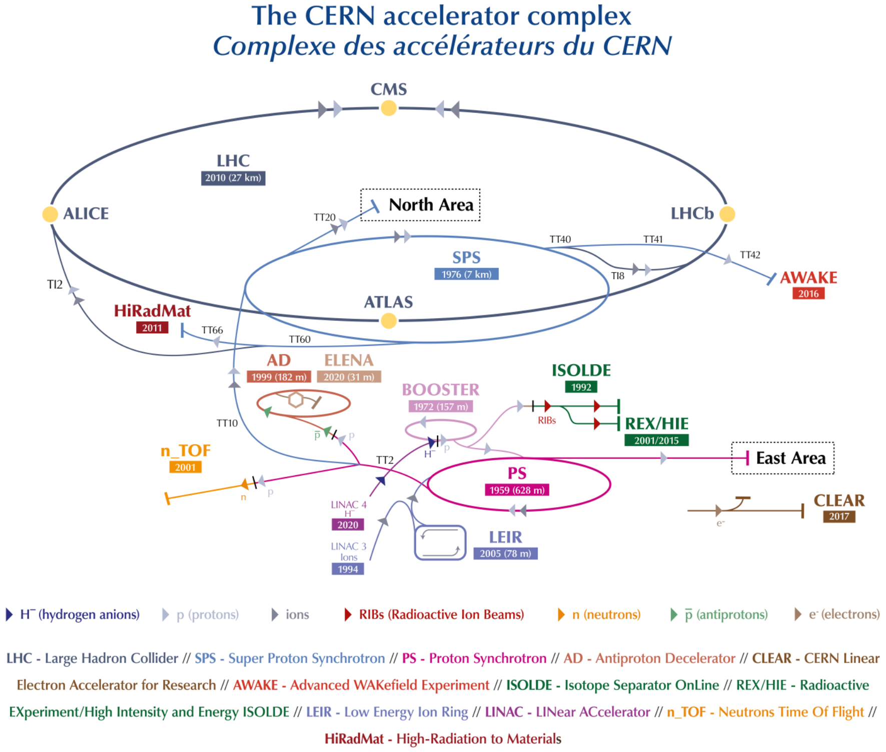

(a)

Figure 3.1: This figure illustrate the LHC system. The figure is from Ref [17]

achieve reliable results.

In this context, a **soft** collision refers to an interaction involving low momentum transfer, typically producing low-energy particles that are often part of the underlying event or background. In contrast, a **hard** collision involves a large momentum transfer, producing high transverse momentum particles and is usually of primary interest in high-energy physics analyses.

Pile-up falls into two main categories:

- **In-time pile-up:** Multiple collisions within the same 25 ns bunch crossing as the hard-scattering.
- **Out-of-time pile-up:** Residual detector signals from previous/subsequent crossings due to finite response times.

These pile-up events adds complexity to event reconstruction and contributes to the background noise and spurious signals in the detector readouts.

Most pile-up is soft, but some less common hard collisions can mimic signal-like features and degrade analysis performance as it would be harder to distinguish it from the primary event.

Apart from the pile-up events, the LHC also need to consider other less-substantial background sources that would affect the data quality, including:

- **Cavern background:** Radiation and stray particles originating from the detector environment. These can introduce additional noise in subdetectors and affect trigger rates.
- **Beam halo:** Peripheral particles near the beam core that stray and interact with the detector. These can cause spurious hits or contribute to forward detector occupancies.
- **Beam gas:** Interactions between beam protons and residual gas molecules in the vacuum pipe. These are non-collision backgrounds and must be distinguished using timing and vertexing.

Although subdominant compared to pile-up, these sources are important to monitor and model since they contribute to noise, can bias event selection, and affect detector calibrations and efficiencies.

The LHC achieved a peak luminosity of $10^{34}\text{cm}^{-2}\text{s}^{-1}$. The HL-LHC upgrade aims to increase this by a factor of 5–7 to $7.5 \times 10^{34}\text{cm}^{-2}\text{s}^{-1}$. The pile-up ($\mu$), or average number of interactions per crossing, is given by:

$$\mu = L \cdot \frac{\sigma_{inel}}{f} \tag{3.1.7}$$

where L is the instantaneous luminosity, σ_{inel} is the inelastic cross-section which typically is around 80 mb for the LHC [18]. f is the bunch crossing frequency and is around 40 MHz (25 nanoseconds between bunches).

In Run-1, the LHC was operating at a collision energy of 7-8 TeV and the pile-up was relatively low, typically around 10-20 interactions per bunch crossing. In Run-2, the collision energy was increased to 13 TeV and the average pile-up increased to around 20 to 50 interactions per bunch crossing and reached up to 60 interactions per bunch crossing during the periods of peak luminosity [19]. In the most recent Run-3, the average pile-up values are expected to be similar or slightly higher than Run-2 [20]. Looking ahead to the

High-Luminosity LHC (HL-LHC) era, the substantial increase in instantaneous luminosity is anticipated to result in significantly higher average pile-up, with around 140 interactions per bunch crossing and peak values potentially exceeding 200 [21, 22].

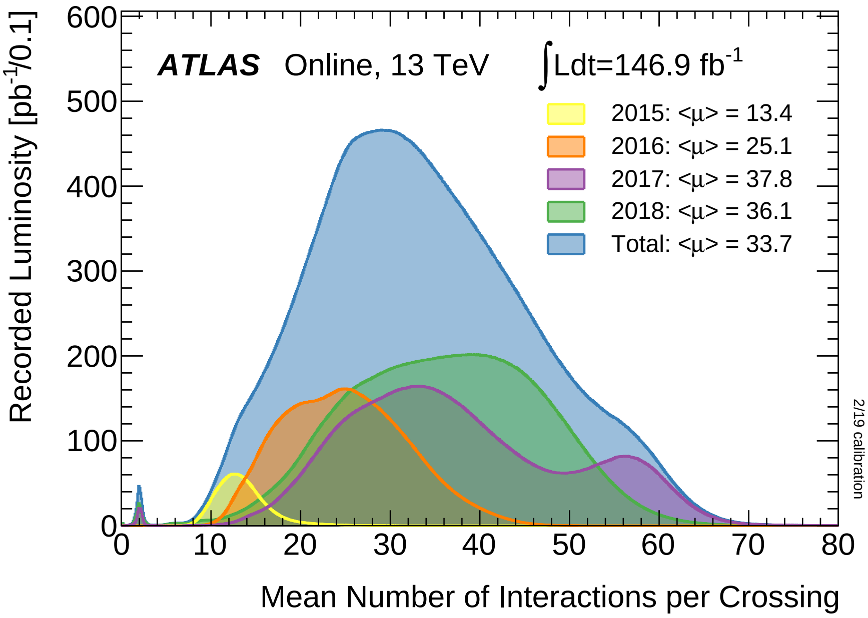

(a)

Figure 3.2: This figure illustrate the average interactions per bunch crossing between 2015 to 2018 period (Run-2). The figure is from ref [23]

3.2 The ATLAS Detector

The ATLAS (A Toroidal LHC ApparatuS) detector is one of the two general-purpose detectors at the LHC and stand as the world's largest volume detector that humans ever constructed for a particle collider. The detector is cylindrical and covers nearly the entire 4π solid angle, with a length of 46 meters and a diameter of 25 meters. The whole detector weighs approximately 7,000 tonnes in total and its design consists of multiple layers of specialised detection system organised around one of the interaction point of the proton-proton collisions around the LHC ring. The data collected from the ATLAS detector are used to conduct searches and measurements for BSM physics and precision measurements, including the di-τ measurement discussed later in this thesis.

Before discussing the detector components, the coordinate system used by ATLAS needs an introduction first to ensure clarity. The ATLAS naturally uses a right-handed cartesian coordinate system with respect to the beam line and the interaction point using three axes: x, y and z that benefits the interpretation of experimental results. The z axis points along the beam line with positive z extending in the direction of one of the proton beams. The x axis points horizontally and perpendicular to the beam line. It is like the radius of the LHC circle where the direction of x is chosen to point from the interaction point towards the centre of the LHC ring. The y axis points vertically upwards towards the ground surface direction to complete the setup of the right-handed system. The x-y plane is also refers as the transverse plane, where the measurable observable such as the transverse momentum (p_T) and the transverse energy E_T are referred to the momentum and energy in the direction of the transverse plane. The spherical coordinates are used to address the angles: The azimuthal angle around the beam line measured from the x axis in the x-y plane is noted as ϕ and the angle θ is used to label the polar angle offset with respect to the beam line.

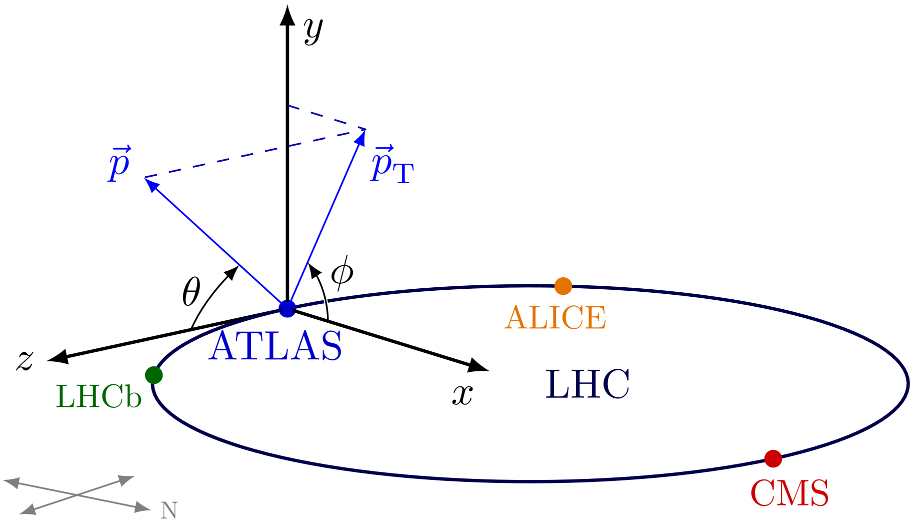

(a)

Figure 3.3: The coordinate system of the ATLAS detector. The figure is from ref [24]

Apart from the cartesian and polar angles, the *rapidity* y is a coordinate commonly used in collider physics that transforms additively under Lorentz boosts along the beam axis:

$$y = \frac{1}{2} \ln \frac{E + p_z}{E - p_z} \tag{3.2.1}$$

where p_z is the longitudinal momentum along the beam axis. Because rapidity differences are Lorentz invariant [25], y is often preferred over the polar angle θ in use. While rapidity is defined using the energy and momentum of the particle, another related quantity named *pseudorapidity* (η) is also often used. The pseudorapidity is given by:

$$\eta = -\ln \tan \frac{\theta}{2} \tag{3.2.2}$$

In the high-energy (massless) limit, the rapidity and pseudorapidity become approximately equal. This makes the pseudorapidity a convenient substitute for rapidity for many situations as it is easier to measure the polar angle θ than to determine the energy and longitudinal (beam) momentum.

The separation of detected objects sometimes are used for event reconstruction and object identifications. This variable ΔR is related to the rapidity y and is quantified by the distance in η-ϕ space:

$$\Delta R = \sqrt{\Delta y^2 + \Delta \phi^2} \tag{3.2.3}$$

This metric is Lorentz invariant under boosts along the beam axis and is widely used for object isolation and clustering.

Particle detection relies on interacting with the particles to infer their properties, and this is exactly how the ATLAS detector is designed; The detector components are optimised to maximise such interactions through momentum transfers for different particle types.

The description of the ATLAS detector in this chapter follows an inside-out approach, with an order of: Inner detector, calorimeter, Muon chambers and an overview of the magnet and trigger system. An illustration of the detector geometry is shown in Figure 3.4, where the detector components forms multiple layers circling around the beam pipe.

3.2.1 The Inner Detector

The Inner Detector (ID) is the innermost component of the ATLAS detector and is designed to track the charged particles produced in the proton collisions. The ID plays an important role in reconstructing particle trajectories, measuring momentum and identify-

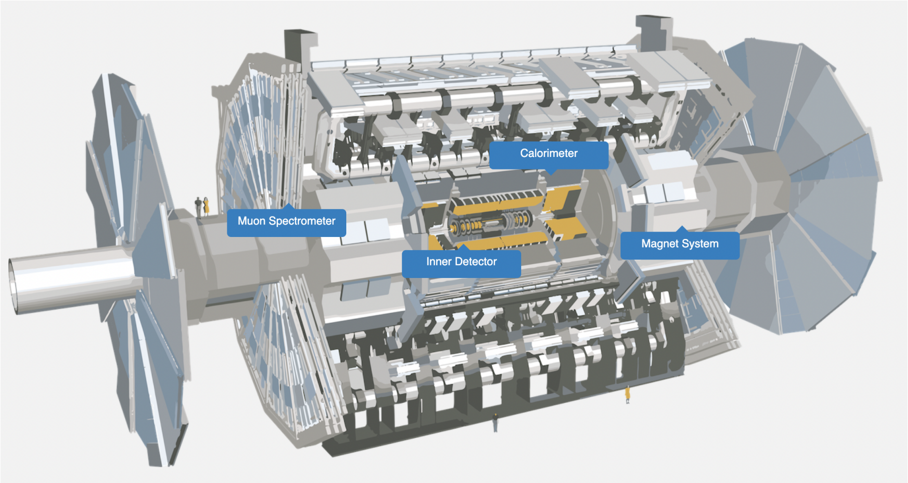

(a)

Figure 3.4: An illustration of the ATLAS detector marked with the sub-components mentioned above. The figure is from the CERN website [26]

ing primary and secondary vertices [27]. The Inner Detector is situated within a superconducting solenoidal magnet that provides a two Tesla magnetic field [28], where the purpose is to bend the paths of charged particles, while the degree and direction of the path curvature would allow the momentum and charge of the particle to be precisely determined respectively.

The Inner Detector is formed of barrel arrangement wrapped around the beam axis and end-capped with disks perpendicular to the z direction that are used to broaden the angular coverage to detect particles with forward/backwards trajectory (parallel to z axis). The Inner Detector consists of three main sub-detectors, each with distinct technologies and functionalities: the Pixel Detector, the Semiconductor Tracker (SCT), and the Transition Radiation Tracker (TRT).

Pixel Detector

The Pixel Detector is the innermost component of the Inner Detector and locates closest to the interaction point. It consists of three barrel layers and three end-cap disks on either side. The detector uses silicon pixel sensors with a very fine granularity, allowing for high-resolution tracking and accurately resolving primary and secondary vertices from the decays of short-lived particles, including the τ lepton (di-τ measurement) and objects such as the b-hadrons. The sensor modules of the detector are made of 46,080 small, discrete detecting element pixel with size 50×400 micrometers, the former number is the width (ϕ direction) and the latter is the length (z direction) [29]. Each pixel is connected to an individual readout channel, which processes the signal generated by a passing charged particle. The readout electronics are also designed to handle high rate of particle hits and are capable of fast signal processing to cope with the LHC's high collision frequency. The detector is equipped with an advanced cooling system to maintain the silicon sensors at optimal operating temperature, typically around -10 °C to minimise the noise and radiation damage. For tracking detectors like the Pixel Detector, minimising the material budget in units of radiation length X_0 is critical to reduce unwanted effects such as multiple scattering, photon conversions, and bremsstrahlung, all of which can degrade the precision of momentum and vertex measurements. Therefore, the supporting structures are made of low-mass materials to reduce the effective thickness to a small fraction of a radiation length per layer. In this way, the low amount of material that particles pass through would minimise the energy lost and extra scatterings.

An additional layer known as the Insertable B-layer (IBL) was added to the Pixel Detector to improve performance in terms of reaching a higher resolution for vertex reconstruction as the IBL is located even closer to the beam pipe. In total, the Pixel Detector hosts around eighty million readout channels to achieve an resolution of around 10 μm in the ϕ direction and 115 μm in the z direction [29].

Semiconductor Tracker (SCT)

The Semiconductor Tracker is located in the intermediate region of the inner detector, surrounding the Pixel Detector and inside the Transition Radiation Tracker. It consists of four barrel layers in the central region and nine end-cap disks on each side [30], covering the forward and backward regions. The SCT spans a cylindrical volume with a radius from approximately 30 cm to 52 cm [31] from the beam axis and extends along the beam line. The SCT uses silicon microstrip sensors with a typical strip pitch of around 80 micrometers, where the strip pitch is the distance between the adjacent strips. The intrinsic spatial resolution is approximately 17 micrometers in the transverse ($R - \phi$) direction and around 580 micrometers in the z direction in the barrel [31]. The high spatial resolution of the SCT combined with the measurements from the Pixel Detector and TRT allows for accurate particle tracks reconstruction. Although the SCT uses one-dimensional silicon microstrip sensors that primarily measure particle hits in the transverse direction, z-position information can be obtained by combining hits from pairs of sensors mounted back-to-back with a small stereo angle [31]. Each SCT module consists of two layers of silicon strips that are rotated relative to each other, when a charged particle passes through both layers, the intersection of the two strip measurements defines a space-point, enabling the reconstruction of the particle's three-dimensional trajectory.

Transition Radiation Tracker (TRT)

The Transition Radiation Tracker (TRT) surrounds the SCT and locate at the outermost layer of the inner detector and is also used for tracking charged particles and provide particle identification, especially for electrons. The structure of the TRT is also consists of a barrel section and two end-cap sections to cover the forward and backward regions. The TRT uses gas-filled straw tubes as its primary detecting elements. Each straw is a thin, cylindrical tube made of a lightweight material that filled with a gas mixture that typically a combination of xenon, CO_2 and O_2 (70%, 27%, 3%) [32]. The TRT includes radiator materials (polypropylene fibres) interleaved with the straw tubes to induce transition radiation and the materials are designed to produce X-ray photons when high-energy charged particles pass through and cause ionisation. Transition radiation occurs when a relativistic charged particle crosses the boundary between materials with different dielectric constants. In the TRT, this effect is exploited by alternating layers of radiator material and gas-filled straws. When a particle passes through these boundaries, it emits transition radiation photons. The energy of this radiation is directly proportional to the particle's relativistic factor, $\gamma = E/m$. By detecting both the ionisation signal and the transition radiation, the TRT can distinguish between different types of charged particles. In particular, electrons produce significantly more transition radiation than heavier particles such as muons or pions at the same momentum, making electron identification especially effective.

In total, there are 351,000 readout channels resulting a spatial resolution of 130 μm in the $R - \phi$ direction and is weaker than the Pixel Detector and the SCT [33]. The TRT does not directly provide precise z-coordinate information. In the barrel (73 planes of tubes), where the straws run parallel to the beam axis [32], the drift time gives radial information, but the z-position is obtained by combining hits from the Pixel and SCT detectors. In the end-caps (80 planes in each), where the straws are radial [32], the TRT contributes to R-direction measurements. Despite its limited longitudinal resolution, the TRT enhances overall momentum resolution by providing a large number of measurement points along the particle trajectory.

3.2.2 The Calorimeter

The particles passed through the inner detector region would first encounter the ATLAS calorimeter system. The calorimeter is designed to measure the energy of both charged and neutral particles such as the electron, photon, and hadrons by absorbing the momentum. However, other particles such as the muon and neutrinos would penetrate through the calorimeter without much energy dissipated as they are minimal ionizing particles (MIPs) and weakly interacting at the LHC energy scale. The calorimeter system consists of two main parts: the Electromagnetic Calorimeter (ECAL) and the Hadronic Calorimeter (HCAL). Both are complemented by the Forward Calorimeter (FCal) to extend coverage into the forward regions. Different absorbing materials are used for the ECAL and the HCAL but are all designed to maximise interactions between the particles and the calorimeter medium, which allows the particles to lose all their energy through interactions. Through the path in the calorimeter, the initial particle entered the calorimeter will eventually create a particle shower consists of a cascade of secondary lower energy particles produced when the particle interact with the matter, and the detectors within the calorimeter will generate signals proportional to the total energy deposited by the particle shower in the active material to capture the momentum of the incident particle. Depending on the initial particle type, the shower have slightly different signatures and can be categorised into two types: Electromagnetic shower and the Hadronic shower . The electromagnetic shower are primarily initiated by electrons or photons and are mostly processed by the Bremsstrahlung radiation ($e \rightarrow e\gamma$): When a high energy electron transverses a material, it would emit photons due to the deceleration in the electric field of atomic nuclei, and the pair production ($\gamma \rightarrow e^+e^-$): where a high energy photon can convert into electron-positron pairs. The Hadronic shower is a more complex process and produced through the strong interaction between the incident particle and the absorbed material nuclei. Due to the differences between the ways of different types of particles dissipating their energy, to measure the momentum efficiently and accurately, different technologies are needed, and thus the calorimeter system is separated into the ECAL and the HCAL sections, which together fills the ϕ coordinate space up to very forward angles and with a pseudorapidity range of up to $|\eta|$.

Electromagnetic Calorimeter

The electromagnetic calorimeter is located closer to the inner detector than the hadronic calorimeter as shown in Figure 3.5. The liquid Argon (LAr) is used as the active sensing medium for ionization, where passing particles ionize the argon atoms and produce electrons, which generate detectable signal and becomes the readout. The LAr was chosen for several reasons:

- **Linearity and uniformity**: Excellent signal linearity over a wide range of energies and response uniformity across the entire detector volume [34].
- **Radiation resistance and stability**: The LAr material is inherently radiation hard and can with stand the high radiation level present in the LHC with high stability without significant degradation in performance [34].
- **Dielectric properties**: The LAr has excellent dielectric properties, which allows it to sustain electric fields [35], allowing fast drift of electrons towards the readout electrodes, which is a important factor for collecting the ionization electrons produced efficiently.
- **Cryogenic temperatures**: LAr operates at cryogenic temperatures (around 87 k), which is beneficial for reducing thermal noises in the detector [28].
- **Low cost**: Argon is relatively abundant and making it feasible to use large volumes in the ATLAS detector.

Apart from LAr as the active material, lead plates are used as the absorber in the ECAL due to their favourable interaction properties. Lead has a short radiation length of 0.56 cm, meaning that an electron loses approximately 63% (i.e. $1 - \frac{1}{e}$) of its energy via bremsstrahlung after traversing just 0.56 cm of lead. Additionally, lead has a relatively long hadronic interaction length of 17.1 cm, which is around 30 times of the its radiation length. These properties making it well-suited to efficiently absorb electromagnetic particles while limiting hadronic interactions. The total thickness of the ECAL corresponds to approximately 22 radiation lengths (but less than one hadronic interaction length), ensuring that electromagnetic showers are fully contained while hadronic showers are largely suppressed. This design choice optimises the ECAL for accurate and clean measurements of electromagnetic particles (electrons and photons), while minimising contamination from hadronic activity.

The LAr and lead are arranged in an accordion geometry to ensure the full azimuthal coverage without gaps and provides uniform response over the entire detector volume. The ECAL is primarily composed of two sections: the Barrel calorimeter, the End-cap calorimeter and the Forward calorimeter. The barrel section covers the central region of the detector up to $|\eta| < 1.475$. The End-cap section are divided into two coaxial wheels to cover the forward region between $1.375 < |\eta| < 3.2$. The forward calorimeter extends the coverage to very forward angles with range $3.1 < |\eta| < 4.9$. Each section consists of three layers of varying granularity, the first layer is the pre-sampler layer with a granularity of $\Delta\eta \times \Delta\phi = 0.025 \times 0.1$ in the barrel region ($|\eta| < 1.52$) and the end-cap region ($1.5 < |\eta| < 1.8$). The layer is designed to correct for energy loss in the material in front of the calorimeter, including the inner detector and the cryostat. The second layer is accordion which is the main layer of the ECAL and acts as sampling layers. Within the accordion section, the first sampling layer has a granularity of $\Delta\eta \times \Delta\phi = 0.0031 \times 0.1$ for both barrel ($|\eta| < 1.475$) and end-cap region ($1.375 < |\eta| < 1.5$). This finer granularity layer is for accurate position determination and for separating the nearby particles with small ΔR to discriminate between showers originated from single or multiple photons. The second sampling layer is having a resolution of $\Delta\eta \times \Delta\phi = 0.025 \times 0.025$ for the same barrel and end-cap regions as the first sampling layer. This layer is where the bulk of the electromagnetic shower energy dissipated and is important for precise energy measurement. The last sampling layer is having a granularity of $\Delta\eta \times \Delta\phi = 0.05 \times 0.025$

for both the barrel and end-cap regions. Despite for the lower granularity, it is an important layer to provide additional sampling to improve energy resolution by resolving the tail of the showers, particularly for high-energy showers that extend deeper into the calorimeter.

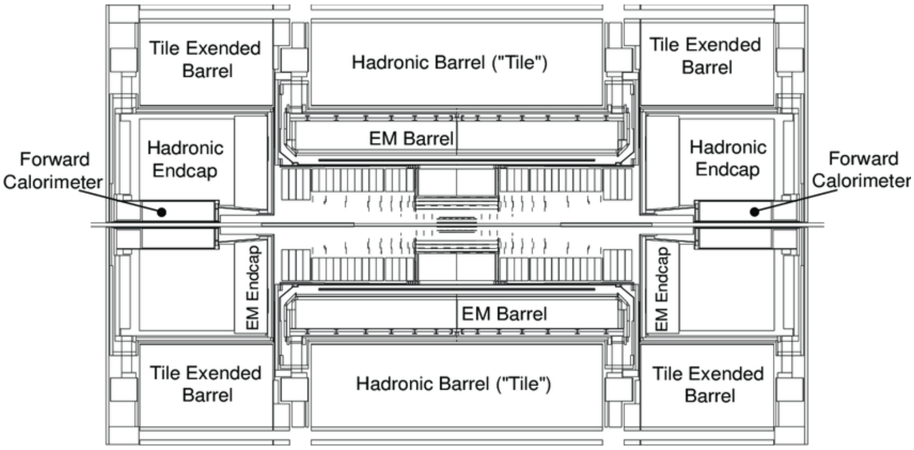

(a)

Figure 3.5: A cross-sectional view of the calorimeter system of the ATLAS detector [36].

Hadronic Calorimeter

Once the electromagnetic showers are stopped at the ECAL, the remaining particles will penetrate the ECAL and reach the hadronic calorimeter section. The HCAL is a complement to the ECAL and is designed to provide energy measurements for particles that primarily interact through the strong interactions, i.e. hadrons. The hadrons lose their energy through inelastic interactions with the dense absorber materials in the calorimeter and would results in the production of multiple secondary particles to create the hadronic shower. The energy is then collected by the active medium and converted into measurable signals. The structure of the HCAL can be divided into three main sections: the Tile calorimeter, the Hadronic End-cap calorimeter, and the Forward calorimeter.

The Tile calorimeter is located at the central barrel region and extends to the end-cap region as illustrated in Figure 3.5. The Tile calorimeter can be sub-divided into two parts, a hadronic tile barrel section in the $|\eta| < 1.0$ region, and two extended barrel sections which cover a pseudorapidity range between $0.8 < |\eta| < 1.7$. Both sections used steel as the absorber material and plastic scintillating tiles as the active medium. Alternating layers of steel and scintillating tiles forms 64 modules arranged in a cylindrical geometry oriented perpendicular to the beam axis to maximise energy deposits. The granularity of the tile calorimeter at both the barrel and extended barrel sections is $\Delta\eta \times \Delta\phi = 0.1 \times 0.1$. Ultraviolet scintillating light is produced when particles passing through the scintillating medium and the light is shifted with optical fibres that are then collected and directed to the photo-multiplier tubes to output measured signal [37].

The Hadronic end-cap calorimeter is located at the end-cap regions of the detector and positioned in front of the forward calorimeter, behind the electromagnetic end-cap calorimeter as labelled in Figure 3.5. It consists of two wheels per end-cap and are each divided into 32 modules to cover the azimuthal angles. The primary absorber material used is copper instead of lead as for the ECAL case. The absorber is made of parallel copper plates that interleaved with gaps filled with LAr. The LAr is again used as the active medium and ionise when charged particles from the hadronic showers pass through, which in turn produce ionised electrons as signal. The coverage of the hadronic end-cap calorimeter range between $1.5 < |\eta| < 3.2$. The granularity is $\Delta\eta \times \Delta\phi = 0.1 \times 0.1$ between $1.5 < |\eta| < 2.5$ and $\Delta\eta \times \Delta\phi = 0.2 \times 0.2$ for $2.5 < |\eta| < 3.2$.

3.2.3 The Muon Chamber

Before reaching the very last detecting component, most particles produced from the central proton collisions will have been stopped by the ATLAS calorimeter system. However, being a minimally ionising particle, the relativistic muons do not dissipate much energy in the ECAL and have long enough lifetime to penetrate through the whole calorimeter system. Therefore, an extra layer of muon chambers (spectrometers) are necessary to capture the muons. The muon spectrometer surrounds the calorimeters and covers the outermost region of the detector. The spectrometers are designed to provide precise measurement of muon tracks over a large volume and high pseudorapidity range.

The muon spectrometers also have the barrel region ($|\eta| < 1.0$) and the end-cap regions $1.0 < |\eta| < 2.7$. Four types of gaseous chambers are utilised in the muon spectrometer system and each optimised for different functions and regions, two of these are tracking chambers used for precision momentum measurement and the other two are used as an efficient trigger system [38]:

- **Monitored Drift Tubes (MDT)**: The MDT are used to provide high-precision measurements of muon tracks, covers a range of $|\eta| < 2.7$ and made of 3 cm diameter pressurised aluminium drift tubes filled with a gas mixture of 93% argon and 7% carbon dioxide. When a muon passes through the tube, electron are produced from the ionisation process and drift towards the wire anode. The drift time of the electrons to the wire anodes is used to determine the position of the muon track.

- **Cathode Strip Chambers (CSC)**: In the forward region $2.0 < |\eta| < 2.7$, the number of MDTs is reduced as the particle flux is twenty times higher than the average in the other section of the muon chambers [38]. The CSC is used in the innermost end-cap region to provide high precision and high rate momentum measurements and consists of multi-wire proportional chamber with cathode strips that read out the position.
- **Resistive Plate Chambers (RPC)**: The RPCs are used in the barrel region for trigging. The RPCs are consists of two parallel electrode plates with a gas gap in between that ionises and triggers when a muon pass through. The purpose for the RPC is to provide a fast timing information for trigging purposes in the $|\eta| < 1.05$ [39].
- **Thin Gap Chambers (TGC)**: Lastly, the TGCs are used in the end-cap region as the second part of the triggering system. The TGC act as a level-1 trigger and would provide fast timing and high efficiency information similar to RPCs but are optimized for the higher particle-flux in the forward regions where the background is higher [40]. Each end-cap has seven layers of TGC and each layer is consists of two resistive grounded cathode planes, with a sheet of closely spaced wires in between [41]. The gap between the anode to the cathode planes (1.4 mm) is thinner than the wire to wire spacing (1.8 mm) [40] and hence reflecting the name.

Due to the layout of the ATLAS detector, where the muon spectrometer forms the outermost layer, muons are the only particles that typically reach this region without being fully absorbed by the inner detector or calorimeters. As a result, muon signals stand out clearly from other particles, allowing for highly efficient and pure reconstruction. This spatial separation, combined with the dedicated tracking chambers and magnetic field in the muon spectrometer, enables precise momentum measurement and unambiguous muon identification.

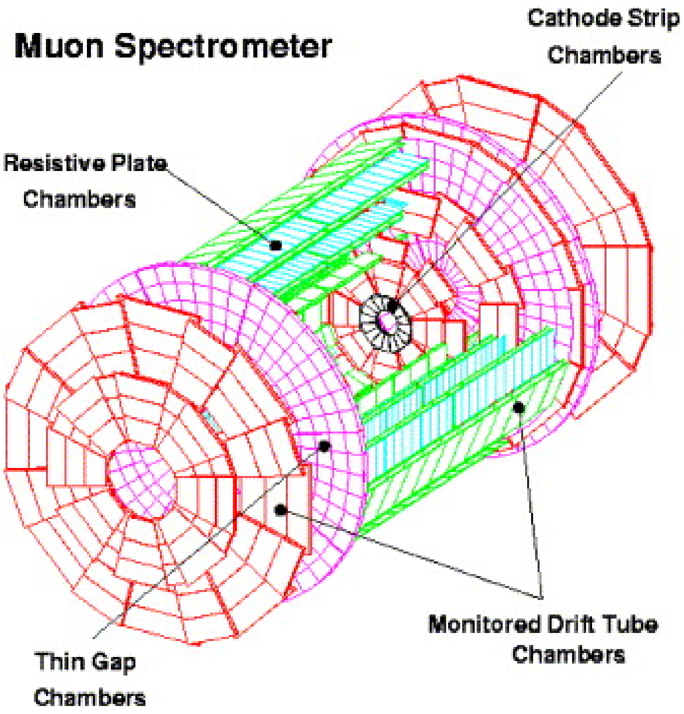

(a)

Figure 3.6: A structural view of the Muon spectrometer system of the ATLAS detector [42].

3.2.4 Magnetic System

The magnetic system that ATLAS have incorporated to its system is one of the most critical components in order to make the detector works. The system is designed to bend the paths of the charged particles for identification and precise momentum measurement purposes. The system consists of a combination of solenoid and toroidal magnets.

The superconducting cylindrical Solenoid magnet made of the niobium-titanium alloy situated inside the calorimeters and the main purpose is to provide a magnetic field for the inner tracking detectors [43]. The magnets with a total dimension of 2.5 m in diameter and 5.3 m long encloses the inner detector and was designed with minimal thickness to reduce the energy loss before particle entering the calorimeters encloses the detector. It generates a uniform magnetic field of two Tesla along the z direction.

The toroidal magnet system surrounds the calorimeters and provides the magnetic field required for the Muon Spectrometer. It consists of three main components: the barrel toroid and two end-cap toroids. The barrel toroid extends longitudinally outside the central solenoid and comprises eight large superconducting coils arranged in an octagonal configuration around the detector. Each coil is approximately 25 meters long and 5 meters in diameter [44], generating a magnetic field primarily in the radial direction. The two end-cap toroids, also composed of eight coils each, supply magnetic fields in the forward regions to enable muon bending and momentum measurements beyond the barrel coverage. Unlike the central solenoid, which produces a uniform axial field, the toroidal magnets generate a non-uniform magnetic field that varies in strength from approximately 0.5 to 1 Tesla [45], depending on the spatial location to ensure the field configuration offers optimal bending power for muons over a wide range of angles and momenta.

The ATLAS detector is equipped with advanced cryogenic systems that maintain the superconducting magnets at temperatures around 4.5 Kelvin. This extremely low temperature is required to keep the magnets in their superconducting state, which allows them to carry very high electrical currents without resistance. Maintaining superconductivity is essential for generating the strong, stable magnetic fields needed for accurate particle tracking and momentum measurement.

3.2.5 Trigger System

During the Run-2 operation period of the LHC, a large amount of data is produced from the proton collision at a frequency of 40 MHz (several thousands of gigabytes per second) where the data comes faster than the writing speed to the disk. However, not all data collected are useful. The trigger system of the ATLAS detector is a crucial component to identify the interested signals efficiently from the vest majority of the low-energy data output to avoid redundant measurements and allows a fast-responding measuring process with the limited bandwidth and computational resources.

The trigger system can be divided into two main levels: the Level-1 trigger (L1) and the High-level trigger. The former is a hardware based trigger and the latter is a software based trigger [47].

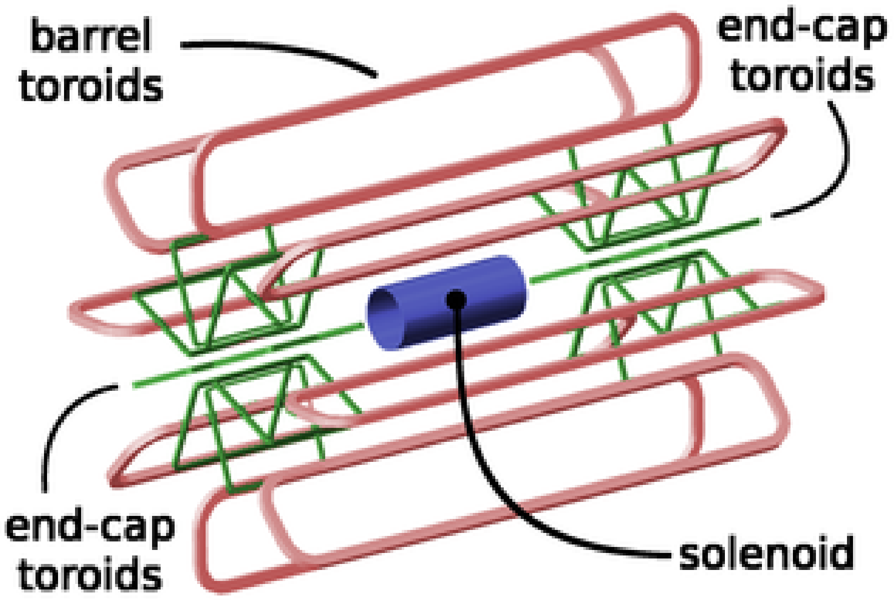

(a)

Figure 3.7: A schematic demonstration of the ATLAS magnetic system [46].

Level-1 trigger

The L1 trigger is responsible for rapidly reducing the data rate from the initial collision rate 40 MHz to about 100 kHz, ensuring only potentially interesting events are selected for further processing by High-Level Trigger. Due to the high frequency of collisions, the L1 trigger must operate within extremely tight latency constraints, approximately 2.5 μs [48]. Within this time, a decision for each event must be made by the L1 trigger. To accommodate this, pipeline buffers are employed in the front-end electronics of each sub-detector [48]. These buffers temporarily store detector signals for the duration of the trigger latency, allowing time for the L1 system to evaluate each event and issue an accept or reject decision. If an event is accepted, its data are read out from the buffer and passed on to the HLT; if not, the buffered data are discarded. There are several components of the L1 trigger:

- **Calorimeter Trigger (L1Calo)**: The calorimeter trigger receives signals from the calorimeter system and identify high-energy deposits with algorithms that are designed to detect electrons, photons, jets, and missing transverse energy (MET). To identify localised energy deposits in the calorimeters, the trigger receives analogue signals that are aggregated in the calorimeter trigger towers to identify clusters of energy deposits. For example, to find a jet candidate, a sliding window approach (discussed in section 3.3.2) was taken to find the local maximum, where the regions with energy above a jet threshold are identified as jet candidates. As for the τ leptons, the identification method is similar to the jet finding algorithm, but optimised for the narrower and more isolated nature of τ decays [47]. The MET calculation can also be performed and is done through calculating the vector sum of the transverse energy in all trigger towers.

The granularity of the L1Calo is $\Delta\eta \times \Delta\phi = 0.1 \times 0.1$ at the barrel region, and a coarser granularity of $\Delta\eta \times \Delta\phi = 0.4 \times 0.4$ at the end-cap regions [49].

- **Muon Trigger (L1Muon)**: The L1Muon trigger utilises the data from the muon spectrometer detectors. The RPCs and TGCs in the muon spectrometer are specifically used for fast pattern recognition and triggering. The L1Muon trigger applies a coincidence logic to the algorithm and ensures only consistent hit patterns are considered and indicate genuine muon tracks.

- **Topological Trigger (L1Topo)** The L1Topo trigger receives inputs from both the L1Calo and L1Muon systems and adds advanced topological processing to the Level-1 trigger by analysing geometric relationships between trigger objects, such as angular separation (ΔR), invariant mass, and relative azimuthal angles. This enables more selective and physics-driven event rejection already at the hardware level.

- **Central Trigger Processor (CTP)** The CTP is the core decision-making unit in the level-1 trigger system. It integrates the trigger information from other level-1 triggers to make a comprehensive decision about whether to accept or reject an event.

High-level trigger (HLT)

The High-level trigger is the second layer of the trigger system and is designed to further filter and refine the selection of events identified by the Level-1 trigger which can then be stored and analysed offline. The HLT has two components: the Level-2 Trigger and the Event Filter. The Level-2 trigger is the initial stage of the HLT, which processes Regions of Interest (RoIs) identified by the L1 trigger to see regional event reconstruction with full detector granularity. The event filter would perform a full event reconstruction using the complete event data and apply more complex algorithms to further filter the accepted events from L1 and L2 triggers. Due to the event reconstruction being computational expensive, the HLT is built as a chain of trigger units. At each stage, partial event data is used and rejects the event immediately if criteria not fulfilled. This can speed up the decision-making process and avoid unnecessary checks using algorithms requiring heavy CPU usage. As a result, the HLT reduces the event rate from about 100 kHz to approximately 1 kHz (i.e. around 1 GB per second) [47]. To further improve the rate, the HLT employs the trigger prescales mechanism to manage the event selection and computational load. The prescale factors are applied to specific triggers or algorithms to reduce the rate at which they process events, where the factors sets only a fraction of events that meets the trigger threshold are processed and recorded. In this way, the prescales help control the event rate at which different triggers operate to ensure the overall rate remains manageable for the limits of the HLT, and also the system can prioritise certain triggers over others based on current needs to adjust the mixture of recorded physics events [50].

In the di-τ analysis, a set of tau triggers from the ATLAS Run 2 data-taking period was used to efficiently select τ lepton candidates while balancing signal efficiency and background rejection. Firstly, the L1-triggers were used for the initial τ identification based on localised energy deposits in the calorimeter, then followed by HLT that refined the selection using advanced tracking and machine learning identification techniques. The detailed trigger list used for the analysis is discussed in section 4.2.2.

3.3 Object reconstruction

The raw electric signals collected from all the previous detector components is difficult to interpret due to detector dependence unless properly transformed into meaningful physical quantities that can be analysed by the analysis team in a more flexible and sustainable manner. This raw data transformation process is the reconstruction and performed using all information collected from all sub-detectors.

3.3.1 Tracks and Vertices

Finding tracks and vertices is a fundamental step in reconstructing physics objects such as electrons, using algorithms that process data from the Inner Detector to determine particle trajectories and their points of origin. The first stage involves hit detection, where signals above a defined threshold are registered in the detector layers. These hits are then grouped into space points in the Pixel Detector and Semiconductor Tracker, and becomes the localised clusters of hits that are used in subsequent pattern recognition. Then, initial track seeds are formed typically using triplets or doublets of space points, and are extended by attaching additional compatible hits from the SCT and TRT. This extension is guided by combinatorial algorithms such as the Kalman filter [51], which is an iterative algorithm that estimates the trajectory of a charged particle by sequentially incorporating new measurements (hits) while accounting for multiple scattering and measurement uncertainties. At each step, the filter predicts the next state of the track (e.g. position, momentum) and updates this prediction using the observed hit, optimally weighting the measurement and prediction based on their uncertainties. This leads to a globally consistent track fit that minimises the total χ^2 across all hits associated with the track. The resulting reconstructed tracks are described using perigee parameters for the later vertex reconstruction step, the parameters are:

- **Impact Parameter** d_0: This is the transverse distance from the primary vertex to the point where the track is closest to the beam line in the z direction. This parameter measures the displacement of the track in the $x-y$ plane. A small d_0 indicates the track is close to the beam line, while a large d_0 can indicate a displaced vertex from a long-lived particle decay.

- **Longitudinal Impact Parameter** z_0: This is the longitudinal distance from the primary vertex to the point where the track is closest to the z direction beam line. This parameter provides the vertical alignment of the track with respect to the primary vertex.
- **Azimuthal Angle** ϕ_0: The angle in the transverse plane ($x - y$) between the x axis and the track's direction at the point of closest distance to the beam line. Describes the direction of track in the plane perpendicular to the beam line.
- **Polar Angle** θ: The angle between the track and the beam line, which describes the inclination of the track relative to the z direction.
- **Transverse Momentum** p_T: The component of the particle's momentum in the $x - y$ plane. This provides the information on the particle's motion in the transverse plane.

Vertex reconstruction involves identifying where particles originate and is usually indicated by the intersection of multiple particle trajectories at their origin. This includes the identification of primary vertices from the initial proton-proton collisions and secondary vertices from the decay of unstable particles. The first step of vertex reconstruction is to select high-quality tracks with small impact parameter d_0 relative to the beam line. If multiple pile-up vertices are present, the vertex reconstruction algorithm must distinguish between them to correctly assign tracks to their respective interaction points. Then, the selected tracks are grouped to a common point in space and run through algorithms like the adaptive vertex fitter or the iterative vertex finder to estimate the primary vertex position [53]. Lastly, the initial position is refined iteratively by minimizing the sum of the track impact parameter residuals. The incompatible tracks are then regrouped for other vertex searching processes, including the secondary vertex [53].

3.3.2 Clustering Algorithms

Clustering algorithms are used for identifying and measuring energy deposits in the calorimeters. These algorithms transform raw detector signals into clusters to extract significant

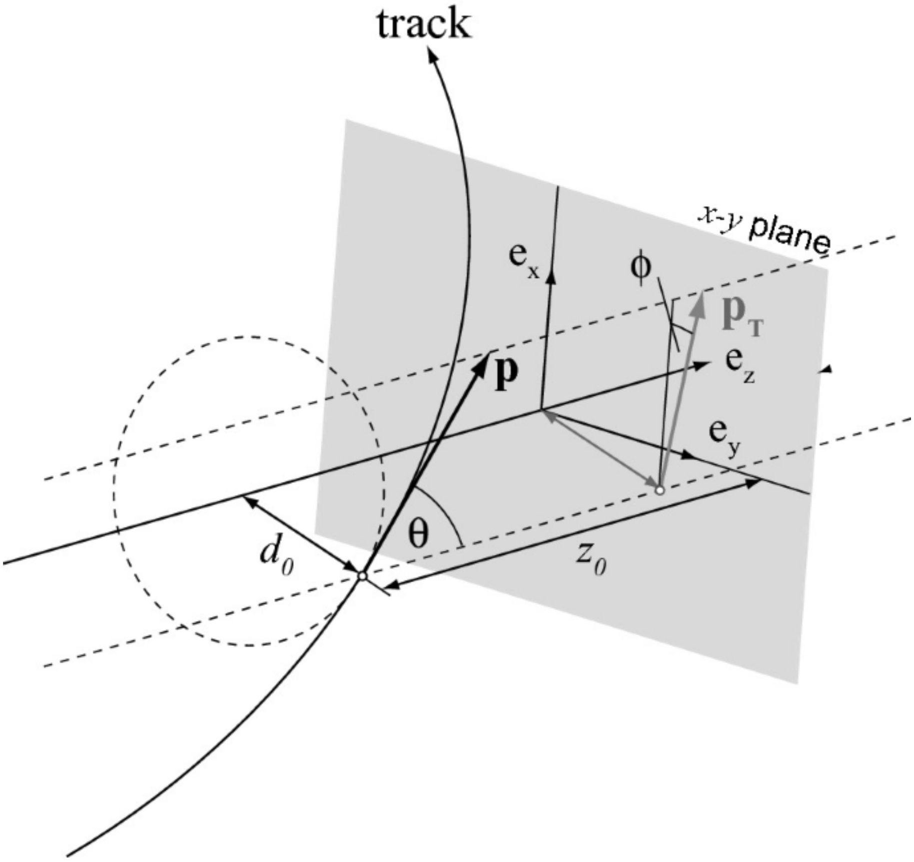

Figure 3.8: The figure shows the definitions of the perigee parameters. The central line represents the beam line with primary vertex defined at the origin of the coordinate system in the figure. The figure is from reference [52]

signal from the hard scattering process from the noise [54], where the noise is mainly from the readout electronics and pile-up [55]. After the clustering process, the total energy deposited can be calculated from the cluster. In ATLAS, there are several categories of such clustering algorithm and each are briefly introduced in the below sub-sections.

Topological Clustering

The purpose for the topological clustering algorithm [56] is to identify and group calorimeter cells with significant energy deposits to form clusters. The building of the cluster starts with seeding cells that have energy signal significance above a threshold [54]:

$$\zeta_{cell} = \frac{E_{cell}}{\sigma_{noise,cell}} \tag{3.3.1}$$

where E_{cell} is the energy deposited in the cell and the denominator is the average expected noise in the cell [54]. To form the final cluster, there are three thresholds defined to compare with the values obtained in equation 3.3.1: seed threshold (high), neighbour threshold (intermediate) and the perimeter (low) threshold. The seed cell threshold ensures that any calorimeter cell with energy above this threshold is identified as a seed cell, typically indicating a significant energy deposit. These seed cells are then ranked from highest to lowest based on their ζ_{cell} values and used to initiate the formation of proto-clusters. Next, the cells directly adjacent to the seed cells that have energy above the lower neighbour threshold $\zeta_{neighbor}$ are the neighbour cells and are added to extend the proto-cluster. For reference, typical values for the seed, neighbour, and perimeter thresholds are 4σ, 2σ, and 0σ above the noise level, respectively [57]. To resolve ambiguities, if the neighbour cell is next to two proto-clusters, the proto-clusters are merged [54]. Lastly, the perimeter cells, which are the cells that below $\zeta_{neighbour}$ but above ζ_{base} are added to the nearest neighbouring proto-cluster to ensure the proto-cluster captures all relevant energy, including the lower-energy deposits at the edges. The process repeats for the neighbouring list of cells until all cells are processed. If multiple local maxima are observed in the cluster, the cluster is split into separate clusters for distinguishing the closely spaced particles [54].

During the use of the topological clustering algorithm, its parameters are carefully tuned to balance the trade-off between capturing all relevant energy deposits and suppressing noise. This optimisation enhances reconstruction efficiency while maintaining high spatial and energy resolution. The algorithm offers several advantages: it is highly adaptable to various particle types and energy deposit patterns, as it does not rely on pre-defined cluster sizes or shapes. Furthermore, it demonstrates strong robustness against noise and is effective at suppressing pile-up contributions, making it well-suited for operation under high luminosity conditions. By applying dynamic thresholds and taking into account the spatial correlations between calorimeter cells, the algorithm achieves precise energy measurements and excellent spatial resolution. In the ATLAS experiment, topological clustering is extensively employed in both the Level-1 and High-Level Trigger systems, as well as in offline data analysis.

Sliding Window Clustering

In contrast to the topological clustering algorithm, the sliding window clustering algorithm involves scanning the calorimeter data with a fixed-size window to find regions with significant energy deposits. The method is straight forward and efficient, making it suitable for online data processing in the trigger system.

The first step for the algorithm is to define a fixed-size window, covering a region of $n \times n$ calorimeter cells, where n can vary depending on the resolution and granularity of the calorimeter and the target particles. This window will then grid-scan across the $\eta - \phi$ plane, where the longitudinal calorimeter cells' energies in each window position are summed together. Through this scan, the algorithm will identify the local maximum of each window as a potential cluster centre. If the summed energy exceeds a pre-defined threshold, a cluster is formed at this position. The initial cluster positions are refined by adjusting the window position to find the exact centre of the energy deposit. To avoid double counting, once a cluster is identified, the cells within the window are marked and not used for further cluster information until the next iteration. Again, if it happens to identify multiple local maxima within a window, the cluster may be split into separate clusters to account for the scenario with closely spaced particles.

Similar to the sliding window, a Cone clustering is also used in ATLAS to identify energy deposits particularly for jets. Instead of a window, it groups calorimeter cells into a fixed cone size and centred around a local maxima seed cell having energy above a threshold. The cone-size is defined with $R = \sqrt{(\Delta\eta)^2 + (\Delta\phi)^2}$ in the $\eta - \phi$ plane, where R is the radius.

The sliding window family algorithms are also used in both Level-1 and High-level trigger system and offline data analysis. Although the algorithm has the edge of being simple and ideal for the real-time execution, it may not be as robust against noise and pile-up effects as the topological clustering algorithm. Therefore, the combination of the algorithums are used to enhance the performance of object reconstruction procedure in ATLAS.

3.3.3 Electron reconstruction

Following the discussion on section 3.3.1 on track candidates and section 3.3.2 on calorimeter cluster candidate reconstruction, the final step in electron identification is to match a track reconstructed in the Inner Detector (ID) to a corresponding energy deposit in the calorimeter. This matching is performed using dedicated algorithms [58]. After a track is selected for reconstruction, its parameters are used to extrapolate the particle's trajectory from the ID to the calorimeter. The extrapolated position of the track at the calorimeter is then compared to the position of the energy cluster and the pair is considered a potential match if the cluster lies within the search windown defined around the extrapolated position. For electrons, which are particularly susceptible to bremsstrahlung radiation due to their low mass, the extrapolation procedure must account for significant energy loss and curvature in the track caused by the magnetic field. To address this, the tracks are refitted using a Gaussian sum filter (GSF) method [59], which improves electron reconstruction by modeling the impact of bremsstrahlung on the momentum and curvature of the track.

The track-cluster matching is also improved using other method such as the Energy/-Momentum ratio consistency and shower shape analysis. The ratio of the cluster energy measured in the ECAL to the refitted track momentum is expected to be close to 1 for electrons with a typical matching criteria of $0.8 < E/p < 1.2$ [60], and the shape of an electron shower in the ECAL tends to be quite specific that can be distinguished from other sources using variables such as the lateral spread $\sigma_{\eta\eta}$, ratio of energy deposited in different ECAL layers E_{ratio} and cluster compactness, etc [61]. Sometimes, to improve the matching accuracy, the momentum of the track is rescaled to match with the energy of the cluster to account for electrons with missing portion of bremsstralung radiation accounted during extrapolation [59]. Also, general matching criteria need to be fulfilled are $|\eta| < 0.05$ to ensure the track and cluster is well-aligned in the η-direction, and $-0.10 < q \cdot (\phi_{\text{track}} - \phi_{\text{cluster}}) < 0.05$, where q is the charge and the term is to account for the charge sign to handle the bending of tracks in the magnetic field and ensure the track and cluster is well-aligned in the ϕ-direction [59]. The asymmetry in the matching criterion arises from the curvature of charged particle tracks in the ATLAS magnetic field and the bremsstrahlung losses experienced by electrons. Electrons tend to radiate bremsstrahlung photons early in their traversal of the detector material, typically before reaching the electromagnetic calorimeter (ECAL). This early energy loss causes a deflection in the electron track, particularly in the azimuthal angle (ϕ), leading to a mismatch between the track and the associated calorimeter cluster. Since the electron track is more affected than the cluster position, especially for low-momentum electrons, the matching window is made asymmetric and has a larger allowance on the negative side (i.e., -0.10) to compensate for this effect. This asymmetry improves the overall track–cluster matching efficiency for electrons.

Electron identification

To distinguish electrons from other background particles, several discriminative variables are used along with techniques to ensure high efficiency and purity. These variables include: energy-momentum ratio (E/p) shower shape ($\sigma_{\eta\eta}$, E_{ratio}), track-cluster matching quality ($\Delta\eta$, $\Delta\phi$), track and calorimeter isolation and combined with tracker information on transition radiations. While early methods relied on cut-based selections, the ATLAS experiment now employs a more powerful likelihood-based identification method [58]. This approach combines multiple input variables into a single likelihood score optimised to separate electrons from backgrounds. For each input variable, probability density functions (PDFs) are constructed from control samples in both data and Monte Carlo simulations for signal (electrons) and background hypotheses. For each electron candidate, the likelihood for both the candidate being signal (electron) $\mathcal{L}_{\text{signal}}$ and background $\mathcal{L}_{\text{background}}$ are calculated by combining the evaluation of the PDFs for each variable at the measured values [58]. A likelihood ratio is then computed as:

$$\mathcal{R} = \frac{\mathcal{L}_{\text{background}}}{\mathcal{L}_{\text{signal}}} \tag{3.3.2}$$

The resulting likelihood ratio $\mathcal{R}$ quantifies how likely a candidate is to be background relative to signal. A lower value of $\mathcal{R}$ indicates a higher probability that the candidate is a true electron. The $\mathcal{R}$ cut is then optimised to balance the trade-off between efficiency and purity based on the desired level of efficiency and background rejection for specific analysis. Such flexibility in the cut value on $\mathcal{R}$ defines various operating points, named as: Loose, Medium and Tight. These working points have an increasing fake electron rejection rates, but consequently dropped in efficiency. For the di-τ analysis, a Medium working point was used for electron identification at the detector-level.

The track and calorimeter isolations mentioned in the previous paragraph are also important steps to help distinguishing electrons. The former type of isolation measures the activity around the electron candidate in terms of tracks and the latter is in terms of energy deposits. In both cases, the region around the electron candidate is defined within a cone of size $R = \sqrt{(\Delta\eta)^2 + (\Delta\phi)^2}$ centered on the electron's direction. For track isolation, the quantity of interest is the scalar sum of the transverse momenta p_{T} of all tracks with $p_{\mathrm{T}} > 1$ GeV within the cone, excluding the electron candidate's track [62]. Then, this sum is compared against a threshold and the electron candidate is only considered isolated if the sum is less than the threshold.

Similarly, the calorimeter isolation requires the sum of transverse energy $E_{\mathrm{T}}^{\mathrm{cone}}$ of all calorimeter cells within the cone to be less than an isolation threshold, excluding those associated with the electron's cluster. The result is further corrected to remove contributions from pile-up and underlying events [62]. These isolation thresholds are again tuned to different working points and are used depending on the needs of the analysis. Two working points, the Loose and Tight isolation working points are defined, where the former has a higher threshold to allow more electrons to pass but with a larger background and the latter would allow less electrons passing but with a higher purity. The isolation criteria used in the di-τ analysis is the FCHighPtCaloOnly isolation working point, where the criteria is $E_{\mathrm{T}}^{\mathrm{cone}} < max(0.015p_{\mathrm{T}}, 3.5\ \mathrm{GeV})$ and no track isolation is applied [63].

3.3.4 Muon reconstruction

Different strategies are used for muon reconstruction to maximise efficiency and coverage while maintaining high purity [64]. Muons are categorised into four reconstruction types: combined, segment-tagged, calorimeter-tagged, and extrapolated muons. Each type uses information obtained from different components of the detector. The most commonly reconstructed muons are combined muons, which use information from both the Inner Detector (ID) and the Muon Spectrometer (MS). Tracks are independently reconstructed in the ID and MS, and then matched by extrapolating tracks from the ID to the MS (and vice versa).If a match is found, the two are combined and refitted using a global fit that accounts for all measurements, providing high-precision momentum resolution.

Segment-tagged muons are reconstructed when a full MS track is not available. Instead, short track segments are reconstructed in the MS, typically in regions with reduced coverage or for low-momentum muons. These segments are matched to ID tracks to confirm the muon hypothesis.

Calorimeter-tagged muons are identified using energy deposits in the calorimeter consistent with a minimum ionising particle. Tracks in the ID are matched to such characteristic calorimeter energy clusters. This strategy is particularly useful for low-momentum muons that may not reach or trigger hits in the MS.

ATLAS uses tracks reconstructed in the ID and the MS and extrapolates them outward through the expected magnetic field and detector material. In some high-η regions, if the MS signal is weak or absent, the extrapolated tracks from the ID can still be accepted as a true muon if it passes through regions in the MS where hits are expected but not necessarily detected due to inefficiencies or gaps, and the track parameters remain consistent with the behavior of a minimum ionising particle like a muon (e.g., straight track, low energy loss). This is especially important for extending the muon identification acceptance for the forward (high-η) regions, where the MS has lower granularity or incomplete coverage.

Muon identification

After reconstruction, the muon candidates are selected by a set of quality requirements using multiple detector component information, and a given set of requirements is again summarized as working point [64]. However, unlike the electrons, these working points are not differ in the threshold of a likelihood. Instead, the muon working points having variable requirements that are different for each of the muon type.

Within the working points, some variables are defined and used as the criteria for muon selections. Firstly, a q/p compatibility is defined as [65]:

$$q/p \text{ compatibility} = \sqrt{\frac{\left|\frac{q}{p_{\mathrm{ID}}} - \frac{q}{p_{\mathrm{MS}}}\right|^2}{\sigma^2\left(\frac{q}{p_{\mathrm{ID}}}\right) + \sigma^2\left(\frac{q}{p_{\mathrm{MS}}}\right)}}$$

where the numerator is the absolute difference between the ratio of the charge q to the momentum p of the muon measured in the Inner Detector and the Muon Spectrometer, and the denominator is the quadratic sum of the corresponding uncertainties [64].

Secondly, a variable ρ' is defined as the absolute difference between the p_T measurements from the Inner Detector and the Muon Spectrometer divided by the p_T of the combined track fit [64]:

$$\rho' = \frac{\left|p_{T,\mathrm{ID}} - p_{T,\mathrm{MS}}\right|}{p_{T,\mathrm{CB}}}$$

Lastly, the normalised χ^2 of the combined track fit is used to determine the track quality. These variables are sensitive to filter out non-prompt muon that are from hadrons, and the combination of the variables are used to set the criteria for the Loose, Medium and Tight muon identification working points using the decrease in number of passes and increase in purity as the metrics. For the di-τ analysis, the Medium identification working point is used.

The isolation of muon is also part of the identification process, in a similar manner to the electrons, the isolation is again defined as the sum of activities around a cone space of a muon candidate, where the transverse momentum and transverse energy are individually summed in the Inner Detector and the calorimeter, which is again used as the isolation metric.

For the track-based isolation, depending on the isolation selection criteria, the cone size ΔR is either 0.2, labelled as $p_{\mathrm{T}}^{\mathrm{cone20}}$ or $min(\frac{10\ \mathrm{GeV}}{p_{\mathrm{T}}^{\mu}}, 0.3)$, labelled as $p_{\mathrm{T}}^{\mathrm{varcone30}}$, where the latter is optimised for topologies where jets or other leptons are expected in close proximity to an energetic muon [66]. The minimum transverse momentum of tracks used in the calculation is either 500 MeV or 1 GeV depending on the need. The calorimeter-based isolation is labelled as $E_{\mathrm{T}}^{\mathrm{topocone20}}$, which is the sum obtained from the topological energy clusters within a cone of $\Delta R = 0.2$ around the muon candidate [65].

For the di-τ analysis, the FCLoose isolation is applied, which requires the calorimeter-based isolation $\frac{E_{\mathrm{T}}^{\mathrm{topocone20}}}{p_{\mathrm{T}}} < 0.20$ and the track-based isolation $\frac{p_{\mathrm{T}}^{\mathrm{varcone30}}}{p_{\mathrm{T}}} < 0.15$ [63]. The track-based isolation is largely pile-up independent, as tracks originating from pile-up vertices or with large transverse impact parameters relative to the primary vertex are rejected. In contrast, the calorimeter-based isolation is more sensitive to pile-up effects. Although corrections are applied to subtract contributions from pile-up and underlying events, these corrections introduce additional uncertainty and can degrade the energy resolution. As a result, when calorimeter-based isolation is used, a tighter requirement is applied to the track-based isolation to mitigate the pile-up dependence. This leads to the asymmetric selection thresholds for track- and calorimeter-based components in the FCLoose isolation working point [65].

The track-based isolation is largely pile-up independent due to the rejection of originated from pile-up vertices or with large transverse impact parameters relative to the primary vertex, On the other hand, the calorimeter based isolation tends to have more pile-up dependence due to the corrections on the contributions from pile-up and underlying events would results in poor energy resolution. As a result, when calorimeter-based isolation based criteria is included, a more stringent selection on track-based isolation is applied to compensate for the pile-up dependence, and hence resulted the asymmetric criteria on track-based and calorimeter-based of the FCLoose isolation selection [65].

3.3.5 τ reconstruction

The tau lepton is the primary focus of the di-τ analysis discussed later in section 4 of this thesis. This section will briefly introduce the procedure of τ reconstruction.

τ identification and isolation

Unlike the electron and muon, the τ lepton is a highly unstable particle with a very short lifetime. When produced in proton-proton collisions, it typically decays before reaching the inner detector of the ATLAS experiment. The τ lepton exhibits a variety of decay channels, where it can decay either leptonically into lighter leptons or hadronically into hadrons. The hadronic decay channel, which occurs about 65% of the time, involves the production of one or more hadrons and presents significant challenges for reconstruction due to the complex nature of the decay products, large number of background hadrons and the rapidity of the decay process.

The first step in the reconstruction of the τ particle involves an initial selection of τ candidates based on reconstructed tracks and calorimeter clusters. This selection typically requires either one or three charged tracks (prongs) and a minimum transverse momentum (p_{T}) threshold. The number of prongs reflects the underlying decay mode of the τ lepton. A one-prong decay may originate from either a leptonic or hadronic decay. In leptonic decays, the τ lepton decays into a lighter lepton and neutrinos, with the single reconstructed track corresponding to the charged lepton. In contrast, one-prong hadronic decays result in a single charged hadron, typically a charged pion, along with neutral particles. Three-prong decays are a signature of hadronic decays where the τ decays into three charged hadrons, usually pions or a combination of pions and kaons. The requirement for an odd number of prongs arises from charge conservation, as the τ lepton carries a net charge of ± 1. A decay with two charged tracks would violate this constraint unless additional charged particles were involved, which is not typical for dominant τ decay modes. As such, tau reconstruction focuses on identifying one-prong and three-prong decays, which cover the vast majority of hadronic τ decays, while multi-prong decays with five or more tracks are very rare and difficult to distinguish from background hadronic jets.

The τ candidates tracks are also tested against the impact parameter. The tracks produced from τ decays are typically narrower and collimated compared to those from other processes. This topology contrasts with broader and more diffuse track distributions arising from other processes such as QCD jet production, where charged hadrons are produced in a less constrained, higher-multiplicity environment. In QCD jets, tracks tend to be more dispersed, have varying momenta and vertex associations, and are less likely to exhibit the isolated, pronged structure characteristic of hadronic τ decays. The groups of tracks with lower impact parameter and correct multiplicity (one/three prong) are matched against the calorimeter clusters using several criteria: 1.*)* A small d_0 would indicates the tracks are closely aligned with the cluster in the transverse plane, suggesting they are from the same τ decay. 2.*)* A common $\Delta R < 0.2$ criteria is used for the angular distance matching which is larger than that used for electrons or photons as τ decays often produce wider jets [67].

3.*)* An energy matching is also used, where the transverse energy of the cluster is compared to the transverse momentum of the track. The sum of the tracks p_T for τ candidates should be consistent within $0.7 < \frac{E_T^{cluster}}{\sum p_T^{tracks}} < 1.3$ [68] where the flexibility is to account for neutral particles in the decay.

Apart from the matching between tracks and energy clusters, the τ candidates are also required to pass the isolation criteria as the τ candidates are expected to be isolated from other tracks and clusters. This selection requires the surrounding space to have low additional activity to help distinguishing τ decays from other hadronic jets and pile-up effects. The isolation selection can be divided into two section: the track isolation and the calorimeter isolation. The track isolation is defined as the sum of the transverse momentum of the tracks around the τ candidate ($\Delta R < 0.2$ in the $\eta - \phi$ plane) should below a threshold of typically around 1 to 2 GeV for a tight isolation criteria. The calorimeter isolation uses the energy sum of the transverse energy detected from the calorimeter cells within a cone ($\Delta R < 0.2 - 0.4$) around the τ candidate and is again compared to another threshold, which is typically around 5 to 10 GeV to ensure minimal calorimeter activity around the τ candidate [68]. Together, the dynamical combined isolation variable: $Iso_{combined} = \sum p_T^{tracks} + \sum E_T^{calo}$ [68] is used and usually required to be less than 5 to 15 GeV for a τ candidate isolation, where the exact values are determined through detailed studies and optimisations for specific cases, depending on the desired balance between τ identification efficiency and background rejection.

To reject misidentified τ_{had} from true tau decays, the ATLAS also employs a Recurrent Neural Network-based classifier (RNN ID), trained on sequential information from the tracks and calorimeter deposits, specifically, on a wide range of τ leptons on a relatively unpolarised sample of pure γ^* Drell-Yan production [69]. The output score of the RNN is used to define working points: Loose, Medium and Tight. These working points are again representing trader-offs between efficiency and purity, e.g. the Loose working point is having a high τ efficiency but lower background rejection. The thresholds are tuned such that the efficiency for real taus is around 70%, 60%, and 40% respectively for the Loose, Medium, and Tight working points [70].

Since the different detector components may detect the same object independently, the same set of tracks and calorimeter clusters can be associated to more than one reconstructed object. To adjust this, an overlap removal algorithm is applied to remove the objects corresponding to the same detector-level signals. The criteria of removal in the algorithm is to use the angular separation between two reconstructed objects. Except for the tau-muon overlap scenario, the angular separation is computed using the objects' rapidity y, where $\Delta R_y = \sqrt{(\Delta y)^2 + (\Delta\phi)^2}$ [71]. As for the tau-muon overlaps, the pseudorapidity η is used instead and the angular separation is computed as $\Delta R_\eta = \sqrt{(\Delta\eta)^2 + (\Delta\phi)^2}$ [71]. All overlap removal scenarios are listed in table 3.1.

Object to remove	Object to keep	Criteria
tau	electron	The tau is removed if $\Delta R_y < 0.2$.
tau	muon	The tau is removed if $\Delta R_\eta < 0.2$.
electron	muon	If they share a track, the electron is removed if the muon is associated with a signature in the muon spectrometer, otherwise the muon is removed.
jet	electron	Any jet within $\Delta R_y = 0.2$ of an electron is removed.
jet	muon	Any jet within $\Delta R_y = 0.2$ of a muon is removed.
electron	jet	Any electron within $\Delta R_y = 0.4$ of a jet is removed.
muon	jet	Any muon within $\Delta R_y = 0.4$ of a jet is removed.
jet	tau	Any jet within $\Delta R_y = 0.2$ of a tau is removed.

Table 3.1: Criteria applied to perform the overlap removal between reconstructed objects. The criteria are listed following the order of application.

3.3.6 Jets and b-jets

Jets are collimated sprays of particles resulting from hadronisation of quarks and gluons. The reconstruction of jet objects requires information from the Inner Detector and the calorimeter. The Jets usually deposit a large amount of energy in the calorimeter and are grouped into clusters using the algorithms described in section 3.3.2. From here, several algorithms are used to reconstruct jets from the calorimeter clusters and tracks with the most commonly used one being the Anti-k_t algorithm. It defines jets by iteratively clustering particles based on their relative distances in the transverse momentum space. In particle-flow jet reconstruction, the algorithm is initialized by treating particle-flow objects (PFOs) as proto-jets, incorporating both tracking and calorimeter information. The distances between each pair of proto-jets and between each proto-jet and the beam are then computed. This distance is given by [72]:

$$d_{ij} = \min\left(\frac{1}{p_{T,i}^2}, \frac{1}{p_{T,j}^2}\right)\frac{\Delta R_{ij}^2}{R^2}$$

where the term $\Delta R_{ij} = \sqrt{(\eta_i - \eta_j)^2 + (\phi_i - \phi_j)^2}$ is the distance between the proto-jets in the η-ϕ plane, and R is a parameter that determines the size of the jet clustered. The distance between a proto-jet i to the beam is given by: $d_{i,B} = \frac{1}{p_{T,i}^2}$ [73, 72].

Next, the algorithm identifies the smallest distance d_{min} among all the calculated distances, if d_{min} happens to be between the proto-jets d_{ij}, the proto-jet i and j are merged to form a new proto-jet, if d_{min} is a $d_{i,B}$, the proto-jet i would be declared as a final jet and removed from the list of proto-jets. The distance calculation and clustering step is then repeated using the new set of proto-jets until all proto-jets have been clustered into final jets [73].

For the analysis discussed in this thesis, the jet objects are built from Particle Flow objects using the anti-k_t algorithm with $R = 0.4$ [58]. Also, part of the analysis cares about the multiplicity of a specific type of jet, namely, the b-jets. b-jets are jets originate from the hadronisation of bottom quarks. Due to the relatively long lifetime of the b-hadrons (hadrons formed of b quarks), the b-hadrons can travel a measurable distance within the detector before decaying, which leading to secondary vertices displaced from the primary interaction. The process of identifying jets originated from b-quarks is called *b-tagging*. Different algorithms are used for b-tagging and can be broadly classified into two categories: the low-level and the high-level tagging algorithms. The low-level algorithms focus on basic properties and are relatively straightforward methods using features directly related to the behaviours of b-hadrons to identify b-jets. The first type is the impact parameter based method [74], which uses the significance of the transverse impact parameter of tracks within a jet. Tracks from b-hadron decays tend to have larger impact parameters as b-hadrons travel a measurable distance before decaying, therefore, measure how far tracks are displaced from the primary vertex is indicative of a b-hadron decay. Secondly, the secondary vertex finding algorithm SV1 [74] is also used to reconstruct the secondary vertices by clustering tracks that originate from a common decay point, which is a strong indicator of the presence of b-jet. The algorithm starts from identifying the possible two-track vertices built with all tracks associated with the jet, and then iteratively run on all contributed tracks to fit one secondary vertex. Tracks with large χ^2 values are removed and the fit is repeated until the χ^2 threshold value and a vertex invariant mass < 6 GeV [74] are reached. The high-level algorithms [75] employ advanced techniques such as multivariate analysis and machine learning methods, including boosted decision trees and neural networks to combine multiple features for b-tagging.

Chapter 4

A high mass $\tau\tau$ cross section measurement

To extract meaningful physics quantities from the data collected through particle detectors, measurements are performed. The primary motivation behind conducting searches and measurements using ATLAS data is to explore the interactions of particles produced in proton collisions. This not only probes current theories and can enhance the sensitivity to constraining new theories through the comparison of experimental results with theoretical predictions, but also has the potential to discover new particles.

Traditionally, such measurements and searches rely on specific theoretical frameworks or assumptions to interpret the experimental data, meaning that the measurement is tailored to the theoretical assumption in the first-place. These type of measurements are valuable in terms of maximizing the sensitivity to the specific model by dedicated constraints. However, this high-mass $\tau\tau$ measurement was designed with a focus on flexibility and reusability in terms of reinterpretation by employing a more model-independent approach. This approach avoids any preconceived assumptions or biases about the underlying physics in its interpretation or prediction.

In this method, raw, unbiased data are measured directly from experiments by exploiting the capabilities of the detector, meaning to focus on a kinematic region that closely matches the detector's acceptance (i.e. the fiducial region). By avoiding extrapolations based on theoretical assumptions and subtracting backgrounds only to measure a dedicated process of interest, the measurement is instead constructed in terms of the observable final state particles, disregarding the invisible components (e.g. neutrinos) and not assuming intermediate steps in the decay chain which would enhance the objective comparisons with various theoretical models.

This method allows for the consideration of a wider range of processes with similar final states in the measurement, shifting assumptions such as the signal composition to the theoretical side. This flexibility enables theorists to use the measurement results for straightforward comparisons by adjusting their models directly (e.g., signal compositions) and comparing them to the experimental result. Additionally, this approach improves the precision of Standard Model (SM) predictions by providing precise, unbiased data that can refine theoretical calculations. Thus, model-independent measurements enhance the reinterpretability of analyses by avoiding predefined model assumptions, benefiting both new physics searches and improvements in SM predictions.

4.1 Motivation for the measurement

To further reduce the unexplored kinematic regions of the LHC run 2 data and enhance the power of setting constraints on theoretical models, the analysis focuses on the high mass di-τ region that was not previously analysed. The analysis presented in this thesis has several motivations:

- Anomalies in rare decay of B mesons (bottom quark and an anti-quark) to a c meson $b \to cl\nu$ rates have been observed at the LHCb experiment. Specifically, the decay rates of b mesons to pairs of muons deviated from Standard Model (SM) predictions [1]. Although subsequent studies [76, 77] confirmed that the result is consistent with the SM in the electron and muon channel, the anomaly in the $b \to c\tau\nu$ decay channel involving third-generation particles remains unresolved [1, 77]. Theoretical models such as the U(1) Leptoquark model suggests that significant deviations are expected in this channel [2].

$$R(D^*) = \frac{Br(\overline{B} \to D^*\tau^-\bar{\nu}_\tau)}{Br(\overline{B} \to D^*\ell^-\bar{\nu}_\ell)} \tag{4.1.1}$$

One explanation to this anomaly shown in equation 4.1.1 involves new physics with preferential coupling to the third-generation fermions, such as the Leptoquarks [3]. Leptoquarks (LQs) are hypothetical particles that can couple to both leptons and quarks, and they are predicted to interact more strongly with the third generation of fermions. This analysis will be sensitive to such scenarios, thus providing constraints on models that include these particles or similar new physics.

- Similar measurement have been performed for the high-mass lighter leptons e^+e^- and $\mu^+\mu^-$ by the ATLAS and CMS experiments [78, 79, 80], as well as the searches. To achieve a complete picture of high-mass dilepton production and fully exploit the Run 2 dataset, the $\tau\tau$ final state must also be measured. This will aid in validating the data and strengthening constraints on related BSM scenarios, including those involving VLL, LQs or Z' bosons as briefly discussed in section 2.5.1.

To address these objectives, the analysis has been divided into two components:

1. A dedicated detector-level search for heavy leptoquarks strongly coupled to third-generation fermions, using likelihood fits, with an extra b-jets multiplicity variable to enhance sensitivity. This is motivated by the expected signature of LQ model decays preferentially to third-generation leptons accompanied with b-jets.
2. An model-independent unfolded measurement of the differential di-lepton cross-section, based on visible observables kinematics in the fully hadronic τ decay channel.

The main result of this thesis is the unfolded invariant mass distribution of the $\tau\tau$ system in the hadronic decay channel, covering all contributing processes that yield the visible $\tau\tau$ final state.

4.2 Event Selection

In any particle physics analysis, event selection is a crucial first step to extract meaningful results from vast amounts of experimental dataset. It serves to define the fiducial phase space of interest; the kinematic region in which measurements will be made. This process involves choosing events that satisfy specific criteria where the process of interest is extracted while minimising contributions from background noise. A good acceptance boundary will in turn enhance the signal-to-background ratio, thereby increasing the sensitivity of the analysis to the phenomena under investigation (i.e. the various BSM signals in this case). The selection strategy is guided by a combination of theoretical expectations, background distributions, trigger acceptance, detector capabilities, and overall optimisation.

Due to the variety of possible τ-lepton decay modes, different selection criteria are applied to different final states.The full analysis is therefore originally separated into three signal regions based on the τ decay modes:

1. The fully hadronic decay channel ($\tau_{\text{had}}\tau_{\text{had}}$).
2. The semi-leptonic decay channel with an electron and hadronic τ ($e\tau_{\text{had}}$).
3. The semi-leptonic decay channel with a muon and hadronic τ ($\mu\tau_{\text{had}}$).

All three channels are included in the signal search, each complemented by a b-jet multiplicity variable to enhance sensitivity in the likelihood fit. However, only the fully hadronic channel is used for the unfolded differential cross-section measurement and the b-jet related variables will be measured in the future. The $e\mu$ channel, which could serve as an alternative final state, is excluded from this analysis. This is primarily because it lacks direct hadronic τ signatures, and is already well-covered by existing $e\mu$-based dilepton searches. Additionally, the focus here is on hadronic decays where the third-generation signature can be more distinctive and the background composition is markedly different. Thus, the chosen channels provide both a unique and complementary view of the high-mass $\tau\tau$ final states.

4.2.1 Fiducial region

Before introducing the detailed particle-level selection criteria that define the fiducial region, a few relevant terms need to be clarified first.

- **Prompt lepton**: Leptons not originating from hadron decay.

- **Born lepton**: Leptons produced in the high-energy collision without undergoing subsequent interactions, prior to the QED Final State Radiation (FSR) [81]
- **Bare lepton**: Leptons after QED FSR [81]
- **Dressed lepton**: Leptons that are surrounded by a cloud of particles which are typically predominantly photons through QED FSR. The four momentum of the nearby radiated photons within a cone of $\Delta R = 0.1$ are added to adjust the lepton's momentum to account for overall energy loss through QED, hence *dressed*.

A fiducial region refers to a well-defined region of phase space that corresponds to the detector's acceptance range, so that measurements are conducted. This region is defined based on observable properties of the particles and events that can be directly measured by the detector, allowing a reduction of model dependence, which facilitates direct comparison between experimental results and theoretical predictions. Fiducial events are therefore referring to events that satisfy the fiducial selections based on the kinematic properties of particles involved. To preserve this model-independence and making the measurement to be as fiducial as possible, all processes producing at least two hadronic decaying taus are treated as signal for the fully hadronic decay channel. The signal is solely defined by the visible final states particles and the $m_{\ell\ell}^{\mathrm{vis}}$ observable is defined from the visible lepton momenta. For the τ_{had} candidates, this is equal to the visible momentum of its decay products with excluding the invisible products such as the neutrinos; for the light leptons, this is defined by the dressed lepton momentum. No signal extraction steps (i.e., background subtraction to isolate a specific process) is performed to avoid theory bias, as doing so would inevitably introduce theory dependence about the background model and signal compositions. This is because distilling signals relies on theoretical models to estimate the expected background contributions accurately. These theoretical models would introduce assumptions about the processes and interactions contributing to the background component of the signal final states. Consequently, the resulting measurement is inherently dependent on the accuracy and validity of the models. By this way, the measurement maintains a more model-independent approach and providing raw measured data without bias introduced.

The main sources of signal are from the Drell-Yan and $t\bar{t}$ processes, meanwhile, the subdominant processes such as multi-boson, single-top processes producing potential τ candidates are included in the unfolded inclusive di-lepton cross-section result. This would again be an example of demonstrating the reinterpretation power of these kind of measurement, where the signal distillations can be done at the post-unfolding analysis stage, providing extra flexibility for theory testings where the composition of background or signal can be later adjusted at the theoretical-level during the reinterpretation stage.

The hadronic τ decays are labeled as τ_{had} and are required to be prompt to define a clean fiducial region with minimal model-dependence. The visible momentum sum of these decay products are required to yield $p_{\text{T}} > 20$ GeV and $|\eta| < 2.47$, excluding the calorimeter crack region $1.37 < |\eta| < 1.52$. For light leptons, which typically carry a smaller momentum fraction from τ decay, the requirement of prompt and dressed is maintained but requiring the momentum sum of $p_{\text{T}} > 7$ GeV for both particles instead and used a slightly different $|\eta|$ range. For electrons, the requirement is $|\eta| < 2.47$ (excluding $1.37 < |\eta| < 1.52$) and for muon is $|\eta| < 2.5$. Other than the leptons, the truth jets are built from stable particles that travelled at least 10 mm before decaying (i.e. $c\tau > 10$ mm), and are clustered using the anti-k_T algorithm with a clustering radius of $R = 0.4$, where the non-prompt neutrinos and light leptons from hadron decays are included. Prompt leptons and their associated photons are excluded from the jet clustering. For the kinematic requirements, the cluster needs to yield $p_{\text{T}} > 20$ GeV and $|y| < 4.4$. Also, the jets are considered as a fiducial b-jet if a weakly-decaying, ghost-associated b-hadron is present with $p_{\text{T}} > 5$ GeV, where ghost-association is a technique used in the anti-kT algorithm using very low-energy particles, namely *ghost particles*, that are included in the jet to trace b-hadrons. As previously mentioned, to increase the sensitivity of the analysis to BSM theory that favours third generation particles, which typically involves b-jets. the fiducial events are also further categorised by the number of b-jets into bins of 0, 1, and ≥ 2, and will be measured in the future after the release of the initial results.

Events with fewer than one accepted particle-level τ_{had} are non-fiducial events and disregarded. For the $\tau_{\text{had}}\tau_{\text{had}}$ channel, at least two fiducial τ_{had} in an event are required. The decay products of the pair with larger transverse momentum p_{T}, referred to as the leading pair, is used to build the $m_{\ell\ell}^{\text{vis}}$ if more than two are accepted in an event. Table 4.1 below summarise the fiducial region selection to all defined objects at the particle-level for the analysis, including the light leptons which are not used in the unfolding measurement discuss in the thesis, but included in the search part of the analysis.

Fiducial Particle	Condition
Truth muons	p_T > 7 GeV, $\|\eta\|$< 2.5
Truth electrons	p_T > 7 GeV, $\|\eta\|$< 2.5
Truth taus	p_T > 20 GeV, $\|\eta\|$< 2.47 and not in crack region
Truth jets	p_T > 25 GeV, $\|\eta\|$< 2.47 and not in crack region, $\|y\|$< 4.4

Table 4.1: Fiducial selection criteria for various truth particles in for the measurement. The conditions ensure the selection of prompt particles within specified transverse momentum and pseudorapidity ranges, excluding the crack region where detector sensitivity is reduced.

4.2.2 Trigger selection

As previously mentioned in section 3.2.5, the analysis utilised a set of L1 and HLT triggers for balancing efficient signal selection and background rejection. The list of triggers used for the fully hadronic channel selection is shown in Table 4.2.

Table 4.2: Trigger list for the di-tau fully-hadronic channel

Year	Period	Trigger name
2015	All	HLT_tau80_medium1_tracktwo_L1TAU60
		HLT_tau35_medium1_tracktwo_tau25_medium1_tracktwo_L1TAU20IM_2TAU12IM
2016	A	HLT_tau80_medium1_tracktwo_L1TAU60
		HLT_tau80_medium1_tracktwo_L1TAU60_tau50_medium1_tracktwo_L1TAU12
	B-D3	HLT_tau125_medium1_tracktwo
		HLT_tau80_medium1_tracktwo_L1TAU60_tau50_medium1_tracktwo_L1TAU12
	D4-end	HLT_tau160_medium1_tracktwo
		HLT_tau80_medium1_tracktwo_L1TAU60_tau50_medium1_tracktwo_L1TAU12
2017	B1-B7	HLT_tau160_medium1_tracktwo
		HLT_tau80_medium1_tracktwo_L1TAU60_tau50_medium1_tracktwo_L1TAU12
	B8-end	HLT_tau160_medium1_tracktwo_L1TAU100
		HLT_tau80_medium1_tracktwo_L1TAU60_tau60_medium1_tracktwo_L1TAU40
2018	B-J	HLT_tau160_medium1_tracktwoEF_L1TAU100
		HLT_tau80_medium1_tracktwoEF_L1TAU60_tau60_medium1_tracktwoEF_L1TAU40
	K-endxs	HLT_tau160_medium1_tracktwoEF_L1TAU100
		HLT_tau160_mediumRNN_tracktwoMVA_L1TAU100
		HLT_tau80_medium1_tracktwoEF_L1TAU60_tau60_medium1_tracktwoEF_L1TAU40
		HLT_tau80_mediumRNN_tracktwoMVA_L1TAU60_tau60_mediumRNN_tracktwoMVA_L1TAU40

The analysis used the unprescaled (active) triggers with the least strict event selections for each data taking period to ensure selecting as much events/statistics as possible. As shown in Table 4.2, there are a mixture of single- and di-τ_{had} triggers employed with logical OR. In the trigger naming convention, components such as `L1TAU60` or `L1TAU100` refer to L1 calorimeter-based triggers, where the number denotes the transverse energy threshold in GeV. Other components, such as `HLT_tau80`, refer to HLT stages, where the number again indicates the transverse momentum threshold in GeV. The label `medium` denotes the tau identification working point used, while `tracktwo` indicates that tracking information is used in tau reconstruction. Reconstructed τ candidates are required to have a transverse momentum exceeding the respective trigger thresholds. For the di-τ triggers, two τ_{had} candidates must be reconstructed near the triggering τ_{had} objects.

4.2.3 Event reconstruction and additional detector level selection

Having optimised cuts are essential to achieving a precision measurements with robust sensitivity. The detector-level cuts are summarised in Table 4.3. Although the numerical values of the kinematic cuts are largely correlated to the fiducial case as both selections are aiming to achieve the objective of optimising the signal efficiency and they are intrinsically linked by this purpose, however, they represent different aspects of event selection where detector-level selections refers to the process of applying cuts to experimental data / simulations based on the response of the detector system itself and taken account the limited efficiency of ATLAS's object reconstruction rather than at the particle-level.

Firstly, the hadronic τ candidates are seeded by jets built from locally calibrated topological clusters (3.3.2) with the anti-k_t jet reconstruction algorithm [73] using a radius parameter $R = 0.4$ in the analysis framework. The tau candidates must also have $|\eta|< 2.47$ and $p_{\mathrm{T}} > 20$ GeV after applying the τ_{had} energy scale (TES) corrections to the visible momentum. The correction aims to adjust the measured energy of τ leptons to better match their true energy, where the correction factor is derived from comparing the measured τ energy and the expected energy based on theoretical predictions of control samples with well-known true τ energy. The τ_{had} decays are identified using the tight RNNIP identification working point as explained in section 3.3.5.

Electrons and muons with large energy deposits in the calorimeter can often be associated with large background processes such as photon conversions, misidentified hadrons and therefore contaminate the signal by faking τ_{had} decays. To further improve the purity and increase the statistical significance of any observed signals, the light lepton ($Z \to ee$, $Z \to \mu\mu$) backgrounds with large energy deposits are rejected with a specialised trained eBDT to discriminate between prompt electrons and τ_{had} decays. The calo-tagged muons have a particular high mis-identification rate in the central η region compared to muons identified using other techniques such as tracking in the inner detector due to poor coverage of the ATLAS muon system. Therefore, for this region, the τ_{had} candidates within the $\Delta R < 0.1$ of a calo-tagged muons are rejected. Also, selecting events with a specific number of charged tracks (N_{tracks}) associated with the tau decay vertex is a common strategy. Specifically, the requirements of $N_{\text{tracks}} = 1$ or $N_{\text{tracks}} = 3$ is motivated by the desire to isolate τ leptons decays while minimising the background contamination. The τ leptons can decay into various final states, including one-prong ($N_{\text{tracks}} = 1$) and three-prong ($N_{\text{tracks}} = 3$) decay modes. In the one-prong mode decays, the tau decays predominantly into a single charge hadron (usually pion) and a neutrino, whereas in the three-prong mode decays, the tau decays mostly into into three charged pions with neutrinos. Therefore, by constraining the number of tracks, the tau decay of interest are enriched and the background from source like the QCD multijet events, where jets are misidentified as τ candidates are suppressed.

Since the different detector components may detect the same object independently, the same set of tracks and calorimeter clusters can be associated to more than one reconstructed object. To adjust this, an overlap removal algorithm is applied to remove the objects corresponding to the same detector-level signals. The criteria of removal in the algorithm is to use the angular separation between two reconstructed objects. Except for the tau-muon overlap scenario, the angular separation is computed using the objects' rapidity y, where $\Delta R_y = \sqrt{(\Delta y)^2 + (\Delta\phi)^2}$ [71]. As for the tau-muon overlaps, the pseudorapidity η is used instead and the angular separation is computed as $\Delta R_\eta = \sqrt{(\Delta\eta)^2 + (\Delta\phi)^2}$ [71]. All overlap removal scenarios are listed in Table 3.1.

Prompt light leptons are also part of the signals in the $\ell + \tau_{\text{had}}$ channels. The candidate light leptons are required to have $p_{\mathrm{T}} > 7$ GeV since they tends to carry a small proportion of the original τ_{lep} momentum due to the presence of neutrinos and large mass difference. The electrons are also further required to fall within the fiducial region of the inner tracker and the electromagnetic calorimeter ($|\eta| < 2.47$). The MEDIUM electron identification operating point [58] is used to balance between the efficiency and truth positive rate of identified electrons, and the electron candidates are also required to pass the FCHIGHPTCALOONLY isolation [58], where it calculates the sum of transverse momentum within a specific cone around the electron candidate's direction, excluding contributions from tracks associated with the primary interaction vertex and select electrons transverse energy below the threshold to find the prompt electron candidates, and are isolated from nearby hadronic activities. On the other hand, muon candidates are required to have $|\eta| < 2.5$ and pass the MEDIUM identification working point and the FCLOOSE isolation working point is used [65]

The jets are constructed from Particle Flow objects using the anti-k_t algorithm with radius parameter $R = 0.4$ [58] and the resulted jets are further corrected to the corresponding particle-level jet p_{T} using simulation [82]. After these calibrations, jets with $p_{\mathrm{T}} < 25$ GeV are filtered. A multi-variate discriminant method Jet Vertex Tagger (JVT) [83] is used to identify primary interaction vertex jets and remove jets with $p_{\mathrm{T}} < 60$ GeV and $|\eta| < 2.4$ that have large estimated energy proportion from pile-up collision vertices. For jets above the thresholds, the requirement becomes unnecessary since the high- p_{T} jets are typically associated with the hard scatter process of interest and mostly from the primary vertex. Additionally, high pseudorapidity and p_{T} indicate the jets are lying in regions with optimal performance of the detector and pile-up effects are minimised [83].

To identify hadronic jets with b-hadrons, the `DL1r` b-tagging algorithm is used [74]. The analysis employs the working point corresponding to a b-jet identification efficiency of 77% in an inclusive sample of b-jets from $t\bar{t}$ events. The tagging performance, including the efficiency for identifying b-jets and the mistag probabilities for c-jets and light-flavour jets, is derived from dedicated control samples in collision data [74, 84]. The mistag rate for light-flavour jets is evaluated in Z+jets events. These events offer a clean and well-modelled environment due to two main reasons: (1) the initial state of Z+jets production is primarily composed of light quark–antiquark annihilation or gluon–gluon fusion processes, and does not typically involve heavy-flavour quarks; (2) the Z boson decays into pairs of leptons, allowing precise reconstruction of the boson and simplifying background discrimination. The abundance and cleanliness of this process make it ideal for evaluating light-jet misidentification rates. The mistag rate is extracted using the *flipped tagger* method [85], where the selection criteria for the b-tagging algorithm are inverted. This reversal enhances the presence of non-b-jets in the selected sample. By comparing the distributions of jets before and after the tag-flipping, the probability of misidentifying a light-flavour jet as a b-jet can be quantified.

All reconstruction-level selections are listed in Table 4.3

Particle Category	**Conditions**
Electrons	$\lvert\eta^{BE}\rvert < 2.47$ and not in crack region $p_T > 7$ GeV pass FCHighPtCaloOnly isolation Pass Medium ID working point
Muons	$p_T > 7$ GeV $\lvert\eta\rvert < 2.5$ pass Medium ID working point pass FCLoose isolation
Photons	$\lvert\eta\rvert < 2.47$
Taus	$p_T > 20$ GeV $N_{\text{tracks}} = 1$ or 3 pass tight ID by RNN electron veto by eBDT calo-tagged muon removal within $\Delta R < 0.1$
Jets	$\lvert y\rvert < 4.4$ $p_T > 25$ GeV $p_T < 60$ GeV and $\lvert\eta\rvert < 2.4$ JVT pile-up removal b-jets ID with DL1r tagger with 77% WP

Table 4.3: Reconstruction-level object selections

4.2.4 Additional channel selections

As mentioned in the introduction of section 4.2, the full analysis signal regions are divided into three channels defined by the decay modes of the tau candidates: (1) $\tau_{\text{had}}\tau_{\text{had}}$ channel, (2) $e\tau_{\text{had}}$ channel and (3) $\mu\tau_{\text{had}}$ channel. All regions require at least two identified leptons with visible invariant mass $m_{\ell\ell}^{\text{vis}} > 100$ GeV. The opposite-sign region is the signal region and the same-sign region is treated as the background validation region for closure tests on fake τ analysis as discussed in section 4.4.1. The analysis signal selections criteria for these channels are list in table 4.4:

Channels	**Conditions**
$\tau_{\text{had}}\tau_{\text{had}}$ channel	leading τ_{had} p_T > 90 GeV sub-leading τ_{had} p_T > 60 GeV standard ”OR” logic gate for single and di-τ triggers (detector-level) loose τ_{had} eBDT working point Events with any light leptons events are vetoed τ pass tight WP (detector-level)
$e\tau_{\text{had}}$ channel	τ_{had} p_T > 25 GeV ep_T > 27 GeV single electron trigger Medium τ_{had} eBDT WP to remove $Z \to ee$ fake taus Veto if > 2 leptons
$\mu\tau_{\text{had}}$ channel	τ_{had} p_T > 25 GeV μp_T > 27 GeV single muon trigger Loose τ_{had} eBDT WP Veto if > 2 leptons

Table 4.4: Analysis channel selections

4.3 Monte Carlo event generation

Monte Carlo (MC) event generators are fundamental tools for particle physics measurements and searches and play a vital role in virtually every aspect of particle physics research. They are used to simulate expected outcome of the experiment (without having to re-run it in real life) by simulating the interaction between particles within the high-energy collisions. For the measurements, the MC generators are used to simulate signal sample with the process of interest, and also used for simulating background and BSM samples for validation studies and fitting purposes. Event generators including Herwig [86], Pythia8 [87], Sherpa [88] and Madgraph [89] are all widely used in data analysis for particle physics. For the purpose of the LHC and the ATLAS, the event generators are used to provide a theoretical framework for the high-energy proton-proton collisions. This section aims to introduce the general idea of event sample generation and then provide an overview to all the samples that are used for the analysis.

In high-energy proton collisions at the LHC, correctly modelling the strong interaction between the quarks and gluons within the colliding hadrons is the key to achieving an accurate simulation. A common name *parton* is used to address the quarks and gluons from the colliding protons. The term *hard scattering* is referring to the primary interaction between the involved partons (quarks and gluons) at high momentum transfer, where the typical momentum transfer involved is much larger than the QCD confinement scale. With this hierarchy of scales, it enables a factorisation scale, denoted by μ^2, to separate between the short distance perturbative regime where pQCD applies, and the long distance, soft and non-perturbative regime influenced by confinement. To describe the complete collision, the description of these interactions is treated in two distinct parts: (1) the hard scattering and (2) the parton distribution functions (PDFs).

For the hard scatterings, these interactions involve the exchange of high-energy virtual particles and can be incorporated into the perturbative QCD theoretical framework due to the asymptotic freedom feature of QCD. Asymptotic freedom means that the strength of the strong interaction, governed by the coupling constant α_s, decreases at higher energies or in other word, shorter distances. which suggests that the quarks and gluons behave as nearly as free particles at high energy or short distances. This feature allows the application of perturbative techniques to calculate cross-sections as interactions between partons become weak and calculable through a series expansion in terms of the small coupling constant $\alpha_s(\mu^2)$, so that the higher order terms in the series become less significant and allowing sufficient precision.

On the other hand, QCD confinement dominates at large distances, and the parton-level description as free particles becomes invalid. Therefore, the large distance component of the interaction with soft hadronic phenomena, such as the hadronisation of partons becomes non-perturbative and one cannot derive it from the first-principle (pQCD). Instead, due to the internal structure of protons, some other models encoding information about the momentum and spin distributions of partons, and can describe the probability density function of finding a parton with some certain fraction of the initial hadron's momentum are necessary to provide an accurate description to the collision. These models are called the Parton Distribution Functions (PDFs) and would provide the initial conditions for calculating the cross-sections of the scattering process and capture the long-distance interactions between the partons.

To combine the two sides of the interactions, the factorisation theorem [90] states that the cross-section for a hadron-hadron collision can be factorised into the product of the hard scattering cross-section and the PDFs of the colliding partons:

$$\sigma(h_1 h_2 \to X) = \sum_{i,j} \int dx_1 dx_2\, f_i(x_1, \mu^2)\, f_j(x_2, \mu^2)\, \hat{\sigma}_{ij}(x_1 p_1, x_2 p_2, \alpha_s(\mu^2), \mu^2) \quad (4.3.1)$$

Within this expression, the $\sigma(h_1 h_2 \to X)$ represents the total cross-section for the process $h_1 h_2 \to X$, and $f_i(x_1, \mu^2)\, f_j(x_2, \mu^2)$ are the PDFs of finding parton i and parton j with momentum fraction x_1 and x_2 in hadron h_1 and hadron h_2 respectively, where the dependence of initial PDFs on energy scale and momentum fraction are determined from global fits to experimental data such as the Drell-Yan process and deep inelastic scattering. The parton distribution functions (PDFs) are extracted by evolving these data points to a common scale using the DGLAP evolution equations, rather than fitting all data at a fixed reference scale like Q_0^2 [91]. The $\hat{\sigma}_{ij}(x_1 p_1, x_2 p_2, \alpha_s(\mu^2), \mu^2)$ components represents the hard scattering cross-section for the interaction of parton i from hadron h_1 with momentum $x_1 p_1$ and parton j from hadron h_2 with momentum $x_2 p_2$, and also depends on the the strong coupling constant α_s evaluated at the factorisation scale μ^2. Therefore, to model the entire proton-proton collision, the integral is taken across the population of the partons within the protons [92].

To compute equation 4.3.1 with the MC generators, the process order is represented by Figure 4.1. It starts with hard scatter and can be simulated with the matrix element and the state of the art is up until the Next-to-next-to-Leading-Order (NNLO) to account for the loop corrections [93]. This is illustrated as the red components in Figure 4.1. Then, with the outgoing partons being coloured and radiating gluons as they move, this creates a shower of partons, which connect from the hard scatterings and is made of the sequential chain of emissions of partons (quarks, gluons), and represented by the branch-like QCD structure in Figure 4.1. When connecting the steps on matrix element and parton showers generation, there are redundant phase space that are covered by both generation procedures. These overlaps can lead to double counting of emissions, and therefore, need to be removed to ensure a smooth transition between the matrix element and parton shower regions.

As partons radiate and lose energy through the parton shower, the hardness of interaction will decrease; the momentum transfer in the interactions scales down until it reaches a point where the pQCD breaks down [94]. At this stage, confinement takes over, leading to the formation of colour-singlet hadrons in a process known as hadronisation. This is sketched in Figure 4.1 as the flat oval shape in green at the end of each QCD branch. During hadronisation, the quarks and gluons produced in the parton shower are no longer free but combine to form hadron states that are colour-neutral. This process involves the creation of quark-antiquark pairs from the vacuum, with the energy being more favourable then splitting the quarks further apart. The resulting hadron bound states are produced within the jet and manifest as the dark green final-state particles. In addition to the hard scattering processes, there is also accompanying hadronic activity that are not directly related to the primary scattering process, including initial-state radiation (ISR), final-state radiation (FSR), parton remnants and multiple parton interactions (MPI). These softer and less energetic event is referred as the underlying events which represented by the purple part in Figure 4.1. Lastly, the yellow lines in the plot represents the photon emissions that occurred during various interactions.

Figure 4.1 from reference [95] illustrates the process of simulating the proton-proton collision and represent the production process of the MC samples that were used in this di-tau analysis.

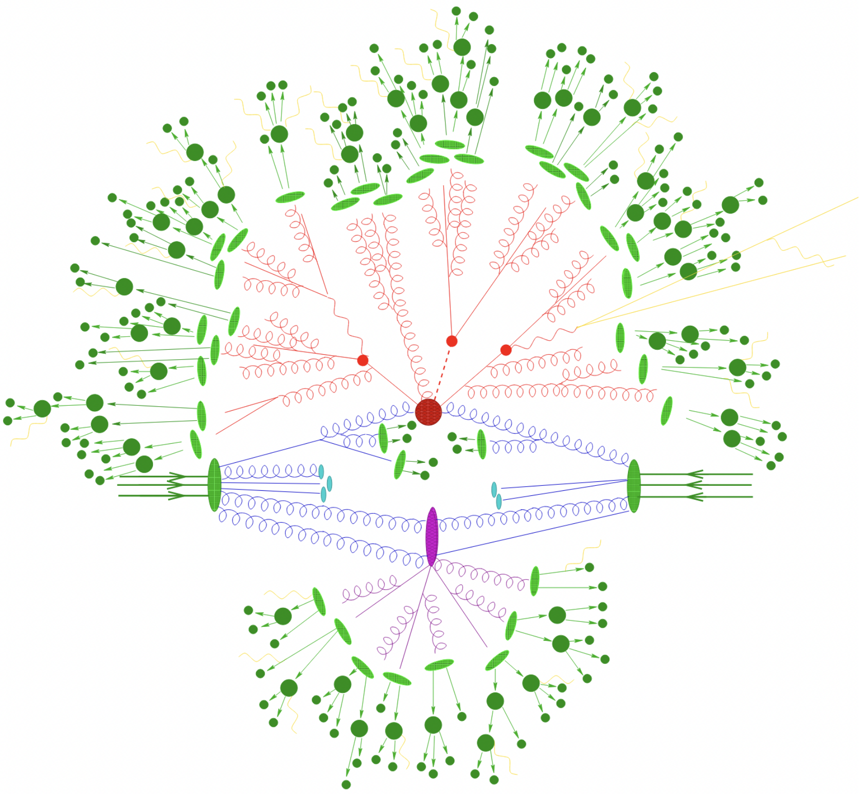

(a)

Figure 4.1: Figure showing the Monte Carlo simulation process of the proton-proton collision. The hard scatter is the central in red and the blue QCD branches represents the redistribution of energy and momentum in the parton shower among the partons as they radiate and evolve, such as the gluon bremsstrahlung and quark-antiquark pair production. The bright green blobs are the colour-singlets from the hadronisation process and darker blobs are the decayed products of the hadrons. Lastly, the purple section is the softer, underlying events with the purple blob represents the parton remnants after the initial hard scattering process and the yellow lines are photon emissions. The figure is from ref[95].

4.3.1 Monte-Carlo Samples

After the brief introduction on Monte-Carlo event generation in section 4.3, it is also essential to introduce the MC samples used for the analysis regions. These samples serves as the foundation upon which the subsequent steps of the analysis are built. The subsections below will introduce each of the MC samples used for the analysis.

Drell-Yan production $Z \rightarrow \tau\tau$

The Drell-Yan sample, along with the $t\bar{t}$ 4.3.1 sample are the two major component of τ candidate sources and together,they make up 95% of the event yield in the signal region phase space. The Drell-Yan process occurs when a quark and anti-quark annihilate and produce an intermediate boson which then decays into a lepton-antilepton pair with the possibility of the leptons being a τ pair as shown in Figure 4.2.

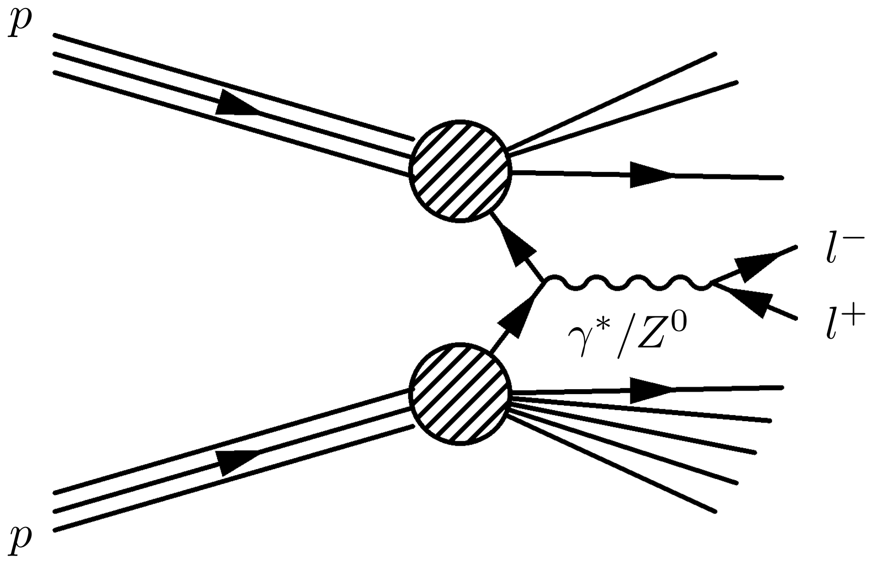

(a)

Figure 4.2: The Feynman diagram illustrating the production of a Drell-Yan process. Figure from reference [96].

The `SHERPA` 2.2.11 generator using next-to-leading-order (NLO) matrix element (ME) for up to two partons and leading-order (LO) matrix elements for up to five partons calculated with the Comix [97] and OPENLOOPS [98, 99, 100] libraries to facilitate the accurate and efficient simulations, where the Comix is a tree-level matrix element generator as part of the `SHERPA` framework and the OPENLOOPS is specialised to generate one-loop scattering amplitudes. The hard scatterings merged and matched with the `SHERPA` parton shower [101] using the MEPSatNLO prescription [102, 103, 104, 105] with a dedicated set of tuned parameters developed by the `SHERPA` authors. The NNPDF[3.0nnlo] PDFs [106] set was used for both hard scattering and parton shower.

An alternative sample with the `POWHEGBOX`[v1] [107, 108, 109, 110] MC event generator was used for the simulation at NLO accuracy of the hard-scattering processes of W, Z boson production and decay in the electron, muon and τ lepton channels. For the parton shower, hadronisation and underlying event components, it was interfaced to `PYTHIA`[8.186] [111] with parameters set according to the AZNLO tune [112]. On the PDFs' side, The CT[10nlo] PDF set [113] was used for the hard scattering processes and the CTEQ[6L1] PDF set [114] was used for the parton shower component. Lastly, the QED final-state radiation corrections were modelled with PHOTOSpp[3.52] [115], and the EVTGEN[1.2.0] software package [116] was used to decay bottom and charm hadrons.

$t\bar{t}$ production

The top-antitop ($t\bar{t}$) process involves the production of intermediate W boson from top quark decays which later decays into leptons, where true τ candidates are produced as shown in Figure 4.3 and is also a major signal component for the analysis signal region.

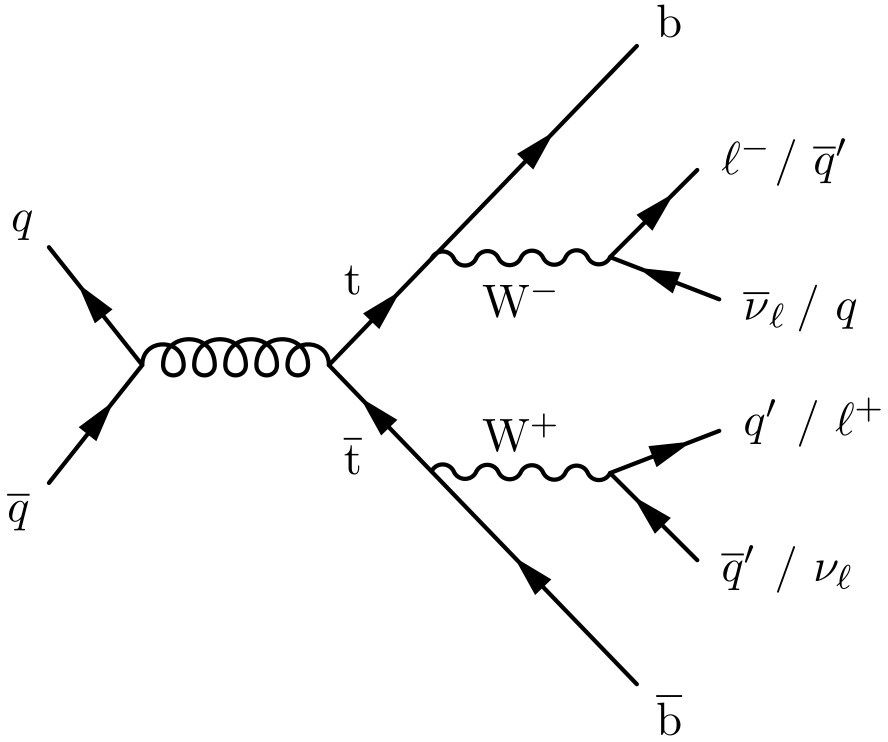

(a)

Figure 4.3: The Feynman diagram illustrating the production of a τ candidate from $t\bar{t}$ process, figure from reference [117].

The production of $t\bar{t}$ events was simulated using the `POWHEGBOX`[v2] [118, 107] generator at the NLO accuracy using the NNPDF[3.0nlo] [106] PDF set and the `hdamp` parameter, where the parameter is used to influence the high-energy radiation in the simulation of parton showers and the matching between the fixed-order matrix elements and the parton showers. Specifically in this case, the parameter controls the hardness of the first gluon emission beyond the born level in simulation of the top quark productions. The parameter is set to a value related to the mass of the top quark which regulates the high p_T radiation in the parton shower (less than the `hdamp` setting) against which the $t\bar{t}$ system recoils and help smoothing the transition between the matrix element calculations and the parton shower [119]. For the sample used, the `hdamp` parameter was set to 1.5 (i.e. 1.5 of top mass). The events are then interfaced to `PYTHIA`[8.230] [120] to model the parton shower, hadronisation, and underlying event, with the parameters set according to the A14 tune [121] and use the NNPDF[2.3lo] set of PDFs [122].

Some alternative samples were also used to check for the impact of using different parton shower and hadronisation model by comparing to the nominal $t\bar{t}$ sample showered using an alternative generator. Instead of `PYTHIA`, the event samples were interfaced with `HERWIG`[7.04] [86, 123, 124], using the H7UE set of tuned parameters [121] and the MMHT[lo] PDF set [125]. To assess the uncertainty in the matching of NLO matrix elements to the parton shower, the `POWHEGBOX` sample was compared to a event sample generated with `MadGraph5` NLO[2.6.0] [126] and showered with `PYTHIA`[8.230] [120]]. The `MadGraph5` NLO used the NNPDF[3.0nlo] PDF set [106] and the `PYTHIA` component used the A14 set of tuned parameters [121].

The decay of the bottom and charm hadrons for both samples were simulated with EVTGEN[1.6.0] [116].

Single top production

Other than the $t\bar{t}$ production, the single top production processes can also produce τ candidates from decays. There are several possible production channels.

- The associate production of top quarks with W bosons (tW) shown in Figure 4.4 was simulated using `POWHEGBOX`[v2] [118, 107] generator at NLO accuracy in QCD using the five-flavour scheme. In this scheme, the five lightest quarks (up, down, charm, strange, and bottom) are treated as massless and included in the proton PDFs, with the NNPDF3.0nlo set [106] used in the simulation. To prevent overlap with top quark pair production, which can share topologically similar Feynman diagrams and final states with single top processes, the diagram removal (DR) scheme [127] was applied. This method eliminates overlapping contributions at the matrix element level prior to parton showering, thus ensuring that the simulated sample accurately reflects pure single top tW production.

The parton showering, hadronisation, and underlying event modelling were performed using `PYTHIA`[8.230] [120], configured with the A14 tune [121] and the NNPDF[2.3lo] set of PDFs [122]. To estimate the modelling uncertainty, an alternative sample with varied showering conditions was compared to the nominal sample.

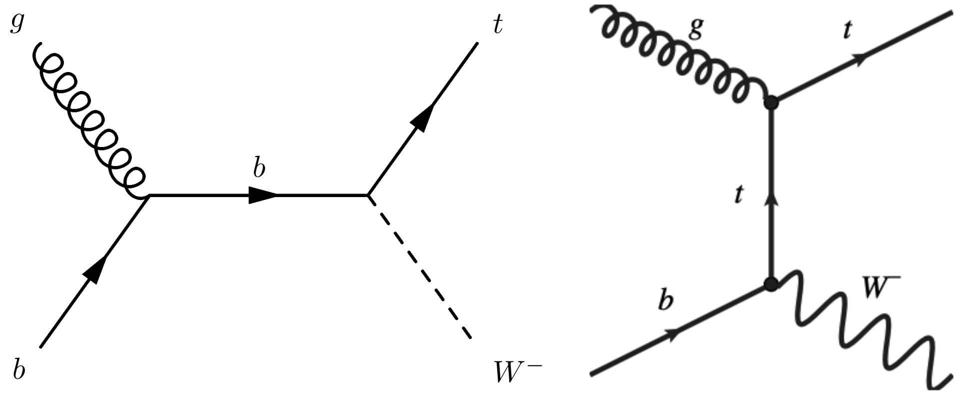

(a) (b)

Figure 4.4: The Feynman diagram illustrating the production of a single top tW production process, the τ candidate can be generated from further W boson decays through both the directly produced W boson and the W boson produced from the top decay. (a) s-channel, (b) t-channel. Figures from reference [96].

- The single-top t-channel production shown in Figure 4.5 (a) was also modelled with the `POWHEGBOX`[v2] [118, 107] generator at NLO in QCD, but used the four-flavour scheme (excluding bottom and top). This is because a bottom quark is directly involved in a hard scattering process, and in this way, a more precise description of the bottom quark involvement is achieved by treating it as a massive quark in the hard scattering and without assumptions about its distribution in the proton. The NNPDF[3.0nlo] PDF set [106] were used and the events were then interfaced with the A14 tune [121] and the NNPDF[2.3lo] set of PDFs [122].

- The single-top s-channel production shown in Figure 4.5 (b) is modelled using the same setting as the t-channel, except using the five-flavour scheme instead of four.

The uncertainties due to the parton shower and the hadronisation model was again evaluated by comparing the nominal sample to an alternative sample. In this case, the alternative sample events are generated from `POWHEGBOX`[v2] [118, 107] and

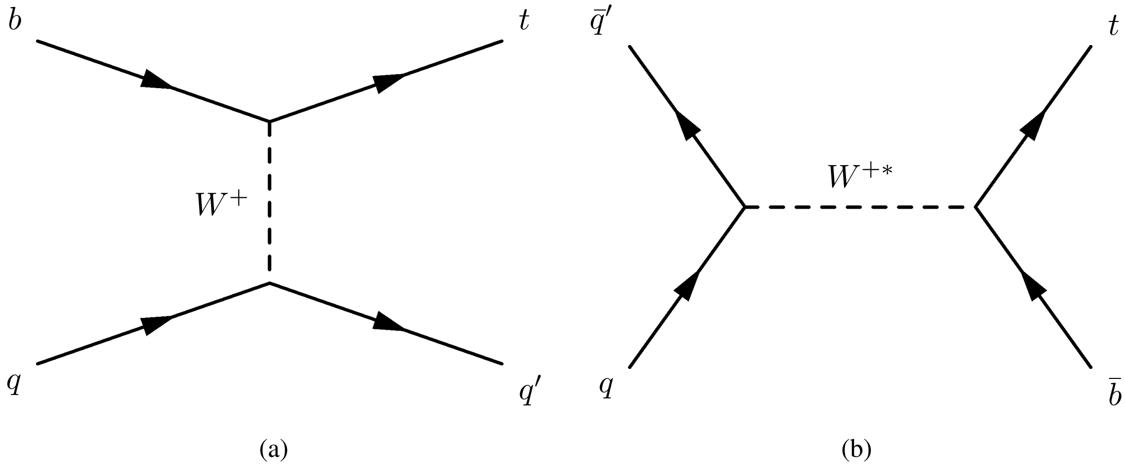

(a) (b)

Figure 4.5: (a) The Feynman diagram illustrating the production of a top particle from single t-channel process, where the τ candidate is produced through the decay of the top particle. (b) The Feynman diagram illustrating the production of a top particle from single top s-channel process, τ candidate is generated through further top decays. Figures taken from reference [96].

were interfaced to `HERWIG`[7.04] [86, 123, 124], using the H7UE set of tuned parameters [121] and the MMHT[lo] PDF set [125].

Lastly, to assess the NLO matrix elements matching uncertainties to the parton shower, the same approach was used as for the $t\bar{t}$ sample. The nominal sample was compared with a sample generated using the `MadGraph5`$_{\text{NLO}}$[2.6.2] [126] generator at NLO in QCD with five-flavour scheme and the NNPDF[2.3$_{\text{NLO}}$] [122] PDF set, then interfaced with `PYTHIA`[8.230] [120]], using the A14 set of tuned parameters [121] and the NNPDF[2.3$_{\text{LO}}$] PDF set.

Multi-boson production

These samples involve bosonic final states and include fully leptonic and semi-leptonic decays with at least one τ candidate in the final state. They are simulated with the `SHERPA`[2.2.11] [123] generator at the NLO accuracy for the matrix element calculation for up to one additional parton, and at LO accuracy for up to three additional parton emissions. Samples for the loop-induced processes (gg → VV) were generated using LO matrix elements for up to one additional parton emission for both the fully leptonic and semi-leptonic final states. The events are then interfaced to the `SHERPA` parton shower using the MEPS@NLO prescription [128, 129, 104, 105]. The virtual QCD corrections were provided by the OPENLOOP library [98, 99, 100], and the NNPDF[3.0 nnlo] [122] set of PDFs was used along with the set of tuned parton shower parameters developed by the `SHERPA` authors.

Leptoquark production

One of the purposes for this analysis is to be able to set constraints for the Leptoquark signals that could potentially be contributing to the high-mass Drell-Yan production.

The simplified U_1 model for vector leptoquarks and a scalar leptoquark are used [130] for interpretation in the search. The vector leptoquark signal samples are generated using the `vector_LQ_UFO` UFO model, which allows for separate contributions from the BSM-SM interference and the pure BSM amplitude in the matrix element calculations. In the off-shell regime, the kinematics of the are similar between the SM and BSM terms. Therefore, the initial event generation is performed using a pure SM amplitude at leading order, with up to two additional jets included using the `CKMM-L` merging scheme. These events are subsequently reweighted to represent predictions for a range of leptoquark coupling scenarios. The reweighting is performed for different values of key leptoquark parameters: $\beta_L^{b\tau}$ (β_L^{33}) corresponds to the coupling to purely third-generation left-handed fermions; $\beta_R^{b\tau}$ and β_L^{23} are the pure right-handed third generation coupling and pure left-handed coupling across second and third generations respectively [130].

The interaction term of the Lagrangian including the vector leptoquark is [3]:

$$\begin{aligned}\mathcal{L}_{\text{int}} &= \frac{g_U}{\sqrt{2}}\left(\beta_L^{ij}\bar{Q}_L^{i,a}\gamma_\mu L_L^j + \beta_R^{ij}\bar{d}_R^{i,a}\gamma_\mu \ell_R^j\right)U_1^{\mu,a} + \dots \\ &= \frac{g_U}{\sqrt{2}}\left(\beta_L^{33}\bar{t}_L\gamma_\nu\nu_\tau + \beta_L^{33}\bar{b}_L^a\gamma_\mu\tau_L + \beta_L^{23}\bar{c}_L^a\gamma_\mu\nu_\tau\right)U_1^{\mu,a} + \dots\end{aligned}$$

(4.3.2)

where the term g_U represents the coupling constant of the leptoquark and $U_1^{\mu,a}$ is the leptoquark field with colour index a and lorentz index μ. For the leftmost term within the bracket $\beta_L^{33}\bar{t}_L\gamma_\nu\nu_\tau$ represents the interaction between the third generation left-handed top quark (t_L) and left-handed tau neutrino with leptoquark (U_1). The middle term $\beta_L^{33}\bar{b}^a_L\gamma_\mu\tau_L$ represents the interaction between left-handed bottom quark (b_L) and tau lepton with the leptoquark. The rightmost term $\beta_L^{23}\bar{c}^a_L\gamma_\mu\nu_\tau$ represents the interaction between the left-handed charm quark and tau neutrino with leptoquark. Leptoquarks can be produced in various modes. Figure 4.6 illustrates the leptoquark pair-production, single-leptoquark production and Drell-Yan t-channel exchange available in the U_1 leptoquark model. At very high leptoquark mass, the phase space and parton luminosity required for producing such massive particles become more restrictive due to the availability of high-momentum partons (higher x values) within the protons, and the energy required to produce such high mass particles approaching the practical limits of the collider's capabilities. Therefore, the parton PDFs significantly suppress the production rate. However, even if direct production is suppressed, off-shell leptoquarks can still contribute virtually to observable processes involving lepton pairs. in the presence of off-shell leptoquarks, additional $t-$channel diagram appears and modifies the total amplitude of the process by introduction new interference terms between the SM and BSM contributions. For the U_1 leptoquark model considered here, this interference is destructive, so that the BSM amplitude partially cancels out the SM amplitude. As a result, the total cross-section and the shape of the invariant mass distribution are distorted, especially at the high masses where the interference term becomes more impactful. Therefore, the interference reduces the total probability of observing $\tau\tau$ pair compared to the SM-only prediction.

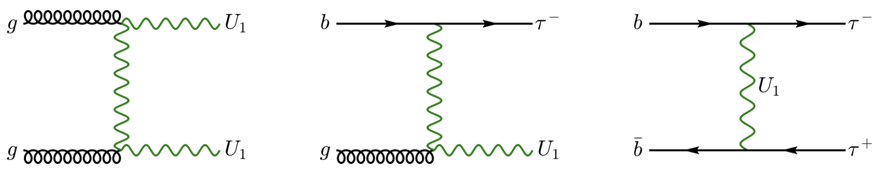

Figure 4.6: The Feynman diagrams illustrating the (left) leptoquark pair production, (middle) single-leptoquark production and (right) Drell-Yan t-channel leptoquark exchange.

Such a BSM sample with potential off-shell leptoquark was simulated with `MadGraph5_AMC@NLO`[2.2.2] [126], using LO-accuracy matrix elements with up to two final-state partons in addition to the Leptoquark mediated interactions. The Matrix element calculations used the NNPDF3.0$_{\text{NLO}}$ set of PDFs [122] (-sliced). Here, slicing refers to dividing the phase space of the simulated events into different kinematic regions (i.e. slices), typically based on the total scalar sum of the transverse momenta in the event or on the number of additional partons in the matrix element calculation [131]. This is done to improve event generation efficiency and sampling of rarer events, especially in BSM scenarios like those involving off-shell leptoquarks. Events were interfaced to `PYTHIA`[8.186] [111] for the modelling of the parton shower, hadronisation and underlying event. The overlap between the matrix element and the parton shower emissions was removed using the CKKM-L merging procedure by adding weights to events to ensure a smooth transition and discard events that fall into the overlapping region using rejection algorithm [132, 133]. The A14 tuned parameters of `PYTHIA` was used with the NNPDF2.3$_{\text{LO}}$ PDF set [122] and the bottom and charm hadron decays are modelled with with EVTGEN[1.6.0] [116]. More details on this sample used for unfolding injection test is described in section 4.6.6.

4.4 Background Estimation and Fakes

Part of the objective for an analysis is to extract the true signals from the raw data by eliminating contamination from background processes. The treatment of backgrounds for the analysis can be divided into two components. The primary background component, also being the only background considered for the unfolded measurement is the QCD multijet, which contributes to the $\tau\tau$ final states background by misidentifying jets from QCD interactions as τ leptons, particularly in the fully hadronic channel. Due to the complexity nature, a dedicated data-driven study on this background is performed and detailed in section 4.4.1. For the search part of the analysis, the background is defined differently, which includes the diboson, single top, electroweak backgrounds, and are modelled with MC samples due to the cleaner final state and the closure test using the same-sign validation region achieved a high-level of agreement.

4.4.1 Jets faking τ

The estimation of the fake τ background via the MC simulation approach is not reliable as the multijet modelling is complex and possess large uncertainties, hence a data-driven technique named *fake factor* [134] was adopted and is a commonly used method in many ATLAS analyses.

The fake factor is an estimate of the fake τ_{had} made by quantifying the rate at which jets are mistakenly identified as τ_{had} using control samples that are fake-enriched. Firstly, an anti-τ identification region is defined where the τ_{had} identification criteria `RNN_score` [134] is inverted so that the τ candidates that failed the τ-ID selection will fall into this region. For the signal region (SR), we require `RNN_score` > 0.8, therefore, for this anti-ID SR, the request is inverted to require at least one τ_{had} candidate has `RNN_score` < 0.8, along with a minimum cut at `RNN_score` > 0.01. Then, the Fake Factor (FF) becomes the transfer factor from an anti-ID region to the corresponding ID region. These factor factors are measured in the dedicated same charge-sign control region (CR) enriched in fake taus, and is determined as the ratio of the number of jets misidentified as τ_{had} candidate (pass the τ-ID criteria) to the number of corresponding candidates failing the criteria (i.e. fulfilling the anti-ID criteria).

$$\text{FF} = \frac{N_{\text{ID}}^{\text{CR}}}{N_{\text{anti-ID}}^{\text{CR}}}\,, \tag{4.4.1}$$

In this way, the FF can be used to extract the background contribution in the SR by adopting the assumption that the efficiency at which jets are misidentified as τ_{had} candidate can be consistently measured in the CR. With assuming the jet properties in the SR are sufficiently similar to those in the CR, the FF measured in the CR are applicable to the SR anti-iD region directly to estimate the number of fake τ_{had} are present in the SR ID region:

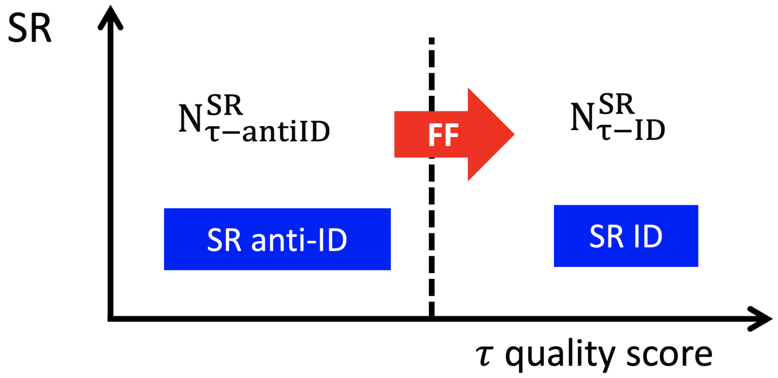

Figure 4.7: Schematic representation of the FF as transfer factor from the SR anti-ID to the SR ID.

$$N^{\mathrm{SR}}_{\mathrm{ID}} = N^{\mathrm{SR}}_{\mathrm{anti-ID}} \times \mathrm{FF} \tag{4.4.2}$$

There are multiple sources of jets faking τ_{had} and individual primitive FF is obtained for each population of jets and would all be reliable as long as the CR in which these FFs evaluated have the same composition as the SR in terms of quark and gluon jets:

- quark-enriched jets from a $Z \rightarrow \mu\mu$ data sample.

$$\mathrm{FF_q} = N^{\mathrm{CR_q}}_{\mathrm{ID}} / N^{\mathrm{CR_q}}_{\mathrm{anti-ID}} \tag{4.4.3}$$

- gluon-enriched jets from a multijet data sample with high Jet Vertex Tagging (JVT) score.

$$\mathrm{FF}^{\mathrm{hjvt}}_{\mathrm{g}} = N^{\mathrm{CR^{hjvt}_g}}_{\mathrm{ID}} / N^{\mathrm{CR^{hjvt}_g}}_{\mathrm{anti-ID}} \tag{4.4.4}$$

- pileup-enriched jets from a multijet data sample with low JVT score.

$$\mathrm{FF}^{\mathrm{ljvt}}_{\mathrm{g}} = N^{\mathrm{CR^{ljvt}_g}}_{\mathrm{ID}} / N^{\mathrm{CR^{ljvt}_g}}_{\mathrm{anti-ID}} \tag{4.4.5}$$

However, this is in practice difficult to achieve. Therefore, a weighted combinatorial strategy is adopted to combine the three primitive fake factors (FFs) into a single, effective FF applicable in the SR. These primitive FFs are provided by the ATLAS Fake Tau Task Force (FTTF), using the methodology detailed in Ref. [134]. The relative contributions of each jet type in the SR are estimated using a template fit

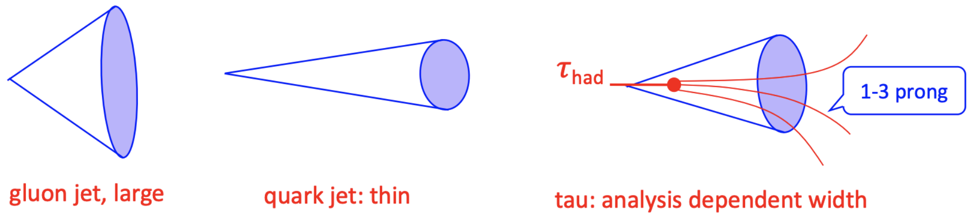

Figure 4.8: Representation of the tau jet with respect to the quark and gluon hadronic jets.

to the τ width variable in the anti-ID region. This exploits the distinct shape differences in the τ width distributions for fake τ candidates originating from gluon jets, quark jets, and heavy-flavour jets. As illustrated in Figure 4.8, each jet type exhibits a characteristic distribution in this observable, allowing the template fit to extract the fractional composition of the fake tau sample. These fractions are then used as weights to combine the corresponding primitive FFs into a single, channel-dependent FF for background estimation.

$$j = \frac{\sum_i \Delta R^i p_t^i}{\sum_i p_t^i}, \tag{4.4.6}$$

The best-fitted relative fractions are extracted from the fit (α parameters) using the `jax` package by minimising the difference between $\mathrm{T_{fakes}}$ and the corresponding $\mathrm{T_{data}}$ template extracted from the anti-ID region, along with a corresponding uncertainty $\Delta\alpha$ which is later taken into account in the total fakes uncertainty. The combined FF is then defined as a linear combination of the primitive FFs, weighted by the relative fractions.

$$\mathrm{T_{fakes}} = \mathrm{ff_q} \cdot \mathrm{T_q} + \mathrm{ff_g^{ljvt}} \cdot \mathrm{T_g^{ljvt}} + \mathrm{ff_g^{hjvt}} \cdot \mathrm{T_g^{hjvt}} \tag{4.4.7}$$

In the $\tau_{\text{had}}\tau_{\text{had}}$ channel, there is an ambiguity for the τ extrapolation when considering the pairing of the two τ_{had} candidates. There are three scenarios: leading τ_{had} being fake, sub-leading τ_{had} being fake and both being fake. We therefore define several categories to account for the different scenarios.

- **B** the leading tau is anti-ID and the sub-leading is ID.
- **C** the leading tau is ID and the sub-leading is anti-ID.
- **D** both taus are anti-ID.

The extrapolated background is then found via the combinatorial formula:

$$\begin{aligned} N_{\text{bkg}} = {} & [\underbrace{N(\tau_{\text{antiID}}\tau_{\text{ID}})}_{\text{Region B}} - \underbrace{N(\tau^t_{\text{antiID}}\tau^t_{\text{ID}})}_{\text{Region B (MC)}}] \cdot FF_1 \\ & + [\underbrace{N(\tau_{\text{ID}}\tau_{\text{antiID}})}_{\text{Region C}} - \underbrace{N(\tau^t_{\text{ID}}\tau^t_{\text{antiID}})}_{\text{Region C (MC)}}] \cdot FF_2 \\ & - [\underbrace{N(\tau_{\text{antiID}}\tau_{\text{antiID}})}_{\text{Region D}} - \underbrace{N(\tau^t_{\text{antiID}}\tau^t_{\text{antiID}})}_{\text{Region D (MC)}}] \cdot (FF_1 FF_2) \end{aligned} \tag{4.4.8}$$

Where the N are indicating the number of events in different categories. The above equation is also equivalent to $B + C - D$ so that the double counted events in region $B + C$ is removed as the ID and anti-ID constraints only applies to the required τ_{had} candidate and without considering the status of the other τ_{had} candidate, similar to the idea of the inclusion-exclusion principle of the probability theory.

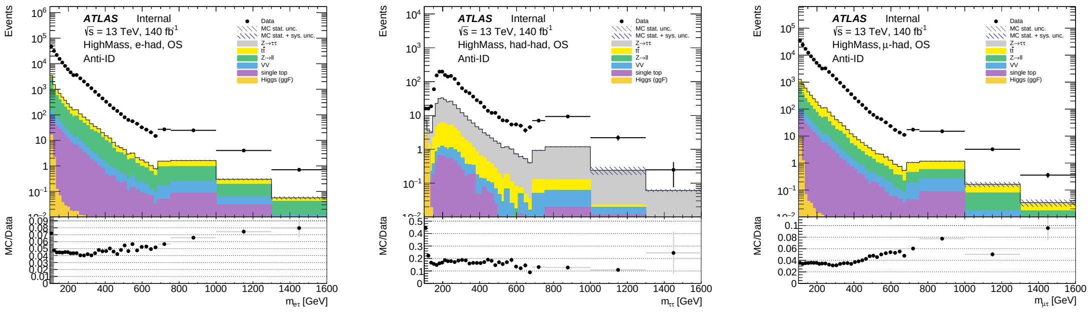

(a) (b) (c)

Figure 4.9: Data and MC comparison for $m_{\ell\ell}^{\text{vis}}$ in the opposite-sign anti-ID region. (a) $\tau_{\text{had}}\tau_{\text{had}}$ channel, (b) the $e\tau_{\text{had}}$ channel, (c) the channel. The lower pad shows the ratio between MC predictions and data. Plots taken from analysis document [135].

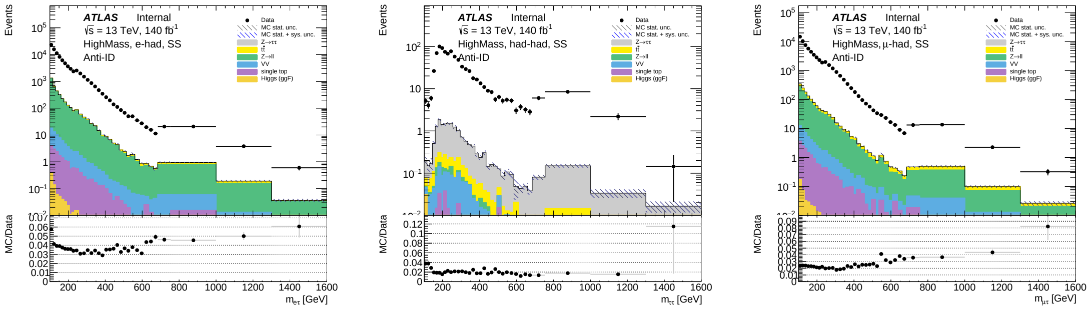

(a) (b) (c)

Figure 4.10: Data and MC comparison for $m_{\ell\ell}^{\text{vis}}$ in the same-sign anti-ID region. (a) $\tau_{\text{had}}\tau_{\text{had}}$ channel , (b) the $e\tau_{\text{had}}$ channel, (c) the channel (c). The lower pad shows the ratio between MC predictions and data. Plots taken from analysis document [135].

4.4.2 Validations of fake background estimation

To justify that MC alone cannot be trusted to estimate fake background, a set of validation plots are produced to make comparisons between data and MC in the opposite and same-sign regions.

The comparison in Figure 4.9 and Figure 4.10 shows that the MCs model only a small fraction of the fakes compared to the data. The following kinematic validation plots (including the di-lepton invariant mass) in Figure 4.11 and Figure 4.12 shows the derived fakes contribution (orange-coloured component) by using the data-driven fake factor method described above.

The new closure plots in Figure 4.11 and Figure 4.12 have much more acceptable closures between the data points and the stack of the data-driven background and MC-driven components. Although some discrepancy are observed, it is still in

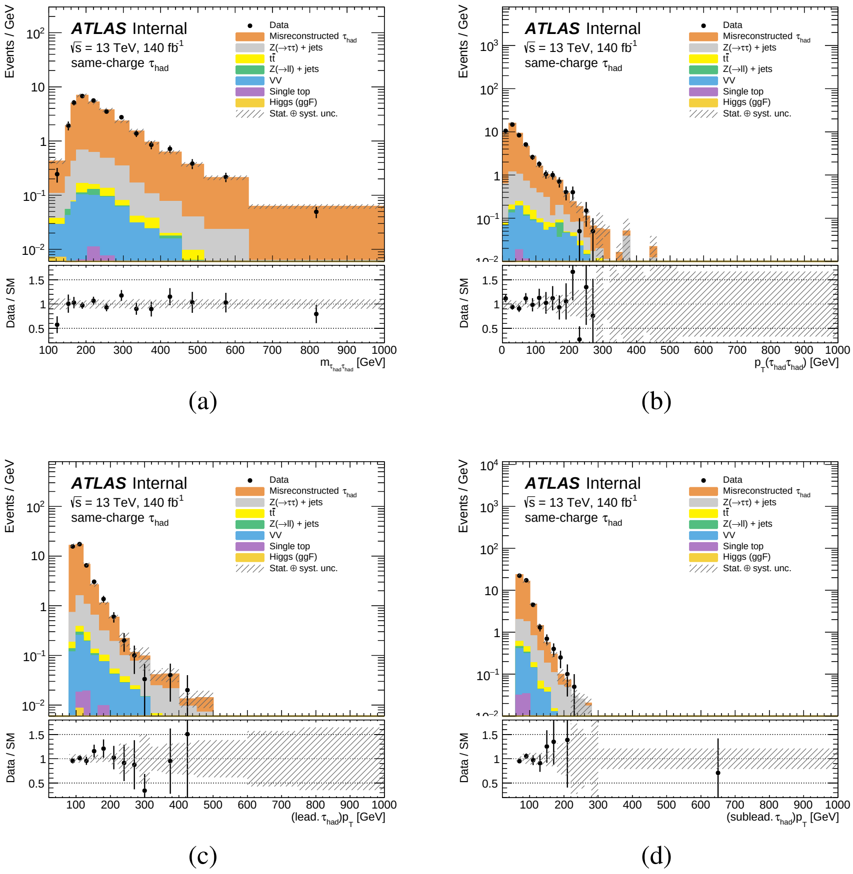
(a) (b) (c) (d)

Figure 4.11: Validation kinematic plots in the SS region for the $\tau_{\text{had}}\tau_{\text{had}}$ channel. (a) $m_{\tau\tau}$, (b) $p_T^{\tau\tau}$, (c) leading lepton p_T, (d) subleading lepton p_T. Plots taken from analysis document [135].

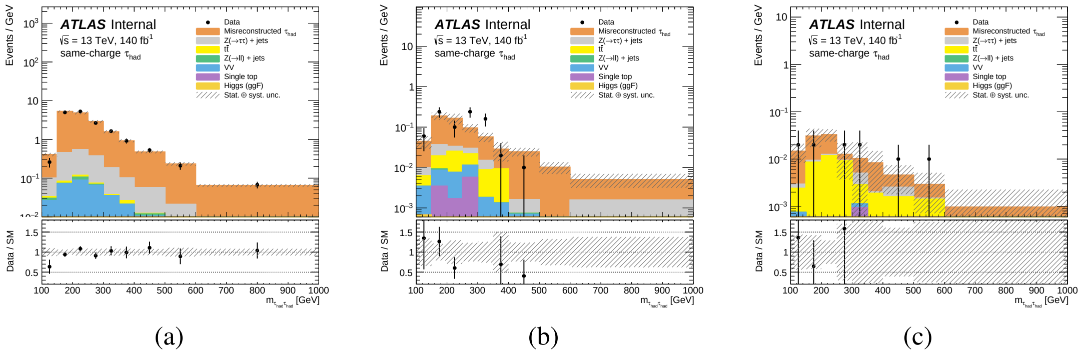
(a) (b) (c)

Figure 4.12: Validation kinematic plots in the SS regions for the $\tau_{\text{had}}\tau_{\text{had}}$ channel. Di-lepton invariant mass distribution for events with (a) 0 b-jets, (b) 1 b-jet, (c) 2 b-jets. Plots taken from analysis document [135].

agreement within the uncertainties. These closures in the same-sign region accompanied with the related systematic uncertainties shows that the fake factor technique is reliable to derive the fake-taus background in the signal region.

4.5 Data-simulation comparison in $\tau_{\text{had}}\tau_{\text{had}}$ channel

The signal for the analysis is composed of various processes that are able to produce τ candidates. The expected SM prediction is taken as the stack of the MC samples mentioned in section 4.3.1, and compared to the collision data in the $\tau_{\text{had}}\tau_{\text{had}}$ channel. Figures 4.13, 4.14, and 4.15 are showing the detailed composition breakdown comparisons of various kinematic observables in regions with different $b-$jet multiplicity. Note that the unfolded fiducial cross-section considered the stack of the events in these regions.

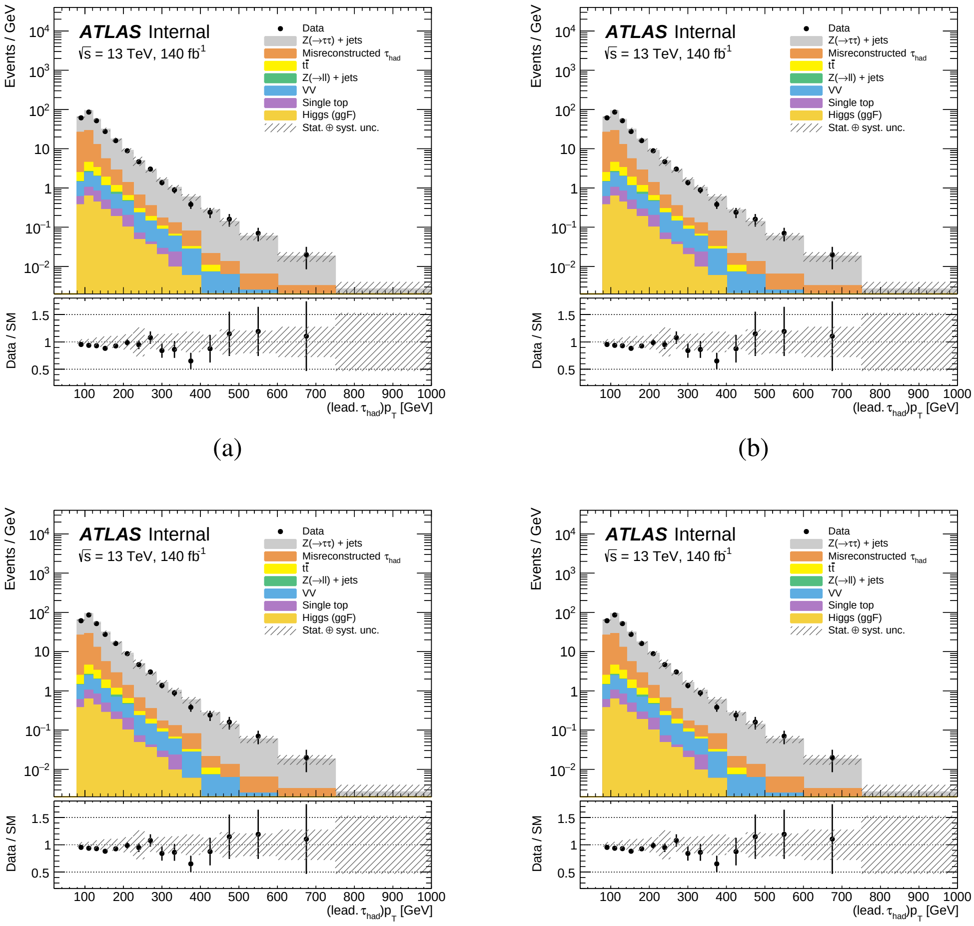

(a) (b)

(c) (d)

Figure 4.13: Data and MC comparison for various kinematic variables made in the 0 b-jet opposite-sign, $\tau_{\text{had}}\tau_{\text{had}}$ region: (a) the leading τ_{had} P_T^{vis}, (b) the subleading τ_{had} P_T^{vis}, (c) the P_T^{vis} of the $\tau_{\text{had}}\tau_{\text{had}}$ system and (d) the visible invariant mass of the $\tau_{\text{had}}\tau_{\text{had}}$ system. Plots taken from analysis document [135].

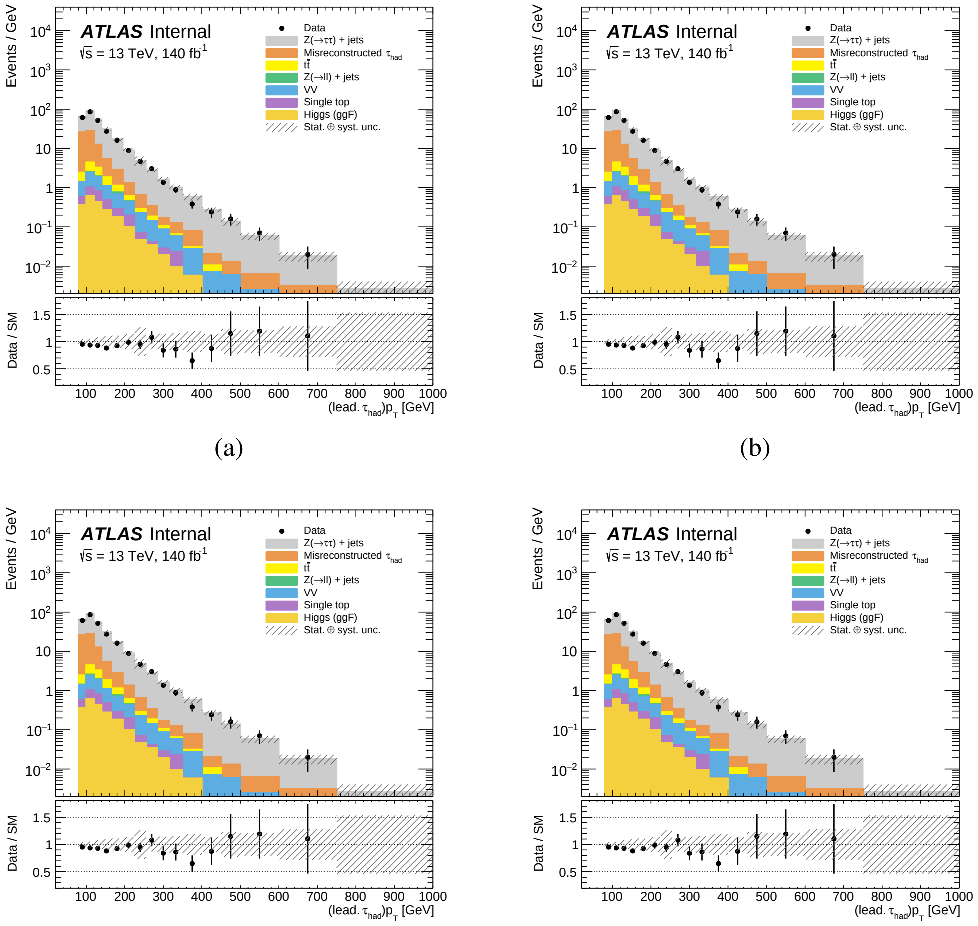

(a)

(b)

(c)

(d)

Figure 4.14: Data and MC comparison for various kinematic variables made in the 1 b-jet opposite-sign, $\tau_{\text{had}}\tau_{\text{had}}$ region: (a) the leading τ_{had} P_T^{vis}, (b) the subleading τ_{had} P_T^{vis}, (c) the P_T^{vis} ofthe $\tau_{\text{had}}\tau_{\text{had}}$ system and (d) the visible invariant mass of the $\tau_{\text{had}}\tau_{\text{had}}$ system. Plots taken from analysis document [135].

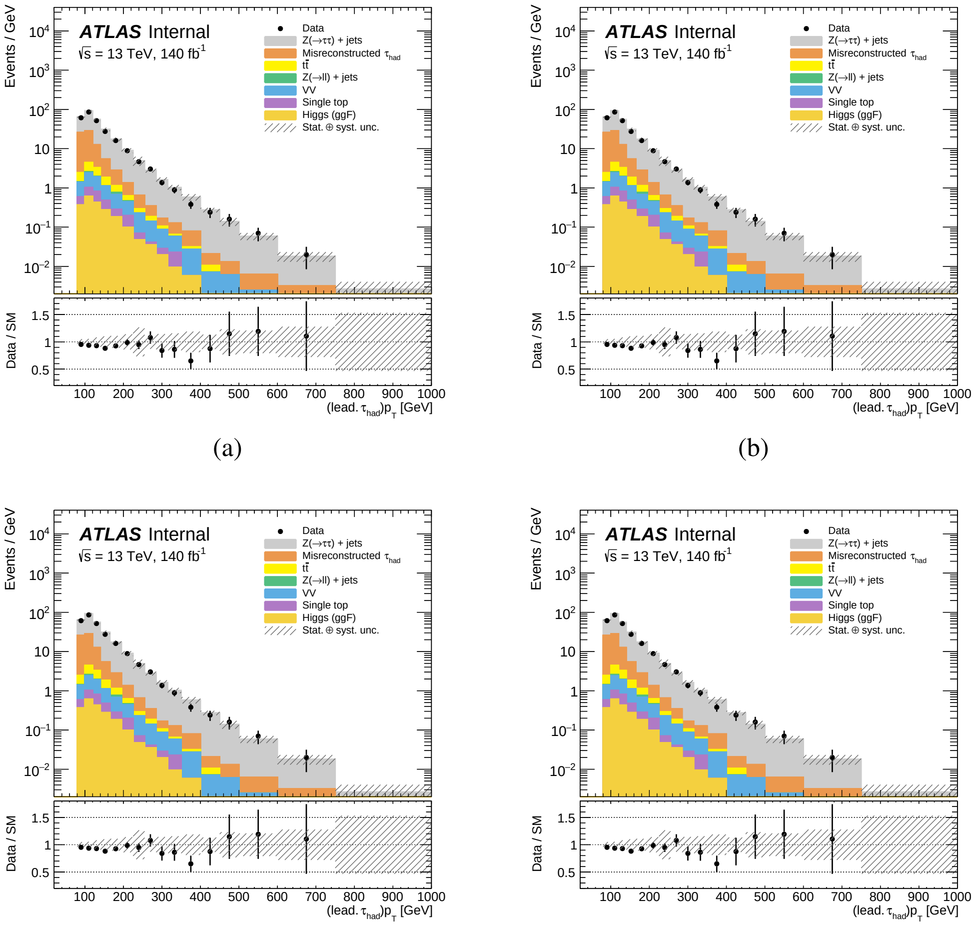

(a) (b)

(c) (d)

Figure 4.15: Data and MC comparison for various kinematic variables made in the 2 b-jet, opposite-sign, $\tau_{\text{had}}\tau_{\text{had}}$ region: (a) the leading τ_{had} P_T^{vis}, (b) the subleading τ_{had} P_T^{vis}, (c) the P_T^{vis} of the $\tau_{\text{had}}\tau_{\text{had}}$ system and (d) the visible invariant mass of the $\tau_{\text{had}}\tau_{\text{had}}$ system. Plots taken from analysis document [135].

4.6 From Detectors to Particles: Unfolding the True Distributions

Recall from section 1 that the primary goal in designing this analysis is to emphasis the reinterpretability and reusability. Consequently, the focus of the unfolded measurement is to obtain the inclusive and model-independent particle-level distributions. These distributions can be directly used to constrain the theoretical models with high flexibility or to compare results from other experiments, including both historical and future data. To clarify this concept, it is essential to realize that when an observable is measured for final states by an experiment such as the ATLAS detector, the measured distribution (i.e. data) is not fully representative of the true particle-level events. Despite the exceptional capabilities of the ATLAS detector, the data acquisition process inevitably introduces distortions and inefficiencies into the measured data. These issues arise from the imperfections of the detection system and the stochastic nature of the data collection, which can introduce random fluctuations and biases and affect the accuracy and fidelity of the measured data relative to the underlying physical processes.

To retrieve the particle-level distribution, an unfolding technique is adopted where the smearing and distortions in the detector-level measured data are corrected.
Naively, the basic idea of unfolding is to derive the relationship between the measured distribution $R(x)$ and the truth distribution $T(y)$. These two distributions are connected via a smearing function $S(x, y)$, which represents the instrumental effects. Here, x and y represent the detector-level and particle-level variables, respectively. The measured distribution can be written in terms of the smearing function as:

$$R(x) = \int S(x, y)T(y)\, dy \tag{4.6.1}$$

Due to the finite and discrete bins are being used in the distributions, this relationship can be incorporated into a response matrix M which reduces the problem to a matrix problem with the equation:

$$x_i = M_{ij} y_i \tag{4.6.2}$$

Where x_i is the detector-level distribution at bin i and y_i is the particle-level distribution at bin i. The M_{ij} represents the smearing effect between the truth bin i and measured bin j. Then, an inversion of the matrix can be used to reverse the data at detector-level to the particle-level histogram.

However, the real unfolding problem is not quite as a simple as an matrix inversion problem as stated in equation 4.6.2. Simply inverting the response matrix M can lead to unstable solutions due to noise and sample size. Instead, the problem is realistically solved by treating as a statistical interference problem and solved using probabilities and regularization techniques. The iterative Bayesian unfolding method [136] motivated by the Bayes' theorem was used and the detailed methodology along with the reasons is explained in section 4.6.1.

4.6.1 Unfolding Methodology: Iterative Bayesian

The introduction of the simplified unfolding idea in section 4.6 should be further adjusted to define the iterative Bayesian unfolding. First, let's define the smearing matrix as the *Folding matrix* R_{ij}. The matrix will represents the estimation of the smearing effects which originated from two components: 1. The finite efficiency of the detector means not all events are captured. 2. The finite resolution of the detector causing the true values of the captured events are measured with some uncertainty. Therefore, each cell of the folding matrix represents a conditional probability scenario:

$$R_{ij} = \frac{P(x \in \text{bin}_i \cap y \in \text{bin}_j)}{P(y \in \text{bin}_j)} \tag{4.6.3}$$

$$= P(x \in \text{bin}_i \mid y \in \text{bin}_j) \tag{4.6.4}$$

Where R_{ij} is the cell of the 2D folding matrix and represents the probability of the event x occurred in bin_i at the particle-level and was reconstructed to the bin_j at the detector-level. Then, based on this folding matrix, we can define the unfolding matrix $\tilde{R_{ij}}$ by inverting the logic of the folding matrix and revert the detector-level back to the particle-level distribution.

$$\begin{aligned}\tilde{R_{ij}} &= P(y \in \text{bin}_j \mid x \in \text{bin}_i) &\quad (4.6.5)\\ &= \frac{P(x \in \text{bin}_i \mid y \in \text{bin}_j) \cdot P(y \in \text{bin}_j)}{P(x \in \text{bin}_i)} &\quad (4.6.6)\\ &= \frac{R_{ij} \cdot P(y \in \text{bin}_j)}{\sum_j R_{ij} \cdot P(y \in \text{bin}_j)} &\quad (4.6.7)\end{aligned}$$

In equation 4.6.6, the Bayes' theorem was adopted [136] where $P(x \in \text{bin}_i \mid y \in \text{bin}_j)$ is defined in equation 4.6.4. The $P(y \in \text{bin}_j)$ corresponds to the probability prior represented by the truth distribution and the denominator is the total probability of the event x being in the truth bin_i.

If the unfolding matrix is obtained, after taking account for the escaped events due to the finite efficiency of the detector, the unfolding procedure may seems trivial, where the unfolding matrix $\tilde{R_{ij}}$ can be directly applied and reverse the measured distribution to the particle-level truth histogram as follows:

$$\mu_j = \frac{1}{\epsilon_j} \sum_i \tilde{R_{ij}} \cdot \text{n}_i \qquad (4.6.8)$$

where μ_j is the unfolding yield of bin j, n_i represents the measured data at bin_j, ϵ is the average reconstruction efficiency in bin_j. This efficiency ϵ_j accounts for the fraction of true events that were actually produced in the proton-proton collision in bin j are successfully detected and reconstructed by the detector. It is encoded in the response matrix $\tilde{R_{ij}}$, and is equal to the row sum of each bin in the 2D response matrix after normalisation towards the truth values at the particle-level. This is the probability that an event fall in the bin would be detected and also selected by the SR selection cuts.

However, equation 4.6.8 does not yet represent a full Bayesian scenario, as it assumes that the distributions are deterministic rather than stochastic. In reality, both the detector-level and particle-level distribution values, denoted as x and y would be considered as random variables. This implies that the prior used in this Bayesian framework is a distribution over a random variable, which is not well-defined in a definitive sense. The true unfolding matrix, therefore, only exists theoretically since the true distribution is a theoretical concept, which is inherently unknown and is precisely what the analysis aims to measure. This may sound dramatic, but having a truth prior is essential for Bayes' theorem to be applicable. This seems to have created a paradoxical situation akin to the chicken or egg first problem.

Therefore, the prior and migration matrix are estimated and improved iteratively. As discussed in section 4.3.1, the Monte Carlo samples are crucial components of the analysis to perform modern measurements. A truth distribution can be modelled using MC that based on current theoretical understanding and providing an initial guess of the true distribution. With this truth estimation, an initial migration matrix is derived using this estimation so that the Bayesian unfolding becomes feasible. To further enhance the reliability of the unfolding procedure, the final unfolded result is derived from an iterative process where the prior and migration matrix are updated with the posterior distribution from the previous iteration. This iterative Bayesian calculation ensures that the unfolding becomes progressively more accurate, and the iteration process can be summarized in the following steps:

- The prior probability is obtained from the initial theoretical truth distribution, where
$$P(y \in \mathrm{bin}\, j) = \frac{\mu_j}{\sum_j \mu_j}. \tag{4.6.9}$$
- Version k of the unfolding matrix is $\tilde{R}^k_{ij}$, where $k = 1$ is the initial iteration.
- The version μ_j^{k+1} of the prior is estimated using version k of the unfolding matrix.
- The version $k + 1$ of the unfolding matrix is then estimated from using the unfolded result μ_j^{k+1} as the prior and calculate the μ_j^{k+2} version of the prior

(i.e. the next iteration).

The stopping criterion for the number of iteration is a hyper-parameter that needs to be optimised. This is determined by a combination of the statistical uncertainty induced from increasing the number of iterations and a small relative χ^2 value between μ_j^{k+1} and μ_j^k of the unfolded spectrum. Detailed studies on the stopping criteria was performed and explained in section 4.6.8 and cross validated in all unfolding performance checks included in this section.

Below is an outlined summary of the inputs introduced above that are required for the unfolding process, along with clarifications of some important terminologies that will be used in the later sections:

- *Response (Migration) matrix* (M_{ij}): This is the unfolding matrix derived from the Monte Carlo simulated reconstruction-level and particle-level distributions. The 2D matrix cells are filled if an event passes both the particle-level and reconstruction-level selections as described in section 4.2. The matrix is used to trace bin-to-bin migrations.
- *Fiducial fraction* (f_i): This is the ratio of events which pass both reconstruction-level and particle-level selections to the events that only required to pass the reconstruction-level selection. This include those events that do not have a particle-level equivalent (with multijet fakes removed beforehand). The measured histogram need to be pre-scaled by the fraction before entering the unfolding process to remove the proportional of events that do not enter into the fiducial region, but passed the reconstruction selection. This correction factor originates from the finite resolution of the detector.
- *Efficiency correction* (ϵ_j): This is the ratio of events which pass both the reconstruction-level and the particle-level selections to the events that pass at the particle-level, including those events that do not have a reconstruction-level equivalent. This step of correction is part of the unfolded distribution calculation as shown in equation 4.6.8.
- *Fiducial purity*: This is the fraction of events that pass both the reconstruction-

level and particle-level selections and, crucially, do not migrate into another bin (i.e. the same reconstruction-level and particle-level bin). This fraction is represented by the diagonal of the normalised response matrix, and is a useful indicator quantity when optimising the unfolding process such as the binning optimisation described in section 4.6.2

- Standard model MC prediction (*prior*): The Iterative Bayesian unfolding technique requires an initial prior distribution for the particle-level observable. To provide a realistic estimate, the SM MC prediction that most accurately models the expected particle-level distribution is used as the prior.

To combine the above inputs, the final corrected response matrix R_{ij} is constructed by:

$$R_{ij} = M_{ij}\epsilon_j f_i \tag{4.6.10}$$

and the full formula for the unfolded differential cross section is:

$$\left(\frac{d\sigma}{dX}\right)_j = \frac{1}{\mathcal{L},\Delta_j}\sum_i R_{ij}\left(N_i^{\text{data}} - N_i^{\text{bkg}}\right) \tag{4.6.11}$$

where $\mathcal{L}$ is the integrated luminosity, Δ_j is the width of the particle-level bin j, N_i^{data} is the number of observed events in detector-level bin i, N_i^{bkg} is the estimated number of background events (multijets) in the same bin, and R_{ij} is the corrected unfolding matrix elements.

4.6.2 Binning optimisation

To enhance the stability of the unfolding process and ensure the reliability of the unfolding output, the binning of the distribution needs to be properly optimised for extracting meaningful physical insights from the data. If the binning is too fine, some bins may contain very few or no events (under-sampled), leading to a very large statistical uncertainty at the bin and would result in an unstable unfolded distribution with large statistical fluctuation amplitudes. On the other hand, if the binning is too coarse, the resolution of the measurement would drop and important details presented in the data may be lost (washed out) which is not ideal to extract shape information through the unfolded result with low resolution. Therefore, to assess the trade-off between the variance (finer bin) and bias (large bin), and to achieve a balance between the uncertainty and the resolution, the binning needs to be optimised. This optimisation ensures that the unfolded distribution has sufficient statistics per bin while minimising bias, which are essential to derive a statistically robust and detailed representation of the underlying particle-level distribution.

The binning of the $m_{\ell\ell}$ distribution was optimised using the following criteria:

- The minimum number of MC events predicted in any given bin for a luminosity of 139 fb^{-1} should be $\geq$ 30. This is to allow sufficient statistics to perform a stable unfolding. The number is based on previous unfolded measurement experiences.
- The fiducial purity as described at the end of section 4.6.1 should be $\geq$ 0.65, keeping the bin-to-bin migrations at a manageable level. If the purity level is not controlled and is too low, the high contamination from events being misidentified between bins would lead to an increase in statistical uncertainty and introduce bias in the unfolded result as the truth distribution is harder to recover accurately due to high instability.

Starting from a very fine-binned $m_{\ell\ell}$ distribution, bins are merged successively until both thresholds are passed. The final optimised binning used for the $m_{\ell\ell}$ distribution has a total of 13 bins, where 12 bins divide the range between 100 GeV $\leq m_{\ell\ell} \leq$ 635 GeV with mostly increasing bin size along the $m_{\ell\ell}$ spectrum. An overflow bin is defined from $m_{\ell\ell} >$ 635 GeV and is also unfolded.

By adopting the optimised binning, Figures 4.16 4.17 show the control plots of the $m_{\ell\ell}$ distribution.

4.6.3 Statistical Uncertainty

For most of the unfolding closure validation plots, the error bars represent the statistical uncertainty obtained directly from the unfolding procedure. As a result, the

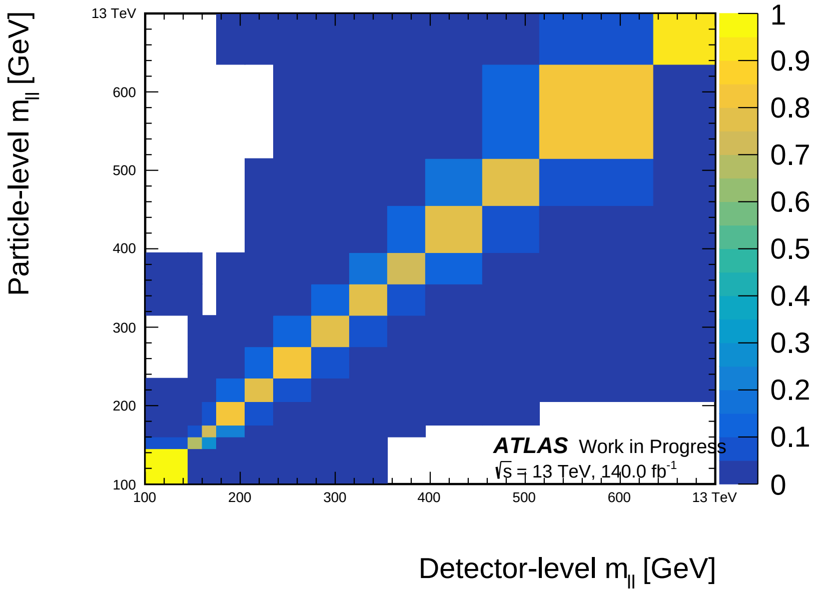

Figure 4.16: The 2D nominal response matrix used for the unfolding check for the $m_{\ell\ell}$ $\tau_{\rm had}\tau_{\rm had}$ channel distribution.

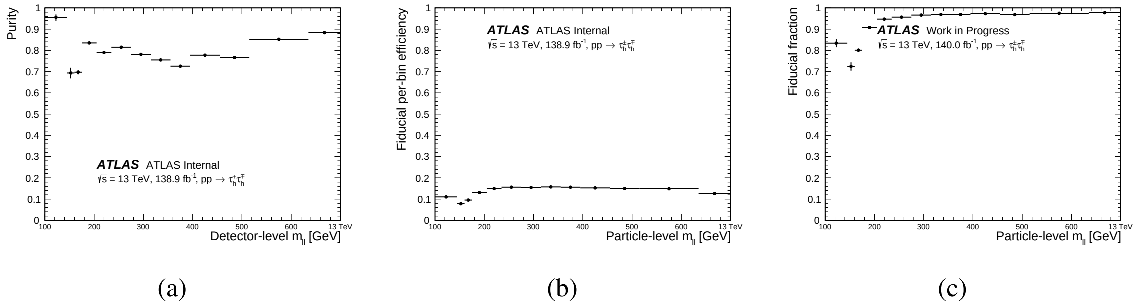

(a) (b) (c)

Figure 4.17: (a) This is the diagonal of the response matrix, which indicates the percentage of events remaining in the same bin at both reconstruction-level and truth-level. (b) This is the efficiency ϵ_j of the detector, which is the ratio of the events passed the truth and reconstruction-level selection to the events passed the truth-level selection. This identify the fraction of events passed truth-level selection and have reconstruction-level equivalent (i.e detected). (c) This is the fiducial fraction f_i, representing the fraction of events that passed both levels of selections and the events passed the reconstruction-level selection. This extracts the fraction of reconstruction-level events with truth equivalent, and is applied to the unfolding input before unfolding is performed.

method for determining this statistical uncertainty is discussed here rather than deferred to the later uncertainty section (Section 4.7), in order to avoid confusion. The statistical uncertainty from the unfolding process was estimated using 2 000 pesudo-experiments; 2 000 toys are created from the nominal reconstruction-level distribution by applying a Gaussian-distributed random variable to each histogram bin. The width of the Gaussian is determined by the Poisson uncertainty $\sqrt{N}$ using the expected number of events N of each bin. The 2 000 toys are then propagated through the unfolding process individually and the root mean square (RMS) spread around the mean unfolded value for each bin is taken to be the expected statistical uncertainty of the unfolding process, representing the potential statistical variance of the unfolded result.

4.6.4 Closure checks

After the unfolding procedure is defined and the optimised binning for the $m_{\ell\ell}$ distribution is determined, a series of unfolding validation checks are performed. These checks ensure that the unfolding remains robust under various scenarios where discrepancies may exist between the Monte Carlo simulation (used as the prior) and the measured data. The following tests are conducted, each designed to probe a different aspect of the method's stability and reliability:

- Naive closure check, section 4.6.4: As a sanity check for the unfolding framework, a closure check between the unfolded result using the MC reconstruction-level distribution as input and the corresponding MC truth distribution.
- Pseudodata closure check, section 4.6.4: This is a less naive closure check after the first sanity check, where a Gaussian-fluctuated MC reconstruction-level distribution is used as the pseudodata unfolding input and the unfolded result is compared to the corresponding MC truth distribution.
- Alternative MC test, section 4.6.4: `SHERPA2.2.11` [88] and `POWHEG + PYTHIA8` are alternatively used for the unfolding test inputs. The unfolded results are compared to their corresponding underlying truth from difference MC sample

sets.

- Re-weighting variation closure checks, section 4.6.5: Following the pseudo-data closure test, which demonstrated that the unfolding closure lies within statistical uncertainties, additional robustness checks are conducted to evaluate the sensitivity of the unfolding procedure to discrepancies between the simulated and the true data lineshapes. These tests involve reweighting the Monte Carlo truth and reconstruction-level distributions to mimic possible lineshape differences that may arise in the measured data due to modelling inaccuracies. The aim is to verify that the response matrix can still yield an unbiased unfolded result under such variations, and that the unfolding procedure does not introduce a bias towards the SM prediction if the data deviates from it.
- Process stack composition variation closure checks, section 4.6.7: Another robuestness check on the unfolding procedure with varied contributions from different processes within the signal stack.
- Mass spectrum shift check, section 4.6.9: An additional unfolding stress test using $m_{\ell\ell}$ simulations with right-shifted distribution.
- BSM injection test, section 4.6.6: Unfolding test using simulations injected with BSM signal to check if the unfolding procedure would bias towards the SM and cover any potential BSM signal that may present within the measured data.
- Hidden observable modelling test, section 4.6.10: An unfolding stress test that applies the ratio between the measured distribution and the prediction to the $m_{\ell\ell}$ simulations used for the unfolding checks. The modelling usually has a lower accuracy compared to the $m_{\ell\ell}$ modelling, so the test is to check if the unfolding procedure remains unbiased and stable if the expected $m_{\ell\ell}$ modelling discrepancy is presumably over-exaggerated by applying the discrepancy from the observable.

The purpose of these unfolding checks, discussed in the corresponding labelled sections, is to build a robust unfolding framework capable of producing reliable results for the $m_{\ell\ell}$ distribution in the $\tau_{\text{had}}\tau_{\text{had}}$ channel from the measured data. To minimise the risk of introducing bias, the unfolding framework was developed using the *blinding* strategy, where the actual data were not accessed until the system had been validated for robustness. This is to ensure the development and optimisation studies are unbiased towards the target data and based solely on simulated data. To achieve this, the full Monte Carlo stack of the signal samples, as discussed in section 4.3.1 was used and the estimated fakes contributions are added into the pseudodata and then subtracted by default in the data processing stage to best replicate the scenario when dealing with the real data. The number of iteration used in the unfolding process was set to two and this choice was determined by a dedicated study as described later in section 4.6.8.

Naive closure check

The first closure check conducted serves as a sanity check. This test verifies the code to see if it is functioning as expected. In this check, The MC reconstruction-level spectrum is used as the unfolding input which representing the measured data, and the corresponding MC truth spectrum is used as the prior for the unfolding setup. By using the nominal migration (response) matrix derived from the pair of MC truth and reconstruction distributions, the unfolded MC reconstruction-level spectrum should precisely match to the truth-level spectrum prior.

Figure 4.18 compares the unfolded result and the SM prediction (i.e. MC truth prior). The bottom panel is indicating the ratio between the two curves on the upper panel. The fact that all ratio located at 1.0 (for all different iterations tested too) across the spectrum suggests that the unfolding setup is working as expected and proves that a known truth can be correctly recovered by the unfolding process.

Basic closure check using pesudodata

To build upon the simple closure check described in section 4.6.4, an asimov closure check was performed on a pesudodata spectrum created based on the MC reconstruction-level spectrum. To generate the pesudodata input, the MC reco-level

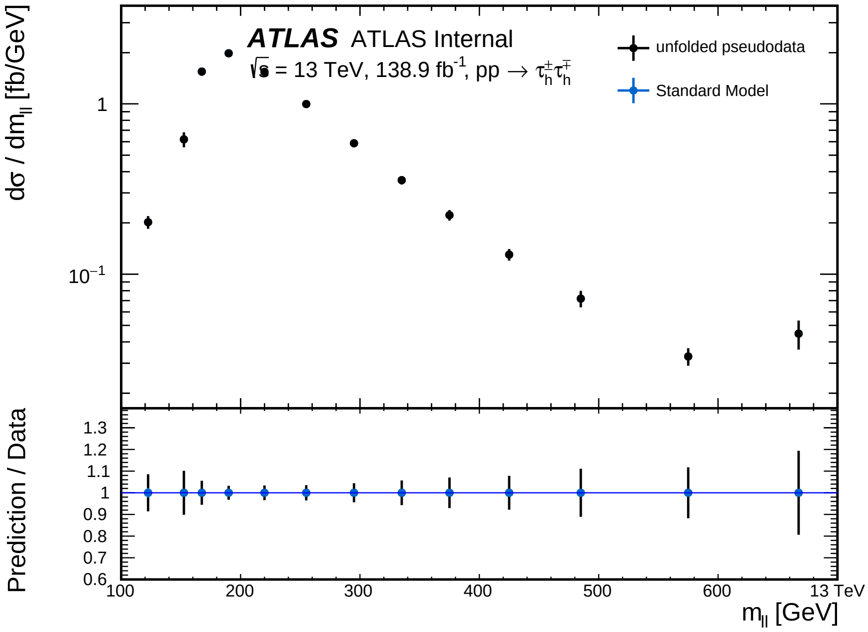

Figure 4.18: Naive closure check of the unfolding setup on the differential cross-section observable for the $m_{\ell\ell}$ $\tau_{\text{had}}\tau_{\text{had}}$ channel distribution. The MC reconstruction spectrum was used as the data and MC truth spectrum as the prior, along with the corresponding response matrix. The error bars are pure statistical uncertainty as described in section 4.7.

distribution was fluctuated on a bin-by-bin basis using Gaussian and the width of each Gaussian is determined by the statistical uncertainty (from toys) of each bin. This method validates the unfolding process by allowing random statistical fluctuation in the posterior, instead of using the directly related pair as shown in section 4.6.4. The result indicates that any randomness within the statistical uncertainty does not affect the results beyond the expected statistical uncertainties. As can be seen in figure 4.19, the distribution closes within the statistical error bar using two iterations (and for all tested iterations too).

Alternative MC test

The unfolding setup was also tested using alternative sets of MC sample instead of the nominal stack. The `SHERPA2.2.11` [88] and `POWHEG + PYTHIA8` generated process stacks are used as the unfolding inputs and the results in figure 4.20 suggest good closure across the distribution. Note that these error bars are not purely statistical anymore to avoid misleading result interpretation. Due to the swap of MC samples, a dominate component of systematic errors are added to the error bars, this

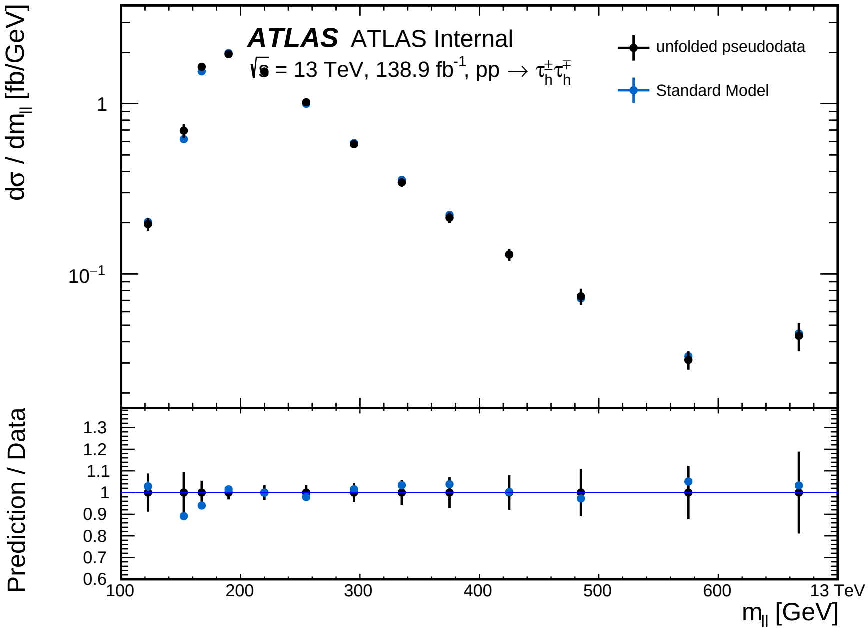

Figure 4.19: Basic asimov closure check of the unfolding setup on the differential cross-section observable for the $m_{\ell\ell}$ $\tau_{\text{had}}\tau_{\text{had}}$ channel distribution. The fluctuated reconstruction spectrum was used as the pseudodata and MC truth spectrum as the prior, along with the nominal response matrix. The error bars are pure statistical uncertainty.

error is discussed in more details in section 4.7.

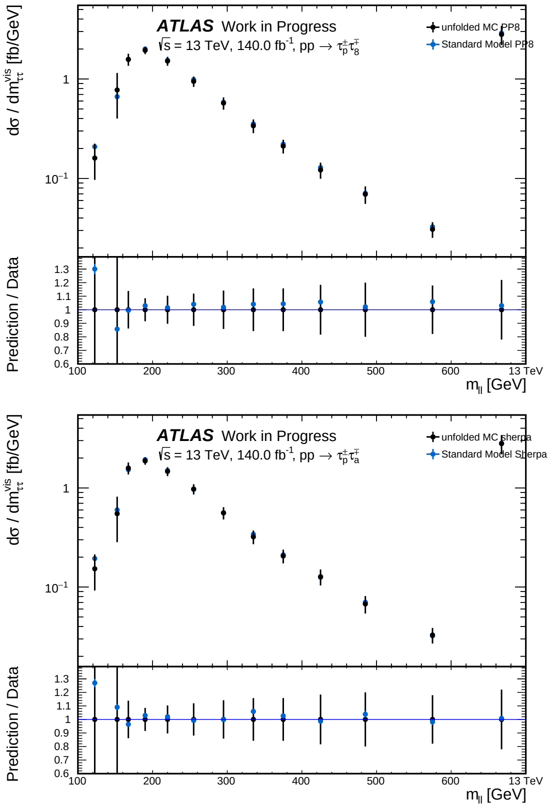

Figure 4.20: (1) The top plot shows the closure test result of using the `SHERPA2.2.11` [88] MC sample stack as unfolding input. (2) The bottom plot alternatively used the `POWHEG + PYTHIA8` MC sample stack. Note that these error bars are not pure statistical, but included the modelling uncertainty of these two set of samples.

4.6.5 Re-weighting studies

To ensure the robustness of the unfolding system beyond the basic closure checks, further validations were conducted using reweighting strategies. While the three closure tests demonstrate consistency under nominal conditions, they are not sufficient to fully validate the reliability of the unfolding in scenarios where mis-modelling of the detector response or truth-level shapes may occur. The reweighting tests are designed to artificially induce shape discrepancies between the original particle- and detector-level distributions used to construct the response matrix and the reweighted distributions used for the test input (detector level) and closure reference (particle level). This simulates potential distortions that might arise in real data, providing a more stringent test of the response matrix's ability to recover the true distribution in the presence of such mismodelling.

The first set of tests involved applying linear reweighting factor functions on an event-by-event basis to the $m_{\tau\tau}$ distribution based on the dilepton mass. This approach tests how effectively the response matrix can adapt to linear changes in the input distributions that were not accounted for in the original MC predictions. The following steps outline the test workflow:

- The selected events were reweighted at the stable taus (pre-decay) kinematic using various linearly-increasing reweighting factors. The factor A, defined as $A = 1.0 + \frac{m_{\tau\tau}}{factor}$, is a varying event-reweighting gradient, and this gradient scales with the $m_{\tau\tau}$ spectrum to account for the fact that MC mis-modelling is less likely in the low $m_{\ell\ell}$, high statistics region and becomes more pronounced as the distribution region extends towards the tail where the $m_{\ell\ell}$ value gets larger. Different ranges of A were achieved for these tests by alternating the division factor in the equation of A to control the rate of change.
- The effect of reweighting events at the stable taus kinematic will be reflected at the visible-level distribution. The full MC stack of all processes is constructed, including the jet faking taus.
- The pseudodata is created from the reconstruction-level spectrum of the full

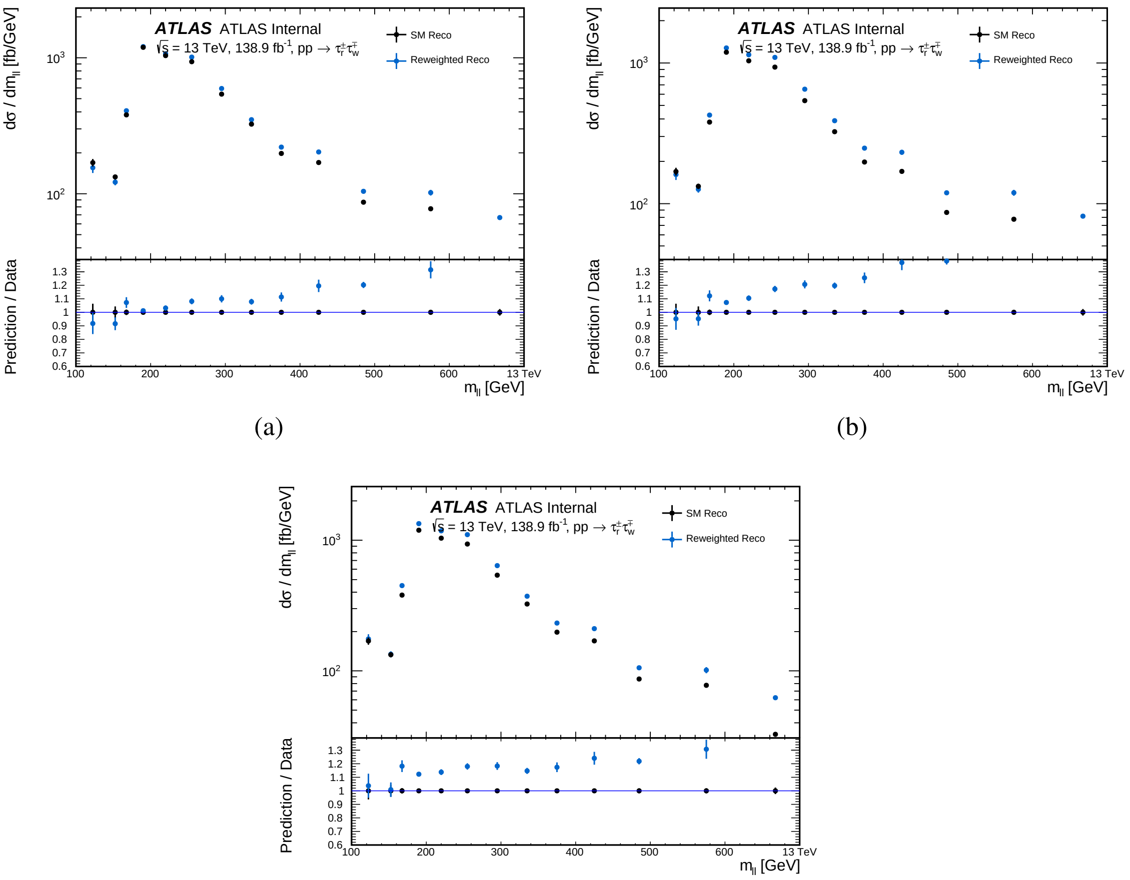

(a) (b)

(c)

Figure 4.21: These plots indicate the level of lineshape variations created for the reconstruction-level distribution compared to the nominal reconstruction-level spectrum. (a) Scaled up by a factor A ranging from 1 to around 1.2. (b) Factor A ranging from 1.1 to 1.5. (c) Factor A = 1.2 across the $m_{\tau\tau}$ bins.

stack using the fluctuation method described in section 4.6.4 to create an extra layer of statistical randomness, so that it better simulates the true scenario.

- The jets faking taus estimated using the method described in section 4.4 are subtracted from the full-stack, along with applying the fiducial correction factors after.
- The pseudodata are unfolded with the nominal response using nominal MC truth as prior and the unfolded result is compared to the linearly reweighted truth.

As shown by the plots in figure 4.22, the closure between the lineshape reweighted MC truth and the unfolded results derived from using the corresponding fluctuated reconstruction-level distributions agreed at a good level, with all the points matched

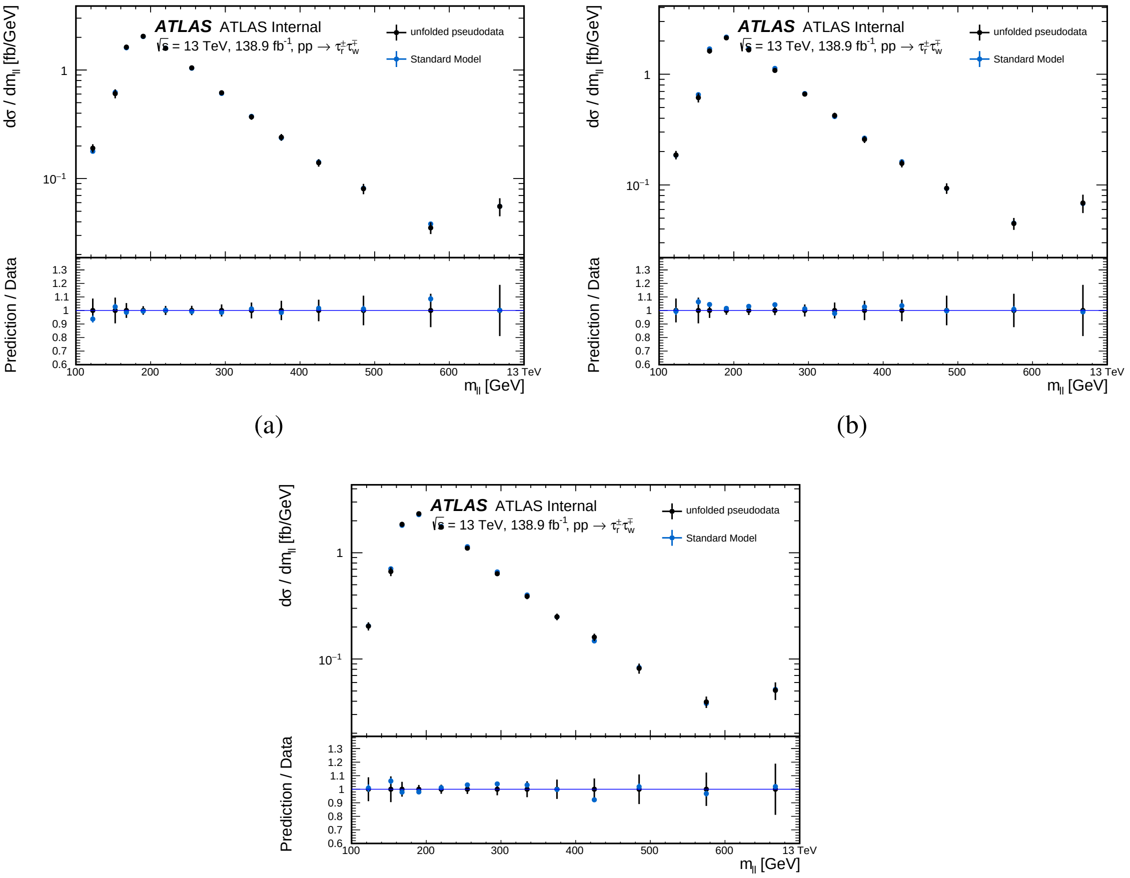

(a)

(b)

(c)

Figure 4.22: These plots compare the unfolded results using the fluctuated reconstruction-level distributions from Figure 4.21 as pseudodata, against the corresponding lineshape-reweighted MC truth. (a) Scaling factor A ranges from 1 to 1.2. (b) Factor A ranges from 1.1 to 1.5. (c) Constant scaling with $A = 1.2$ across the $m_{\tau\tau}$ bins. The error bars show statistical uncertainties only, derived using toys as described in Section 4.6.3.

within the statistical error bars. This demonstrates that if a linear mis-modelling presented in the unseen data, the unfolding system will be able to recover the underlying truth spectrum corresponding to the measured data within the statistical uncertainty and without being biased towards the SM MC predictions.

4.6.6 BSM injection studies

To expand the validation coverage and test for potential new physics effects in the data, a series of BSM signal injection tests were conducted. This test builds upon the reweighting approach in Section 4.6.5, but instead of simulating general lineshape-like mis-modellings, it tests the unfolding system's ability to recover spectra with genuine BSM signal contributions that may present in the data. Getting a good closure result in this test would add significant confidence to the unfolding procedure when evaluating its robustness. The BSM signals may behave very differently from the SM process in terms of efficiencies and bin migrations, therefore, the unfolding process must remain sensitive to such BSM signals, which are among the motivations for the measurement.

Specifically, a Vector Leptoquark (VLQ) signal from the MC sample discussed in section 4.3.1 was injected into the nominal MC stacks to create deviations from the pure SM predictions. As mentioned in the section 4.3.1, the potential VLQ signal was produced from reweighting the nominal SM sample. From the VLQ signals, the weight at 1.5 TeV dilepton mass was used for the injection test as it is having the largest impact and was heavily used in detector-level fitting in the search of the analysis. This weight represents the pure third-generation parameter of the full leptoquark coupling matrix to left-handed fermion fields. Through using this weight, the pure BSM terms, as well as the interference term between the SM and BSM contributions are generated. The full BSM signal used for injection is constructed using the following formula:

$$\text{BSM} = g^2\text{Interference term} + g^4\text{Pure BSM term} \tag{4.6.12}$$

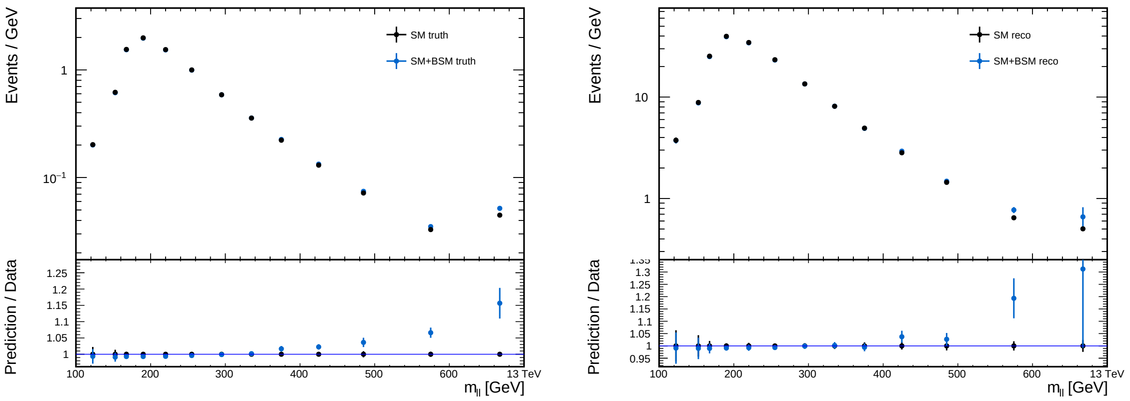

(a) (b)

Figure 4.23: Comparison between the SM prediction and the third generation 1.5 TeV VLQ signal injected SM predictions at both truth and reconstruction levels in the $\tau_{\text{had}}\tau_{\text{had}}$ decay channel. (a) Truth-level. (b) Reconstruction-level.

Where the g factor is shown as $\frac{g_U}{\sqrt{2}}$ in equation 4.3.2 and g^2 corresponds to the squared $b-\tau$ left-handed coupling constant of the $\tau_{\text{had}}\tau_{\text{had}}$ channel derived from the detector-level profile likelihood fits of the $m_{\ell\ell}$ distribution in the search component of the analysis. The maximum level of injection using the derived coupling g at the reconstruction level is around 2 σ from the pure SM prediction. Figure 4.23 shows the significance of the signal injection added to the nominal distributions.

Pseudodata were then created from fluctuating the BSM-injected reconstruction-level distribution, and the corresponding unfolded result is shown in figure 4.24. Further, a stress test was performed by using a value of $g^2 = 5.5$, which is larger than the expected limit $g^2 = 4.46$ used in the first injection test. This creates a larger discrepancy between the nominal response and the BSM-injected unfolding input. The maximum deviation between the central values of the BSM-injected unfolding input and the nominal reconstruction-level distribution reached around 3 σ limit of the statistical uncertainty.

As the plots in figure 4.24 shown, the unfolded results matched the BSM-injected MC truth within the statistical uncertainty across the bins for both injection tests. This suggests that the corresponding BSM-injected truth can be recovered to a good level from the BSM-injected pseudodata using response matrix derived from the MC simulation, which again shows that the response matrix is not heavily biased, and the unfolded result is less-likely to bias the potential BSM signals that may present

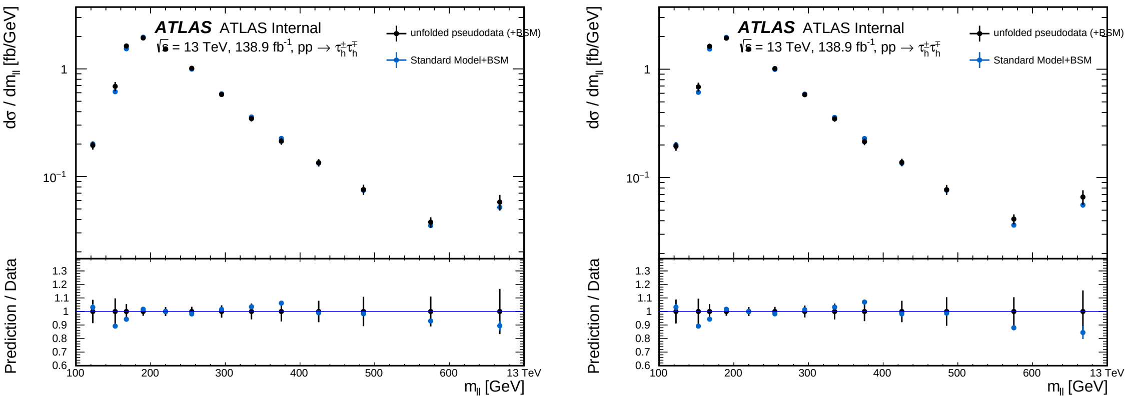

(a) (b)

Figure 4.24: Comparison between the unfolded results from using the SM response and the third generation 1.5 TeV VLQ signal injected SM truth-level predictions in the $\tau_{\text{had}}\tau_{\text{had}}$ decay channel. (a) Maximum deviation created from the signal injection reached 2 σ using $g^2 = 4.46$. This factor was obtained from the search limit fitting procedures. (b) Maximum deviation created from the signal injection reached 3 σ using $g^2 = 5.5$. This test injects an excess of BSM signals from the limit and provides a stronger stress test.

within the measured data towards the SM predictions.

4.6.7 Stack composition variation

The full fiducial MC stack predictions used in the analysis involves combining multiple sources of signals and uncertainties. It is essential to justify the unfolding system's ability to handle variations between the stack composition of the measured data and the MC simulation. Since the measurement focuses on the $\tau_{\text{had}}\tau_{\text{had}}$ decay channel, the primary source of stack composition uncertainty arises from the QCD scale variations. These variations are from the choice of the renormalisation scale factor μ_R and the factorisation scale factors μ_F during theory calculations. The choice of μ_R and μ_F is not fixed by theory, and therefore introduces uncertainty in the MC predictions. The perturbative series is truncated at the NLO, and by varying these scales, it is possible to estimate the uncertainty originating from the truncated higher order terms which represents the higher order QCD corrections that were not included in the nominal calculation.

To analyse the QCD scale variation, the `RIVET` [137] framework was used. The `RIVET` [137] is designed to compare theoretical predictions from MC event generators with the measured experimental data, with each particle-level measurement stored in the library being represented by a `RIVET` routine. Such a `RIVET` routine was developed for the $\tau_{\text{had}}\tau_{\text{had}}$ channel $m_{\ell\ell}$ distribution in this analysis, and the routine was validated by comparing its outputs with the MC truth predictions produced directly from the analysis framework. The validation closure check results are illustrated in Figure 4.25.

The red vertical line in Figure 4.25 (a) indicates the cut $m_{\tau\tau} > 100$ GeV applied during the generation of the analysis sample. This cut has no impact on the validation itself and can be ignored here, as the validation is explicitly confined to this high-mass region (> 100 GeV). The comparison demonstrates excellent agreement between the MC prediction from the analysis framework and the corresponding `RIVET` routine output for the Drell–Yan sample. This confirms that the `RIVET` implementation accurately reproduces the fiducial selection used in the analysis, and is therefore reliable for estimating QCD scale uncertainties for this measurement. Since the Drell–Yan and $t\bar{t}$ processes dominate the phase space within the fiducial region,

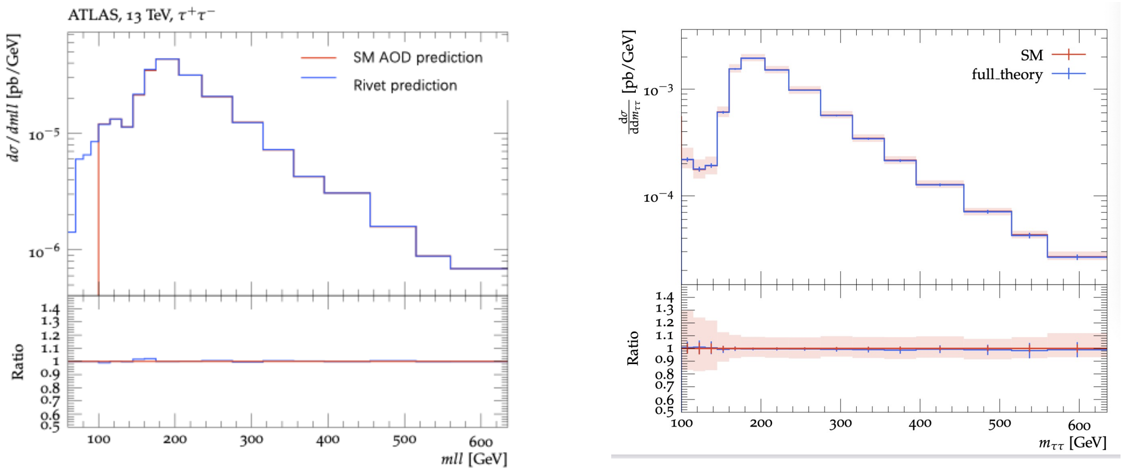

(a) (b)

Figure 4.25: (a) `RIVET` output (blue) vs Analysis Object Data (AOD)-based prediction (truth-level) for the $m_{\ell\ell}$ distribution in the high-mass Drell-Yan b-jet-filtered Drell-Yan sample. (b) `RIVET` output (blue) vs AOD-based prediction for the $m_{\ell\ell}$ distribution at the high-mass Drell-Yan full statistics samples. AOD is a data format that is optimised for analysis tasks that contains relevant information from the raw data focusing on the reconstructed object. Therefore, AOD-based predictions are referring to the simulations that are validated by comparing to the AOD data.

as shown in the figures in section 4.5, QCD scale uncertainties from subdominant topology contributions are neglected.

Figure 4.26 shows the scale variation bands of the $m_{\ell\ell}$ distribution at the particle level. Larger variations are observed in the low-mass region, primarily due to the high p_{T} selection thresholds applied to the τ objects. These thresholds are necessary to ensure high trigger efficiency and to suppress backgrounds, which improves the overall signal purity. However, they also sculpt the original shape of the distribution near the Z-peak by preferentially removing low-momentum τ candidates. This introduces a sharp drop in event yields near the threshold, where the combination of limited statistics and narrow bin widths leads to larger statistical fluctuations. The scale variations for the $t\bar{t}$ process are generally larger than those for Drell–Yan, with uncertainties reaching approximately 9% in the intermediate mass range, as shown in Figure 4.26. When combining these processes into a single stacked prediction, the QCD scale variation uncertainties are added in quadrature. This results in an overall scale uncertainty of approximately ±7% to ±8% in the central mass region, as shown in Figure 4.27.

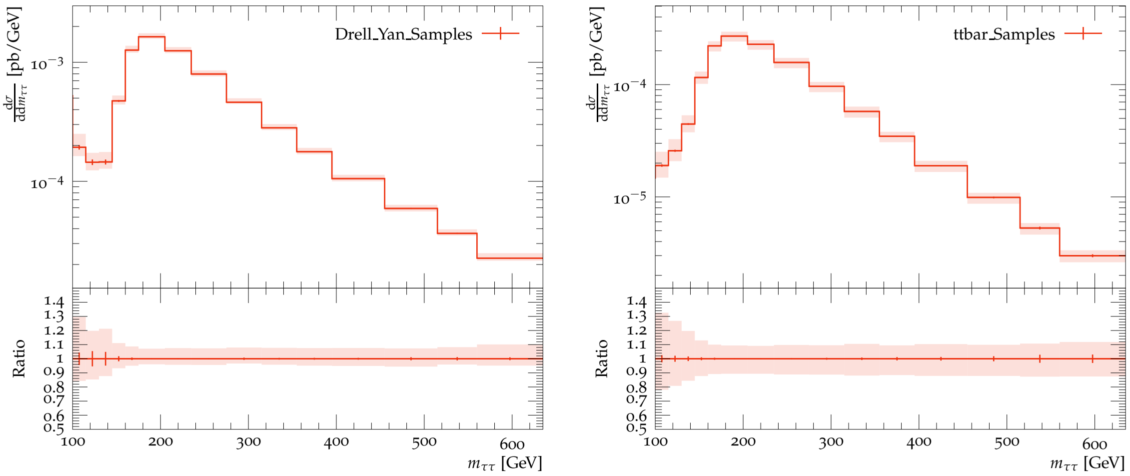

(a)

(b)

Figure 4.26: (a) Scale variation of the Drell-Yan process. (b) Scale variation of the $t\bar{t}$ process.

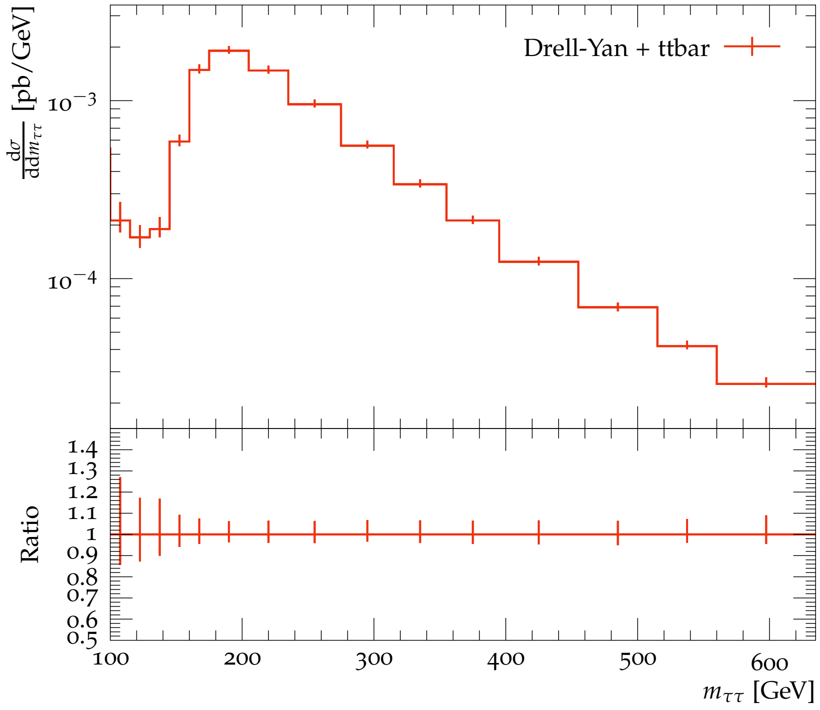

Figure 4.27: Combined scale variation uncertainty of the Drell-Yan and $t\bar{t}$ processes

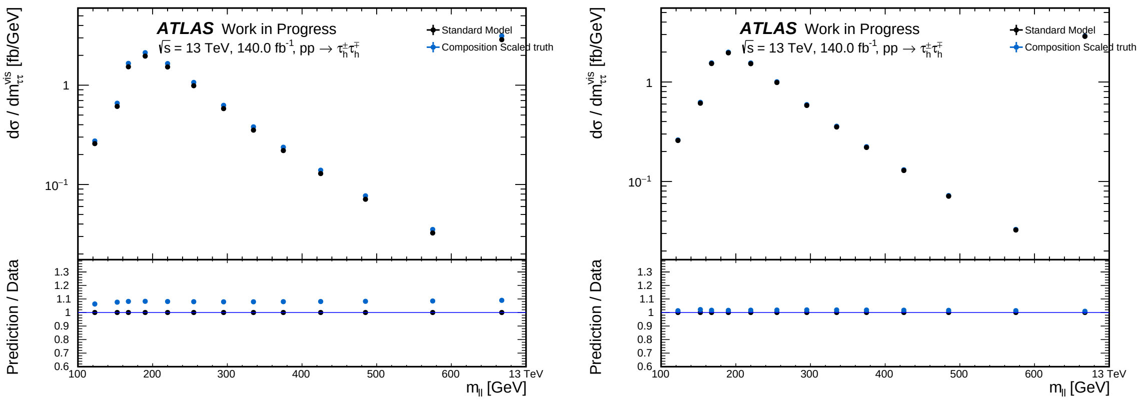

(a) (b)

Figure 4.28: Figure (a) and (b) are showing the variations at the truth-level, where a factor of 1.1 is applied to the Drell-Yan and $t\bar{t}$ components respectively. This, as expected, created around 10% difference between the nominal SM truth and the scaled truth as shown in Figure (a) due to the dominant presence of Drell-Yan process in the stack. On the other hand, the similarly scaled sub-dominant $t\bar{t}$ component created a much less difference as shown in figure (b).

The unfolding test on the stack composition variation of the MC stack is performed by allowing individual processes in the stack to vary within the combined range of the QCD scale uncertainties. Although Figure 4.27 indicates that the uncertainty is approximately 7% in the middle $m_{\ell\ell}$ range using the on-the-fly multiweights of `RIVET`, which is a function of `RIVET` that automatically run the prediction using the QCD scale and PDF variations. In order to stay conservative, we vary the normalisation of individual processes (Drell-Yan, $t\bar{t}$) in the MC stack by 10%. Several pseudodata were created with varying combinations of scale factors for each process between 0.9 and 1.1. Two examples are shown in Figure 4.28.

The unfolding closure tests were then performed onto the stack composition varied distributions, along with statistical fluctuations applied. The results of the test are illustrated in figure 4.29

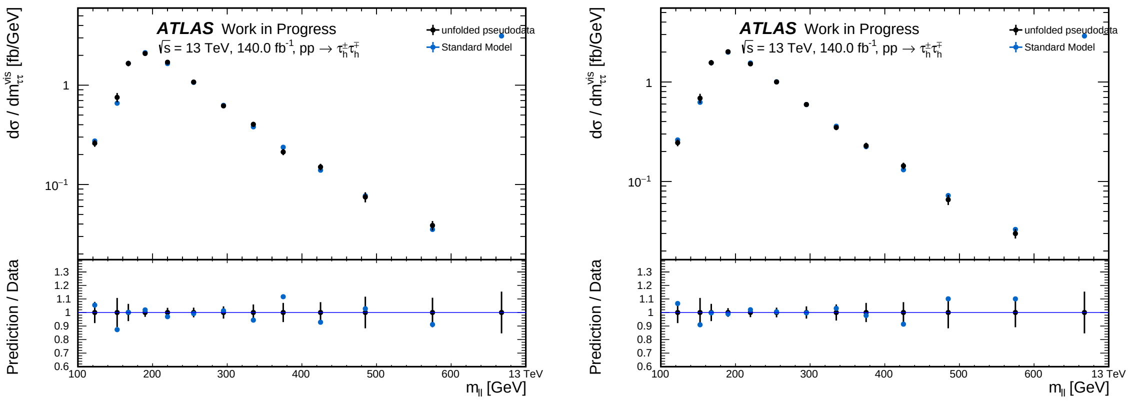

(a) (b)

Figure 4.29: These plots are comparing the unfolding result with varied stack composition from using the nominal response and the corresponding varied truth. Error bars shown are expected statistical uncertainties. Figure (a) and (b) are comparing the output unfolded results with the corresponding input truth-levels with a factor of 1.1 applied to the Drell-Yan and $t\bar{t}$ components respectively. The closure in the ratio plot shows that the unfolding procedure performed well regarding to this stack composition variation.

Again, the unfolding system seems to have passed the stack composition variation checks using the conservative ±10% limit. The closure between the underlying varied MC truth predictions and the corresponding unfolded results agreed within the statistical uncertainties across the spectrum. This shows that the unfolding method can handle the potential situations with varied stack composition in the data and without heavily biasing towards the SM predictions under this deviation.

4.6.8 Tuning the hyper-parameter: number of iterations

The unfolding setting on the number of iterations used should be optimised. This parameter tuning study addresses the trade-off between the bias and the statistical uncertainty of the unfolded result. With more iterations used, any potential bias in the unfolded result tends to decrease, provided that the purity and statistical significance within each bin of the distribution are maintained at a sufficient level since the start. The unfolding process aims to converge towards the truth distribution based on the measured distribution when supported with a reasonable prior distribution at the start of iterating. However, the initial prior used for the first iteration may still be far from the true distribution at particle-level, which could lead to a significant bias. By iteratively updating the prior distribution based on the observed data, the unfolded result would be progressively corrected towards the true distribution that aligns with the observed data, and consequently results in an reduction of bias in the unfolded result with more iterations applied. However, this reduction in bias comes at a cost; as the number of iterations increases, the statistical fluctuations that inherently included in the data can be amplified rather than diminished through the unfolding process. This amplification occurs because each new iteration can reintroduce and reinforce the statistical noise from the previous iterations, which would add stronger belief on treating the noise as signal and can progressively overfitting towards these fluctuations. Consequently, the unfolded result can exhibit increased statistical uncertainty built up from the cumulative effect of the iterations used.

To find the optimal balance between minimising bias and controlling statistical uncertainty, several tests were performed to determine the ideal number of iterations to unfold the $m_{\ell\ell}$ distribution from the measured data.

Before showing the result, let's first define a measure for the bias and the source of the statistical uncertainty used in this test. The bias is evaluated from using a combination of lineshape variations mentioned in section 4.6.5 and the process stack composition variations mentioned in section 4.6.7, where the bias measure is defined by the following equation:

$$\mathrm{Bias}_{\mathrm{bin},i} = (U_i - P_i)/P_i \tag{4.6.13}$$

The equation essentially defines bias as the ratio difference between the unfolded and the particle-level results, where U_i is the unfolded yield and P_i is the corresponding particle-level yield. The statistical uncertainty here is derived from the method discussed in section 4.6.3.

To compare the bias to the statistical uncertainty induced and to account for scenarios where a reduced bias is solely due to unlimited sacrifices from the statistical uncertainty, the *bias significance* variable is used, and is defined as the bias divided by the statistical uncertainty for a given number of unfolding iterations:

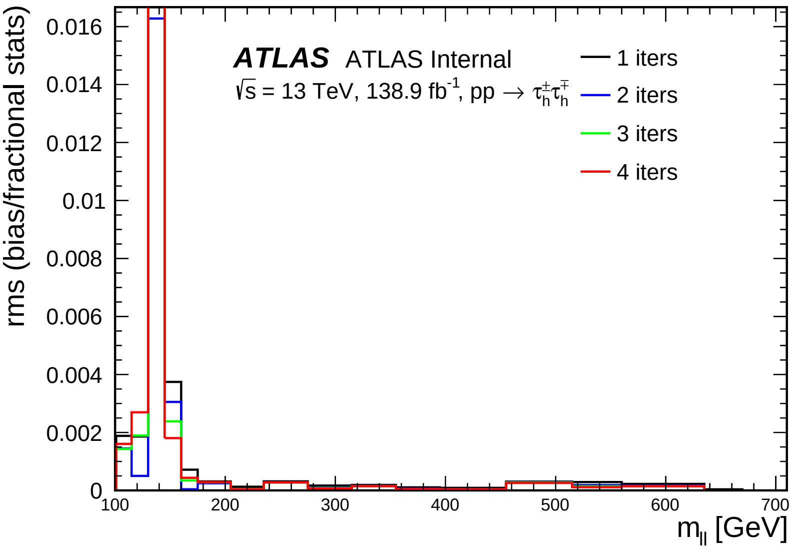

Figure 4.30: RMS combined bias significance for the $m_{\ell\ell}$ distribution

$$\text{Bias Significance}_{\text{bin},i} = \text{Bias}_{\text{bin},i}/\Delta P_i \qquad (4.6.14)$$

The bias significance was determined for each of the lineshape variations and process-composition variations scenarios and the RMS of the bias significance is taken across all the variations.

The result of the RMS combined bias significance is shown in figure 4.30. As can be seen in the plot, the fact that the bias significance across the bins are all very small and being insensitive to the number of unfolding iterations. This seems suggests that a low number of iterations is sufficient to unfold the $m_{\ell\ell}$ distribution. However, if solely looking at figure 4.30, which shows the values of bias significance defined in equation 4.6.14, the reason of having low bias significance difference between different number of iterations remains obscure and different causation could results in different conclusions, such that one can use more iterations to reduce the bias further if the statistical uncertainty is fairly consistent, or vice versa. Therefore, to further confirm the best number of iterations to use, the size of the bias and statistical uncertainty are individually compared in figure 4.31 and the decision on the hyper-parameter is partially made based on the individual changes of each component.

Figure 4.31 shows that, as a function of the number of iterations, the statistical uncer-

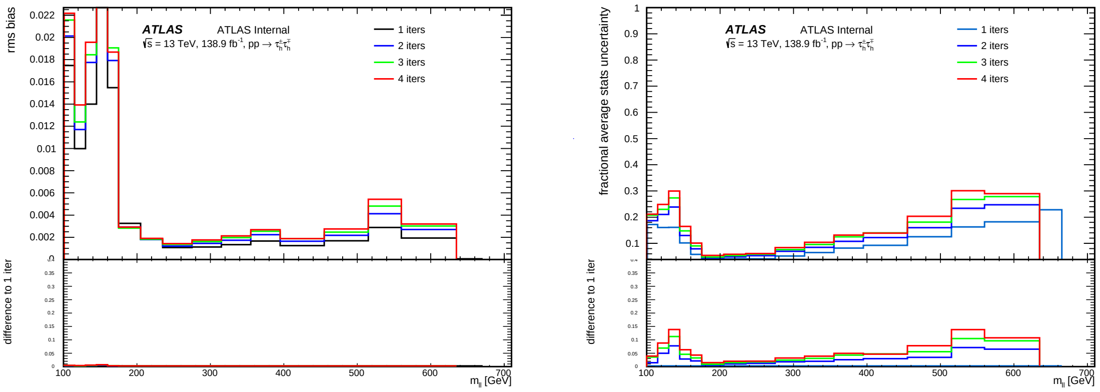

(a) (b)

Figure 4.31: Figure (a) RMS bias ratio comparison where the bottom ratio panel is showing the ratio using one iteration result as the baseline for the $m_{\ell\ell}$ distribution. Figure (b) Fractional statistical uncertainty comparison between the number of iterations. The ratio panel of the plots are deliberately set to the same scale to show how insignificant the changes in bias are, comparing to the changes in statistical uncertainty with respect to the varying number of iterations used.

tainty increases more rapidly than any changes in the residual bias across the bins. This trend suggests that keeping the statistical uncertainty at minimum should be more prioritised over trying to suppress the level of bias, particularly when the bias stabilises or changes only marginally with additional iterations as shown in the figure. In fact, for some bins, the bias already reaches a minimum at one iteration. This indicates that a single iteration effectively shifts the result away from the prior and closer to the data, removing much of the prior-induced bias without yet amplifying statistical fluctuations through overfitting.

However, beyond one iteration, further updates begin to overcorrect small features in the input distribution. These can include the statistical fluctuations that are not representative of genuine structure in the data, which introduces spurious features and increases both the variance and residual bias relative to the true distribution in closure tests. Therefore, purely based on Figure 4.31, one iteration yields the smallest statistical uncertainty and provides an initial indication of optimal unfolding performance.

Nonetheless, it is worth noting that strictly speaking, a single iteration is not quite being *iterative*, and therefore does not fully utilise the iterative Bayesian unfolding algorithm's refinement mechanism. To provide a more quantitative assessment, a

χ^2 test was performed to compare the unfolded distributions from different iteration counts against the underlying MC truth distributions used in closure tests. The test statistic is computed as the sum of the squared differences between the unfolded and truth values, divided by the number of bins (degrees of freedom). The resulted χ^2/dof values for iterations [1, 2, 3, 4, 5] are: [5.91, 3.01, 3.05, 2.64, 2.41]. These results indicate a substantial improvement when increasing from one to two iterations, with diminishing returns thereafter. The two-iteration result shows significantly reduced residual bias while maintaining relatively low statistical uncertainty and importantly, reflects a proper application of the iterative Bayesian unfolding method.

In conclusion, based on the combined evidence from bias-vs-uncertainty behaviour and the χ^2 performance metric, two iterations strike a well-motivated balance between bias suppression, statistical stability, and methodological robustness. Therefore, the unfolding procedure in this analysis adopts two iterations as the default configuration. This choice was also discussed during ATLAS internal meetings, where an agreement was reached to proceed with two iterations.

4.6.9 $m_{\ell\ell}$ spectrum shift test

In addition to the tests described above, another effective test was also performed to further validate the unfolding process. In this test, the $m_{\ell\ell}$ spectrum was shifted by 2 GeV mass on a event-by-event basis. This would introduce a significant bias, as it effectively suggests that the $m_{\ell\ell}$ spectrum has been shifted to the right by 2 GeV, which would significantly affects the corresponding bin efficiencies and migrations. A successful closure between the shifted truth-level spectrum and the unfolded result using the nominal response would suggests that the unfolding process is robust and capable of handling scenarios with extreme biases. In the absence of new detector simulation for this shifted spectrum, the ratio between the shifted lineshape and the nominal lineshape was then used as a reweighting function and applied to the nominal reconstruction-level spectrum. The reweighted reconstruction-level distribution was then fluctuated to create the pseudodata used for this unfolding test, which in turn was unfolded with the nominal SM response matrix. An example of the comparison between the reweighted truth-level and the unfolded distribution from the corresponding pseudodata is shown in figure 4.32.

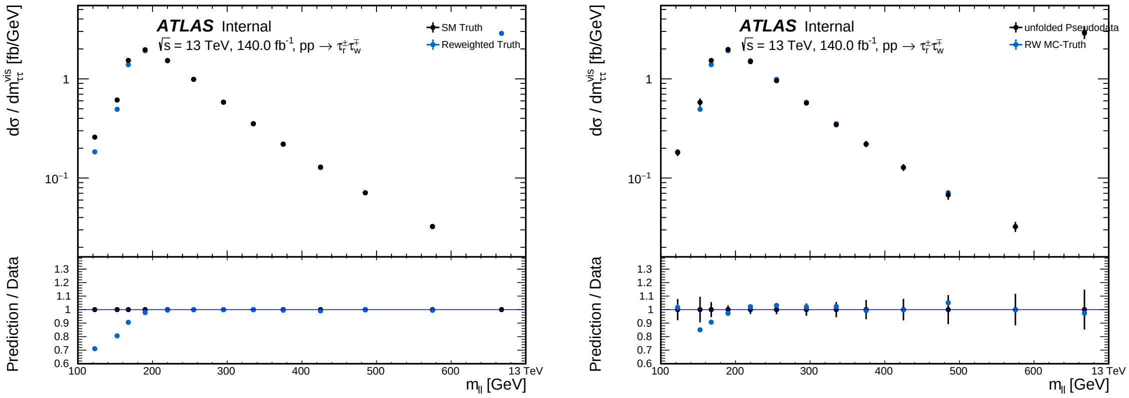

(a) (b)

Figure 4.32: (a) The 2 GeV shifted truth compared to the nominal MC truth prediction. (b) The unfolded result obtained from using the nominal reconstruction-level distribution that reweighted by the ratio between the 2 GeV shifted truth and the nominal truth as the pseudodata, compared to the 2 GeV shifted truth.

Figure 4.32 (b) shows a good closure result between the unfolded distribution and the $m_{\ell\ell}$-shifted truth distribution.

4.6.10 Hidden observable modelling studies

To effectively apply the iterative Bayesian unfolding method to data using a response matrix, the observable under consideration must be reduced to a lower-dimensional representation; such as the invariant di-lepton mass distribution used in this measurement. As a result, the response matrix's dependencies on observables that are not unfolded, which referred as the hidden observables are not explicitly accounted for in the unfolding procedure. This omission may introduce biases into the unfolded results if the hidden observables significantly affect detector response.

In this study, the transverse momentum of the di-lepton system $p_{\mathrm{T}}^{\ell\ell}$ was treated as the hidden observable. The test involved reweighting the $m_{\ell\ell}$ spectrum using bin-by-bin scale factors obtained from comparing the $p_{\mathrm{T}}^{\ell\ell}$ reconstruction-level distribution to the unblinded $p_{\mathrm{T}}^{\ell\ell}$ data. Although $p_{\mathrm{T}}^{\ell\ell}$ is not directly targeted by the unfolding process in this analysis, it is sensitive to detector resolution and acceptance. By reweighting based on the $p_{\mathrm{T}}^{\ell\ell}$ distribution, this test evaluates whether potential biases associated with $p_{\mathrm{T}}^{\ell\ell}$ affect the unfolded $m_{\ell\ell}$ result.

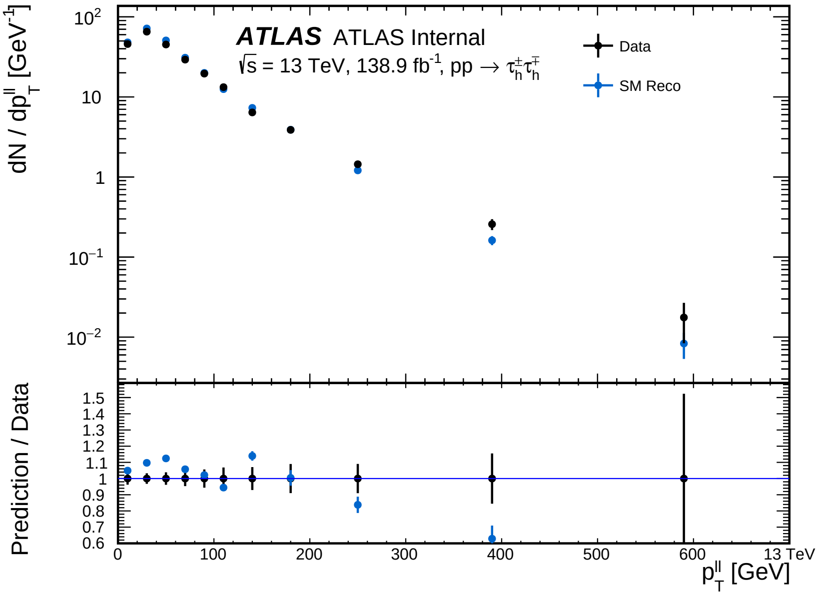

Figure 4.33: The reconstructed $p_{\mathrm{T}}^{\ell\ell}$ distribution compared to the measured data. Some deviations are observed between the simulated distribution and the measured data.

For each bin of the $p_{\mathrm{T}}^{\ell\ell}$ distribution, the ratio between the data and the reconstruction-level distribution was determined and applied to the truth-level MC events on an event-by-event basis to generate a reweighted $m_{\ell\ell}$ spectrum that encodes $p_{\mathrm{T}}^{\ell\ell}$-induced biases. After introducing the statistical fluctuations, the resulting spectrum was treated as pseudodata for unfolding.

Modelling $p_{\mathrm{T}}^{\ell\ell}$ is challenging and often exhibits noticeable discrepancies between MC simulations and real data [138], as illustrated in Figure 4.33. The test was designed to evaluate whether such mis-modeling affects the unfolded $m_{\ell\ell}$ result. If the unfolded result derived from this pseudodata remains stable and is statistically consistent with the underlying truth histogram reweighted by the $p_{\mathrm{T}}^{\ell\ell}$-to-data ratio, it would indicate that the current unfolding setup for the $m_{\ell\ell}$ spectrum is unlikely to heavily depend on the hidden observable or sensitive to potential mis-modellings. This is given by that the $m_{\ell\ell}$ MC simulation is typically more precise than $p_{\mathrm{T}}^{\ell\ell}$ as the invariant mass of the di-lepton system is a relatively straightforward observable that primarily depends on the energies and momenta of the leptons. Therefore, if this test shows good closure, it suggests that the unfolding process is reliable for the $m_{\ell\ell}$ distribution.

By using the reweighting factors derived from Figure 4.33, the effect of the reweight-

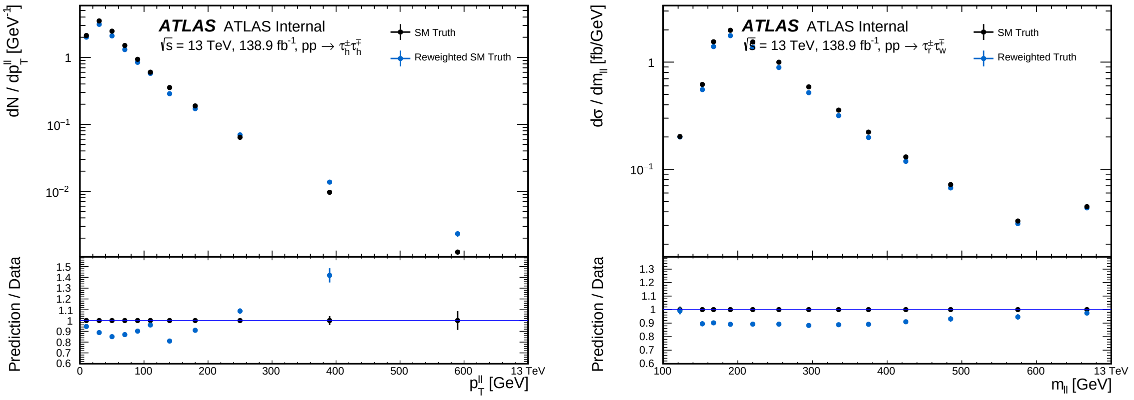

(a) (b)

Figure 4.34: (a) The reweighted truth-level $p_{\mathrm{T}}^{\ell\ell}$ distribution compared with the SM truth-level predictions. Although in a perfect world, these truth-level distributions should have matched, but in reality, these are not expected to be matched, given that the scale factors are derived from detector-level comparisons. (b) The reweighted truth-level $m_{\ell\ell}$ distribution compared to the SM truth-level predictions. As one would expect, the reweighted SM truth distribution created is having visible deviations to the SM truth across the spectrum.

ing factors applied onto the $p_{\mathrm{T}}^{\ell\ell}$ distribution and the corresponding resulted $m_{\ell\ell}$ truth-level distribution are shown in figure 4.34.

The reweighted reconstruction-level distribution are also compared to the measured data to check the effect of reweighting and then unfolded with nominal response matrix. The results are shown in Figure 4.35

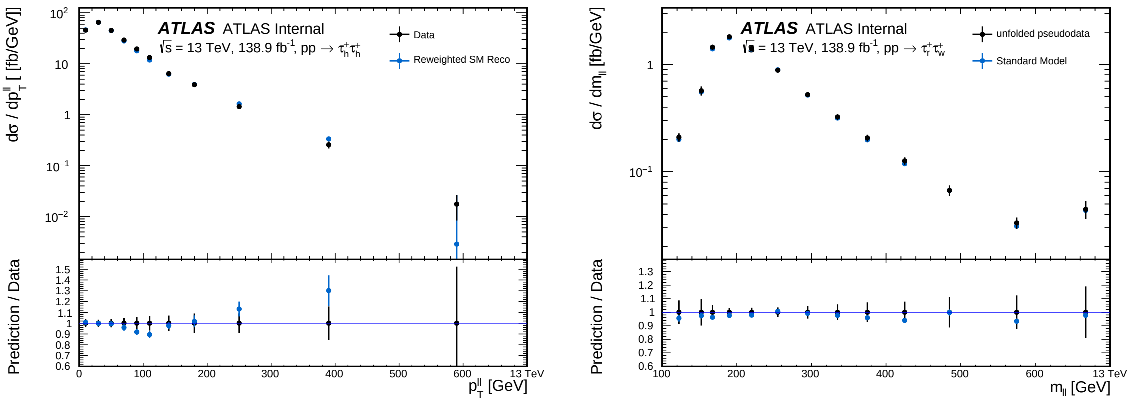

(a) (b)

Figure 4.35: (a) The bin-by-bin reweighted $p_{\mathrm{T}}^{\ell\ell}$ reconstruction-level distribution compared to the measured data. (b) The unfolded reweighted pseudodata compared to the corresponding reweighted SM truth.

According to Figure 4.35 (b), the fact that the closure still reach a good level of agreement indicates that the unfolding system would be able to recover the corresponding underlying truth from the measured data. This suggests that the current unfolding setup will not be significantly impacted by $p_{\mathrm{T}}^{\ell\ell}$-related biases and can tolerate realistic levels of mismodelling in this hidden observable, as shown in Figure 4.33. This reinforce that the unfolding response is not heavily affected by the hidden observable biases and can handle the relatively strong level of disagreement between the MC and data well.

4.6.11 Data-driven closure test

For this test, the MC $m_{\ell\ell}$ distribution is reweighted to the unblinded data to make the detector-level prediction more accurately reflects the measured data. Reweighting factors are derived from the data-to-MC ratio for each bin, and these factors are applied to the MC $m_{\ell\ell}$ distribution on an event-by-event basis again. The resulting reweighted reconstruction-level distribution is then unfolded using the nominal response matrix. The difference between the unfolded result and the corresponding reweighted MC truth distribution is used to estimate the systematic uncertainty of the unfolding method. The test results, as shown in Figure 4.36 demonstrates a good closure.

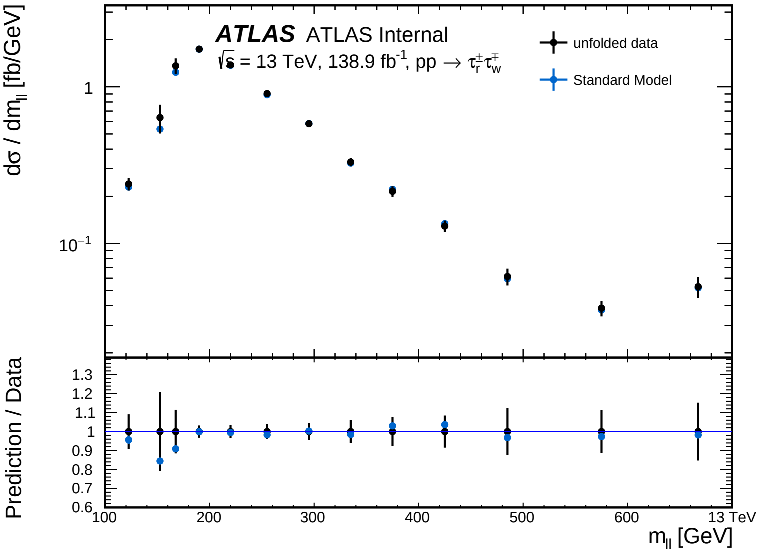

(a)

Figure 4.36: The unfolded result from using the data-driven reweighting reconstruction-level input is compared to the corresponding reweighted truth. Error bars are statistical uncertainty only.

The successful results from various unfolding closure tests conducted under different scenarios presented in this section have demonstrated that the unfolding setup can recover the corresponding particle-level spectrum of the measured data using two iterations. Also, the results indicate that the unfolding process is robust against statistical uncertainties and different types of potential mis-modellings, and at the same time, having a manageable level of bin migrations and no significant dependency on the initial prior distribution. This non-prior dependent characteristic suggests that the unfolded distribution is unlikely to be biased towards the SM predictions, and is able to maintain sensitivity to potential BSM signals in the measured data.

4.7 Measurement uncertainty estimation

Several sources of uncertainties are considered to conclude the analysis uncertainty. The uncertainties can be broadly classified into several categories and are briefly introduced in table 4.5

Table 4.5: A summary of the sources of uncertainties in the Analysis for the unfolded $m_{\ell\ell}$ distribution.

Source of Uncertainty	Description
Modelling	These include the variations of theoretical predictions for contributed production processes as mentioned in section 4.3.1. Multiple alternative samples from different MC generators were used to generate the same process to account for the PDF uncertainties, parton shower uncertainties, etc.
Experimental	This corresponds to knowledge of the experiment apparatus being imperfect, including the ATLAS detector, LHC beam conditions, object reconstruction and final-states identification. These limitations contribute experimental uncertainties in areas such as the luminosity, trigger efficiency, energy resolutions, pile-up, energy scale uncertainties, etc.
Non-fiducial backgrounds	The jet-faking τs are estimated through a data-driven approach (fake factor) as mentioned in section 4.4, and was removed from the opposite-sign signal region. The uncertainty of the estimated fakes also give rise to an ineligible amount of uncertainty to the final unfolded result and the detector-level fit.
Statistical	This is resulted from the nature of doing statistical analysis with sampling. The imperfect closure in the statistical fitting and the statistical fluctuations originated from the unfolding procedures were described in section 4.6.3.
Unfolding systematic	The systematic uncertainty originated from using the iterative Bayesian unfolding method is estimated as described in section 4.6.11.

In this section, the different sources of uncertainties listed in table 4.5 are reported in details.

Modelling uncertainties

The modelling variations for the Drell-Yan, $t\bar{t}$, single top production processes were considered through variations in the MC generators configurations. The MC sample with the highest statistic precision is used as the nominal sample. Each process is also modelled with *alternative* MC sample(s) that differ from the nominal sample in terms of matrix element calculation, parton shower, parameters settings, etc. For each of the alternative sample, a two-point method was employed: the nominal MC stack of all signal processes is replaced by each alternative sample one at a time. The substituted stack is then compared with the nominal stack to calculate the relative difference which corresponds to the modelling uncertainty of the particular substitution.

The sample alternatives used for the two-point approach to find the modelling-uncertainties are mostly described in section 4.3.1. Below is the full list of modelling uncertainties considered on the dominant processes:

- $t\bar{t}$ ***h_damp* variations**: This uncertainty arises from the hardness of the first emission in `POWHEGBOX` matching as mentioned is section 4.3.1. The uncertainty is derived from comparing the nominal sample with parameter α_s(ISR) = h_{damp} = 3·m_t = 517.5 GeV to the alternative sample having it set to 1.5·m_t = 258.75 GeV.
- $t\bar{t}$ **matching/merging scheme**: Difference in matching and merging schemes is probed by comparing the nominal sample `POWHEG + PYTHIA8` (discussed in section 4.3.1) to a sample simulated using `PYTHIA8` [87] with p_{T}(hard) = 1 [95], where the transverse momentum of the hard process is normalised to a unit value to simplify theoretical calculations and comparison to data.
- $t\bar{t}$ **parton-shower model**: The difference in $t\bar{t}$ parton-shower modellings are derived from comparing the nominal sample using `PYTHIA8` [87] for showering and an alternative sample using `HERWIG7` [86] for showering instead.
- $t\bar{t}$ **/ single top interference scheme**: The difference in the *Diagram Removal* (DR) scheme [127] and *Diagram Subtraction* (DS) [127, 119] approaches as mentioned in section 4.3.1 are obtained from comparing the Wt production samples with DS and those with DR. The DR removes specific Feynman diagram contribution to both the matrix element and the parton shower, where the DS modifies the matrix element to account for the parts already included in the parton shower.

- **single top parton-shower model**: The nominal `POWHEG + PYTHIA8` [139, 87] sample, used to simulate the single top process in both s- and t- channel is compared to a `POWHEGBOX + HERWIG7` [139, 86] sample modelled with an alternative parton shower modelling. The samples are described in section 4.3.1
- **Drell-Yan di-τ production modelling**: The impact of differences in the matrix element calculation and parton shower modelling for the Drell–Yan process is assessed by comparing the nominal `SHERPA2.2.11` [88] sample to an alternative sample generated using `POWHEG+PYTHIA8` [139, 87]. Sample descriptions are in section 4.3.1.

The **stack composition** uncertainty considered for the unfolding measurement was estimated by allowing individual processes to float within respective scale uncertainty band (10%). The detailed descriptions are in section 4.6.7.

An **unfolding method** systematic uncertainty is added and was estimated from using the difference between reweighted MC truth and corresponding unfolded result. The procedures are described in section 4.6.11. This uncertainty assesses the potential bias resulted from using the iterative Bayesian unfolding method with two iterations.

To estimate the total modelling uncertainty, the relative differences from each modelling variation are treated as independent and uncorrelated sources. These are then combined in quadrature, providing a conservative and robust estimate of the total uncertainty. This approach accounts for the fact that different modelling effects can shift the prediction in different directions, and ensures that the overall uncertainty reflects the combined impact of all considered variations.

Experimental uncertainties

The accuracy and reliability of the results from the ATLAS experiment depend heavily on accounting for experimental uncertainties. These uncertainties are carefully analysed by considering various components of the experiment. The Combined Performance (CP) uncertainties encompass all types of uncertainties arising from the integrated performance of these components.

The uncertainties considered in the analysis were related to the objects used to define the observables and the signal regions: The τ_{had}, electrons, muons, hadronic jets, and b-jet (for later stages of the measurement). The ATLAS CP groups provide a list of recommended object reconstruction uncertainties for these objects, which are all applied through the analysis framework. The list below illustrates the categories of the uncertainties considered.

– **luminosity**: The uncertainty in the integrated luminosity would affect the total extracted cross-section. The integrated luminosity along with the flat uncertainties for the Run 2 2015-2018 datasets is $139\mathrm{fb}^{-1} \pm 0.83\%$ [140]. This uncertainty was derived based on a calibration of the luminosity scale using $x - y$ beam separation scans, where the methodology is described in details in reference [141], and using the LUCID-2 detector for the baseline luminosity measurements [142].

– **τ_{had} leptons**: Due to the short lifetime of the τ lepton, its decays produce a variety of final states, making both energy measurement and identification particularly challenging. As a result, uncertainties related to the Tau Energy Scale (TES) and the simulation-to-data efficiency corrections for hadronically decaying taus (τ_{had}) are taken into account. These corrections account for differences in particle identification efficiency between simulation and real data. The TES uncertainty is estimated through a calibration procedure using Z boson decays to τ pairs in the semi-leptonic mode [143]. In this method, the reconstructed visible mass of the di-τ system in simulation is compared to that in data to determine appropriate TES corrections. The τ_{had} identification efficiency correction is evaluated using the Tag-and-Probe method [143], also applied to semi-leptonic $Z \to \tau\tau$ events. In this setup, the hadronic τ serves as the probe, while the leptonically decaying τ is used as the tag. The efficiency of the probe tau identification is calculated as the ratio between the number of identified probe τ and the number of tag-probe pairs. This efficiency is measured independently in both data and simulation, and the ratio between them defines a scale factor. This scale factor is applied to simulated events to correct for any mismodelling in τ_{had} identification efficiency.

Lastly, the trigger efficiency uncertainties associated with τ_{had} are also included. These arise due to possible mismodelling in the trigger performance between data and simulation, and are derived using data-driven methods. The corresponding scale factors and their uncertainties are applied to simulated events to reflect the real trigger performance in data. These uncertainties are propagated through to the final result and are particularly important in the hadronic decay channel where tau triggers are a key component of the event selection.

- **mis-identified τ_{had} candidates**: This is essentially the fake uncertainty that detailed in section 4.4. The uncertainties on the τ_{had} candidates mis-tagging rates for the quark, gluon, and pileup-enriched hadronic jets, and the corresponding uncertainties in the fractions of each jet type in the analysis signal region are considered.
- **electron reconstruction and identification**: Uncertainties on the electron momentum and identification efficiency corrections are also considered for the preparation of the future $\ell + \tau_{\text{had}}$ channel analysis. This uncertainty component is automatically removed for the $\tau_{\text{had}}\tau_{\text{had}}$ channel measurement as there are not light lepton final states involved.
- **muon reconstruction and identification**: Uncertainties on the muon momentum and identification efficiency corrections are kept in the analysis framework, but ignored for the same reason as the electron-related uncertainties for the $\tau_{\text{had}}\tau_{\text{had}}$ channel measurement.
- **jet reconstruction**: These are uncertainties correspond to the jet energy scale (JES), resolution and Jet Vertex Tagging (JVT) efficiency corrections as described in section 3.3.6. With the finite resolution of the detector, this source of uncertainty were analysed from calibrations to understand the detector response, and adds non-negligible contributions to the hadronic channel measurement as the decay products from the τ_{had} candidates can form jets. The JVT score for the jets are used to distinguish between jets from hard-scattering

processes and pile-up interactions. The use of the JVT method improve the purity of jets associated with the primary hard-scattering vertex by rejecting the jets likely from the pile-up events, but would introduce systematic uncertainties arise from modelling of the track and vertex properties, difference between data and simulation, etc.

- **b-jet identification**: These uncertainties are associated to the b, c and light jet tagging rate corrections. The unfolded measurement did not apply this uncertainty and were only used for the search component.

Experimental uncertainties pruning

A total of around 260 Combined Performance (CP) recommended experimental systematic uncertainties are considered in the analysis. They are grouped into categories as outlined in the introduction of section 4.7. However, not all of these uncertainties contribute significantly to the total systematic uncertainty. In fact, many are found to have a negligible impact on the final result and can be safely excluded from further consideration. To identify these uncertainties, a pruning procedure was carried out to reduce the computational loads of running the simulation jobs.

The pruning process is performed both before and after the unfolding. The union of the remaining uncertainties from the two pruning procedures are then kept and included in the final uncertainty calculations. The criterion for rejecting a systematic uncertainty is that its relative significance must be less than 10% of the corresponding relative statistical uncertainty across all bins of the $m_{\ell\ell}$ spectrum.

For the pre-unfolding pruning, the check was performed at the reconstruction-level and the statistical uncertainty on the expected number of events is given by the Poissonian approximation $1/\sqrt{N}$, with N being the number of MC generated event in the bin.

For the post-unfolding pruning, the check primarily investigated whether a systematic variation in the distribution used as the pseudodata input for the unfolding system would significantly affected the unfolded truth-level distribution. In this case, the statistical uncertainties used here were derived again from the 2 000, pseudo-experiments as mentioned in section 4.6.3. The average of the unfolded results from the systematically varied pseudodata at $+1\sigma$ and -1σ was obtained and compared to the average unfolded result to find the relative difference. Lastly, this relative difference was then compared to the statistical uncertainty derived from the 2 000 toys. The same 10% threshold as described earlier was used to filter out the systematic uncertainties that contribute negligible effects to the unfolded result relative to the internal statistical uncertainties. The study was performed for both the $\tau_{\text{had}}\tau_{\text{had}}$ and $\ell + \tau_{\text{had}}$ channels, and a total of 69 remaining experimental uncertainties are included in the analysis. The pruning impact on the total uncertainty is negligible both before and after the unfolding. The plot in Figure 4.37 shows the ratio of different CP uncertainty groups before and after pruning at post-unfolding stage.

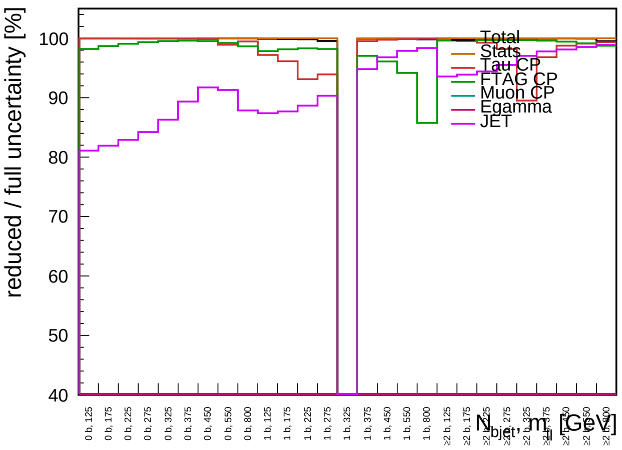

(a) $\tau_{had}\tau_{had}$ region

Figure 4.37: Ratio between the uncertainties before and after pruning on the MC $m_{\ell\ell}$ distribution with b-jet multiplicity after the unfolding. The drop in the middle was due to an empty bin.

The union of the experimental uncertainties surviving the pruning before and after the unfolding is listed below for each reconstructed object.

Muon uncertainties

- Resolution:
    - ∗ MUON_ID
    - ∗ MUON_MS

    - MUON_SAGITTA_RESBIAS
- Energy scale:
    - MUON_SCALE
- Reconstruction:
    - MUON_EFF_RECO_STAT
    - MUON_EFF_RECO_SYS
- Isolation:
    - MUON_EFF_ISO_SYS
- Track to vertex association:
    - MUON_EFF_TTVA_STAT
    - MUON_EFF_TTVA_SYS

Electron uncertainties

- Energy scale:
    - EG_SCALE_ALL
- Reconstruction:
    - EL_EFF_Reco_SIMPLIFIED_UncorrUncertaintyNP8
- Isolation:
    - EL_EFF_Iso_SIMPLIFIED_UncorrUncertaintyNP[8|17]

Tau uncertainties

- Energy scale:
    - TAUS_TRUEHADTAU_SME_TES_DETECTOR
    - TAUS_TRUEHADTAU_SME_TES_INSITUEXP
    - TAUS_TRUEHADTAU_SME_TES_INSITUFIT
    - TAUS_TRUEHADTAU_SME_TES_MODEL_CLOSURE
    - TAUS_TRUEHADTAU_SME_TES_PHYSICSLIST

- Reconstruction:
  - TAUS_TRUEHADTAU_EFF_RECO_TOTAL
- Identification:
  - TAUS_TRUEHADTAU_EFF_RNNID_1PRONGSTATSYSTPTGE40
  - TAUS_TRUEHADTAU_EFF_RNNID_3PRONGSTATSYSTPTGE40
  - TAUS_TRUEHADTAU_EFF_RNNID_HIGHPT
  - TAUS_TRUEHADTAU_EFF_RNNID_SYST
- Trigger:
  - TAUS_TRUEHADTAU_EFF_TRIGGER_STATDATA[2016|161718]
  - TAUS_TRUEHADTAU_EFF_TRIGGER_STATMC[2016|161718]
  - TAUS_TRUEHADTAU_EFF_TRIGGER_SYST[2016|161718]
- Electron veto and overlap removal:
  - TAUS_TRUEELECTRON_EFF_ELEBDT_STAT
  - TAUS_TRUEHADTAU_EFF_ELEOLR_TOTAL

Jet uncertainties

- Energy scale:
  - JET_EffectiveNP_Mixed2
  - JET_EffectiveNP_Modelling[1|2|3]
  - JET_EffectiveNP_Statistical2
  - JET_EtaIntercalibration_Modelling
  - JET_EtaIntercalibration_NonClosure_2018data
  - JET_EtaIntercalibration_TotalStat
  - JET_Pileup_Offset[Mu|NPV]
  - JET_Pileup_RhoTopology
- Energy resolution:
  - JET_JER_DataVsMC_MC16

    - JET_JER_EffectiveNP_[1-11|12restTerm]
- Flavor:
    - JET_Flavor_Composition
    - JET_Flavor_Response
- Flavor tagging:
    - FT_EFF_Eigen_B_[1|2|3]
    - FT_EFF_Eigen_C_0
    - FT_EFF_Eigen_Light_[0|1|2]
    - FT_EFF_extrapolation
    - FT_EFF_extrapolation_from_charm

fakes uncertainties

As discussed in section 4.4.1, the estimation of jet-faking τs utilised the fake factor method, which involves using estimated fake factors and fitting onto primitive templates to extract the correct contributions (α factors) from different sources to find the combined fake factor. Therefore, the process would contribute to the total uncertainty in such ways:

- uncertainty related to the statistics of the primitive templates.
- uncertainty related to the statistics of the primitive fake-factors.
- uncertainty on the template fit parameters.

These uncertainty components are summed in quadrature to obtain the total systematic uncertainty associated to the combined fake factor. Another uncertainty source that is independent to the ones mentioned above is the statistical uncertainty on the number of events in the anti-ID region, which are used in equation 4.4.8 to extrapolate the fakes background. This uncertainty is propagated using the statistical uncertainty on data and MC events to arrive at the statistical uncertainty on the estimated number of events for the fake background, and then combined with the systematic uncertainty from the fakes estimations.

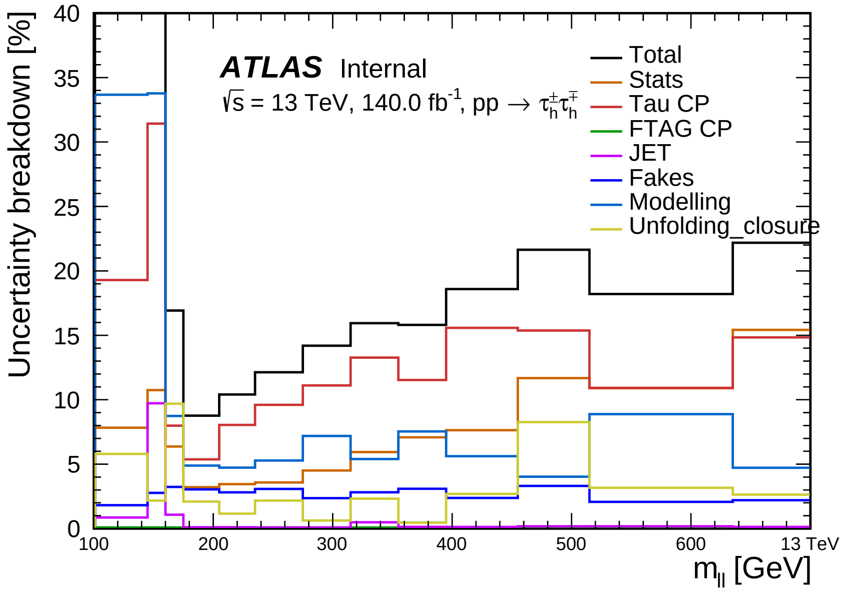

Figure 4.38: The uncertainty breakdown plot illustrating the relative uncertainty contributed from various source of uncertainties.

4.7.1 Combined uncertainty decomposition

The post-unfolding relative uncertainties from all sources are summarised in figure 4.38.

The black curve in figure 4.38 represents the total combined uncertainty of the measurement, calculated by adding in quadrature all individual uncertainty sources shown in the plot. For the $\tau_{\text{had}}\tau_{\text{had}}$ channel's $m_{\ell\ell}$ spectrum, the dominant contributions arise from modelling uncertainties, τ-related experimental uncertainties, and statistical fluctuations across the mass range. Jet- and fake-related uncertainties are subdominant but non-negligible, contributing approximately $1 - 2\%$ to the total uncertainty. In the low-mass region between approximately 100 and 200 GeV, the uncertainty escalated significantly. This is primarily due to the high-p_{T} cut in the analysis selection which sculpted the original shape of the distribution with a steep drop in event yields. Consequently, the reduced statistics and small bin width in this region result in larger relative uncertainties.

4.8 Theoretical uncertainties

- **PDF uncertainties**: The multiweights provided in the MC samples were used to estimate PDF uncertainties (as well as α variations within the PDF). The PDF replicas or eigenvectors are combined using the appropriate prescription for a given PDF family and variation type as implemented in the `LHAPDF` [144] tool. These set of uncertainties are combined for the Drell-Yan and $t\bar{t}$ processes due to their dominant presence in the signal stack.
- **QCD scale uncertainties**: The multiweight technique is again employed to estimate this uncertainty. As described in Section 4.6.7, 7-point scale variations are used to probe the effect of changing the renormalisation and factorisation scales around the nominal Monte Carlo prediction. These variations correspond to combinations where the scale factors are varied individually or simultaneously, with multiplicative factors of 0.5 or 2.0 relative to the nominal configuration of (1.0, 1.0). The resulting uncertainties from these variations are treated as uncorrelated and added in quadrature. The total spread of the variations was found to be approximately 7%, and a conservative uncertainty of 10% is assigned. This uncertainty is applied jointly to the Drell–Yan and $t\bar{t}$ processes, as they dominate the signal composition.

4.9 Inclusive $m_{\ell\ell}$: measured cross-section results

The measured fiducial cross-sections are presented in Table 4.6. The upper row displays the cross-section measured in the fiducial phase space, along with the associated uncertainties discussed in section 4.7. In the lower row, the predictions from different event generators are shown; one uses `SHERPA` at NLO accuracy and the other one uses `POWHEG` interfaced to `PYTHIA8`, also at NLO accuracy. Additionally, a Drell-Yan-only prediction is included, given that the Drell-Yan process dominates the contribution. The theoretical uncertainties associated with the predictions shown in Table 4.6 are a combination of scale and PDF uncertainties.

Overall, the measured fiducial cross-sections from data is in good agreement with both predictions where the quoted errors covers the deviations.

	Full Phase Space
Measured fiducial cross-section [fb]	238.37 ±31.85(syst.) ±12.18(stat.) ±6.88(fakes.) ±34.34(total)
`SHERPA`	247.45 ±32.17
`POWHEG` + `PYTHIA8`	258.61 ±8.14
`SHERPA` **Drell-Yan**	204.10 ±26.68

Table 4.6: The total fiducial cross-sections in the full measured phase space in femtobarns. The measured fiducial cross-section is compared with two particle-level predictions simulated with `SHERPA` and `POWHEG + PYTHIA8`. Since the phase space is dominated by the Drell-Yan contribution, an explicit Drell-Yan prediction from `SHERPA` is also included for comparison.

The unfolded differential cross-section of $m_{\tau\tau}$ in the fully hadronic channel is compared to various MC event generator predictions as shown in figure 4.39. The last bin represents the overflow of the distribution and is treated as an integrated cross-section without bin normalisation. Overall, the central values of the predictions show less agreement with the data at both tails of the spectrum, while there is better agreement in the mid-range of $m_{\ell\ell}$. The pre-peak region exhibits large uncertainties due to the sculpting of the Z-peak distribution, as discussed in section 4.6.7, which leads to the largest differences in the central values between the predictions and the measured data. Generally, the `POWHEG + PYTHIA8` predictions are slightly higher than the `SHERPA` predictions across the spectrum. Despite these differences, the measured data is in good agreement with both `MEPSNLO` and `NLOPS` theory predictions, where all predicted points and unfolded points exhibit overlapping uncertainty bands.

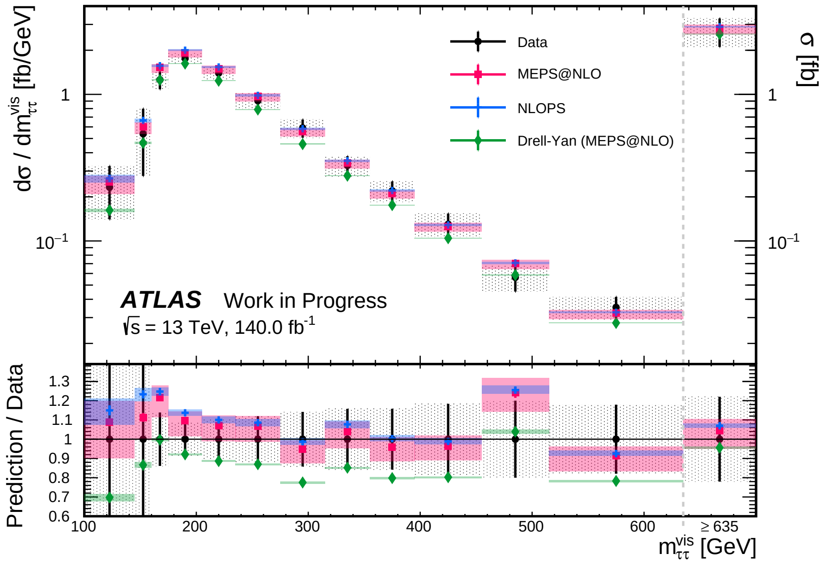

Figure 4.39: Differential cross-section as a function of the di-lepton invariant mass $m_{\ell\ell}$. The upper panel shows the differential cross-section normalised to the $m_{\ell\ell}$ bin sizes, and the bottom panel is showing the ratio of the MC predictions to the measured data. The black dots are representing the unfolded data, and the error bars on the data points are showing the combined uncertainty. The red coloured points are `MEPS@NLO` (`SHERPA`) predictions, the blue coloured points are `NLOPS` (`POWHEG + PYTHIA8`) predictions, and the green coloured points are the `SHERPA` Drell-Yan process only prediction. The different coloured evelopes indicates the total theoretical uncertainties derived from the 7-points scale uncertainties and the pdf uncertainties. The x-axis starts from 100 GeV and extends to 635 GeV, then an overflow bin is shown to represent the integrated cross-section up until the centre-of-mass energy of the LHC collision.

To quantify the level of agreement between the baseline prediction (`MEPS@NLO`) and the data, χ^2 tests are performed on: 1. directly comparing the SM prediction with the observed data, and 2. comparing a data-fitted SM prediction, obtained by minimising the negative log-likelihood using the framework adopted from Ref [145], with the data. The fit is a statistical consistency check between the SM and the data, incorporating information from the data and treating the associated uncertainties as nuisance parameters. Specifically, the main experimental uncertainties on the data and the theoretical uncertainties on the `MEPS@NLO` SM prediction are assigned as nuisance parameters. If the post-fit χ^2 result differs significantly from the pre-fit value, it may indicate that some nuisance parameters were heavily adjusted to better accommodate the data, suggesting potential tension between the prediction and the observation. The χ^2/d.o.f. values for the post-fit and pre-fit results are found to be 3.93/13 and 6.60/13 as shown in Figure 4.40, with the post-fit result showing a modest improvement in agreement, as expected. These results indicate excellent agreement between the predictions and the data.

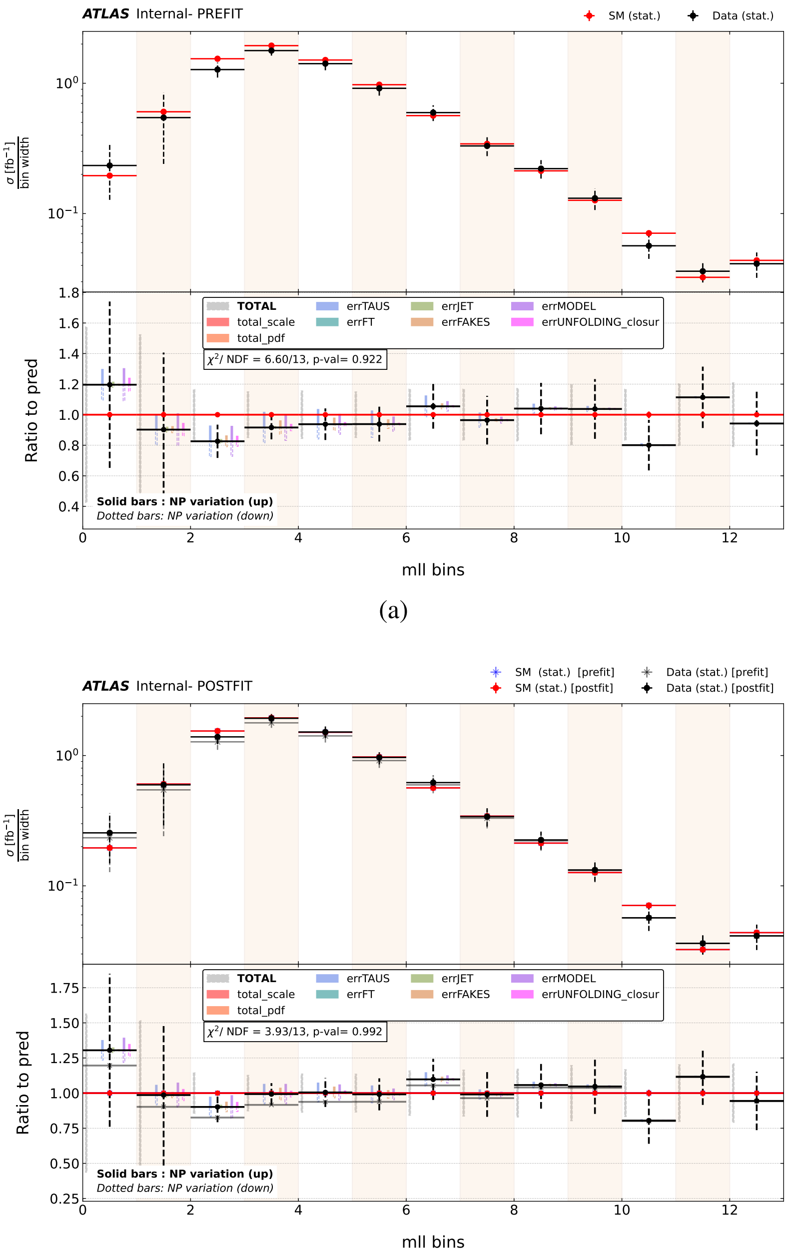

(a)

(b)

Figure 4.40: The fitted distributions of dilepton mass $m_{\ell\ell}$ using the framework from Ref. [145]: (a) SM predictions compared with data pre-fit. (b) SM predictions compared with data post-fit. Plots taken from analysis document [135].

The covariance matrices for the unfolded data are shown in Figure 4.41. The bins are made into equal sizes in the matrix for clarity.

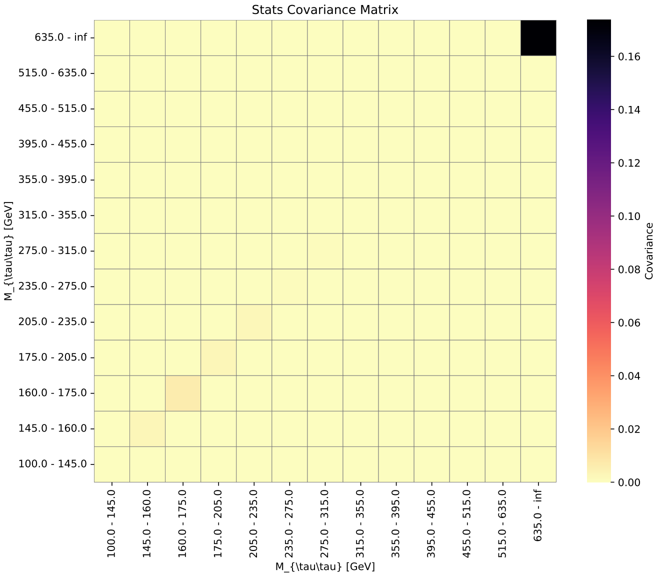

(a)

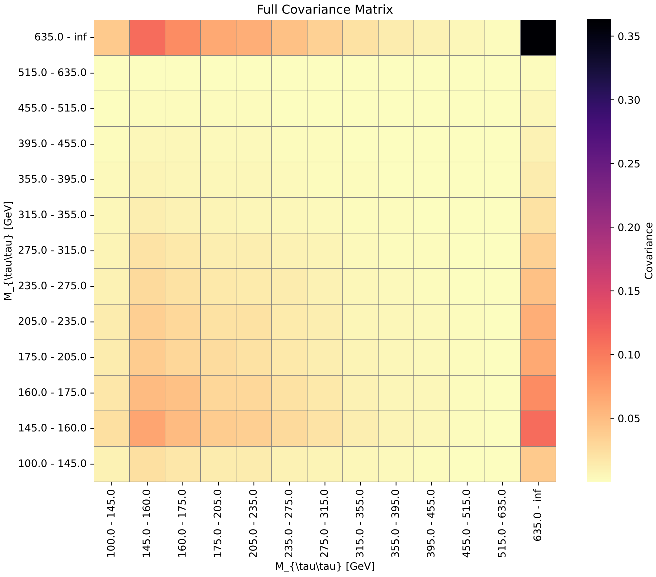

(b)

Figure 4.41: (a) Statistical-only covariance matrix. (b) Full covariance matrix included both statistical and systematics.

Chapter 5

Re-interpretation

In brief, re-interpretation refers to the process of reusing existing measured experimental data and reanalysing it in the context of new or alternative theoretical models. As discussed earlier in this thesis, LHC physics analyses typically fall into two main categories: searches and measurements. The two types of analyses differ in their approach; the searches aim to directly find evidence of BSM physics, treating the SM as the background, and the measurements aim to precisely determine properties of known SM processes, improving our understanding by testing theoretical predictions with high precision. Re-interpretation is especially common in searches for BSM physics, as it allows the exclusion limits or discovery prospects of different models to be continuously updated using newly available theoretical frameworks. While searches are typically more sensitive to targeted new physics signals, they tend to be highly model-dependent and optimised for specific parameter spaces, making it challenging to incorporate their results into updates of SM predictions. Ideally, one could conduct a new search for every new theoretical model using LHC data, but search analyses are computationally intensive and require significant time and resources, whereas new theoretical models can be formulated much more efficiently. The consequence of this situation results an alternative approach of doing model-independent measurements. These measurements are not tailored for any single BSM scenario, but they can be reinterpreted to set constraints on a broad range of models. The main idea of using measurements for re-interpretation is that the presence of new physics would induce deviations in well-measured observables, either directly or indirectly. By analysing potential deviations in the measured distributions, one can scan a variety of BSM models in different parameter spaces and determine whether some parameter regions are already excluded. This scan process of applying existing measurements to constrain new physics models is at the heart of re-interpretation studies and helps maximise the scientific impact of measured LHC data. By systematically identifying which BSM models are worth further investigation (not excluded by current measurements already), re-interpretation efforts can provide directional guidance for future direct searches. A comprehensive discussion on best practices for reinterpretation can be found in the latest LHC Reinterpretation Forum report [146].

This chapter presents the reinterpretation of a minimal third-generation doublet Vector-like Lepton (VLL) model, incorporating the new high-mass $\tau\tau$ measurement described in section 4.9 into the `CONTUR` framework. The theoretical details of the VLL model are reviewed in section 2.5. The chapter begins with an overview of the `CONTUR` methodology, followed by the results of the reinterpretation study with highlighting the impact of the $\tau\tau$ measurement and comparing the constraints obtained with existing ATLAS VLL search limits.

5.1 CONTUR Framework

`CONTUR` (Constraints On New Theories Using `RIVET`) is a tool designed to evaluate how well a new physics model fits within existing SM measurements. The fundamental principle behind `CONTUR` is that any new physics signal would introduce deviations in well-measured SM observables. By using the already published SM measurements, `CONTUR` provides a systematic framework to compare theoretical predictions with experimental results. `CONTUR` operates by predicting the changes of the existing measured observable when a new physics model's effect is introduced and comparing them to the original experimental measurements. If the deviations in a particular parameter space exceed the uncertainty of the measurement, the corresponding model parameters can be excluded, as such deviated signal would have already been observed in the data.

5.1.1 CONTUR Toolkit Structure

CONTUR has multiple functional utilities, and the functions can be summarised into serving two primary functional components:

- **Prediction** - Computes the expected impact of the new physic models on measured SM observables in the specified parameter space.
- **Limit-setting** - Compares the predictions from the **Prediction** step to existing SM measurements and determine the exclusion limit.

A full CONTUR analysis, when starting from scratch (i.e. no existing events samples provided), involves using several external and internal components:

- FeynRules [147] package: A mathematica package that allows physicists to define and implement new physics models upon inputs of Lagrangian, which can then derives the corresponding Feynman rules.
- MC Event Generator: The model from FeynRules [147] is interfaced with event generators for BSM event simulation after being converted into the Universal FeynRules Object [14] (UFO) format. In this study, the `Herwig` [86] event generator was used.
- RIVET [81]: As previously introduced, RIVET is a package that contains a library of analysis routines preserving the structure of experimental results and analysis workflow at the particle level, which ensures accurate comparisons between the BSM+SM and SM distributions.
- CONTUR Method [6]: The likelihood evaluation and exclusion setting process. Results are visualised as heatmaps and exclusion plots.

CONTUR facilitates the prediction of BSM model effects by acting as a wrapper that integrates FeynRules, MC event generation, and RIVET. The BSM model produced in FeynRules is first interfaced to the UFO [14] format to ensure the compatibility with event generators. Before event generation, the free parameter space of the model must be defined so that to enable a grid scan across different parameter values. The `CONTUR` interface automates this process by generating equal number of events for each defined parameter point. It is also important to note that `CONTUR` adapts to the strategy of using inclusive event generation wherever possible, meaning it simulates all possible events within a given process, allowing a broader range of final states to be generated rather than selecting specific final states. This approach aligns with the philosophy of model-independent measurements, which enables a more comprehensive exploration of indirect BSM effects across a variety of observables [6]. Once the events are generated, the `RIVET` [81] package transforms the MC generated events into cross-section histograms using the format information according to the pre-defined structure of each analysis routine and enables evaluations in the later limit-setting step. In standard experimental workflows, analysis teams typically write a `RIVET` routine to capture their analysis fiducial selections and upload measured results onto HEPData [7]. The growing database of `RIVET` routines and HEPData forms the foundation upon which `CONTUR` continuously operates. The complete `CONTUR` toolchain is illustrated in figure 5.1, while a schematic representation of the `CONTUR` workflow is shown in figure 5.2.

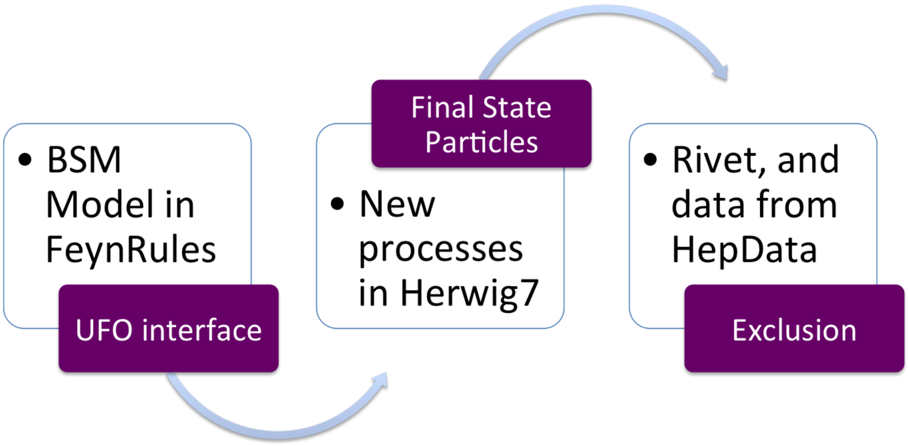

(a)

Figure 5.1: illustration of `CONTUR` toolchain, image from ref [5].

After the events are generated according the grid of user-defined free parameters

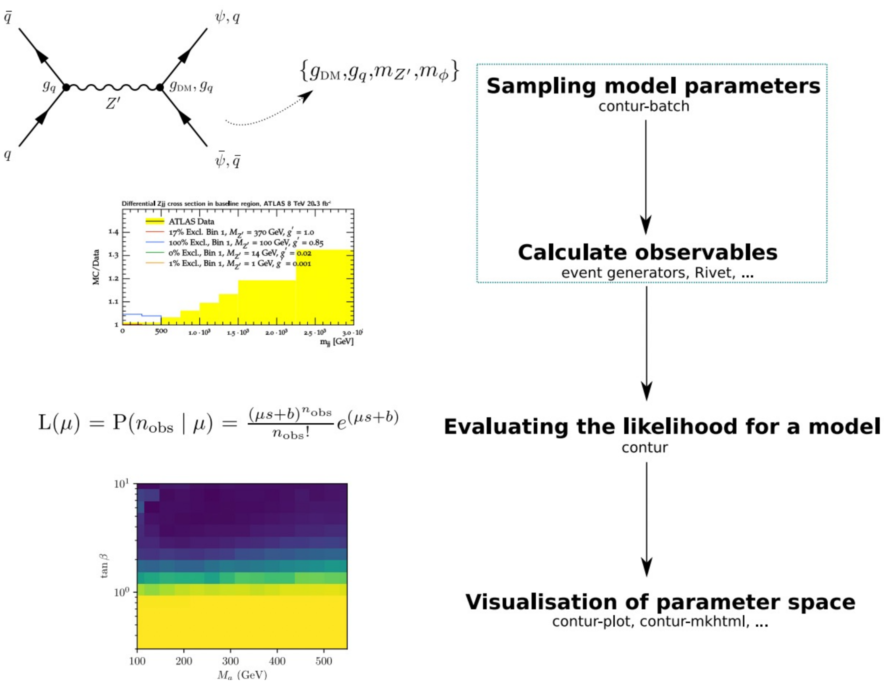

(a)

Figure 5.2: A simplified workflow of using CONTUR to generate exclusion limits. The steps within the dotted box is the prediction function, in which CONTUR act as a wrapper to drive external packages, and the steps outside of the box contributes to the limit-setting function, where the likelihood for the model is evaluated and visualised. Image taken from ref [81].

and processed through the corresponding RIVET routines, the next step involves the limit-setting function. At each grid point, CONTUR evaluates the likelihood of the model by comparing the predicted BSM+SM contributions against the measured SM results. To achieve this, CONTUR categorises a library of measurements, utilising their measured data and their corresponding SM predictions into orthogonal analysis pools based on the final states they probe. The global exclusion limit across the defined parameter space is then determined by selecting the most stringent constraint within each pool, i.e. the largest deviation between the BSM+SM prediction and the SM expectation at each grid point.

As a result, CONTUR provides a systematic approach to determine whether a BSM model has already been excluded (or remains viable) based on existing LHC measurements. A detailed discussion of the statistical methodology and the exclusion-setting procedure can be found in Reference [81] and method section in Ref [148].

5.2 Sensitivity to BSM models

The vector-like Leptons (VLLs) are a hypothetical extension of the SM that introduces new fermionic states with vector-like gauge interactions. Unlike the known chiral SM fermions, which have distinct left-handed and right-handed components under weak interactions, VLLs possess both left and right-handed components transforming identically under the SM gauge group. This property allows them to have a distinct mass term and without the need to acquire mass through the Higgs mechanism. VLL models have been proposed to address several unresolved issues in the SM, including: The origin of neutrino masses, flavour anomalies (B-meson decay), gauge coupling unification, etc.

Among the various VLL models, which differ in their mixing patterns with SM leptons, the high-mass $\tau\tau$ measurement is expected to be most sensitive to third-generation VLLs. This sensitivity arises from their potential mixing with the τ lepton and the possibility of direct or virtual VLL production, which can contribute to decays involving τ final states.

Previous searches have established exclusion limits on the mass of third-generation VLLs, while studies on future high-energy proton-proton colliders have explored the discovery prospects of VLLs mixing with the τ lepton [13]. The theoretical details of VLL models were enclosed in section 2.5. In this section, the impact of the new $\tau\tau$ measurement on the `CONTUR`-based exclusion for third-generation VLLs is discussed and compared to the dedicated search result.

5.2.1 `CONTUR` results and the role of the $\tau\tau$ measurement

The introduction of the VLL doublet model in the previous theory sections showed that the unfolded $\tau\tau$ differential cross-section could serve as a crucial probe in constraining the models' parameter spaces. To assess this sensitivity, a `CONTUR` study was performed, focusing on the simplest doublet VLL model, with the parameter space defined by the VLL mass $M_{\tau'}$ and the mixing parameter ϵ.

For this `CONTUR` scan, the values of $M_{\tau'}$ and ϵ were logarithmically sampled over the ranges of 80 GeV to 3000 GeV and 0.001 to 0.1 respectively. A total of 200 points were sampled and formed into a parameter grid as shown in Figure 5.3. Each of the 40 $M_{\tau'}$ values sampled corresponding to five different values of ϵ. For each of the sampled point, 30,000 events were generated using the `Herwig` [86] MC event generator, parameterised with the respective values of $M_{\tau'}$ and ϵ.

The results of the `CONTUR` scan are presented in Figure 5.3, where the x-axis is the mass of $M_{\tau'}$ and the y-axis being the mixing parameter ϵ. Figure 5.3 (a) shows the confidence-level (CL) region of the scan, where dark-yellow-coloured region indicates the region with CL > 0.95, and the green region indicates the 0.65 < CL < 0.95 range. An important observation from the plot is that the exclusion limit remains almost independent of ϵ, This behaviour is in line with theoretical expectations, as all decay widths scale proportionally to ϵ^2, making the mass parameter $M_{\tau'}$ being the dominant factor in determining the exclusion limits. Figure 5.3 (b) shows the same parameter region as Figure 5.3 (a) but indicates the dominant measurement pools, where each coloured area indicates a specific measurement having a dominant contribution on excluding the parameter space. The colour codes for Figure 5.3 (b) plots are shown at the bottom of Figure 5.3. This plot highlight the dominant contribution from the $\tau\tau$ measurement, which shown by the white-coloured region on the left plot. Previously, this region was mainly constrained by the four-lepton measurements as shown by the right plot in Figure 5.3 (b), but with adding the new high-mass $\tau\tau$ measurement, the exclusion limit has improved.

A comparison between the two plots in Figure 5.3 (b) illustrates the noticeable improvement in the 2σ exclusion limit represented by the vertically solid line. Specifically, the limit of using the SM predictions improved from a previous result shown in reference [149] of excluding $M_{\tau'} \leq 280$ GeV to around $M_{\tau'} \leq 410$ GeV, and the expected limit improved to around $M_{\tau'} \leq 500$ GeV and arrived roughly at the red dotted line shown in the previous dominant pool plot, which indicates the HL-LHC 2σ exclusion limit estimated from method described in ref [150].

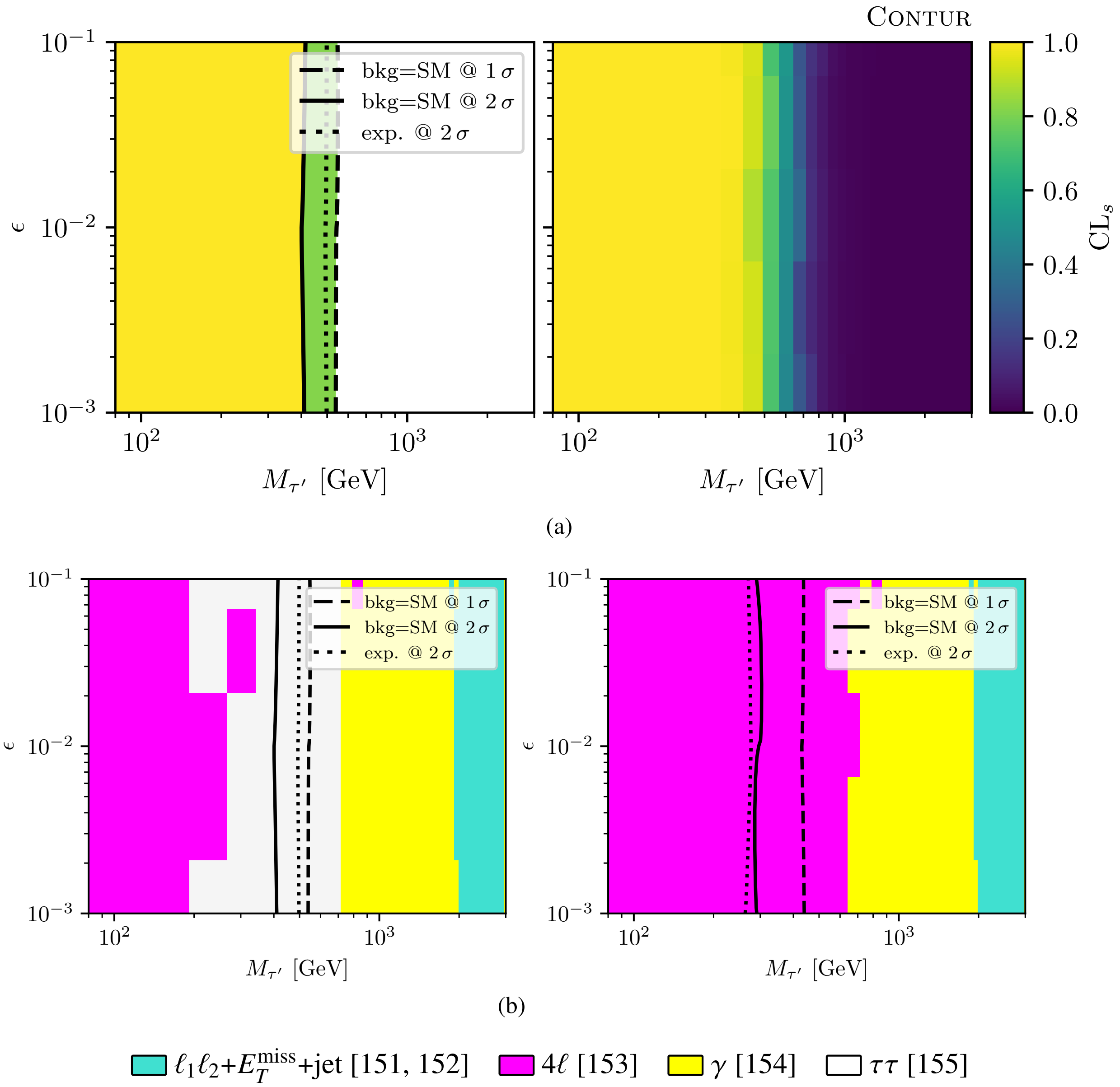

(a)

(b)

Figure 5.3: The `CONTUR` exclusion limits are calculated, where 1 σ and 2 σ represent the 68% CL and 95% CL, respectively. The first two lines (dashed and full lines) in the plot legends show the exclusion limit computed using the SM prediction as the background, while the last line shows expected limit. (a) The hybrid plot, where the left plot shows the exclusion limit. The yellow coloured section indicates the $CL \geq 95\%$ region, and the green section indicates the $\leq 65\%\ CL < 95\%$ region. The right plot shows the heatmap of CLs, granulated for each grid point. (b) The plots indicate the analyses pool that gives the largest exclusion limit for each point. The left plot is the updated dominant pool plot using the new $\tau\tau$ measurement, while the right plot is the previous dominant pool plot result [149] without including the new measurement. The coloured legend with references for each analysis is shown at the bottom.

Compare to ATLAS search results

A dedicated search [156] was done by ATLAS using the run-2 LHC data for this exact third-generation VLL doublet model that was discussed in the section above. The limit plot is shown in Figure 5.4 (a) and was taken from the paper [156].

Since the `CONTUR` study does not generate exclusion curve with respect to cross-section directly, a direct comparison between Figure 5.3 and the limit plot in Figure 5.4 is not straightforward, as the y-axis definitions differ between the two plots. To enable a meaningful comparison, for each of the 5 grid points that has the same $M_{\tau'}$, but with different ϵ setting, the point with the smallest ϵ setting is picked out as it generates the smallest total cross-section among them (although difference is minimal). These points are plotted as a function of $M_{\tau'}$ with the y-axis representing the total cross-section, and the same axis scale and range as Figure 5.4 (a) for easier comparison. The result curve is shown in Figure 5.4 (b).

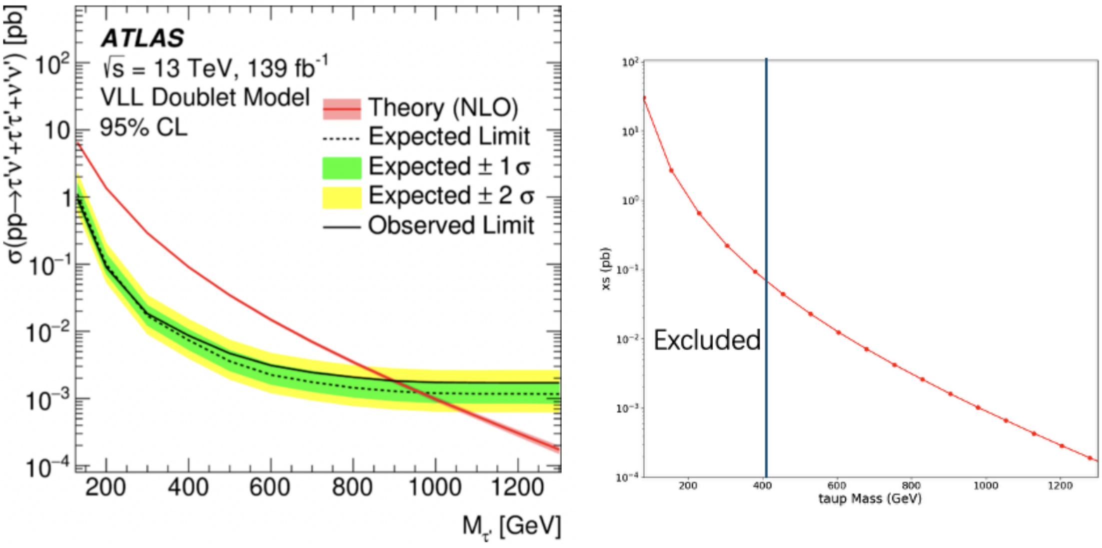

(a) (b)

Figure 5.4: Figure (a) 13 TeV VLL doublet search shows the directly excluded regions based on the cross-sections. The results excluded third-generation $M_{\tau'}$ mass region between 130-970 GeV [156] as the observed cross-section (solid black line) dropped below the the theoretical cross-section (red line). Figure (b) is the cross-section results plotted from `CONTUR` event generation information for each unit mass point of τ' in figure 5.3. The top and bottom of the y-axis at the right plot is made to level with the cross-section axis on the left plot at 10^2 and 10^{-4} to enable an easier comparison. The `CONTUR`-excluded areas are marked on the right plot, which is the left side of the vertical dark blue line.

As shown in Figure 5.3, while the precise shape of the exclusion boundary in the cross-section parameter space from CONTUR is difficult to define, the results indicate that all parameter space with $M_{\tau'} \leq 410$ GeV is excluded. Referring to Figure 5.4 (b), the point at $M_{\tau'} = 400$ GeV corresponds to a production cross-section of approximately 0.1 pb, which is in close agreement with the NLO theoretical prediction shown by the solid red line in Figure 5.4 (a).

However, the dedicated ATLAS search achieves a stronger exclusion limit, reaching $M_{\tau'} \sim 900$ GeV, as it excludes smaller cross-sections than those excluded by CONTUR. This distinction can be visualised by noting that the CONTUR exclusion line roughly follows the NLO theory curve on the left plot, whereas the ATLAS exclusion extends to lower cross-sections. Additionally, the ATLAS search excludes VLL masses up to higher values, whereas CONTUR does not reach as far. Nevertheless, another CONTUR scan was performed for the lower mass region with the same granularity. The exclusion result is shown in figure 5.5.

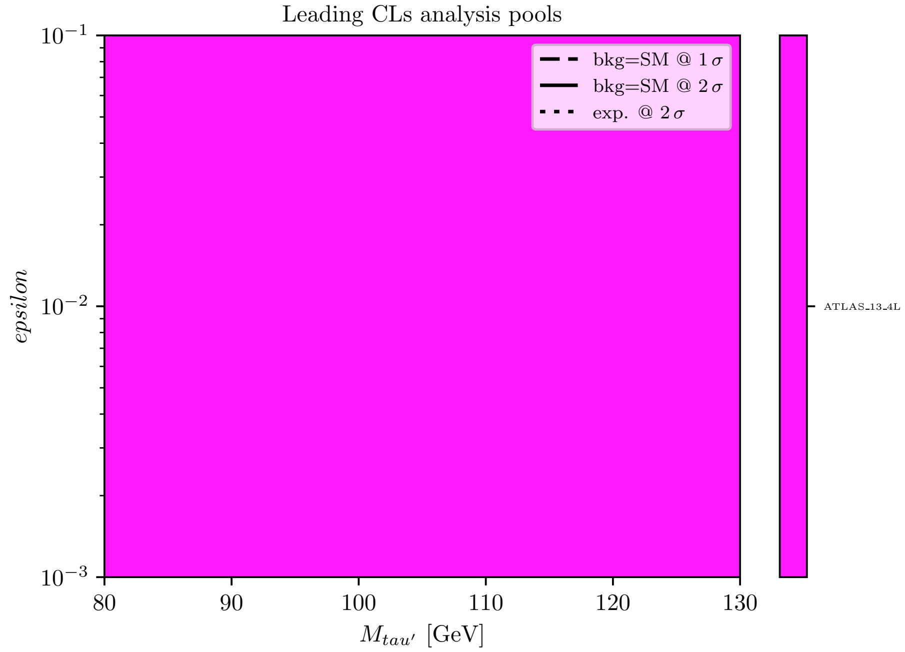

Figure 5.5: The figure shows the exclusion region of the low mass scan. The full parameter space for this scan is excluded by the ATALS four lepton measurement [153]

As shown in figure 5.5, CONTUR is able to exclude this search-unexplored region at 80 GeV $\leq M_{\tau'} \leq$ 130 GeV. In fact, the exclusion is dominantly contributed by the four lepton measurement [153]. This is expected as the high mass $\tau\tau$ measurement probed region with dilepton final states mass above 100 GeV. This demonstrates the utility of CONTUR, where the BSM scenario is compared to all available SM measurements at once and a global exclusion can be derived using the combined efforts of all SM measurements.

The inclusion of the new $\tau\tau$ measurement has proven valuable in improving the `CONTUR` exclusion limit for the VLL doublet model, although it does not match the sensitivity of the dedicated ATLAS search. This is expected, as the ATLAS search is specifically tailored towards the dedicated regions with optimised tunnings for event selection, background suppression and machine learning techniques to enhance sensitivity to the model. In contrast, the $\tau\tau$ measurement is not optimised for vector-like leptons, but rather aims to provide an inclusive signal measurement. Consequently, `CONTUR` exclusions naturally inherits larger uncertainties from the SM measurements, reducing its exclusion power on a particular model, and is further constrained by binned measurement results instead of using full event level data.

However, the strength of `CONTUR` framework's exclusion lies in its ability to provides a complementary method by examining a broader range of final states, without the need to spend large efforts (years) on building a dedicated search which only works on a specific model. It allows us to assess whether indirect constraints from existing SM measurements can match or even surpass dedicated searches in certain parameter space regions, such as the composite dark matter model study [157]. While in the case of this VLL doublet model, `CONTUR`'s upper limit exclusion is indeed weaker than the ATLAS search at high mass region, even with the inclusion of the newly measured high-mass $\tau\tau$ cross-section. However, the `CONTUR` result is able to constrain the search-unexplored lower mass region from using broader SM measured results and it remains highly valuable for testing other BSM models with third-generation lepton final states, such as the Z' models. Moreover, since the current $\tau\tau$ result includes only a single differential observable, future updates incorporating additional distributions and a larger dataset will further enhance the sensitivity of `CONTUR` and its potential impact on BSM reinterpretation.

Chapter 6

Conclusion

The search for Beyond Standard Model (BSM) physics is a core objective of the ATLAS experiment at the large hadron collider. Analysing the collected particle collision data is essential for testing existing theories and provide insights onto the direction on where the theoretical and experiment development should aim at. The direct approaches of analysis rely on dedicated direct searches, which are optimised in event selection and background suppression for specific new physics scenarios. However, complementary model-independent measurements offers an powerful alternative, which emphasis on maximising the research effort and extending our sensitivity to a broader range of possible deviations from the SM, obtaining search-comparable level of limits in short period of time, or providing an initial discovery prospects for various theoretical models.

In chapter 4, this thesis presents a high-mass $\tau\tau$ differential cross-section measurement using 139fb^{-1} of proton-proton collision data collected at $\sqrt{s} = 13$ TeV by ATLAS. This measurement explores a previously uncharted kinematic regime by employing a fiducial phase-space definition that enables direct comparisons with theoretical predictions, and enhances its reinterpretation potential for constraining BSM physics scenarios involving similar final states. The inclusive (i.e. independent of specific signal assumptions) differential cross-sections with respect to the $\tau\tau$ invariant mass were obtained at the particle level using the Iterative Bayesian Unfolding technique. This approach allows theorists to test a wide range of BSM models without requiring individual detector-level corrections, which facilitating efficient reinterpretation studies. In chapter 5, the thesis presents the results of using the `CONTUR` framework to assess the impact of this measurement in setting constraints on the third-generation Vector-Like Lepton (VLL) doublet model. With the addition of the new 13 TeV high-mass $\tau\tau$ measurement, `CONTUR`'s sensitivity to third-generation lepton interactions were improved and the resulted `CONTUR` plots shows that the upper range of excluded $M_{\tau'}$ mass extended from around 280 GeV to 410 GeV. While the ATLAS direct search remains dominant in the limit-setting power for the third-generation doublet VLL model, the `CONTUR` method can still be useful in other unexplored BSM models as the `CONTUR` analysis demonstrated exclusion potential with using a measurement of only one distribution and a much broader signal selection compared to the dedicated search analysis. Moreover, `CONTUR` is able to provide a new lower bound (80 GeV) of the excluded $M_{\tau'}$ range, which extended ATLAS search limit from 130 GeV $\leq M_{\tau'} \geq$ 970 GeV down to approximately 80 GeV. This demonstrates the utility of precision SM measurements in setting indirect constraints on BSM models, without the need for additional dedicated searches unless a strong discovery potential is indicated. The measurement could also contribute to extend the exclusion range for other BSM models involving τ final states, potentially achieving meaningful results within days.

Bibliography

[1] Roel Aaij et al. “Measurement of the ratio of branching fractions $\mathcal{B}(\bar{B}^0 \to D^{*+}\tau^-\bar{\nu}_\tau)/\mathcal{B}(\bar{B}^0 \to D^{*+}\mu^-\bar{\nu}_\mu)$”. In: *Phys. Rev. Lett.* 115.11 (2015). [Erratum: Phys.Rev.Lett. 115, 159901 (2015)], p. 111803. DOI: `10.1103/PhysRevLett.115.111803`. arXiv: `1506.08614 [hep-ex]`.

[2] Ishtiaq Ahmed and Abdur Rehman. “LHCb anomaly in $\boldsymbol{B\to K^*\mu^+\mu^-}$ optimised observables and potential of $\boldsymbol{Z'}$ Model”. In: *Chin. Phys. C* 42.6 (2018), p. 063103. DOI: `10.1088/1674-1137/42/6/063103`. arXiv: `1703.09627 [hep-ph]`.

[3] Claudia Cornella et al. “Reading the footprints of the B-meson flavor anomalies”. In: *JHEP* 08 (2021), p. 050. DOI: `10.1007/JHEP08(2021)050`. arXiv: `2103.16558 [hep-ph]`.

[4] Nilanjana Kumar and Stephen P. Martin. “Vectorlike Leptons at the Large Hadron Collider”. In: *Phys. Rev. D* 92.11 (2015), p. 115018. DOI: `10.1103/PhysRevD.92.115018`. arXiv: `1510.03456 [hep-ph]`.

[5] Jonathan M. Butterworth et al. “Constraining new physics with collider measurements of Standard Model signatures”. In: *JHEP* 03 (2017), p. 078. DOI: `10.1007/JHEP03(2017)078`. arXiv: `1606.05296 [hep-ph]`.

[6] A. Buckley et al. “Testing new physics models with global comparisons to collider measurements: the Contur toolkit”. In: *SciPost Phys. Core* 4 (2021), p. 013. DOI: `10.21468/SciPostPhysCore.4.2.013`. arXiv: `2102.04377 [hep-ph]`.

[7] Eamonn Maguire, Lukas Heinrich, and Graeme Watt. “HEPData: a repository for high energy physics data”. In: *J. Phys. Conf. Ser.* 898.10 (2017). Ed. by Richard Mount and Craig Tull, p. 102006. DOI: `10.1088/1742-6596/898/10/102006`. arXiv: `1704.05473 [hep-ex]`.

[8] D. Griffiths. *Introduction to Elementary Particles*. New York, USA: John Wiley Sons, 1987.

[9] David Galbraith. *Standard Model tikz diagram*. `https://davidgalbraith.org/portfolio/ux-standard-model-of-the-standard-model/`. 2024.

[10] James T. Wheeler. *Classical Mechanics: Noether’s Theorem*. `https://www.physics.usu.edu/Wheeler/ClassicalMechanics/CMNoetherTheorem.pdf`. Accessed: 2024-05-18. 2013.

[11] Author Unknown. *Higgs Potential*. `https://tikz.net/higgs-potential/`. Accessed: 2024-05-18.

[12] Feyza Baspehlivan et al. “Why should we search for vector-like leptons?” In: (Jan. 2022). arXiv: `2201.08251 [hep-ph]`.

[13] Prudhvi N. Bhattiprolu and Stephen P. Martin. “Prospects for vectorlike leptons at future proton-proton colliders”. In: *Phys. Rev. D* 100.1 (2019), p. 015033. DOI: `10.1103/PhysRevD.100.015033`. arXiv: `1905.00498 [hep-ph]`.

[14] Celine Degrande et al. “UFO - The Universal FeynRules Output”. In: *Comput. Phys. Commun.* 183 (2012), pp. 1201–1214. DOI: `10.1016/j.cpc.2012.01.022`. arXiv: `1108.2040 [hep-ph]`.

[15] Particle Data Group. *Kinematics Review*. [Online; accessed January 30, 2025]. 2022. URL: `https://pdg.lbl.gov/2022/reviews/rpp2022-rev-kinematics.pdf`.

[16] Maurizio Vretenar et al. *Linac4 design report*. Vol. 6. CERN Yellow Reports: Monographs. Geneva: CERN, 2020. DOI: `10.23731/CYRM-2020-006`. URL: `https://cds.cern.ch/record/2736208`.

[17] Esma Mobs. “The CERN accelerator complex in 2019. Complexe des accélérateurs du CERN en 2019”. In: (2019). General Photo. URL: `https://cds.cern.ch/record/2684277`.

[18] A. Donnachie and P. V. Landshoff. “Total cross sections”. In: *Physics Letters B* 296.1-2 (1992), pp. 227–232. DOI: `10.1016/0370-2693(92)90832-O`.

[19] J. T. Boyd. “LHC Run-2 and future prospects”. In: *CERN Yellow Rep. School Proc.* 5 (2022). Ed. by C. Duhr and M. Mulders, p. 247. DOI: `10.23730/CYRSP-2021-005.247`. arXiv: `2001.04370 [hep-ex]`.

[20] Georges Aad et al. “The ATLAS experiment at the CERN Large Hadron Collider: a description of the detector configuration for Run 3”. In: *JINST* 19.05 (2024), P05063. DOI: `10.1088/1748-0221/19/05/P05063`. arXiv: `2305.16623 [physics.ins-det]`.

[21] *Expected pileup values at the HL-LHC*. Tech. rep. All figures including auxiliary figures are available at `https://atlas.web.cern.ch/Atlas/GROUPS/PHYSICS/PUBNOTES/ATL-UPGRADE-PUB-2013-014`. Geneva: CERN, 2013. URL: `https://cds.cern.ch/record/1604492`.

[22] Michael Benedikt. *Pileup mitigation at the LHC: Current status and future prospects*. Technical Report CERN-BE-2022-001. CERN, 2022. URL: `https://cds.cern.ch/record/2802720/files/CERN-BE-2022-001.pdf`.

[23] ATLAS Collaboration. *Luminosity Public Results for Run 2*. [Accessed: 29-May-2024]. 2023. URL: `https://twiki.cern.ch/twiki/bin/view/AtlasPublic/LuminosityPublicResultsRun2`.

[24] M. Anastasopoulos et al. “Data-Preparation Quality and Performance of the ATLAS Level-1 Muon Endcap Trigger for Run 2”. In: *Instruments* 4.2 (2020), p. 18. DOI: `10.3390/instruments4020018`. URL: `https://www.researchgate.net/figure/Illustration-of-the-coordinate-systems-used-at-the-ATLAS-experiment-in-the-geographical_fig1_341809520`.

[25] Ed Daw. *Lecture 7: The Large Hadron Collider (LHC)*. [Accessed: 29-May-2024]. 2012. URL: `https://www.hep.shef.ac.uk/edaw/PHY206/Site/2012_course_files/phy206rlec7.pdf`.

[26] ATLAS Collaboration. *Discover ATLAS: Detector*. [Accessed: 29-May-2024]. 2024. URL: `https://atlas.cern/Discover/Detector`.

[27] ATLAS Collaboration. "The ATLAS Experiment at the CERN Large Hadron Collider". In: *European Physical Journal C* 70.3 (2010). [Accessed: 29-May-2024], pp. 1177–1233. DOI: `10.1140/epjc/s10052-010-1495-4`. URL: `https://cds.cern.ch/record/1262789/files/EurPhysJC.3FBE7E53d01.pdf`.

[28] A. Yamamoto et al. "Design and development of the ATLAS central solenoid magnet". In: *IEEE Transactions on Applied Superconductivity* 9 (July 1999), pp. 852–855.

[29] ATLAS Collaboration. "The ATLAS Inner Detector Sensor Modules". In: *ATLAS Experiment Documentation* (2022). The sensor modules of the inner detector are made of 46,080 small, discrete detecting element pixels, each with a size of 50 × 400 micrometers. URL: `https://atlas.cern/doc/inner_detector/sensor_modules`.

[30] Georges Aad et al. "Operation and performance of the ATLAS semiconductor tracker". In: *JINST* 9 (2014), P08009. DOI: `10.1088/1748-0221/9/08/P08009`. arXiv: `1404.7473 [hep-ex]`.

[31] A. Ahmad, Z. Albrechtskirchinger, et al. "The silicon microstrip sensors of the ATLAS semiconductor tracker". In: *Nuclear Instruments and Methods in Physics Research Section A: Accelerators, Spectrometers, Detectors and Associated Equipment* 578.1 (2007), pp. 98–118.

[32] A. Vogel. *ATLAS Transition Radiation Tracker (TRT): Straw Tube Gaseous Detectors at High Rates*. Technical report. Geneva: CERN, Apr. 2013.

[33] ATLAS Collaboration. “ATLAS Inner Detector: Readout Channels and Spatial Resolution”. In: *ATLAS Technical Documentation* (2023). In total, there are 351,000 readout channels, resulting in a spatial resolution of 130 μm in the R-ϕ direction, which is weaker than the Pixel Detector and the SCT. URL: `https://atlas.cern/doc/inner_detector/readout_channels`.

[34] Huaqiao Zhang. “The ATLAS liquid argon calorimeter: Overview and performance”. In: *Journal of Physics: Conference Series* 293 (Apr. 2011). DOI: `10.1088/1742-6596/293/1/012044`. URL: `https://doi.org/10.1088/1742-6596/293/1/012044`.

[35] A. La Rosa et al. *Performance of the ATLAS Liquid Argon Calorimeter after Three Years of LHC Operation*. Technical Report ATL-LARG-PROC-2013-002. [Accessed: 29-May-2024]. CERN, 2013. URL: `https://cds.cern.ch/record/1547314/files/ATL-LARG-PROC-2013-002.pdf`.

[36] W Lampl. “Optimizing the Energy Measurement of the ATLAS Electromagnetic Calorimeter”. Presented on 18 Jan 2006. Vienna, Tech. U., 2006. URL: `https://cds.cern.ch/record/923625`.

[37] Georges Aad et al. “Operation and performance of the ATLAS tile calorimeter in LHC Run 2”. In: (Jan. 2024). arXiv: `2401.16034 [hep-ex]`.

[38] E. Diehl et al. *Construction and Testing of the ATLAS Muon Spectrometer*. Technical Report SN-ATLAS-2003-030. CERN, 2003. URL: `https://cds.cern.ch/record/676896/files/sn-atlas-2003-030.pdf`.

[39] Sandro Palestini. “The muon spectrometer of the ATLAS experiment”. In: *Nuclear Physics B - Proceedings Supplements* 125 (2003), pp. 337–345.

[40] Koichi Nagai. “Thin gap chambers in ATLAS”. In: *Nuclear Instruments and Methods in Physics Research Section A: Accelerators, Spectrometers, Detectors and Associated Equipment* 384.1 (1996). BEAUTY ’96, pp. 219–221.

[41] E. Etzion et al. “The certification of ATLAS thin gap chambers produced in Israel and China”. In: *IEEE Symposium Conference Record Nuclear Science*. 2004. DOI: `10.1109/NSSMIC.2004.1462188`. URL: `http://dx.doi.org/10.1109/NSSMIC.2004.1462188`.

[42] J. R. Carter, P. I. Papanestis, and D. P. C. Sankey. “The trigger chambers of the ATLAS muon spectrometer: production and tests”. In: *Nuclear Instruments and Methods in Physics Research Section A: Accelerators, Spectrometers, Detectors and Associated Equipment* 530.1-2 (2004), pp. 199–210. ISSN: 0168-9002. DOI: `10.1016/j.nima.2004.05.041`. URL: `https://www.sciencedirect.com/science/article/abs/pii/S0168900204016511`.

[43] A. Yamamoto et al. “Progress in ATLAS central solenoid magnet”. In: *IEEE Trans. Appl. Supercond.* 10 (2000). Ed. by B. Cornett and Y. Jensen, pp. 353–356. DOI: `10.1109/77.828246`.

[44] CEA. *The Magnetic System of the ATLAS Experiment*. Accessed: 2024-05-29. 2023. URL: `https://irfu.cea.fr/en/Phocea/Vie_des_labos/Ast/ast_visu.php?id_ast=3010`.

[45] The ATLAS Collaboration. “The ATLAS Experiment at the CERN Large Hadron Collider”. In: *Journal of Instrumentation* 3 (Aug. 2008). DOI: `10.1088/1748-0221/3/08/S08003`. URL: `https://doi.org/10.1088/1748-0221/3/08/S08003`.

[46] ATLAS Collaboration. *Measurement of Magnetic Field with the Giant ATLAS Solenoid*. Accessed: 2024-05-28. 2021. URL: `https://www.golabz.eu/ils/measurement-of-magnetic-field-with-the-giant-atlas-solenoid`.

[47] Martin zur Nedden. *The Run-2 ATLAS Trigger System: Design, Performance and Plan*. Technical Report. Geneva: CERN, Dec. 2016. URL: `https://cds.cern.ch/record/2223838`.

[48] ATLAS Collaboration. *ATLAS High-Level Trigger, Data Acquisition and Controls: Technical Design Report*. Tech. rep. CERN, 2003. URL: `https://cds.cern.ch/record/616089`.

[49] P.A. Zyla et al. “Review of Particle Physics”. In: *Progress of Theoretical and Experimental Physics (PTEP)* 2020.8 (2020), p. 083C01. DOI: `10.1093/ptep/ptaa104`.

[50] F. Winklmeier. “Real-time configuration changes of the ATLAS high level trigger”. In: *2010 17th IEEE-NPSS Real Time Conference*. 2010, pp. 1–5. DOI: `10.1109/RTC.2010.5750436`.

[51] *Performance of the ATLAS Inner Detector Track and Vertex Reconstruction in the High Pile-Up LHC Environment*. Tech. rep. All figures including auxiliary figures are available at `https://atlas.web.cern.ch/Atlas/GROUPS/PHYSICS/CONFNOTES/ATLAS-CONF-2012-042`. Geneva: CERN, 2012. URL: `https://cds.cern.ch/record/1435196`.

[52] D. Pfeiffer et al. “LHC Physics: The ATLAS Experiment”. In: *Particle Physics Reference Library*. Ed. by C. Fabjan and H. Schopper. Springer, 2021, pp. 245–307. DOI: `10.1007/978-3-030-87938-9_5`. URL: `https://link.springer.com/chapter/10.1007/978-3-030-87938-9_5#citeas`.

[53] G. Piacquadio, K. Prokofiev, and A. Wildauer. “Primary vertex reconstruction in the ATLAS experiment at LHC”. In: *Journal of Physics: Conference Series* 119.3 (July 2008), p. 032033. DOI: `10.1088/1742-6596/119/3/032033`.

[54] ATLAS Collaboration. “Topological cell clustering in the ATLAS calorimeters and its performance in LHC Run 1”. In: *The European Physical Journal C* 77.7 (July 2017). DOI: `10.1140/epjc/s10052-017-5004-5`.

[55] W. Lampl et al. *Calorimeter Clustering Algorithms: Description and Performance*. Technical Report ATL-LARG-PUB-2008-002, ATL-COM-LARG-2008-003. Geneva: CERN, Apr. 2008. URL: `https://cds.cern.ch/record/1099735`.

[56] Georges Aad et al. "Topological cell clustering in the ATLAS calorimeters and its performance in LHC Run 1". In: *Eur. Phys. J. C* 77 (2017), p. 490. DOI: `10.1140/epjc/s10052-017-5004-5`. arXiv: `1603.02934 [hep-ex]`.

[57] G. Aad et al. "Readiness of the ATLAS Liquid Argon Calorimeter for LHC collisions". In: *Eur. Phys. J. C* 76.10 (2016), p. 666. DOI: `10.1140/epjc/s10052-016-4499-7`. arXiv: `1609.02820 [hep-ex]`.

[58] Morad Aaboud et al. "Electron reconstruction and identification in the ATLAS experiment using the 2015 and 2016 LHC proton-proton collision data at $\sqrt{s} = 13$ TeV". In: *Eur. Phys. J. C* 79.8 (2019), p. 639. DOI: `10.1140/epjc/s10052-019-7140-6`. arXiv: `1902.04655 [physics.ins-det]`.

[59] *Improved electron reconstruction in ATLAS using the Gaussian Sum Filter-based model for bremsstrahlung*. Tech. rep. All figures including auxiliary figures are available at `https://atlas.web.cern.ch/Atlas/GROUPS/PHYSICS/CONFNOTES/ATLAS-CONF-2012-047`. Geneva: CERN, 2012. URL: `https://cds.cern.ch/record/1449796`.

[60] Georges Aad et al. "Electron and photon performance measurements with the ATLAS detector using the 2015–2017 LHC proton-proton collision data". In: *JINST* 14.12 (2019), P12006. DOI: `10.1088/1748-0221/14/12/P12006`. arXiv: `1908.00005 [hep-ex]`.

[61] ATLAS Collaboration. "Electron and photon energy calibration with the ATLAS detector using LHC Run 1 data". In: *Journal of Instrumentation* 9.05 (2014), P05009. DOI: `10.1088/1748-0221/9/05/P05009`.

[62] Georges Aad et al. "Performance of electron and photon triggers in ATLAS during LHC Run 2". In: *Eur. Phys. J. C* 80.1 (2020), p. 47. DOI: `10.1140/epjc/s10052-019-7500-2`. arXiv: `1909.00761 [hep-ex]`.

[63] ATLAS Collaboration. *Muon reconstruction and identification in the ATLAS experiment*. `https://cds.cern.ch/record/2810287/files/ATL-PHYS-SLIDE-2022-168.pdf`. 2022.

[64] Georges Aad et al. “Muon reconstruction performance of the ATLAS detector in proton–proton collision data at $\sqrt{s}$ =13 TeV”. In: *Eur. Phys. J. C* 76.5 (2016), p. 292. DOI: `10.1140/epjc/s10052-016-4120-y`. arXiv: `1603.05598 [hep-ex]`.

[65] Georges Aad et al. “Muon reconstruction and identification efficiency in ATLAS using the full Run 2 pp collision data set at $\sqrt{s}$ = 13 TeV”. In: *Eur. Phys. J. C* 81.7 (2021), p. 578. DOI: `10.1140/epjc/s10052-021-09233-2`. arXiv: `2012.00578 [hep-ex]`.

[66] Keith Rehermann and Brock Tweedie. “Efficient Identification of Boosted Semileptonic Top Quarks at the LHC”. In: *JHEP* 03 (2011), p. 059. DOI: `10.1007/JHEP03(2011)059`. arXiv: `1007.2221 [hep-ph]`.

[67] ATLAS Collaboration. “Reconstruction and identification of hadronically decaying tau leptons in the ATLAS experiment”. In: *The European Physical Journal C* 76.5 (2016), p. 295. DOI: `10.1140/epjc/s10052-016-4095-8`.

[68] ATLAS Collaboration. “Performance of tau-lepton reconstruction and identification in ATLAS using pp collisions at √s = 13 TeV”. In: *The European Physical Journal C* 78.12 (2018), p. 1004. DOI: `10.1140/epjc/s10052-018-6499-9`.

[69] ATLAS Collaboration. *Performance of tau-lepton identification in 2017 ATLAS data*. ATL-PHYS-PUB-2019-033. 2019. URL: `https://cds.cern.ch/record/2688062/files/ATL-PHYS-PUB-2019-033.pdf`.

[70] ATLAS Collaboration. “Reconstruction, energy calibration, and identification of hadronically decaying tau leptons in the ATLAS experiment”. In: *Eur. Phys. J. C* 81.4 (2021), p. 349. DOI: `10.1140/epjc/s10052-021-09064-6`. arXiv: `2012.11279 [hep-ex]`.

[71] ATLAS Collaboration. “The ATLAS Experiment at the CERN Large Hadron Collider”. In: *JINST* 3 (2008), S08003. DOI: `10.1088/1748-0221/3/08/S08003`.

[72] ATLAS Collaboration. “Jet energy scale measurements and their systematic uncertainties in proton-proton collisions at $\sqrt{s}$ = 13 TeV with the ATLAS detector”. In: *Physical Review D* 96.7 (2017), p. 072002. DOI: `10.1103/PhysRevD.96.072002`.

[73] Matteo Cacciari, Gavin P. Salam, and Gregory Soyez. “The anti-k_t jet clustering algorithm”. In: *JHEP* 04 (2008), p. 063. DOI: `10.1088/1126-6708/2008/04/063`. arXiv: `0802.1189 [hep-ph]`.

[74] Georges Aad et al. “ATLAS b-jet identification performance and efficiency measurement with $t\bar{t}$ events in pp collisions at $\sqrt{s}$ = 13 TeV”. In: *Eur. Phys. J. C* 79.11 (2019), p. 970. DOI: `10.1140/epjc/s10052-019-7450-8`. arXiv: `1907.05120 [hep-ex]`.

[75] “Performance of b-Jet Identification in the ATLAS Experiment”. In: *JINST* 11 (2016), P04008. DOI: `10.1088/1748-0221/11/04/P04008`. arXiv: `1512.01094 [hep-ex]`.

[76] LHCb Collaboration. “Test of lepton universality in rare $b \to s\ell^+\ell^-$ decays”. In: *CERN Document Server* (2022). eprint: `https://cds.cern.ch/record/2845047/files/LHCb-PAPER-2022-046.pdf`.

[77] LHCb and Belle II Collaborations. “New limits for lepton universality violations in leptonic and semileptonic B-meson decays”. In: *Phys. Rev. Lett.* 131 (2023), p. 051803. DOI: `10.1103/PhysRevLett.131.051803`. URL: `https://link.aps.org/doi/10.1103/PhysRevLett.131.051803`.

[78] Georges Aad et al. “Measurement of the high-mass Drell–Yan differential cross-section in pp collisions at sqrt(s)=7 TeV with the ATLAS detector”. In: *Phys. Lett. B* 725 (2013), pp. 223–242. DOI: `10.1016/j.physletb.2013.07.049`. arXiv: `1305.4192 [hep-ex]`.

[79] Georges Aad et al. “Measurement of the double-differential high-mass Drell-Yan cross section in pp collisions at $\sqrt{s}$ = 8 TeV with the ATLAS detector”. In: *JHEP* 08 (2016), p. 009. DOI: `10.1007/JHEP08(2016)009`. arXiv: `1606.01736 [hep-ex]`.

[80] Albert M Sirunyan et al. “Measurement of the differential Drell-Yan cross section in proton-proton collisions at $\sqrt{\mathrm{s}} = 13$ TeV”. In: *JHEP* 12 (2019), p. 059. DOI: `10.1007/JHEP12(2019)059`. arXiv: `1812.10529 [hep-ex]`.

[81] Andy Buckley et al. “Rivet user manual”. In: *Comput. Phys. Commun.* 184 (2013), pp. 2803–2819. DOI: `10.1016/j.cpc.2013.05.021`. arXiv: `1003.0694 [hep-ph]`.

[82] Georges Aad et al. “Jet energy scale and resolution measured in proton–proton collisions at $\sqrt{s} = 13$ TeV with the ATLAS detector”. In: *Eur. Phys. J. C* 81.8 (2021), p. 689. DOI: `10.1140/epjc/s10052-021-09402-3`. arXiv: `2007.02645 [hep-ex]`.

[83] *Tagging and suppression of pileup jets with the ATLAS detector*. Tech. rep. All figures including auxiliary figures are available at `https://atlas.web.cern.ch/Atlas/GROUPS/PHYSICS/CONFNOTES/ATLAS-CONF-2014-018`. Geneva: CERN, 2014. URL: `https://cds.cern.ch/record/1700870`.

[84] Georges Aad et al. “Measurement of the c-jet mistagging efficiency in $t\bar{t}$ events using pp collision data at $\sqrt{s} = 13$ TeV collected with the ATLAS detector”. In: *Eur. Phys. J. C* 82.1 (2022), p. 95. DOI: `10.1140/epjc/s10052-021-09843-w`. arXiv: `2109.10627 [hep-ex]`.

[85] *Calibration of light-flavour b-jet mistagging rates using ATLAS proton-proton collision data at $\sqrt{s} = 13$ TeV*. Tech. rep. All figures including auxiliary figures are available at `https://atlas.web.cern.ch/Atlas/GROUPS/PHYSICS/CONFNOTES/ATLAS-CONF-2018-006`. Geneva: CERN, 2018. URL: `https://cds.cern.ch/record/2314418`.

[86] Johannes Bellm et al. “Herwig 7.1 Release Note”. In: (May 2017). arXiv: `1705.06919 [hep-ph]`.

[87] Torbjorn Sjostrand, Stephen Mrenna, and Peter Z. Skands. “PYTHIA 6.4 Physics and Manual”. In: *JHEP* 05 (2006), p. 026. DOI: `10.1088/1126-6708/2006/05/026`. arXiv: `hep-ph/0603175`.

[88] T. Gleisberg et al. "Event generation with SHERPA 1.1". In: *JHEP* 02 (2009), p. 007. DOI: `10.1088/1126-6708/2009/02/007`. arXiv: `0811.4622 [hep-ph]`.

[89] Johan Alwall et al. "MadGraph 5 : Going Beyond". In: *JHEP* 06 (2011), p. 128. DOI: `10.1007/JHEP06(2011)128`. arXiv: `1106.0522 [hep-ph]`.

[90] Zoltan Nagy and Davison E. Soper. "On factorization scheme suitable for NLO Monte Carlo event generators". In: *JHEP* 06 (2009), p. 114. DOI: `10.1088/1126-6708/2009/06/114`. arXiv: `0811.1911 [hep-ph]`. URL: `https://arxiv.org/abs/0811.1911`.

[91] Ringaile Placakyte. "Parton Distribution Functions". In: *31st International Symposium on Physics In Collision*. Nov. 2011. arXiv: `1111.5452 [hep-ph]`.

[92] Walter Greiner and Stefan Schramm. *Quantum Chromodynamics*. Springer, 2007. ISBN: 9783540005204.

[93] Gütschow C. *Monte Carlo for the LHC*. 2017. URL: `https://www.hep.ucl.ac.uk/postgrad/teaching/lhc/MC_2017.pdf`.

[94] Michael H. Seymour and Marilyn Marx. "Monte Carlo Event Generators". In: *69th Scottish Universities Summer School in Physics: LHC Physics*. Apr. 2013, pp. 287–319. DOI: `10.1007/978-3-319-05362-2_8`. arXiv: `1304.6677 [hep-ph]`.

[95] Andy Buckley et al. "General-purpose event generators for LHC physics". In: *Phys. Rept.* 504 (2011), pp. 145–233. DOI: `10.1016/j.physrep.2011.03.005`. arXiv: `1101.2599 [hep-ph]`.

[96] Institute for Theoretical Physics, University of Zurich. *Feynman Diagrams Listing*. `https://www.physik.uzh.ch/~che/FeynDiag/Listing.php#id5`. Accessed: 2024-07-27.

[97] Steffen Schumann. "W+jets as a background to top physics: The Quest for many jets". In: *Nuovo Cim. C* 033.4 (2010). Ed. by J. D'Hondt et al., pp. 149–157. DOI: `10.1393/ncc/i2010-10660-7`. arXiv: `1007.3454 [hep-ph]`.

[98] Alessandro Ballestrero et al. “Precise predictions for same-sign W-boson scattering at the LHC”. In: *Eur. Phys. J. C* 78.8 (2018), p. 671. DOI: `10.1140/epjc/s10052-018-6136-y`. arXiv: `1803.07943 [hep-ph]`.

[99] F. Cascioli, P. Maierhöfer, and S. Pozzorini. “Precise Higgs-background predictions: merging NLO QCD and squared quark-loop corrections to four-lepton + 0, 1 jet production”. In: *J. High Energy Phys.* 2012 (01 2012), p. 058. DOI: `10.1007/JHEP01(2012)058`. arXiv: `1109.0541 [hep-ph]`.

[100] Ansgar Denner, Stefan Dittmaier, and Lars Hofer. “COLLIER: a FORTRAN-based Complex One-Loop LIbrary in Extended Regularizations”. In: *Comput. Phys. Commun.* 212 (2017), pp. 220–238. DOI: `10.1016/j.cpc.2016.10.013`. arXiv: `1604.06792 [hep-ph]`.

[101] Steffen Schumann and Frank Krauss. “A Parton shower algorithm based on Catani-Seymour dipole factorization”. In: *J. High Energy Phys.* 2008 (03 2008), p. 038. DOI: `10.1088/1126-6708/2008/03/038`. arXiv: `0709.1027 [hep-ph]`.

[102] Stefan Hoeche et al. “QCD matrix elements + parton showers: The NLO case”. In: *J. High Energy Phys.* 2013 (04 2013), p. 027. DOI: `10.1007/JHEP04(2013)027`. arXiv: `1207.5030 [hep-ph]`.

[103] Stefan Hoeche et al. “Systematic event generator tuning for the LHC”. In: *Eur. Phys. J. C* 73 (4 2013), p. 2509. DOI: `10.1140/epjc/s10052-013-2509-4`. arXiv: `1201.5882 [hep-ph]`.

[104] Stefano Catani, Stefano Dittmaier, and Zoltan Trocsanyi. “One-loop soft and collinear divergences in parton-parton scattering”. In: *Phys. Lett. B* 500 (1-2 2001), pp. 149–160. DOI: `10.1016/S0370-2693(01)00065-X`. arXiv: `hep-ph/0011222 [hep-ph]`.

[105] Stefan Hoeche et al. “Matching parton showers and matrix elements”. In: *J. High Energy Phys.* 2009 (05 2009), p. 053. DOI: `10.1088/1126-6708/2009/05/053`. arXiv: `0903.1219 [hep-ph]`.

[106] Richard D. Ball et al. “Parton distributions for the LHC Run II”. In: *J. High Energy Phys.* 2015 (04 2015), p. 040. DOI: `10.1007/JHEP04(2015)040`. arXiv: `1410.8849 [hep-ph]`.

[107] Paolo Nason et al. “SHERPA: a Monte Carlo event generator”. In: *J. High Energy Phys.* 2004 (11 2004), p. 040. DOI: `10.1088/1126-6708/2004/11/040`. arXiv: `hep-ph/0409146 [hep-ph]`.

[108] Stefano Frixione, Paolo Nason, and Carlo Oleari. “Matching NLO QCD computations with Parton Shower simulations: the POWHEG method”. In: *J. High Energy Phys.* 2007 (11 2007), p. 070. DOI: `10.1088/1126-6708/2007/11/070`. arXiv: `0709.2092 [hep-ph]`.

[109] Simone Alioli et al. “A general framework for implementing NLO calculations in shower Monte Carlo programs: the POWHEG BOX”. In: *J. High Energy Phys.* 2010 (06 2010), p. 043. DOI: `10.1007/JHEP06(2010)043`. arXiv: `1002.2581 [hep-ph]`.

[110] Simone Alioli et al. “NLO single-top production matched with shower in POWHEG: s- and t-channel contributions”. In: *J. High Energy Phys.* 2009 (09 2009), p. 111. DOI: `10.1088/1126-6708/2009/09/111`. arXiv: `0907.4076 [hep-ph]`.

[111] Torbjorn Sjostrand, Stephen Mrenna, and Peter Z. Skands. “A Brief Introduction to PYTHIA 8.1”. In: *Comput. Phys. Commun.* 178 (2008), pp. 852–867. DOI: `10.1016/j.cpc.2008.01.036`. arXiv: `0710.3820 [hep-ph]`.

[112] Georges Aad et al. “Measurement of the Z/γ^* boson transverse momentum distribution in pp collisions at $\sqrt{s} = 7$ TeV with the ATLAS detector”. In: *JHEP* 09 (2014), p. 145. DOI: `10.1007/JHEP09(2014)145`. arXiv: `1406.3660 [hep-ex]`.

[113] Hung-Liang Lai et al. “New parton distributions for collider physics”. In: *Phys. Rev. D* 82 (7 2010), p. 074024. DOI: `10.1103/PhysRevD.82.074024`. arXiv: `1007.2241 [hep-ph]`.

[114] Jon Pumplin et al. "New generation of parton distributions with uncertainties from global QCD analysis". In: *J. High Energy Phys.* 2002 (07 2002), p. 012. DOI: `10.1088/1126-6708/2002/07/012`. arXiv: `hep-ph/0201195 [hep-ph]`.

[115] Piotr Golonka and Zbigniew Was. "The tauola-photos-F environment for the TAUOLA and PHOTOS packages, release II". In: *Eur. Phys. J. C* 45 (1 2006), pp. 97–107. DOI: `10.1140/epjc/s2005-02396-4`. arXiv: `hep-ph/0506026 [hep-ph]`.

[116] David J. Lange. "The EvtGen particle decay simulation package". In: *Nucl. Instrum. Meth. A* 462 (1-2 2001), pp. 152–155. DOI: `10.1016/S0168-9002(01)00089-4`.

[117] Feynman.Net. *Top Quark Pair Production*. Accessed: 1 March 2025. 2025. URL: `https://feynm.net/ttbar/#ttbar-009`.

[118] Stefano Frixione, Paolo Nason, and Giovanni Ridolfi. "Matching NLO QCD and Parton Showers in Heavy Flavour Production". In: *J. High Energy Phys.* 2007 (08 2007), p. 126. DOI: `10.1088/1126-6708/2007/08/126`. arXiv: `0707.3088 [hep-ph]`.

[119] *Studies on top-quark Monte Carlo modelling for Top2016*. Tech. rep. All figures including auxiliary figures are available at `https://atlas.web.cern.ch/Atlas/GROUPS/PHYSICS/PUBNOTES/ATL-PHYS-PUB-2016-020`. Geneva: CERN, 2016. URL: `https://cds.cern.ch/record/2216168`.

[120] Torbjorn Sjostrand et al. "An Introduction to PYTHIA 8.2". In: *Comput. Phys. Commun.* 191 (2015), pp. 159–177. DOI: `10.1016/j.cpc.2015.01.024`. arXiv: `1410.3012 [hep-ph]`.

[121] *ATLAS Pythia 8 tunes to 7 TeV data*. Tech. rep. All figures including auxiliary figures are available at `https://atlas.web.cern.ch/Atlas/GROUPS/PHYSICS/PUBNOTES/ATL-PHYS-PUB-2014-021`. Geneva: CERN, 2014. URL: `https://cds.cern.ch/record/1966419`.

[122] Richard D. Ball et al. “Parton distributions with LHC data”. In: *Nucl. Phys. B* 867 (2 2013), pp. 244–289. DOI: `10.1016/j.nuclphysb.2012.10.003`. arXiv: `1207.1303 [hep-ph]`.

[123] Johannes Bellm, Stefan Gieseke, and Patrick Kirchgaesser. “Improving the description of multiple interactions in Herwig”. In: *Eur. Phys. J. C* 80.5 (2020), p. 469. DOI: `10.1140/epjc/s10052-020-8002-y`. arXiv: `1911.13149 [hep-ph]`.

[124] Johannes Bellm et al. “Herwig 7.0 / Herwig++ 3.0 Release Note”. In: *Eur. Phys. J. C* 76 (4 2016), p. 196. DOI: `10.1140/epjc/s10052-016-4018-8`. arXiv: `1512.01178 [hep-ph]`.

[125] L. A. Harland-Lang et al. “Parton distributions in the LHC era: MMHT 2014 PDFs”. In: *Eur. Phys. J. C* 75.5 (2015), p. 204. DOI: `10.1140/epjc/s10052-015-3397-6`. arXiv: `1412.3989 [hep-ph]`.

[126] J. Alwall et al. “The automated computation of tree-level and next-to-leading order differential cross sections, and their matching to parton shower simulations”. In: *JHEP* 07 (2014), p. 079. DOI: `10.1007/JHEP07(2014)079`. arXiv: `1405.0301 [hep-ph]`.

[127] Sarah Heim et al. “Next-to-leading order QCD corrections to s-channel single top quark production and decay at the LHC”. In: *Phys. Rev. D* 81 (2010), p. 034005. DOI: `10.1103/PhysRevD.81.034005`. arXiv: `0911.0620 [hep-ph]`.

[128] Jennifer Kile and Julian von Wimmersperg-Toeller. “Simulation of $e^+e^- \rightarrow$ Hadrons and Comparison to ALEPH Data at Full Detector Simulation with an Emphasis on Four-Jet States”. In: (June 2017). arXiv: `1706.02269 [hep-ex]`.

[129] A. Bermudez Martinez, F. Hautmann, and M. L. Mangano. “TMD evolution and multi-jet merging”. In: *Phys. Lett. B* 822 (2021), p. 136700. DOI: `10.1016/j.physletb.2021.136700`. arXiv: `2107.01224 [hep-ph]`.

[130] Pouya Asadi et al. “Searching for leptoquarks at future muon colliders”. In: *JHEP* 10 (2021), p. 182. DOI: `10.1007/JHEP10(2021)182`. arXiv: `2104.05720 [hep-ph]`.

[131] Johan Alwall, Simon de Visscher, and Fabio Maltoni. “QCD radiation in the production of heavy colored particles at the LHC”. In: *JHEP* 02 (2009), p. 017. DOI: `10.1088/1126-6708/2009/02/017`. arXiv: `0810.5350 [hep-ph]`.

[132] Leif Lönnblad. “Correcting the colour-dipole cascade model with fixed order matrix elements”. In: *Journal of High Energy Physics* 2002.05 (2001), p. 046. DOI: `10.1088/1126-6708/2002/05/046`. arXiv: `hep-ph/0112284 [hep-ph]`.

[133] Leif Lönnblad. “ThePEG 1.5 - A Toolkit for High Energy Physics Event Generation”. In: *The European Physical Journal C* 71 (2011), p. 1661. DOI: `10.1140/epjc/s10052-011-1661-8`. arXiv: `1101.2242 [hep-ph]`.

[134] Vojtech Pleskot et al. *Universal Fake Factor Method*. Tech. rep. Geneva: CERN, 2023. URL: `https://cds.cern.ch/record/2864863`.

[135] Chris Pollard et al. *Measurements and searches in high-mass $\tau\tau$ production with the ATLAS detector*. Tech. rep. Geneva: CERN, 2022. URL: `https://cds.cern.ch/record/2810706`.

[136] G. D’Agostini. *Improved iterative Bayesian unfolding*. 2010. arXiv: `1010.0632 [physics.data-an]`.

[137] Christian Bierlich et al. “Robust Independent Validation of Experiment and Theory: Rivet version 3”. In: *SciPost Phys.* 8 (2020), p. 026. DOI: `10.21468/SciPostPhys.8.2.026`. arXiv: `1912.05451 [hep-ph]`.

[138] University of Cambridge. *Theoretical High Energy Physics at the University of Cambridge*. `https://www.hep.phy.cam.ac.uk/research/theory`. Accessed: 2024-07-23. 2024.

[139] Carlo Oleari. “The POWHEG-BOX”. In: *Nucl. Phys. B Proc. Suppl.* 205-206 (2010). Ed. by Johannes Blümlein, Sven-Olaf Moch, and Tord Riemann, pp. 36–41. DOI: `10.1016/j.nuclphysbps.2010.08.016`. arXiv: `1007.3893 [hep-ph]`.

[140] *Luminosity determination in pp collisions at $\sqrt{s} = 13$ TeV using the ATLAS detector at the LHC*. Tech. rep. All figures including auxiliary figures are available at `https://atlas.web.cern.ch/Atlas/GROUPS/PHYSICS/CONFNOTES/ATLAS-CONF-2019-021`. Geneva: CERN, 2019. URL: `https://cds.cern.ch/record/2677054`.

[141] Georges Aad et al. “Luminosity determination in pp collisions at $\sqrt{s} = 13$ TeV using the ATLAS detector at the LHC”. In: *Eur. Phys. J. C* 83.10 (2023), p. 982. DOI: `10.1140/epjc/s10052-023-11747-w`. arXiv: `2212.09379 [hep-ex]`.

[142] G Avoni et al. “The new LUCID-2 detector for luminosity measurement and monitoring in ATLAS”. In: *JINST* 13.07 (2018), P07017. DOI: `10.1088/1748-0221/13/07/P07017`. URL: `https://cds.cern.ch/record/2633501`.

[143] Lara Mason. “Measurements of the ATLAS tau trigger reconstruction and identification efficiencies using 2016 data from pp collisions at$\sqrt{s} = 13$ TeV”. MA thesis. Melbourne U., 2017.

[144] Andy Buckley et al. “LHAPDF6: parton density access in the LHC precision era”. In: *Eur. Phys. J. C* 75 (2015), p. 132. DOI: `10.1140/epjc/s10052-015-3318-8`. arXiv: `1412.7420 [hep-ph]`.

[145] Georges Aad et al. “Differential cross-sections for events with missing transverse momentum and jets measured with the ATLAS detector in 13 TeV proton-proton collisions”. In: *JHEP* 08 (2024), p. 223. DOI: `10.1007/JHEP08(2024)223`. arXiv: `2403.02793 [hep-ex]`.

[146] Waleed Abdallah et al. “Reinterpretation of LHC Results for New Physics: Status and Recommendations after Run 2”. In: *SciPost Phys.* 9.2 (2020),

p. 022. DOI: 10.21468/SciPostPhys.9.2.022. arXiv: 2003.07868 [hep-ph].

[147] Adam Alloul et al. "FeynRules 2.0 - A complete toolbox for tree-level phenomenology". In: *Comput. Phys. Commun.* 185 (2014), pp. 2250–2300. DOI: 10.1016/j.cpc.2014.04.012. arXiv: 1310.1921 [hep-ph].

[148] P. Harrison and The CONTUR Collaboration. *Method*. Website. Accessed: 30 January 2025. n.d. URL: https://hepcedar.gitlab.io/contur-webpage/method/index.html#toolchain.

[149] Emma Elkington. *Constraining Vector-Like Lepton Models at the Large Hadron Collider*. Project Report. University College London, Department of Physics & Astronomy, Aug. 2024.

[150] Jon Butterworth et al. "Dark matter from anomaly cancellation at the LHC". In: *Phys. Rev. D* 110.7 (2024), p. 075001. DOI: 10.1103/PhysRevD.110.075001. arXiv: 2405.03749 [hep-ph].

[151] Georges Aad et al. "Inclusive and differential cross-sections for dilepton $t\bar{t}$ production measured in $\sqrt{s} = 13$ TeV pp collisions with the ATLAS detector". In: *JHEP* 07 (2023), p. 141. DOI: 10.1007/JHEP07(2023)141. arXiv: 2303.15340 [hep-ex].

[152] Georges Aad et al. "Measurements of $W^+W^-+ \geq 1$ jet production cross-sections in pp collisions at $\sqrt{s} = 13$ TeV with the ATLAS detector". In: *JHEP* 06 (2021), p. 003. DOI: 10.1007/JHEP06(2021)003. arXiv: 2103.10319 [hep-ex].

[153] Georges Aad et al. "Measurements of differential cross-sections in four-lepton events in 13 TeV proton-proton collisions with the ATLAS detector". In: *JHEP* 07 (2021), p. 005. DOI: 10.1007/JHEP07(2021)005. arXiv: 2103.01918 [hep-ex].

[154] Georges Aad et al. "Measurements of the Higgs boson inclusive and differential fiducial cross-sections in the diphoton decay channel with pp colli-

sions at $\sqrt{s} = 13$ TeV with the ATLAS detector". In: *JHEP* 08 (2022), p. 027. DOI: `10.1007/JHEP08(2022)027`. arXiv: `2202.00487 [hep-ex]`.

[155] ATLAS Collaboration. *Differential measurements of high-mass di-tau production, searches for high-mass particles with couplings to third-generation fermions, and contsraints on τ-lepton relevant EFT operators, including an interpretation of the τ-lepton anomalous magnetic and electric moments, using $\sqrt{s} = 13$ TeVproton-proton collision data collected with the ATLAS detector*. CERN CDS. ATL-COM-PHYS-2022-444. 2022. URL: `https://cds.cern.ch/record/2810706/files/ATL-COM-PHYS-2022-444.pdf`.

[156] Shalini Epari. "Searches for vector-like leptons in ATLAS". In: *PoS* LHCP2024 (2025), p. 014. DOI: `10.22323/1.478.0014`.

[157] J. M. Butterworth et al. "New sensitivity of LHC measurements to composite dark matter models". In: *Phys. Rev. D* 105.1 (2022), p. 015008. DOI: `10.1103/PhysRevD.105.015008`. arXiv: `2105.08494 [hep-ph]`.